UNIVERSITY OF SOUTHAMPTON

FACULTY OF ENGINEERING, SCIENCE
& MATHEMATICS

Optoelectronics Research Centre

Pulsed Laser Deposition of Thick Multilayer Garnet Crystal Films for Waveguide Laser Devices

by

Timothy Christopher May-Smith

Thesis submitted for the Degree of Doctor of Philosophy

April 2005

UNIVERSITY OF SOUTHAMPTON

ABSTRACT

FACULTY OF ENGINEERING, SCIENCE & MATHEMATICS

OPTOELECTRONICS RESEARCH CENTRE

Doctor of Philosophy

PULSED LASER DEPOSITION OF THICK MULTILAYER GARNET CRYSTAL FILMS FOR WAVEGUIDE LASER DEVICES

by Timothy Christopher May-Smith

The main aim of this project was to use the technique of pulsed laser deposition (PLD) to fabricate thick multilayered garnet crystal planar waveguides with rare-earth ion doped cores for use as planar waveguide laser devices. Planar waveguides are of interest because of the implications of their structure, which allows for lasing, pumping and heat dissipation to each have a unique axis of operation, and the confinement properties of planar waveguide lasers result in lower pump power thresholds, higher gains per unit pump power and higher efficiencies than their bulk counterparts. Thick planar waveguide lasers are desirable because they can be pumped by high power diode laser arrays, and suffer less from the detrimental effect of particulates (a practically unavoidable side effect of the PLD technique). The use of multilayers allows a device with a high numerical aperture to be fabricated and the careful choice of the cladding layer thicknesses and refractive indices allows good beam quality output to be produced using diode pumping. Other aims of the project were to fabricate a self-imaging waveguide amplifier and explore other applications of thick garnet crystal films such as the possibility of using a highly doped thick film as a thin-disk laser device.

The PLD growth conditions were optimised and all of the deposited garnet crystal films were found to be highly textured crystal and had compositions close to bulk crystals. The deposition of thick films without a high occurrence of particulates was made possible by the use of multiple growth runs with target repositioning and reconditioning between growth runs. Two thick Nd:GGG films were fabricated and subsequently operated as laser devices when pumped by a Ti:sapphire laser and a diode laser array. The absorption and fluorescence properties of the Nd:GGG films were found to be close to bulk, but slightly broadened. Minimum threshold pump powers of 17.8 mW and 7.44 W were observed for the Nd:GGG films with Ti:sapphire pumping and diode pumping respectively. Maximum slope efficiencies of 32.0% and 11.2% were obtained with the Nd:GGG films with Ti:sapphire pumping and diode pumping respectively. A maximum laser output of 4.0 W was produced from one of the Nd:GGG films using diode pumping. Loss estimates of < 0.1 dBcm^{-1} and < 0.4 dBcm^{-1} were obtained for the two Nd:GGG films that were operated as laser devices. The effect of self-imaging was observed in a YAG capped Nd:GGG film. A thick YbAG film was fabricated to be used as a thin-disk laser, though lasing has not been observed from experiments so far. Films of YGG, Nd,Cr:YSAG, Cr:GSAG and Nd,Cr:GSGG have been deposited, proving the potential of the optimal growth conditions found for the current setup. A four-layer film of YGG, Nd,Cr:GSGG and YAG was deposited and is awaiting laser trial experiments.

Now that the technique of thick garnet crystal film deposition via multiple growth runs has been established, the potential of thick garnet crystal films needs to be exploited. Multilayer structures with more ideal geometries need to be fabricated to make optimal waveguide laser devices and difficulties resulting from thermal expansion mismatch need to be addressed so that side-pumping can be performed with diode laser arrays.

"The greatest thing you'll ever learn

Is just to love and be loved in return."

Eden Ahbez

List of Contents

List of Tables

List of Figures

Author's Declaration

I, **Timothy Christopher May-Smith**, declare that this thesis entitled *Pulsed Laser Deposition of Thick Multilayer Garnet Crystal Films for Waveguide Laser Devices* and the work presented in it are my own. I confirm that:

- this work was done wholly or mainly while in candidature for a research degree at the University of Southampton;
- where any part of this thesis has previously been submitted for a degree or any other qualification at this University or any other institution, this has been clearly stated;
- where I have consulted the published work of others, this is always clearly attributed;
- where I have quoted from the work of others, the source is always given. With the exception of such quotations, this thesis is entirely my own work;
- I have acknowledged all main sources of help;
- where the thesis is based on work done by myself jointly with others, I have made clear exactly what was done by others and what I have contributed myself (see next page);
- parts of this work have been published (see Appendix I for details).

Signed: …… Date: …….

The following table details the sources of collaboration for work performed jointly with others that has contributed towards this thesis. I carried out all of the film fabrication by myself, and unless otherwise stated in the table below, all polishing, waveguide preparation, characterisation and laser experiments were performed by myself (a dash in the table below indicates that the work was carried out by myself alone).

Sample/s	**Structural and compositional characterisation**	**Polishing and waveguide preparation**	**Laser experiments**
40 μm thick Nd:GGG film	-	C. Grivas [a]	C. Grivas [a]
50 μm thick Nd:GGG film	-	-	[Ti:sapphire pumping] - [Diode pumping] J. Wang [b]
Wedge-polished 30 μm thick Nd:GGG film	M. J. F. Healy [c]	n/a	n/a
27 μm thick YAG capped Nd:GGG film	-	-	J. Wang [d]
18 μm thick YbAG film	-	-	P. Wang [e]
YGG, Nd,Cr:YSAG, Cr:GSAG and Nd,Cr:GSGG single-layer films	-	n/a	n/a
Four-layer film of YGG, Nd,Cr:GSGG and YAG	-	n/a	n/a

a. Polishing, waveguide preparation and laser experiments with the 40 μm thick Nd:GGG film were performed jointly with C. Grivas (ORC, University of Southampton).

b. Diode pumping of the 50 μm thick Nd:GGG film was performed jointly with J. Wang (ORC, University of Southampton).

c. Rutherford backscattering analysis on a wedge-polished 30 μm thick Nd:GGG film was performed by M. J. F. Healy (Ion Beam Analysis Facility, Cranfield University).

d. Self-imaging experiments with the 27 μm thick YAG capped Nd:GGG film were performed jointly with J. Wang (ORC, University of Southampton).

e. Lasing trial experiments with the 18 μm thick YbAG film were performed by P. Wang (ORC, University of Southampton).

Signed: …… Date: …….

Acknowledgements

The work presented in this thesis has been supported by EPSRC under the funding of grant number GR/R74154/01. I also acknowledge the receipt of an EPSRC studentship and further funding from the ORC.

I would like to thank Rob, Christos and Dave for all of the help and advice they have given me throughout the project. In particular, Rob has been fantastic with everything from simply coming up with ideas, to discussing physics and helping me correct my writing, and Christos has been an essential guide to experimental work. Thanks also go to Jing and Pu for making some experiments possible that would have been very difficult for me to do without them. Special thanks go to Steve B for 'keeping PLD real', and to the masters of polishing, Corin, Christos, Simon and Alex for passing the art on to me. Thanks to all of the technicians for making things and helping me make things, and in particular thanks to Niel for helping me keep the excimer laser operational. Thanks also to everybody else at the ORC that has helped to make my work possible.

Thanks to M. J. F. Healy (Ion Beam Analysis Facility, Cranfield University) for the Rutherford backscattering analysis, and thanks to the EPSRC National Crystallography Centre (Chemistry Department, University of Southampton) for letting me use the diffractometers.

Big thanks to my wife Claire for buying me clothes and supporting me throughout the ups and downs of student life, and thanks to my parents for being so dependable and teaching me the potential rewards of hard work. Thanks to the guys for sharing the experience of lunch with me, and thanks to my office mates for being quiet. Special thanks go to Iain for taking care of me in San Francisco. Finally, thanks to Tim for such an uplifting friendship (and thanks to La for taking care of Tim).

Symbols and Abbreviations

A, B	Example elemental species.
A_1, A_2 and A_3	Constants.
a_0 and $\bar{a}_0$	Lattice parameters for unstressed bulk crystal and a stressed film respectively.
a_1, a_2 and a_3	Dispersion relations.
A_S	Surface area of a grey-body.
A_XB_Y	Example compound consisting of species A and B in the ratio X:Y.
BBO	Beta barium borate (BaB_2O_4).
BNN	Barium sodium niobate ($Ba_2NaNb_5O_{12}$).
CBPLD	Crossed-beam pulsed laser deposition.
CCD	Charged coupled device.
C_p and C_v	Specific heat at a constant pressure and volume respectively.
$C_p(T)$	Temperature dependent heat capacity per unit mass.
CVD	Chemical vapour deposition.
cw	Continuous-wave.
D	Crystal plane spacing.
d	Depth of waveguide core.
d_a	Depth removed by ablation.
DC	Direct current.
d_f and d_s	Film and substrate thicknesses respectively.
DRS	Diffuse reflectance spectroscopy.
$\mathbf{E}(x, y, z, t)$	Full electric field function of a guided mode.
$\mathbf{E}(x, y)$	x and y dependence of the electric field function of a guided mode.
EDX	Energy dispersive X-ray analysis.
E_f and E_s	Young's moduli of a film and substrate respectively.
EO	Electro-optic.
E_x, E_y and E_z	x, y, and z-components of $\mathbf{E}$ respectively.
f_1 and f_2	Fractional population in the lower and upper laser levels respectively.
f_A and f_B	Stoichiometry factor for species A and B respectively (equation 4.5.2).
f_i	Stoichiometry factor for species i (equation 4.5.3).
F_L	Laser fluence.
$F_{L\text{-}th}$	Threshold laser fluence for ablation.

FWHM	Full width half maximum.
GAG	Gadolinium aluminium garnet ($Gd_3Al_5O_{12}$).
GGG	Gadolinium gallium garnet ($Gd_3Ga_5O_{12}$).
GSAG	Gadolinium scandium aluminium garnet ($Gd_3Sc_2Al_3O_{12}$).
GSGG	Gadolinium scandium gallium garnet ($Gd_3Sc_2Ga_3O_{12}$).
h	Planck's constant.
$\mathbf{H}(x, y, z, t)$	Full magnetic field function of a guided mode.
$\mathbf{H}(x, y)$	x and y dependence of the magnetic field function of a guided mode.
H_A and H_B	Height of the RBS spectrum plateau corresponding to species A and B respectively.
HR and HT	High reflectance and high transmittance respectively.
H_x, H_y and H_z	x, y and z-components of **H** respectively.
$I_o(t)$	Time dependent laser intensity.
IR	Infra-red
I_s	Saturation intensity of the laser transition.
k	Boltzmann's constant.
$K(T)$	Temperature dependent thermal conductivity.
K_A and K_B	Kinematic factor for species A and B respectively.
KGW	Potassium gadolinium tungstate ($KGd(WO_4)_2$).
K_i	Kinematic factor for species i.
KTP	Potassium titanyl phosphate ($KTiOPO_4$).
l	Cavity length (length of the laser medium).
L_{abs}	Absorption depth.
LACVD	Laser-assisted chemical vapour deposition.
l_c	Cavity length (length of an external cavity).
L_{diff}	Diffusion depth.
L_{eff}	Launch efficiency.
LIPSS	Laser induced periodic surface structures.
L_{lenses}	Loss factor for lenses before the waveguide input face.
LMA	Large-mode-area.
LPE	Liquid phase epitaxy.
L_{PL}	Round trip propagation loss exponent.
m	Integer = mth mode number.
M	Maximum number of supported modes above the fundamental.
m_1	Mass of incident ions.
MBE	Molecular beam epitaxy.
MEMS	Micro-electro-mechanical systems.
m_i	Mass of plume constituent or sample atom i.
MMI	Multimode interference.
MO	Magneto-optic.
MOCVD	Metal-organic chemical vapour deposition.
M_p	Melting point.

M_x^2 and M_y^2	M-squared values for a laser beam in the x and y directions respectively.
n	Refractive index of a cavity (core region).
n_0, n_1, n_2 and n_3	Refractive indices of the outer region, superstrate, core and substrate respectively.
N_0^1	Population density of the lower laser level.
NA	Numerical aperture.
N_A and N_B	Number density of species A and B respectively.
n_e, n_i and n_n	Electron, ion and neutral number densities respectively.
P_1 and P_2	Power before the input and after the output waveguide faces respectively.
P_{abs}	Absorbed power.
P_{CO2}	Output power of the CO_2 laser
P_E	Power emitted by a grey-body.
PECVD	Plasma enhanced chemical vapour deposition.
P_l	Laser output power.
PLD	Pulsed laser deposition.
P_p	Incident pump power.
$P_{p\text{-}th}$	Incident pump power threshold for lasing.
P_{th}	Absorbed pump power threshold for lasing.
r	Radial coordinate.
R	Radius of curvature of sample bending due to stress.
$R(T)$	Temperature dependent reflection coefficient.
R_1 and R_2	Reflectivity of the feedback and output coupling mirrors respectively.
R_{2A} and R_{2B}	Reflectivities of output coupling mirrors A and B respectively.
RBS	Rutherford backscattering analysis.
R_G and R_Y	GGG-air and YAG-air Fresnel reflectivities.
RHEED	Reflection high-energy electron diffraction.
R_M	Input mirror pump light reflectivity.
RSPLD	Rapid sequential pulsed laser deposition.
S and F	Normalised laser and pumping power respectively.
S_1	Average stopping power of a material for ingoing path of ion.
S_{2A} and S_{2B}	Average stopping power of a material for outgoing path of ion after scattering from species A and B respectively.
S_a	Stopping power of a material for path a.
SAW	Surface acoustic wave.
SBN	Strontium barium niobate ($Sr_xBa_{1-x}Nb_2O_6$).
SEM	Scanning electron microscopy.
SHG	Second harmonic generation.
T	Temperature.
t	Time dimension.
$T(x, t)$	Temperature inside the target.
TE	Transverse electric.
TM	Transverse magnetic.

T_o	Initial temperature of the plasma at the beginning of unsteady adiabatic expansion.
T_{OC}	Transmission exponent (of the output and feedback mirrors).
TVD	Thermal vapour deposition.
UAE	Unsteady adiabatic expansion.
UHV	Ultra-high vacuum.
U_i	First ionisation potential.
UV	Ultra-violet.
v_f and v_s	Poisson's ratios for a film and substrate respectively.
v_i	Velocity of a plume constituent.
$w(z)$	Spot size (as a function of z).
w_l and w_p	Average spot sizes of the output and pump laser beams respectively.
$w_l(z)$ and $w_p(z)$	Spot sizes (as a function of z) of the output and pump laser beams respectively.
w_{lx}, w_{px}, w_{ly} and w_{py}	Average spot sizes of the output and pump laser beams in the x and y directions respectively.
$w_{lx}(z)$, $w_{px}(z)$, $w_{ly}(z)$ and $w_{py}(z)$	Spot sizes (as a function of z) of the output and pump laser beams in the x and y directions respectively.
w_o	Spot size at the beam focal point.
X	Number of species A for every Y of species B.
x, y and z	Two transverse axes and propagation axis respectively.
$X(T)$	Position of the plasma edge perpendicular to the target surface.
X_o, Y_o and Z_o	Initial positions of the plume edge at the beginning of unsteady adiabatic expansion.
XRD	X-ray diffraction.
Y	Number of species B for every X of species A.
$Y(T)$, $Z(T)$	Transverse position of the plasma edge.
YAG	Yttrium aluminium garnet ($Y_3Al_5O_{12}$).
YAP	Yttrium aluminium perovskite ($YAlO_3$).
YbAG	Ytterbium aluminium garnet ($Yb_3Al_5O_{12}$).
YGG	Yttrium gallium garnet ($Y_3Ga_5O_{12}$).
YIG	Yttrium iron garnet ($Y_3Fe_5O_{12}$).
YSAG	Yttrium scandium aluminium garnet ($Y_3Sc_2Al_3O_{12}$).
YSGG	Yttrium scandium gallium garnet ($Y_3Sc_2Ga_3O_{12}$).
Z	Average charge of a plume constituent.
Z_A and Z_B	Nuclear charge of species A and B respectively.
z_o	Value of z at the beam focal point.
α	Absorption coefficient.
$\alpha(T)$	Temperature dependent absorption coefficient.
α_{film}, $\alpha_{substrate}$	Thermal expansion coefficients for the film and substrate respectively.
α_{IB}	Inverse Bremsstrahlung absorption coefficient.
α_p	Pump absorption coefficient.

α_{PL} and α_{SL}	Waveguide and substrate propagation loss respectively.
β	z-component propagation constant
γ	Ratio of specific heats (C_p/C_v).
ΔT	Temperature difference.
$\Delta\lambda$	Longitudinal mode separation.
ε	Electric permittivity.
ε_1, ε_2 and ε_3	Electric permittivity of the superstrate, core and substrate respectively.
ε_E	Emissivity of a grey-body.
η	Slope efficiency.
η_A and η_B	Slope efficiencies for output coupling mirrors *A* and *B* respectively.
η_{pl}	Spatial overlap of the pump and laser beams.
η_{plA} and η_{plB}	Spatial overlap efficiency of the pump and laser beams when using output coupling mirrors *A* and *B* respectively
η_q	Fraction of absorbed photons that lead to population of the upper laser level (quantum efficiency).
η_{qA} and η_{qB}	Quantum efficiencies of the laser using output coupling mirrors *A* and *B* respectively.
θ	Grazing angle of X-rays.
θ_c	Critical angle.
θ_{guided}	Incident angle of guided light.
$\theta_{launched}$	Launching angle of light.
θ_{NA}	Maximum apex angle of launched light that will go on to be guided.
θ_s	Scattering angle of ions.
κ_{td}	Thermal diffusivity.
Λ	Self-imaging length.
λ	Wavelength.
μ	Magnetic permeability.
μ_1, μ_2 and μ_3	Magnetic permeability of the superstrate, core and substrate respectively.
ν	Frequency of the laser used for ablation.
ν_l	Frequency of the output laser radiation.
ν_p	Frequency of the pump laser radiation.
ν_{ps}	Plasma frequency.
$\rho(T)$	Temperature dependent density.
σ_e	Emission cross-section.
σ_f	Stress in a film.
σ_S	Stefan-Boltzmann constant.
σ_{th}	Stress in a film resulting from thermal expansion mismatch.
τ	Pulse duration.
τ_{fl}	Lifetime of the upper laser level.
φ, φ'	Phase offset.
ω	Angular frequency.

Chapter 1

Introduction

1.1 Pulsed laser deposition

Pulsed laser deposition (PLD) is a technique for the fabrication of thin films, and can be applied to a wide range of materials. A pulsed laser (usually ultra-violet (UV) wavelength) is used to ablate a target, and a plasma plume is formed by the ejected material; the plasma plume then expands away from the target surface and interacts with the chamber atmosphere until it reaches the substrate, where it is deposited as a thin film. The substrate can be heated to assist with nucleation and allow crystal growth, and a background gas can be used to help control the film composition.

PLD in its most basic form was first reported in 1965 [1], when it was discovered by scientists experimenting with applications for lasers. More focussed use and studies of PLD did not occur until 1987, however, when it became popular as a technique for fabricating high temperature superconducting thin films [2; 3]. Since then, PLD has been used to fabricate films of a wide range of types of materials, such as superconductors, metals, dielectrics, ferroelectrics, glasses and semiconductors. These films have found many different applications in optics and electronics, such as waveguides, amplifiers, lasers, filters and detectors. Table 1.1.1 summarises the reporting of some of the most significant advances in the field of PLD in the form of a time-line; some of the advances that are of particular relevance to the research presented here are also included.

1969	First growth of metal films [4].
1985	First growth of semiconductor films [5].
1986	
1987	First growth of superconducting films [2].
1988	First growth of glass films [6]. First growth of simple oxide films [7].
1989	
1990	First growth of ferroelectric films [8]. Start of continuous reporting of the growth of optical films.
1991	First theoretical investigations [9; 10].
1992	Several more theoretical investigations [11; 12]. Techniques for the improvement of film quality [13; 14].
1993	First waveguiding films [15]. First growth of garnet crystal films [16].
1994	
1995	Significant increase in the reporting of the growth of optical films.
1996	First laser operation of a film [17].
1997	Losses of 0.5 $dBcm^{-1}$ in a film [18].
1998	Reduction in particulate occurrence using a pulsed gas-jet [19].
1999	Technique for producing large area films by substrate scanning [20].
2000	Studies into the effect of particulates on the laser performance of films [21].
2001	First capped waveguide laser film [22]. Further techniques for large area films [23].
2002	First rib waveguides from films fabricated by PLD [24]. Reduction in particulate occurrence using a second laser to heat the plume [25].
2003	
2004	Films with thickness up to 135 μm and highly textured crystallinity [26]. Losses of 0.1 $dBcm^{-1}$ and laser operation of a 40 μm thick film [27].
2005	First laser operation of a rib waveguide based on a film fabricated by PLD [28]. First growth of a multilayer garnet crystal film [first reported here].

Table 1.1.1: Time-line of some significant advances in the field of PLD.

The number of publications per year reporting the growth of thin films by PLD can be used as an indication of the rate of growth in the use of PLD since 1987. Figure 1.1.1 shows the results of year specific searches for reports of thin films grown by PLD (using the ISI Web of Science database [29]). There was a sudden jump in the number of publications reporting the growth of thin films by PLD between 1990 and 1991; this was mainly due to an increase

in the reports of superconducting thin films, and shows when the use of PLD became truly widespread. Since 1991, the number of publications per year has increased steadily as new materials have been used and new experimental enhancements have been introduced.

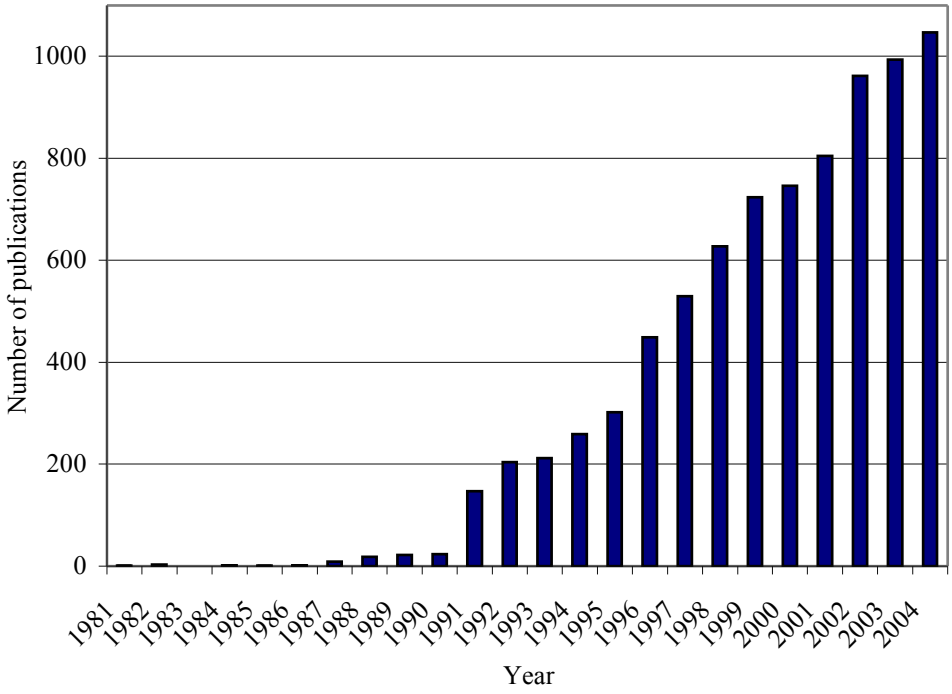

Figure 1.1.1: The number of publications reporting the growth of films by PLD per year from 1981 to 2004.[1]

PLD is a very flexible technique because film growth can be controlled by varying several growth parameters, including the background gas species and pressure, the ablating laser wavelength, energy, pulse duration and repetition rate, the temperature of the substrate, and the target surface to substrate distance. However, this number of growth parameters can also be a disadvantage because finding optimal growth conditions for a specific material can be difficult and time consuming. PLD can be used with a very wide range of materials because the ablation process is a form of congruent evaporation; in particular, this allows multicomponent materials with complex stoichiometries to be deposited. PLD can have a relatively fast growth rate ($> 10\,\mu m$ per hour) due to the highly directional plume distribution, and experimentation with film materials can be simple because bulk samples of the material are often available and suitable for use as targets. The apparatus is also relatively simple to manage, maintain and re-align when compared to rival deposition

1 The data for figure 1.1.1 was found by performing year specific searches using the search term "film* AND pulsed AND laser AND (deposit* OR ablat* OR evaporat*)" in the *topic* search field.

techniques, and there is usually no need for undesirable toxic gases or substances. The flexibility of PLD makes it ideal for the fabrication of multilayers of different film materials, and this is one of the reasons why it is the preferred fabrication technique for the research discussed in this thesis.

A well known, and perhaps the main, disadvantage with PLD is the occurrence of particulates in the deposited films [21]. Particulates are a big problem when fabricating optically waveguiding thin films because they form scattering centres at the film surface and contribute significantly to the overall propagation loss. Particulates arise in the PLD fabrication process due to two main processes, incomplete vaporisation of the target material and exfoliation. Incomplete vaporisation of the target material is difficult to prevent entirely because it is an inherent consequence of the ablation process, whereas exfoliation is caused by overuse of the same spot on the target and can therefore be minimised by repositioning and reconditioning of the target. The problem of particulates must be addressed for films fabricated by PLD to be realised as high quality devices.

1.2 Planar waveguide lasers

There are several motivations for the study of planar waveguide devices in general. For example, an ultimate application would be optically integrated circuits, where planar versions of optical switches, modulators, filters, interferometers, couplers, sources, detectors and amplifiers are all required. Another factor in need of constant improvement is the efficiency of coupling light from optical fibres to planar devices, and vice versa.

Planar waveguide laser devices are also of interest because of the implications of their structure, which allows for lasing, pumping and heat dissipation to each have a unique (and orthogonal) axis of operation, as shown in figure 1.2.1. This allows planar waveguide devices to be pumped relatively easily by high power diode laser arrays, and heat sinks can be used to provide efficient cooling without obstructing the pumping and lasing directions. The confinement properties of planar waveguide lasers result in much improved spatial overlap of pump and signal beams when pumping is performed in the same axis as laser operation, resulting in planar waveguide lasers with lower pump power thresholds, higher gains per unit pump power and higher efficiencies than their bulk counterparts. Also, planar waveguide devices are very compact, making them convenient for use in many applications where large bulk lasers are not practical.

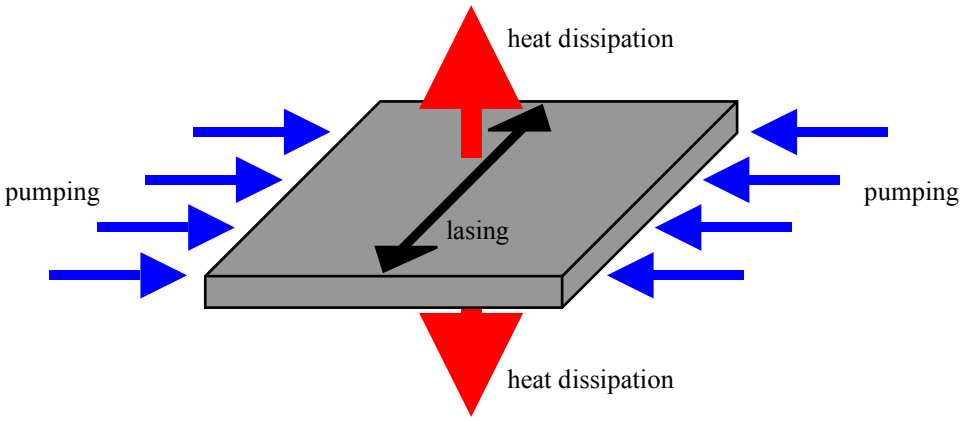

Figure 1.2.1: Pumping, lasing and heat dissipation operating on orthogonal axes of a planar waveguide laser.

A problem with thin single-layer planar waveguides is that the numerical aperture (NA) limits the efficiency of focussing of diode laser array pump light into the waveguides, and with the advent of today's very high power diodes (hundreds of watts) that are available, there is more pump power than can be used effectively. Thicker films can be used to increase the NA, allowing a higher pump power to be used, but the consequence is highly multimode operation, reducing the spatial overlap of the pump and laser beams, and therefore the quality of the spatial distribution of the laser output. The problem of limited NA with optical fibres was overcome by the use of cladding layers [30; 31]; the pump light is guided by an inner cladding region and is absorbed as it crosses through the core region. Cladding layers increase the effective absorption length of the pump beam, but this is not a problem for optical fibres because it is relatively easy to fabricate longer devices.

The same technique can be used to improve the NA of planar waveguide devices, but the implications of such geometries in planar waveguide form are slightly different. The thickness of core needed for single-mode operation would be too small for planar waveguide devices to operate because the increased effective absorption length would be beyond practical device lengths. Instead, larger cores can be used and the important factor becomes the ratio of the core to cladding thicknesses, and if this ratio is chosen correctly, the higher order modes will extend into the cladding region and only the fundamental mode will be selected due to the limited gain region. This more advanced planar waveguide cladding geometry is more analogous to large-mode-area (LMA) fibre lasers [32; 33] than to standard double-clad geometries. Advanced cladding layer geometries should allow the fabrication of planar waveguide laser devices with near diffraction-limited beam quality (in the guided direction) at high output powers (> 10 W) [34].

Thick multilayer geometries will also help to reduce the effect of particulates in PLD grown films. It has been shown that the effect of particulates can be reduced by burial below the film surface [21], either by increasing the film thickness, or deposition of a capping layer. Also, thicker films and multilayer geometries will inherently have lower propagation losses than thin single-layer films because the pump and laser light will be confined further away from the film surface-air boundary where particulates form scattering centres.

1.3 Thick films used as thin-disk lasers

The thin-disk laser has been a focus of attention in recent years due to the advantages of such a system over bulk lasers. Efficient cooling is possible because of the large surface area to volume ratio, and the effect of thermal lensing is small because the temperature gradient is in line with the laser axis. By using multiple passes of the pump beam and increasing the pumped area, the output power of the thin-disk laser is highly scalable, and can reach kilowatt levels [35].

Ytterbium is an attractive choice for a laser dopant because of its relatively simple electronic structure; it doesn't suffer from excited state absorption, cross relaxation or upconversion [36]. However, lasing at a wavelength of 1.03 μm is based on a quasi-four-level system, meaning that high pump power densities and adequate cooling are required to overcome the problem of reabsorption loss. High pump power densities can be realised using high power indium gallium arsenide (InGaAs) diode laser arrays, and the thin-disk laser geometry lends itself well to cooling solutions. Laser operation has been achieved in Yb:YAG (Yb:$Y_3Al_5O_{12}$) thin-disks [35; 37], and modelling calculations have shown that an optimum thickness has to be used for the optical efficiency to be maximised, and the optimal thickness decreases as the dopant concentration is increased [35]. It is possible to make YAG crystals with very high dopant concentrations of ytterbium because the ionic radii of Yb^{3+} and Y^{3+} are so similar; 100% substitution only changes the unit cell size of YAG by 1.5% [38]. The optical efficiency is ultimately optimal for a ytterbium concentration of 100%, but the optimal thickness for such a high dopant concentration is < 100 μm [35], and a disk this thin would be very fragile.

Films of Yb:YAG solve the problem of fragility that arises as the disk thickness decreases below 100 μm, and the substrate can be used to dissipate heat away from the film. PLD is an ideal technique for the fabrication of Yb:YAG films, and the possibility of depositing film

layers additional to the laser film allow specialist devices to be made. For example, a Q-switched Yb:YAG thin-disk laser film may be fabricated by the addition of a layer doped with the saturable absorber ion Cr^{4+} [39].

1.4 Garnet crystal

Garnet crystal is optically isotropic, has a good transparency range, low rate of thermal expansion and high mechanical strength, making it an ideal laser host material. In particular, YAG has been used extensively with various different dopants to make bulk lasers. Garnet crystal makes an excellent choice for the fabrication of laser films, and deposition of the different garnets such as YAG, YGG ($Y_3Ga_5O_{12}$), YSAG ($Y_3Sc_2Al_3O_{12}$), YSGG ($Y_3Sc_2Ga_3O_{12}$), GAG ($Gd_3Al_5O_{12}$), GGG ($Gd_3Ga_5O_{12}$), GSAG ($Gd_3Sc_2Al_3O_{12}$) and GSGG ($Gd_3Sc_2Ga_3O_{12}$) is an attractive way of achieving epitaxial multilayer structures because of the good lattice match and slightly different refractive indices of these alternative garnets. The readily available undoped YAG crystal substrates are ideal because YAG has a lower refractive index than all of these other garnets, allowing waveguiding to occur. Table 1.4.1 summarises the available data for the different refractive indices, thermal expansion coefficients, lattice constants and lattice mismatches relative to YAG, of the alternative garnets mentioned above.

Material	Refractive index (at λ = 1.06 µm)	Thermal expansion coefficient ($\times 10^{-6}$ K^{-1})	Lattice constant (Å)	Lattice mismatch to YAG
YAG	1.82 [40]	6.9 [41]	12.006 [42]	-
YGG	1.91 [40]	-	12.273 [43]	2.2%
YSAG	1.86 [44]	-	12.271 [44]	2.2%
YSGG	1.93 [45]	8.1 [45]	12.446 [46][2]	3.7%
GAG	-	-	12.113 [47]	0.89%
GGG	1.95 [48]	8.3 [49]	12.383 [50]	3.1%
GSAG	1.89 [51]	7.7 [52]	12.389 [53][3]	3.2%
GSGG	1.94 [40]	8.0 [49]	12.544 [54]	4.5%
YbAG	1.83 [36]	8.6 [55]	11.939 [56]	-0.56%

Table 1.4.1: Various properties of some garnet crystals.

2 The only crystallographic data available was for $Y_3Sc_{1.43}Ga_{3.57}O_{12}$ and this has been used as an approximation of YSGG.

3 The only crystallographic data available was for $Gd_{2.91}Sc_{1.80}Al_{3.15}O_{11.80}$ and this has been used as an approximation of GSAG.

1.5 Summary of results and significant achievements

The results obtained throughout the research project are summarised below and the significant achievements are highlighted. All claims to date are to the best of our knowledge at time of writing.

- Two thick Nd:GGG films were fabricated and subsequently operated as laser devices when pumped by a Ti:sapphire laser and a diode laser array; this is the first report to date of a waveguide fabricated by PLD to lase when pumped by a diode laser array. The films were found to be highly textured crystal and had compositions close to bulk Nd:GGG crystal.
- Minimum threshold pump powers of 17.8 mW and 7.44 W were observed for the Nd:GGG films when Ti:sapphire pumping and diode pumping was used respectively.
- Maximum slope efficiencies of 32.0% and 11.2% were obtained with the Nd:GGG films when Ti:sapphire pumping and diode pumping was used respectively.
- A maximum laser output of 4.0 W was produced from the diode pumped Nd:GGG film; this is the highest laser output to date from a film grown by PLD.
- A loss estimate of < 0.1 dBcm^{-1} was obtained for one of the Nd:GGG films, the lowest loss to date for a waveguide fabricated by PLD.
- The effect of self-imaging was observed in a YAG capped Nd:GGG film; this is the first report to date of the observation of such an effect in a waveguide fabricated by PLD.
- A thick YbAG film was fabricated but lasing has not been observed from experiments so far; this YbAG film is the first to date to be fabricated by PLD without the need for subsequent annealing. The film was found to be highly textured crystal and had a composition close to bulk YbAG crystal.
- Films of YGG, Nd,Cr:YSAG, Cr:GSAG and Nd,Cr:GSGG have been deposited; this is the first report to date of the deposition of YGG, YSAG and GSAG films by PLD. All of the films were found to be highly textured crystal and had compositions close to bulk crystals.

- A four-layer film of YGG, Nd,Cr:GSGG and YAG was deposited and is awaiting laser trial experiments; this is the first report of such an advanced garnet crystal multilayer structure to be fabricated by PLD.

1.6 Structure of this thesis

To set the benchmarks for high quality optical films, the results achieved previously with optically waveguiding films fabricated by PLD are summarised in Chapter 2. Also, a selection of alternative techniques for fabricating planar waveguides are presented to set the place of PLD in the field. An overview of the theoretical aspects of PLD and lasers is presented in Chapter 3, and the experimental and analytical techniques used throughout the course of the research project are discussed in Chapter 4. Analysis and results from thick Nd:GGG films can be found in Chapter 5 and the results from other garnet films are discussed in Chapter 6. A summary of the conclusions drawn from the project and the directions for future work can be found in Chapter 7. A list of publications that have resulted from the project is shown in Appendix I.

Chapters 2-4 are mainly background in context, including theory, experimental and analytical techniques, experimental observations, and discussion of some of the problems experienced, whereas Chapters 5 and 6 are made up entirely of results. This layout was decided to be optimum in terms of clarity.

Chapter 2

Background

2.1 Introduction

To gain an insight into the motivations for the research presented in this thesis, and its place in the field, it is useful to consider some background information. The results achieved previously with optically waveguiding films grown by PLD allow the quality of the results presented in this thesis to be assessed, and the consideration of other techniques for fabricating planar waveguides provides a setting for the discussion of the advantages and disadvantages of PLD.

2.2 History of optically waveguiding films grown by pulsed laser deposition

The number of publications per year reporting the deposition of optical or waveguiding films by PLD is an immediate indication of the growth rate in the use of PLD for optically waveguiding films. Figure 2.2.1 shows the results of year specific searches for reports of optical or waveguiding films grown by PLD using the ISI Web of Science database [29].

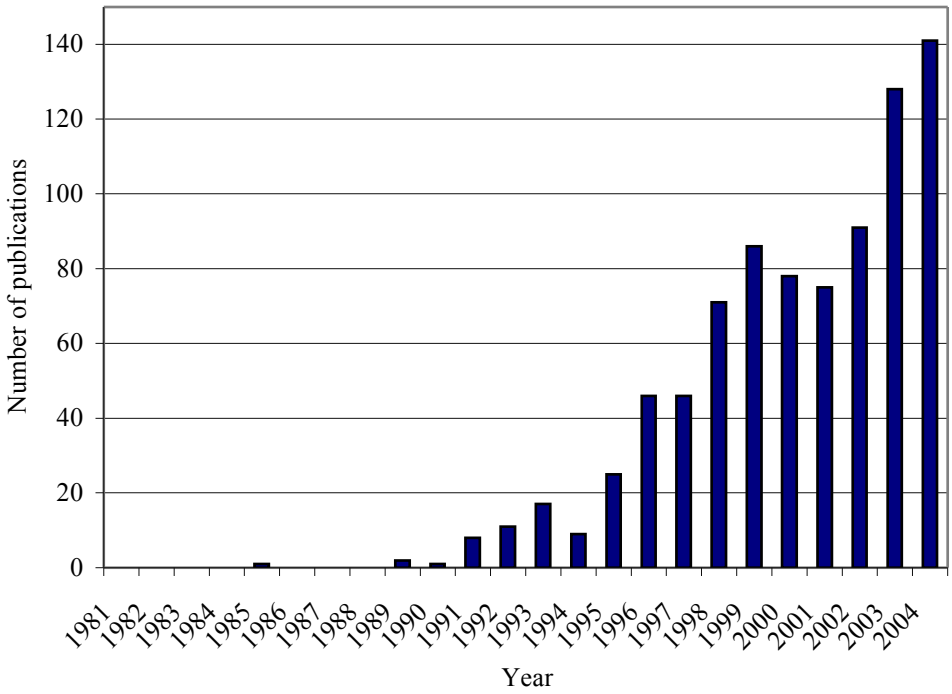

Figure 2.2.1: The number of publications reporting the growth of optical or waveguiding films by PLD per year from 1981 to 2004.[4]

A wide range of optically waveguiding materials have been grown by PLD, however only a selection of these materials has been chosen for further discussion, based on the results of qualitative analysis. It is likely that some reports will have been neglected either because they weren't found by the search terms used or because they were unobtainable at the time of writing.

2.2.1 Garnets

The use of garnet crystals as bulk laser host materials began soon after the invention of the laser [57]. The advantages presented by a planar waveguide geometry using garnets are numerous, including higher efficiency via improved output and pump beam overlap and reduced pump power thresholds. However, the range of fabrication techniques suitable for the growth of thin garnet films is limited because of the multicomponent nature of these

4 The data for figure 2.2.1 was found by performing year specific searches using the search term "(optical OR waveguid* OR (wave AND guid*)) AND film* AND pulsed AND laser AND (deposit* OR ablat* OR evaporat*) NOT (super AND conduct*) NOT superconduct* NOT CVD NOT YBaCuO NOT YBa2Cu3O*" in the *topic* search field. The results were filtered automatically by the exclusion terms and were also filtered manually because the search term "optical" produced a lot of false hits.

crystals. PLD is an ideal fabrication process for garnets because it can overcome this problem. PLD work with garnets has mainly focussed to date on YAG and GGG, due to both their relative ease of growth, and relatively closely matched lattice constants (YAG: 12.006 Å [42], GGG: 12.383 Å [50]; 3.1% lattice mismatch).

The growth of undoped GGG by PLD was first reported in 1995 [58], and there have been several reports since of doped GGG film growth by PLD. Neodymium has been a popular dopant for GGG films and successful growth of Nd:GGG on YAG has been reported on several occasions [17; 18; 21; 26; 27; 59; 60], as well as Cr:GGG and co-doped Nd/Cr:GGG [61; 62]. Until the recent growth of a 135 µm thick Nd:GGG film discussed in this thesis [26], films with a reported thickness up to 8 µm only had been grown, whilst losses as low as 0.5 $dBcm^{-1}$ had been obtained for Nd:GGG films prior to the result of 0.1 $dBcm^{-1}$ discussed in this thesis. In general, the fluorescence properties of Nd:GGG films have been similar to that of bulk Nd:GGG, and films have also been successfully used as laser media [17; 18; 27; 59] and absorbed power thresholds close to theoretical values have been obtained.

Rare-earth and transition metal ion doped YAG films have also been grown by PLD, however, lasing of YAG based films has not been reported to date. Growth of Nd:YAG on various substrates [60; 63-66] and YAG doped with Cr^{4+} [61], Tb^{3+} [67], Yb^{3+} [68] and Er^{3+} [69] has been reported. YAG based films with thickness up to 5 µm only have been grown by PLD, and the fluorescence properties of doped YAG films have been found to be similar to that of bulk. So far, there has been only one report of the growth of an alternative garnet (discussed previously in Chapter 1), namely Nd,Cr:GSGG [70].

Another garnet that has been grown is YIG ($Y_3Fe_5O_{12}$), which is a magneto-optic (MO) material, making it suitable for magnetic field sensing devices. Growth of YIG by PLD was first reported in 1991 [71] and since then, single-mode buried waveguides of YIG with losses of ~ 1 $dBcm^{-1}$ have been grown [72; 73]. YIG films have also been further developed into planar waveguide magneto-optic devices [74], and in particular for applications such as magnetic sensors [75], optical current transformers [76] and electric current sensors [77].

The advantages of using garnet crystal to make thin film based optical devices have made it an attractive choice of material for PLD, and devices have been successfully fabricated from several different garnet crystal species. As more work is conducted towards the growth of garnet crystal devices using PLD, the quality of the films is expected to improve sufficiently that PLD can compete directly with other film fabrication techniques.

2.2.2 Simple Oxides

Bulk lasers based on simple oxides such as sapphire (Al_2O_3) and yttria (Y_2O_3) are frequently used, owing to the excellent transparency range, low thermal expansion, high mechanical strength and good thermal conductivity properties of such materials. This range of favourable qualities also makes their use in a planar waveguide geometry an attractive prospect. The relatively simple stoichiometry and crystal structures of these oxides makes them ideal for thin film growth by PLD, and successful growth of sapphire has been reported on several occasions.

Alumina can exist in several different phases/forms. Sapphire is the crystalline alpha phase and has a structure that can be described as either rhombohedral or hexagonal. This structure makes sapphire an anisotropic material in terms of thermal and optical properties, meaning that in general only single crystal films can have useful optical applications. Growth of sapphire films by PLD can be challenging because polycrystalline growth tends to result in fracturing upon cooling.

Thin sapphire films have been grown by PLD with the inclusion of various different dopants, one of the most widely used being titanium [60; 78-81]. A Ti:sapphire planar waveguide geometry offers great advantages over the bulk form which requires a high pump power density, expensive pump sources and consistent crystal quality over a large volume. Lasing of Ti:sapphire thin films of up to 12.3 µm in thickness [60; 79] with losses as low as 1.5 $dBcm^{-1}$ has been observed [60] and erbium doped sapphire thin films [82-84] with losses of 4 $dBcm^{-1}$ [83] have been grown by PLD. Rib waveguides have been fabricated using Ti:sapphire thin films grown by PLD and subsequent processing by photolithography and ion beam etching [24; 28; 85]. Lasing has recently been achieved in Ti:sapphire ribs with a sapphire capping layer, and an absorbed pump power threshold of 265 mW was observed for lasing at a wavelength of 792.5 nm [28]. The ribs were found to have losses of ~ 1.7 $dBcm^{-1}$ and excellent optical confinement properties with measured beam propagation factors M_x^2 and M_y^2 of 1.3 and 1.2 for the directions in-plane and perpendicular to the plane respectively [28; 85].

Yttria thin films have also been grown by PLD [86-89] and good results have been achieved using (0001) oriented sapphire substrates [87; 88], where single crystal growth of (222) oriented yttria has been observed. Sapphire is a good choice of substrate for yttria films because it has a lower refractive index (yttria: $n = 1.78$, sapphire: $n = 1.75$ (at $\lambda = 1.06$ µm)), making optical waveguiding possible in the film. Use of erbium as a dopant for yttria films

has been widely reported [87-89] and losses as low as 1 $dBcm^{-1}$ have been observed for Er:yttria films [87; 89]. Eu:yttria films have been grown on sapphire [90-92] and fused-silica substrates [93], and waveguiding has been observed with a propagation loss of ~ 1 $dBcm^{-1}$ [93]. Nd:YAP ($YAlO_3$) thin films have been grown by PLD [66; 94] with thickness up to 11.2 µm and losses as low as 1 $dBcm^{-1}$ [94], and fluorescence properties in line with expectation have also been observed.

The consistently low losses observed in films of simple oxides such as sapphire and yttria have proven their potential for high quality optical devices. The fabrication of buried rib waveguide lasers using Ti:sapphire films fabricated by PLD has shown that with the application of advanced processing techniques subsequent to deposition, high quality optical devices can be realised from films grown by PLD.

2.2.3 Ferroelectrics

There has been a great deal of interest in ferroelectric materials because of the many applications of their properties. The nonlinear, electro-optic, thermoelectric, piezoelectric, acousto-optic, photoelastic, photorefractive and pyroelectric properties displayed by ferroelectrics make them ideal for use in optical components for a range of applications such as optical switches, sensors, micro-electro-mechanical systems (MEMS) and integrated optoelectronics. Planar waveguide versions of these optical components can be fabricated from PLD grown films with subsequent further processing. Problems can be experienced with ferroelectric films due to physical fragility and susceptibility to damage via the photorefractive effect. Ferroelectric films are optically anisotropic, meaning that films must be single crystal to be of any significant use for optical applications. Ferroelectric films must also be single domain for advantage to be taken of the many effects that are dependent upon the dipole polarisation. Multi-domain films may be converted into single domain films by re-poling after growth, but this is undesirable since it involves the use of electrodes above and below the sample, and this is experimentally difficult to achieve with a film configuration because the substrate is in the way.

Lithium niobate ($LiNbO_3$) has undoubtedly been the most widely researched ferroelectric material with PLD because of its nonlinear, photorefractive, piezoelectric, photoelastic, thermoelectric, acousto-optic and electro-optic properties. Lithium niobate films have been grown on sapphire [95-101], and on silicon substrates with a silicon dioxide (SiO_2) buffer

layer [102; 103], and films have also been grown with Nd^{3+} [104] and Er^{3+} [105] doping. Films with thickness up to 2 µm have been grown [102] and losses of ~ 3 $dBcm^{-1}$ have been observed for lithium niobate films grown on sapphire [96; 97; 101].

The growth of several other ferroelectric materials by PLD has been investigated, but none have experienced as much success as lithium niobate. Potassium niobate ($KNbO_3$) films have been grown on magnesium oxide (MgO) substrates [106-109] with thickness up to 1 µm as part of investigations into their suitability for applications using their nonlinear optical properties and the electro-optic effect. SBN ($Sr_xBa_{1-x}Nb_2O_6$), also of interest because of its nonlinear optical properties, has been deposited on magnesium oxide and fused silica substrates [110; 111] with thickness up to 6 µm; Eu^{3+} doped SBN films have also been grown [112; 113]. Lithium tantalate ($LiTaO_3$) films have been grown on sapphire substrates [114; 115] with thickness up to 0.8 µm and losses as low as ~ 0.6 $dBcm^{-1}$ [115], and some lithium tantalate films have been successfully used as SAW filters [114].

Optical quality barium titanate ($BaTiO_3$) films have been grown [116-120] with losses of 3 $dBcm^{-1}$ [118-120], and cobalt doped films [121] have been grown in an attempt to simultaneously increase the photorefractive gain and decrease the response time. Optical waveguiding has been achieved in a film of lanthanum titanate ($LaTiO_3$) deposited on silicon dioxide [122]. BBO (BaB_2O_4) is a suitable material for second harmonic generation (SHG) due to its wide optical transparency range, large SHG coefficient and high damage threshold, and BBO films have been deposited on silicon, silicon dioxide and sapphire substrates [123]. KTP ($KTiOPO_4$) displays similar properties to BBO, and both undoped [124; 125] and erbium doped KTP film growth has been reported [126; 127]. BNN ($Ba_2NaNb_5O_{12}$) is a nonlinear material that is difficult to grow in bulk form; optical quality BNN films have been grown on KTP substrates [128-130] with losses as low as ~ 1.0 $dBcm^{-1}$ [128; 129].

Experiments with ferroelectrics have shown that they are hard to grow using PLD, and although the loss observed in some films has been relatively low, the problem of obtaining single-domain films has made the transition of film to device difficult.

2.2.4 Glasses

Glass is an optically isotropic material with a good transparency range, making it ideal for optical applications. Thin film glass growth by PLD has a lot of potential because the lack of crystal constraints should make high film quality relatively simple to achieve.

Erbium-ytterbium co-doped glass films [131; 132] with losses of 11 $dBcm^{-1}$ [131] have been grown by PLD; the co-doped configuration of Er,Yb:glass is of interest because the ytterbium acts as a sensitiser for the erbium ions, providing improved absorption properties. Chalcogenide glasses are of interest because of their photo-stimulated properties such as photobleaching, photo-darkening, photo-doping and the photorefractive effect. Gallium lanthanum sulphide (GaLaS) chalcogenide glass films have been deposited on various substrate materials [15; 133] with thickness up to 1.35 µm and losses of 6 $dBcm^{-1}$ [133]. Lead germanate glass is of interest because it displays large photoinduced refractive index changes. Lead germanate glass has been deposited on various substrate materials by PLD [134-136] with losses as low as 2.1 $dBcm^{-1}$ [136]. The relatively poor losses observed in glass films deposited by PLD so far have limited the device applications of glass films. However, glass films may still be of use as cladding or coating layers rather than core layers.

2.2.5 Semiconductors

The two materials discussed here have not been used to form waveguide laser cavities in the traditional sense. Instead, laser cavities have been formed by self-assembled hexagonal micro-crystallites. The films grow with an in-plane hexagonal periodic structure and laser cavities are formed by integer multiples of these hexagonal units. Cadmium sulphide (CdS) films have been grown by PLD [137-139] and micro-cavity lasing as described above has been observed [138; 139]. Zinc oxide (ZnO) films have been grown on various substrates [140-145] and losses as low as 2.8 $dBcm^{-1}$ have been achieved [146]. Investigations have been made into the waveguiding properties of some PLD grown zinc oxide films [140; 141; 146] and micro-cavity lasing as described above has been observed [147]. The results so far with semiconductor films grown by PLD have been promising, but are not yet at the level of competing with alternative techniques.

2.2.6 Summary

Table 2.2.1 summarises the most significant achievements and properties for different optically waveguiding materials grown by PLD.

Material	Biggest film thickness (μm)	Lowest loss ($dBcm^{-1}$)	Most significant results
Garnet crystals:			
GGG	135 [26]	0.1 [26; 27]	Lasing [17; 18; 27; 59]
YAG	5 [61; 68]	-	Fluorescence [61; 64; 65; 67; 68]
YIG	4.5 [75]	1 [73]	Waveguiding [72; 73] & MO effect [71; 74-77]
GSGG	-	-	Fluorescence [70]
Oxides:			
Al_2O_3	12.3 [60; 79]	1.5 [60]	Lasing [60; 79] & ribs [24; 28; 85]
Y_2O_3	1.5 [93]	1 [87-89; 93]	Fluorescence [87; 88; 90; 91; 93]
YAP	11.2 [94]	< 1 [94]	Fluorescence [94]
Ferroelectrics:			
$LiNbO_3$	2 [102]	3 [96; 97]	Waveguiding [96; 98], SHG [95; 97; 99; 105], EO effect [95; 97] & fluorescence [104]
$KNbO_3$	1 [106]	-	-
SBN	6 [111]	-	Fluorescence [112; 113]
$LiTaO_3$	0.8 [115]	0.6 [115]	Waveguiding [115]
$BaTiO_3$	9 [121]	3 [118-120]	Waveguiding [117-120] & EO effect [120]
$LaTiO_3$	-	-	Waveguiding [122]
BBO	-	-	SHG [123]
KTP	1 [124]	-	Waveguiding [126; 127], SHG [124] & fluorescence [126; 127]
BNN	-	1 [129]	Waveguiding [128-130]
Glasses:			
Doped glass	1.5 [132]	11 [131]	Waveguiding [131; 132]
GaLaS	1.5 [15]	7 [133]	Waveguiding [15; 133]
Lead germanate	2.7 [136]	2.1 [136]	Waveguiding [135; 136] & photosensitivity [135]
Semiconductors:			
CdS	2 [138]	-	Lasing [138; 139]
ZnO	1 [141-143]	2.8 [146]	Lasing [147]
Others:			
Nd:KGW	-	5 [148]	Waveguiding & fluorescence [148]

Table 2.2.1: Summary of the results from optical waveguides grown by PLD.

A trend of success by material type (equation 2.2.1) can be inferred from table 2.2.1:

$$\text{Garnets} > \text{Simple Oxides} \geq \text{Ferroelectrics} >> \text{Glasses} \qquad \textbf{(2.2.1)}$$

2.3 Other techniques of thin film fabrication

All of the alternatives to PLD presented in this section are other ways of making thin films and subsequently using the films as waveguides. Consideration of these alternative techniques allows the advantages and disadvantages of PLD to be discussed particularly in terms of the technique itself, rather than just in terms of the quality of the devices produced.

2.3.1 Thermal vapour deposition

Thermal vapour deposition (TVD) is performed in a vacuum chamber as shown in figure 2.3.1, where the material to be deposited is heated to its melting point, and the substrate is arranged in a suitable position so that the vapour released is deposited as a thin film coating. TVD is suitable for use with film materials that have a simple stoichiometry and structure, making it ideal for the deposition of thin coatings of metals. TVD cannot easily be used for films with complex stoichiometries because the different vapour pressures of the film constituents would lead to films with an incorrect stoichiometry. TVD offers little control over the path taken by the evaporated material between source and substrate, with the consequence of slow growth rates, chamber contamination and inefficient use of the source material.

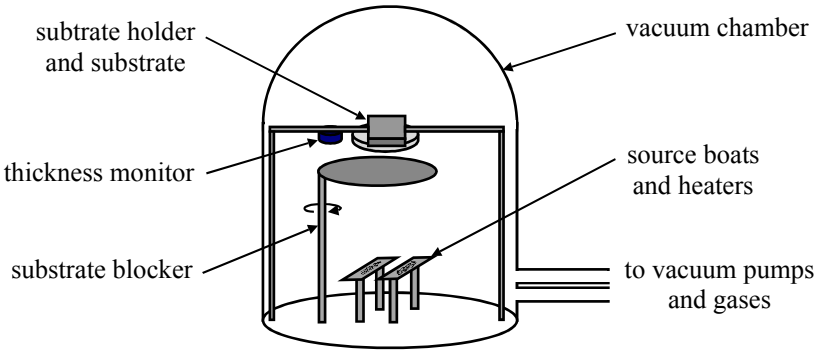

Figure 2.3.1: Thermal vapour deposition chamber.

2.3.2 Sputtering

Sputtering is performed in a vacuum chamber as shown in figure 2.3.2, where ions (usually Ar^+) are accelerated by an electric field (1-2 kV) onto the target surface.

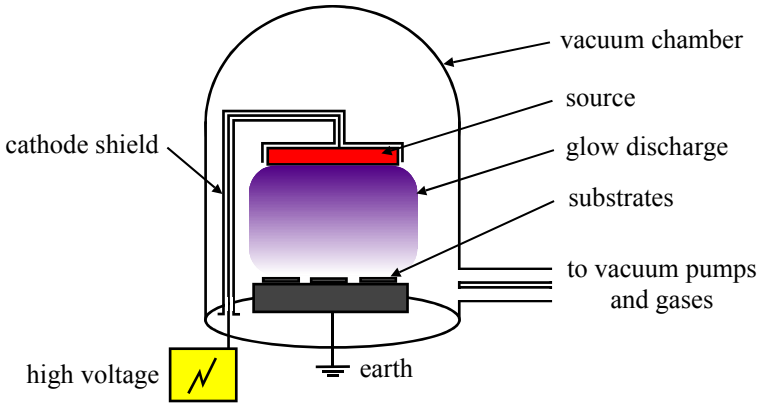

Figure 2.3.2: Sputtering chamber.

Bombardment of the target causes material to be ejected, and deposited as a thin film coating on the substrate. Sputtering is a good technique for making thin film coatings of materials with a simple stoichiometry, and is popular as a technique for coating scanning electron microscope (SEM) samples with gold in preparation for analysis, but suffers from the same disadvantages as TVD. Sputtering deposition rates can be increased by the use of magnetic fields, and growth of $Na_{0.5}K_{0.5}NbO_3$ and lithium niobate films by this so-called magnetron sputtering technique has been reported [149; 150]. In both cases, the films were subjected to optical analysis and losses of 1.2 $dBcm^{-1}$ were observed for the lithium niobate films [150].

2.3.3 Chemical vapour deposition

Chemical vapour deposition (CVD) involves the use of a mixture of chemicals called precursor gases that are passed across a substrate in a vacuum chamber or tube. A simple CVD tube apparatus is shown in figure 2.3.3 as an example of the basic principle. The precursor gases contain the film materials in a diluted form, and react with the substrate upon contact, causing deposition and some gas by-products to be released. The temperature of the substrate is critical in determining what is deposited on the substrate.

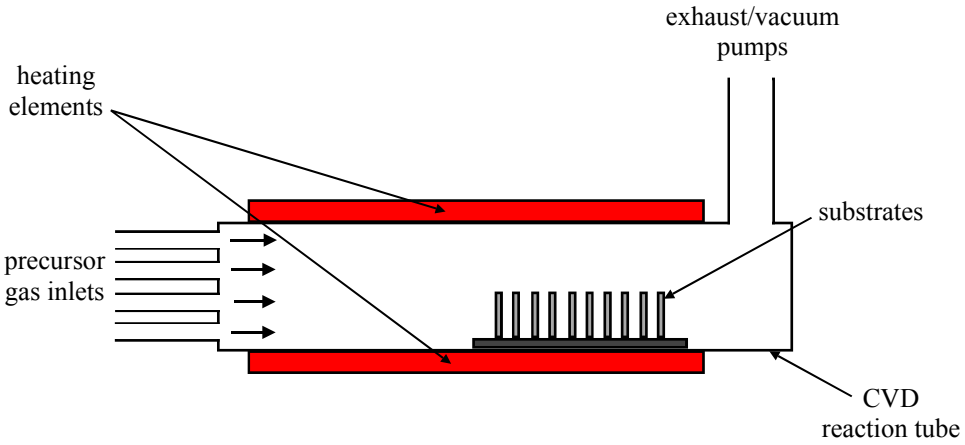

Figure 2.3.3: Simple CVD tube apparatus.

Many different forms of CVD exist, including laser assisted (LACVD), metal-organic (MOCVD) and plasma enhanced (PECVD). With LACVD, the extra energy provided by the laser can accelerate reactions and increase the deposition rate in particular areas of the substrate. MOCVD uses special mixes of metal and organic compounds for the precursor, allowing film materials with complex stoichiometries to be deposited, whereas PECVD uses a precursor in a plasma state to alter the reaction dynamics. CVD can be used for the deposition of many different film materials, but is limited by the range of suitable substrate and precursor combinations. In general, CVD is a slow deposition method, though some of the enhanced forms of CVD can give higher growth rates. A major drawback of CVD is the complication of the apparatus and precursor gases, and in particular, safe management of the toxic gases involved can present a challenge. The MOCVD technique has been used to grow epitaxial YAG films with a high crystal quality [151].

2.3.4 Liquid phase epitaxy

With liquid phase epitaxy (LPE) (shown in figure 2.3.4), substrates are dipped into a hot saturated solution of film material, and as the solution is cooled (often supercooled), the film material condenses out of the solution and is deposited on the substrate. The composition, temperature and cooling rate of the solution determine the characteristics of the film, such as stoichiometry and thickness. LPE can be complicated to set up and is limited to materials for which a suitable solvent is available. The search for a suitable solvent in the initial stages of experimenting can lead to a long wait when starting growth of a new material, but once the

setup is perfected the fabrication time can be relatively quick. LPE offers good control over film stoichiometry, but control of the crystal orientation can often be difficult, and there can be problems with dopant concentration homogeneity.

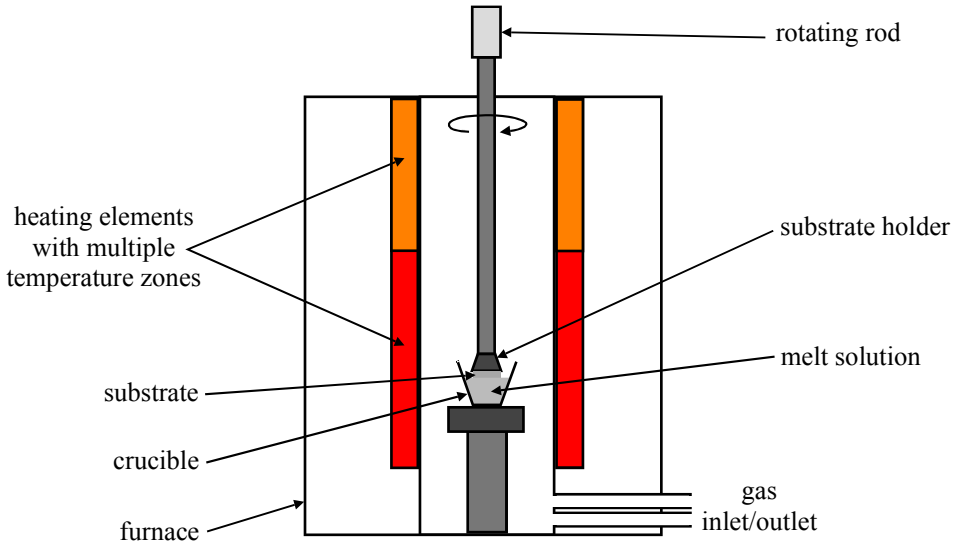

Figure 2.3.4: Liquid phase epitaxy apparatus.

The growth of garnet crystals by LPE is well established and models describing different processes of the technique have been produced [152]. There have been many reports of successful growth of high quality garnet films including YIG for magneto-optic applications [153; 154], Nd:YAG for waveguide laser applications [155-157], Yb:YAG for thin-disk laser applications [158], Co,Si:YAG for use as a saturable absorber layer [159], and Nd:GGG for channel waveguide laser applications [160]. Significantly, lasing has been observed in films grown by LPE [157; 158; 160], proving its potential for the fabrication of high quality crystal films and making it the biggest deposition based rival technique to PLD.

2.3.5 Molecular beam epitaxy

Molecular beam epitaxy is performed in an ultra-high vacuum (UHV) chamber as shown in figure 2.3.5, where several molecular beams of different compounds are directed at a substrate, combining on the surface to make up the correct film stoichiometry and be deposited as a film.

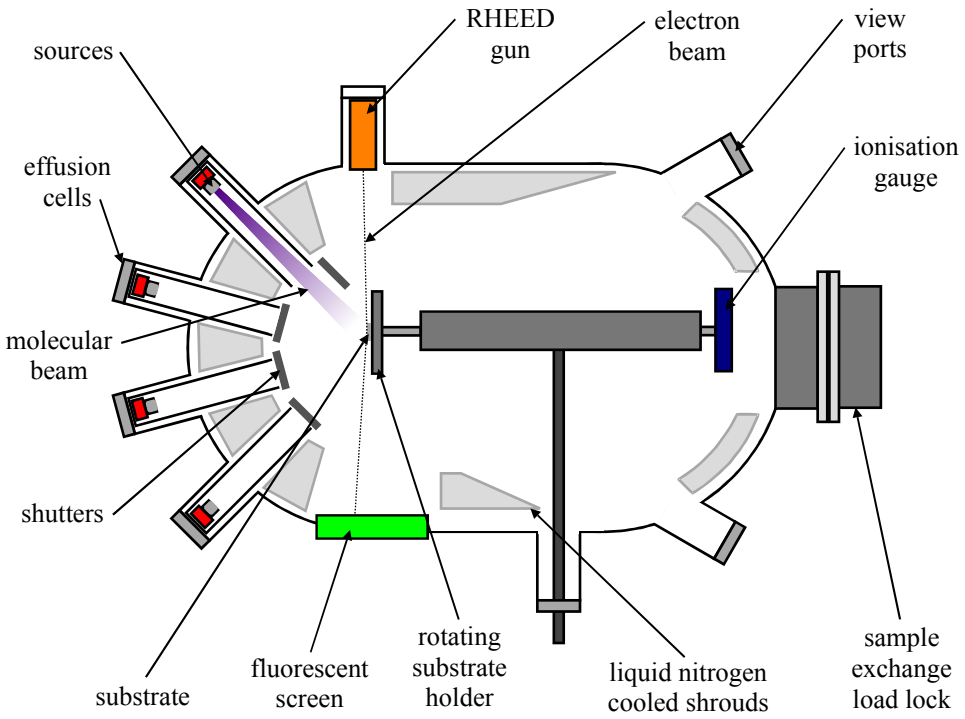

Figure 2.3.5: Molecular beam epitaxy chamber.

The use of separate effusion cells for each different molecular beam make MBE an ideal technique for the fabrication of several film layers of different materials, which has lead to its wide use in the semiconductor industry, where complex multilayer structures with precise thicknesses are required. Fabrication of films in an UHV environment allows in-situ reflection high-energy electron diffraction (RHEED) analysis to be performed, which makes it possible to monitor properties such as film thickness, substrate temperature and the arrangement of surface atoms in an MBE system. MBE is ideal for the fabrication of thin films (as thin as single atomic layers) and thin multilayers of different materials, but is limited in its usefulness for the growth of thick films by its relatively slow growth rate and high cost. The complexity of the apparatus can also be a big disadvantage because it can take a long time to set up and refine for a particular type of film material growth. MBE has been applied to the deposition of optical thin film waveguides and successful growth of Pr^{3+}-doped calcium fluoride (Pr^{3+}:CaF_2) and Nd-doped lanthanum fluoride (Nd:LaF_3) has been reported [161; 162]; also, lasing of the Nd-doped lanthanum fluoride was observed.

2.3.6 Sol-gel

A sol is a colloidal suspension of solid particles in a liquid phase solution, which forms a gel when it is dried enough that the particles form a continuous suspension. Substrates can be coated in sol-gel by dipping, spinning or spraying, and the sol-gel then forms solid films when dried. Thick films can be grown by multiple coating runs, but the range of materials that can be grown with sol-gel is limited by the number of suitable chemical precursors used for the sol. Figure 2.3.6 shows an overview of the sol-gel fabrication process.

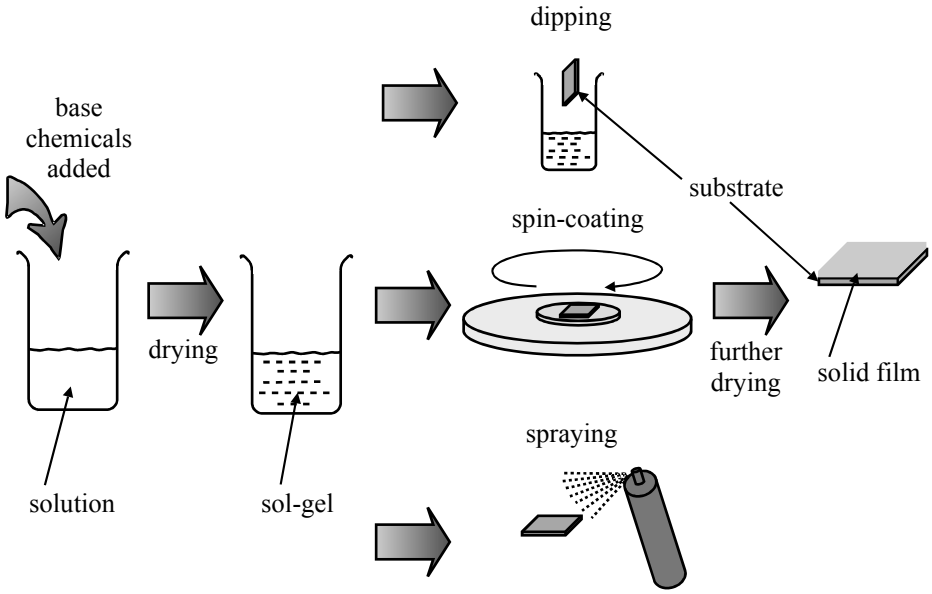

Figure 2.3.6: Overview of the sol-gel fabrication process.

The sol-gel technique is generally not suitable for the growth of multicomponent materials with complex stoichiometries, and epitaxial growth can be difficult to achieve. The growth of some simple oxide optical waveguides such as yttria [163; 164] and titanium oxide (TiO_2) [165; 166] has been reported, and some titanium oxide films grown by sol-gel have been further developed into channel waveguides by subsequent laser writing and etching [165; 166].

2.3.7 Direct and thermal bonding

The technique of direct bonding involves several steps, the first of which is to polish the plane surfaces of two pieces of bulk material to an optical flatness and ensure that they are clean of any dirt or other particles. When brought together, the two surfaces bond due to

Van der Waals forces, and in the case of thermal bonding, this process is assisted by heating of the two layers. Figure 2.3.7 shows an overview of the direct bonding fabrication process. It can be very difficult to make thin films using direct bonding because the thin film layer is prone to cracking at some point in the fabrication process. This problem can be overcome by bonding a thick layer and polishing back to the desired thickness, but this remedy makes the fabrication of multilayers by direct bonding impractical and time consuming. When using thermal bonding, materials with a similar thermal expansion coefficient must be chosen to avoid cracking upon cooling. Successful fabrication of Nd:YAG, Nd:GGG and Ti:sapphire thin film waveguides by direct bonding has been reported [167-169]. In the case of an Nd:YAG on sapphire sample, losses less than 0.2 $dBcm^{-1}$ were observed and efficient laser operation was achieved [169].

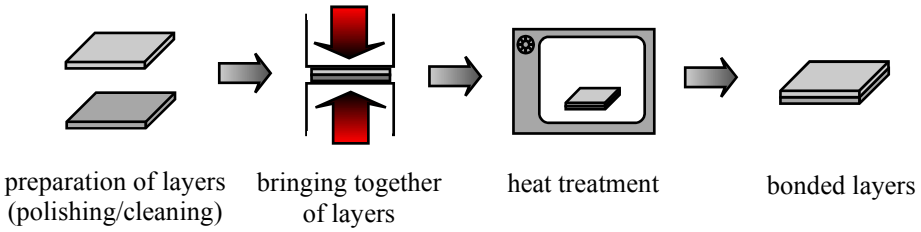

Figure 2.3.7: Overview of the direct bonding fabrication process.

2.3.8 Summary

Film fabrication technique	Typical growth rate (μm/hr)	Multi-component compound growth	Comments
TVD	0.1	Bad	Mainly used for basic films or coatings of metals.
Sputtering	0.1	Bad	Used for electronic and semiconductor materials, optics and protective coatings.
CVD	1	Moderate	Used for electronic and semiconductor materials, structural and protective coatings.
LACVD	0.5	Moderate	Experimental technique with many applications for optoelectronic, semiconductor and MEMS materials, structures and coatings. Assistance of a laser can allow 3D structures to be grown.
PECVD	1	Moderate	Experimental technique with many applications for optoelectronic, semiconductor and MEMS materials, structures and coatings. Plasma provides benefits such as increased growth rate.
MOCVD	0.5	Moderate	Experimental technique with many applications for optoelectronic, semiconductor and MEMS materials, structures and coatings.
LPE	10+	Good	Experimental technique with many applications for optoelectronic and semiconductor materials, and is particularly good for crystal growth. Very high growth rates can be obtained.
MBE	0.5	Moderate	Mainly used for semiconductor and electronic materials but has also been applied to some optical materials with basic compounds.
Sol-gel	n/a	Poor	Mainly used for glasses and ceramics. It is often difficult to achieve good crystal growth.
Direct bonding	n/a	n/a	Experimental technique that is versatile in terms of materials and has many applications for optoelectronic, electronic and semiconductor materials and structures. Can offer layer and substrate combinations not available with other techniques.
PLD	10+	Excellent	Experimental technique that is versatile in terms of materials and has many applications for optoelectronic, electronic and semiconductor materials. Congruent evaporation allows complex stoichiometries to be deposited, and growth rates can be very high.

Table 2.3.1: Summary of film fabrication techniques.

2.4 Other techniques of waveguide fabrication

The following methods are all alternative techniques for the fabrication of waveguides, and work by modifying existing substrates or films to create a region with a higher refractive index than its surroundings which can subsequently be used as a waveguiding region or layer. Consideration of these alternative techniques allows the advantages and disadvantages of PLD to be discussed particularly in terms of the film-waveguide structure.

2.4.1 Indiffusion

The substrate is coated with a thin layer (15-150 nm) of a suitable metal, and then placed in an oven heated to ≥ 1000 °C for a suitable length of time (several hours/days). The high temperature allows the metal layer to diffuse into the substrate and form a region of increased refractive index. Whole surfaces can be indiffused to make waveguiding films, or strips can be indiffused to make channel waveguides as shown in figure 2.4.1.

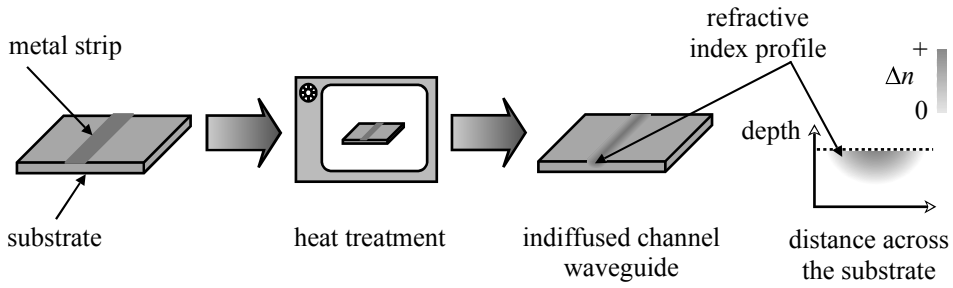

Figure 2.4.1: Overview of the indiffusion waveguide fabrication process.

Laser dopant species can be indiffused, but in this case it is often necessary to indiffuse another metal first because typical laser dopant concentrations are not high enough to produce a significant refractive index change by themselves. The effectiveness of this technique is limited by the range of metals suitable for diffusion in a particular material, and the time it takes for indiffusion to take place limits the thickness of waveguides. Optical waveguides fabricated by the indiffusion of nickel [170], and waveguide lasers fabricated by the indiffusion of neodymium [171] have been reported.

2.4.2 Ion-exchange

Substrates are immersed in a bath of molten salt, so that the alkali ions in the salt slowly exchange with the ions in the substrate, creating a region of altered refractive index. The rate of ion-exchange can be controlled by changing the temperature or by the application of an electric field across the sample. A mask can also be used to create strips of ion-exchanged areas to make channel waveguides, as shown in figure 2.4.2, or other mask designs can be used to produce more complex waveguiding structures. The technique of ion-exchange suffers from similar limitations as indiffusion, however success has been experienced with the technique, and the fabrication of neodymium based waveguide lasers by ion-exchange has been reported [172; 173].

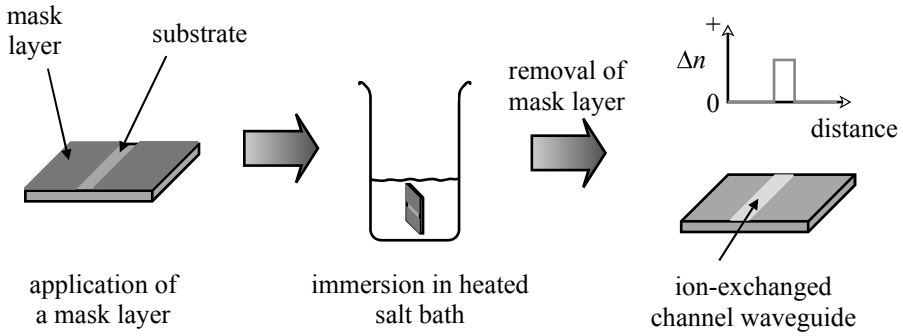

Figure 2.4.2: Overview of the ion-exchange waveguide fabrication technique.

2.4.3 Ion implantation

Ions (typically light ions such as protons or He^+) accelerated to high energies (~ a few MeV) can be used to damage the crystal lattice of materials, causing a change in refractive index as shown in figure 2.4.3. High energy ions incident on a substrate lose their energy near the surface by firstly electron excitation, and subsequently by interaction with the ions in the crystal lattice. The ion energy can be varied to control the depth at which most of the damage occurs. Higher energy ions produce a damaged region well below the surface, whereas lower energy ions produce a damaged region closer to or at the surface. Ion implantation can create regions of increased or decreased refractive index. For the case when an increased refractive index region is produced, waveguiding can occur without further processing. To utilise regions of decreased refractive index, a layer must be produced below an unaffected surface region, where waveguiding can occur, or a well profile must be produced using two damaged regions, allowing waveguiding to occur in the central

unaffected region. This technique can be applied to many different materials. As an example relevant to the materials of interest in this thesis, waveguides based on Er:YAG have been fabricated by He^+ implantation [174], and Nd:YAG waveguides have been fabricated by proton implantation [175].

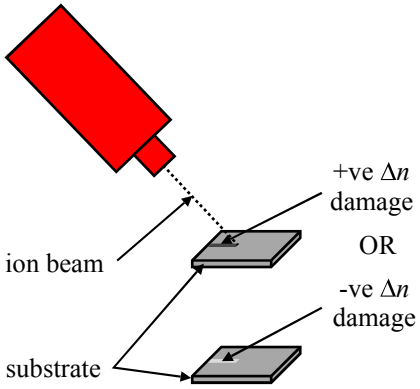

Figure 2.4.3: Examples of refractive index profiles suitable for producing waveguiding regions.

2.4.4 Etching/ion beam milling

Photolithography can be used, with subsequent etching or ion beam milling, to create raised waveguiding structures such as ribs. An overview of the fabrication process is shown in figure 2.4.4, with ion beam milling shown as an example.

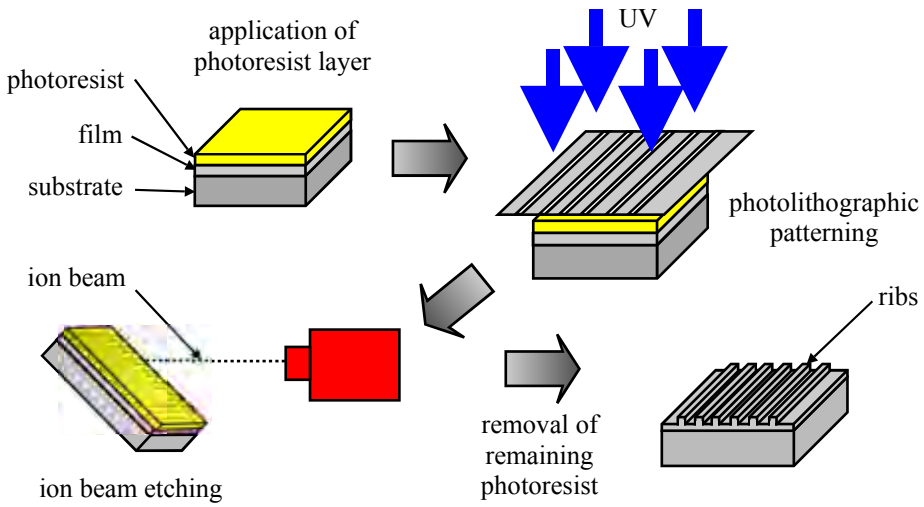

Figure 2.4.4: Overview of the etching technique of rib waveguide fabrication (ion beam milling shown as an example).

A suitable mask is used with photolithography to produce strips of developed photoresist, and subsequent etching by chemicals or ion beam milling then leads to the undeveloped areas being etched/removed at a faster rate than the developed areas. When any remaining photoresist is cleaned off, several raised rib structures remain, allowing multiple waveguiding ribs to be fabricated on a single film. The confinement of light in the horizontal plane of the guide as well as the vertical can improve the modal properties and laser operation of planar waveguide lasers. Rib waveguides based on Ti:sapphire and Nd:GGG have been fabricated by this technique [24; 28; 85; 160], and lasing has been observed for both Ti:sapphire [28] and Nd:GGG ribs [160].

2.4.5 Direct writing

A focussed laser beam can be used to produce a refractive index change in a material. The change will be produced at and near the focal point of the laser and can be permanent or temporary depending on the laser intensity and the material in use. By tracking the laser beam through the material as shown in figure 2.4.5, channel regions of different refractive indices suitable for waveguiding can be made.

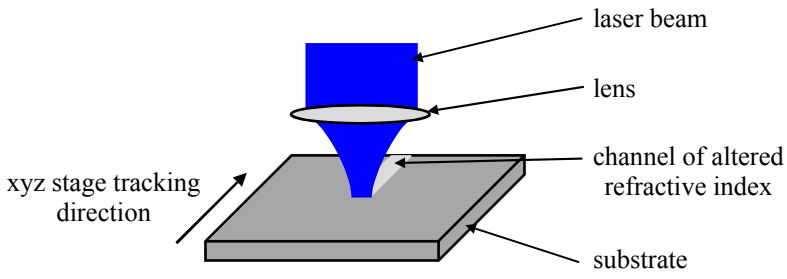

Figure 2.4.5: Direct writing waveguide fabrication technique.

Channel waveguides have been fabricated in gallium lanthanum sulphide [176] and various waveguide devices have been fabricated in silica by direct writing [177].

2.4.6 Summary

Waveguide fabrication technique	Technique complexity	Material range applicable to	Comments
indiffusion	simple	wide	Tends to be slow and often the indiffusion of two elements is needed to get a laser dopant and a sufficient refractive index change.
Ion-exchange	moderate	moderate	Tends to be slow. Suitable for the creation of complex channel structures and only limited by the mask used in the photolithography process.
Ion implantation	difficult	wide	Capable of making complicated waveguiding structures due to its ability to produce positive and negative changes to refractive index.
Etching/ion beam milling	difficult	very wide	Ribs have the same intrinsic loss as the original sample since the rib itself isn't modified. Confinement can be improved by the subsequent growth of a capping layer.
Direct writing	moderate	narrow	Limited in its material range due to problems with retention of the refractive index change. Fast, simple and versatile technique.

Table 2.4.1: Summary of waveguide fabrication techniques.

2.5 Conclusions

- Pulsed laser deposition is a proven and established technique for the fabrication of high quality films suitable for optical waveguiding. PLD can produce films with a high crystal quality and low propagation losses.
- The growth of garnet crystal by PLD has matured to the point of being able to compete with other techniques, and offer advantages such as high growth rates and relatively simple experimental complexity.
- The main competitors to PLD, for the fabrication of thick garnet crystal films and multilayers, are LPE and direct bonding.
- When used in conjunction with a rib fabrication technique, PLD is ideal for the fabrication of buried rib waveguides that are highly useful in the optoelectronics industry (because light can be coupled from them into optical fibres).

Chapter 3

Theory

3.1 Introduction

Some aspects of PLD theory are discussed here along with some elemental waveguide and laser theory. The discussion of PLD theory presented here is mainly qualitative with only some of the more relevant equations reproduced. A basic overview of waveguide theory will be discussed to show how the solutions to more complex geometries can be derived. Some laser theory will also be discussed and equations needed for the analysis of results will be presented.

3.2 PLD theory

The overall process of PLD is determined by several codependent variables, which has made the formulation of theoretical models difficult. There have been several attempts at producing theoretical models of PLD and though none have succeeded in capturing all of the physics involved, some success has been experienced by modelling individual parts of the PLD process [9; 10; 178-186], which is logically split into three phases: the laser-target interaction (ablation phase), the plume-background gas interaction (plume phase) and the plume-substrate interaction (film growth phase). It is easier to discuss these three phases separately, and it is also useful to discuss the codependencies of the variables in PLD and how they can be managed to produce high quality films with minimal experimentation. The

discussion of PLD theory presented here is a general overview of the technique in its basic form without any advanced modifications, and is intended to be mainly qualitative, though some of the more important equations will be included.

3.2.1 Ablation phase

The ablation phase is logically split into two further subsections; the pure laser-target interaction and the subsequent interaction of the ablating laser pulse with the material ejected from the target before the laser pulse ends.

3.2.1.1 Laser-target interaction

The initial interaction of the ablating laser pulse with the target material depends upon the properties of the target material and the ablating laser pulse. An ideal target will:

- not reflect well at the ablating laser wavelength to allow the initial part of the pulse access below the target surface as quickly as possible (the reflectance of the target is less important once the target is heated because the surface properties will change);
- have a short absorption depth for the wavelength of the laser used for ablation to ensure that the energy is absorbed in a tightly confined area;
- have a low thermal diffusivity to ensure that energy from the ablating laser pulse is not used inefficiently by conduction away from the ablation site.

The volume heated by a laser pulse is determined by the spot size and the larger of the absorption depth or diffusion depth [187], shown in equations 3.2.1 and 3.2.2 respectively.

$$L_{diff} = 2\sqrt{(\kappa_{td}\tau)} \qquad \textbf{(3.2.1)}$$

L_{diff} = diffusion depth, κ_{td} = thermal diffusivity, τ = pulse duration.

$$L_{abs} = \frac{1}{\alpha} \qquad \textbf{(3.2.2)}$$

L_{abs} = absorption depth, α = absorption coefficient.

In the case where the absorption depth is larger than the diffusion depth, the depth of material removed by ablation can be related to the fluence of the laser and the threshold fluence for ablation as in equation 3.2.3 [188].

$$d_a = \frac{1}{\alpha} \ln \left| \frac{F_L}{F_{L-th}} \right| \qquad \textbf{(3.2.3)}$$

d_a = depth removed by ablation, F_L = laser fluence, $F_{L\text{-}th}$ = threshold fluence for ablation.

The ideal properties of a laser used for ablation are short wavelength and short pulse duration, as short wavelengths tend to have smaller absorption depths, and short pulse durations minimise heat conduction away from the ablation site because the time that the target has to react to the laser pulse is minimised. These ideal properties for target material and ablating laser allow for the type of ablation required for PLD, congruent evaporation, which is especially required when multicomponent target materials are used because it is important for the stoichiometry of the target to be preserved for deposition on the substrate. Excimer lasers are commonly used for PLD because of their short wavelengths (193 nm - argon fluoride (ArF), 248 nm - krypton fluoride (KrF), 308 nm - xenon chloride (XeCl), 351 nm - xenon fluoride (XeF)) and short pulse durations (~ 10-20 ns).

The mechanism for the absorption of the initial part of the laser pulse is electron excitation. When a laser with a short pulse duration is used, further absorption of the pulse is dominated by non-thermal mechanisms such as single-photon and multi-photon absorption, and dielectric breakdown [189-191]. Free electrons are accelerated by the electric field of the laser pulse and gain enough energy to ionise the atoms they collide with causing more electrons to be freed, and hence adding to the process. Above a certain threshold of laser fluence, this effect leads to heating of the atoms within the material and causes material to be ejected. As the target absorbs more energy by the laser pulse, energy conservation forces the ejection velocity of the target material to increase and a plasma plume is formed [192]. The different processes involved in ablation are shown in figure 3.2.1, and a description of the different stages follows:

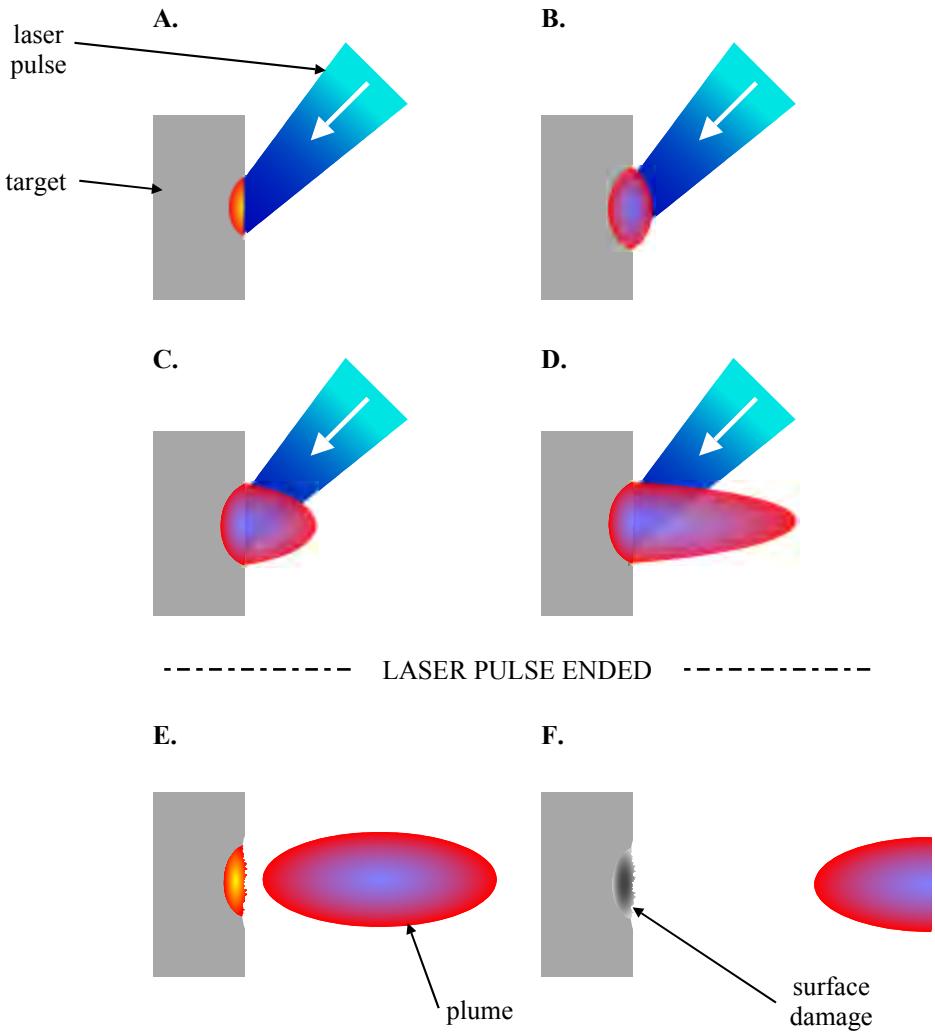

Figure 3.2.1: The different stages of ablation.

A. The laser pulse hits the target and the target surface starts to melt.

B. The heat is conducted slightly deeper into the target as the laser pulse continues and the temperature rises sharply, causing the material to start to evaporate. At this early stage, the ejected material is still relatively transparent and the laser pulse continues to heat the target surface.

C. More material is ejected from the target surface as the laser pulse continues and the surface temperature rises to a maximum. The ejected material is now dense enough to absorb energy directly from the laser pulse and enough energy is absorbed for it to enter a plasma state and expand away from the target surface as a plume.

D. The plume partially absorbs the laser pulse; this reduces heating of the target surface by the laser pulse and limits further ejection of material from the target.

E. The laser pulse ends and the plume continues to expand adiabatically away from the target surface, which in turn begins to cool.

F. The target surface continues to cool and solidifies in a damaged state, which will be rough and may have an altered stoichiometry from the bulk of the target. Features such as cones, ripples, laser induced periodic surface structures (LIPSS), particulates and larger droplets may be present on the surface.

The temperature of the target in the initial stages of absorbing the laser pulse (before the absorption of the pulse by the plume complicates the problem) can be determined by the heat flow equation shown as equation 3.2.4 [11], which is reduced to one-dimension because the thermal diffusion distance in nanosecond timescales is much smaller than the transverse dimensions of the laser beam.

$$\rho(T)C_p(T)\frac{\partial T(x,t)}{\partial t} = \frac{\partial}{\partial x}\left(K(T)\frac{\partial T(x,t)}{\partial x} \right) + \left(1-R(T)\right) I_o(t)\alpha(T)e^{-\alpha(T)x} \qquad \textbf{(3.2.4)}$$

x = direction perpendicular to the plane of the target, $\rho(T)$ = temperature dependent density, $C_p(T)$ = temperature dependent heat capacity per unit mass of the target, $T(x, t)$ = temperature inside the target, $K(T)$ = temperature dependent thermal conductivity, $R(T)$ = temperature dependent reflection coefficient, $I_o(t)$ = time dependent laser intensity, $\alpha(T)$ = temperature dependent absorption coefficient.

The temperature dependence of the properties such as heat capacity, thermal conductivity and absorption coefficient make the heat flow equation very difficult to solve even under the simplification of reducing the problem to modelling the temperature at the target surface.

The dimensions of the laser spot influence the shape of the plume; a large laser spot results in a plume that is directed mostly perpendicular to the target surface, whereas small laser spots lead to plumes that expand more in directions parallel to the target surface [193-195]. Figure 3.2.2 shows this effect and includes a vector representation of the relative velocities of plume components at different distances from the target surface, in the directions parallel and perpendicular to the target surface [193].

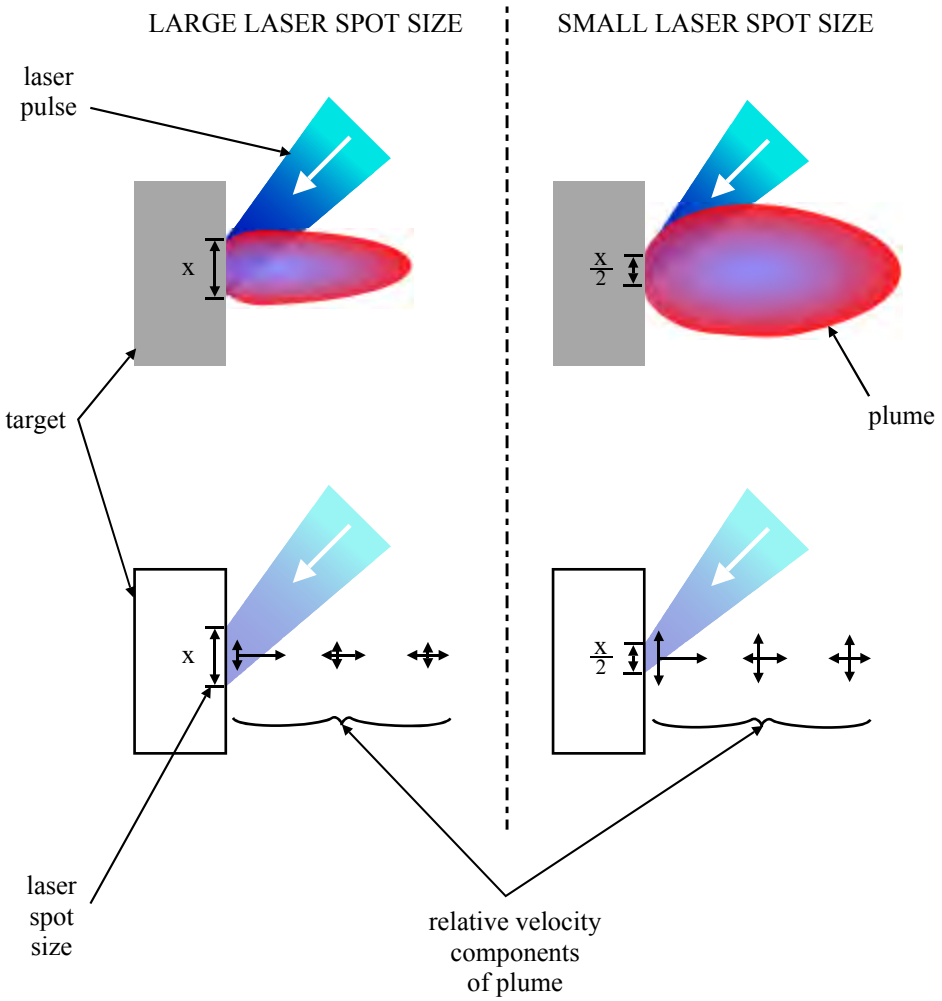

Figure 3.2.2: The dependence of plume expansion on the laser spot width.

This phenomenon has been named the 'flip over effect' when described in reports because a laser spot with a small width leads to a large rate of plume expansion in the same axis, whereas a laser spot with a larger width leads to a smaller rate of plume expansion in the same axis [194; 196] (this behaviour is similar to diffraction; smaller laser spot sizes lead to higher rates of divergence). The effect has been reproduced in a model based on gas-dynamics equations [196]; the expansion of the plume was calculated to be faster in the initially smaller axis, meaning the expanding shape of the plume is dependent upon its initial dimensions which are determined by the laser spot shape. Many PLD setups use excimer lasers for ablation and this effect has particular implications for such a laser because the spot shape (if not corrected by lenses) is typically rectangular, leading to an elliptical plume cross-section.

3.2.1.2 Laser-plume interaction

The plume undergoes isothermal expansion before the end of the laser pulse; whilst the temperature remains fairly constant, the pressure, volume and ionisation of the plume increases. The expansion of the plume in this isothermal regime is predicted by gas-dynamic equations as shown in equation 3.2.5 [193].

$$X(t)\left[\frac{1}{t}\frac{\mathrm{d}X}{\mathrm{d}t}+\frac{\mathrm{d}^2X}{\mathrm{d}t^2}\right]=Y(t)\left[\frac{1}{t}\frac{\mathrm{d}Y}{\mathrm{d}t}+\frac{\mathrm{d}^2Y}{\mathrm{d}t^2}\right]=Z(t)\left[\frac{1}{t}\frac{\mathrm{d}Z}{\mathrm{d}t}+\frac{\mathrm{d}^2Z}{\mathrm{d}t^2}\right] \quad \textbf{(3.2.5)}$$

$X(t)$ = position of the plasma edge perpendicular to the target surface, $Y(t)$ and $Z(t)$ = transverse positions of the plasma edge, t = time.

Partial absorption of the laser pulse by the plume limits the power that reaches the substrate and controls further ejection of material. This effect is dependent upon the cross-section [181] and the fluence of the laser pulse. Low laser fluences result in relatively transparent plumes and further ejection of material is only slightly limited, whereas high laser fluences result in highly ionised plumes that absorb the laser pulse much more [179] and significantly limit further ejection of material from the target surface. Inverse Bremsstrahlung is thought to be the dominant mechanism for absorption when very high power densities (> 100 MWcm^{-1}) are involved and a fully ionised plasma is achieved early in the pulse. However, for relatively low fluences such as those used for the deposition of films reported in this thesis, absorption via inverse Bremsstrahlung is thought to be relatively weak and photo-ionisation via bound-bound or bound-free transitions has been suggested as an alternative dominant mechanism for absorption of the laser pulse by the plasma [197].

Modelling of the photo-ionisation process is difficult because calculating the absorption spectrum of a plasma is challenging, especially for UV and the case where the plume has a complex composition. The absorption coefficient for the inverse Bremsstrahlung process can be simplified and is shown as equation 3.2.6 [10]. It is assumed that the frequency of the laser used for ablation is greater than the plasma frequency as shown in equation 3.2.7 [198], else it would be reflected by the plasma.

$$\alpha_{IB}=3.69\times10^{8}\,\frac{Z^3 n_i^{\,2}}{T^{0.5}\nu^3}\left(1-e^{-h\nu/kT}\right) \quad \textbf{(3.2.6)}$$

α_{IB} = absorption coefficient, Z = average charge, n_i = ion density, T = temperature of the plasma, ν = frequency of the laser used for ablation, h = Planck's constant, k = Boltzmann constant.

$$\nu_{ps} = 8.97 \times 10^3 \left(n_e \right)^{0.5} \quad \textbf{(3.2.7)}$$

ν_{ps} = plasma frequency, n_e = electron number density.

A critical ion density for reflection of the incoming laser pulse can be calculated from equation 3.2.7. Modelling of the laser-plume interaction has been improved by the use of a simulated absorption coefficient [198], proving that the transparency of the plume is critical to its development before the laser pulse has ended.

3.2.2 Plume phase

The fluence of the laser is critical in determining the initial properties of the plume and therefore also how it continues to develop. A plume with a larger recession velocity can be obtained by increasing the laser fluence [193]. Increasing the laser fluence also leads to higher maximum surface temperatures [193], a larger crater in the target, and a plume with a higher temperature and higher ionisation fraction [195]. When fluences of order Joules per cm^2 are used, plasmas can reach temperatures up to and exceeding 10,000 K [199]. The velocity of plasma constituents due to the conversion of thermal energy to kinetic energy is predicted by equation 3.2.8 [199].

$$v_i = \left(\frac{2}{\gamma - 1} \right) \left(\frac{\gamma k T}{m_i} \right)^{0.5} \quad \textbf{(3.2.8)}$$

v_i = velocity of a plume constituent, γ = ratio of specific heats (C_p/C_v) for the plume, m_i = mass of a plume constituent i.

The ionisation fraction can be calculated from the Saha equation shown below (equation 3.2.9). Using typical values for the parameters in the Saha equation and a temperature of 10,000 K, an ionisation fraction of over 80% is predicted for a typical PLD plasma plume [199]. It can be seen from the Saha equation that the plume ionisation will be limited by the exponential term until the first ionisation potential, U_i, is a few times that of the plume energy kT. Typical first ionisation potentials are of order 10 eV, meaning the plume ionisation fraction won't start to increase significantly until plume temperatures rise above 6000 K.

$$\frac{n_i}{n_n} = 2.4\times10^{15}\,\frac{T^{3/2}}{n_i}\,e^{-U_i/kT} \qquad \textbf{(3.2.9)}$$

n_i = ion number density, n_n = neutral number density, U_i = first ionisation potential.

The interaction of the plume with the chamber atmosphere is critical in determining the plume properties upon arrival at the substrate. The plume undergoes unsteady adiabatic expansion (UAE) once the laser pulse has ended [200], and is predicted by gas-dynamic equations as shown in equation 3.2.10 [193] (although this is only strictly true when depositing in vacuum conditions, since there is some exchange of energy between the plume and the background gas when a background gas is used). It is assumed that in this regime there is no further injection of particles or input of energy into the plume, since the pulse has ended. Thermal energy is converted into kinetic energy as the plume expands, but the temperature of the plasma does not decrease indefinitely because of energy from recombination. The rate of expansion is greatest in the axis with the largest density and pressure gradient, and the plume expands quickly away from the target because the laser spot size is much larger than the depth of ablation. The dependence of plume expansion on the pressure gradients present in the initial stages of the plasma also explains the flip over effect discussed earlier.

$$X(t)\left[\frac{\mathrm{d}^2X}{\mathrm{d}t^2}\right] = Y(t)\left[\frac{\mathrm{d}^2Y}{\mathrm{d}t^2}\right] = Z(t)\left[\frac{\mathrm{d}^2Z}{\mathrm{d}t^2}\right] = \frac{kT_o}{m_i}\left[\frac{X_oY_oZ_o}{X(t)Y(t)Z(t)}\right] \qquad \textbf{(3.2.10)}$$

T_o = initial temperature of the plume edge at the beginning of UAE, m_i = mass of a plume constituent i, X_o, Y_o, Z_o = initial positions of the orthogonal edges of the plume at the beginning of UAE.

The angular distribution of the plume front has been found to be best described by $(\cos\theta)^n$, and the value of the exponent n can vary from 2 to 20, however it is typically found to have a value between 10 and 12 [195].

A high background gas pressure leads to more collisions of plume constituents [199], causing the plume to be slowed and more confined [193], and energy is transferred into the background gas as a shock-wave [201]. A higher background gas pressure also produces a sharper plume boundary [199] and can lead to less even growth, despite the fact that the plume is more homogenised [185]. The background gas pressure influences the plume fluorescence as shown in figure 3.2.3; increasing the background gas pressure from vacuum

will at first appear to make the plume larger due to the increase in fluorescence caused by extra collisions and the increase in fluorescence brightness caused by confinement, then as the background gas pressure is increased further the plume will be seen to shrink due to further confinement.

The species of background gas can also affect the characteristics of the plume, and can be chosen so that it influences the stoichiometry of the plume; for instance oxygen can be used to counter the effect of deficiency in the plume caused by loss of oxygen in the ablation process, and the stoichiometry of the plume can be adjusted by oxidation of the constituents [202]. Oxidation of plume constituents can also help to control the crystalline phase of the deposited film [201].

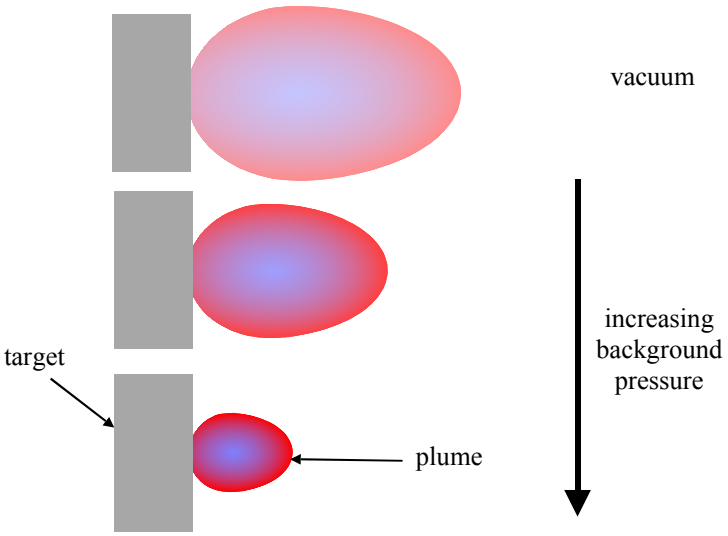

Figure 3.2.3: The effect of background gas pressure on plume fluorescence (darker parts of the plume represent higher fluorescence brightness).

The target-substrate distance can also affect the composition of the deposited film [203], and must be chosen correctly so that the plume possesses ideal properties for deposition. In terms of film nucleation (which will be discussed further in the next section), the fluence, target-substrate distance and background gas pressure must be tuned so that the energy of the plume is ideal when it reaches the substrate surface; too high an energy may lead to desorption[5] and a film with incorrect stoichiometry, whereas too low an energy may lead to poor film crystallinity. If the target-substrate distance is kept constant for experimental simplicity, the background gas pressure and laser fluence must be varied together so that the deposition rate remains constant [204], which has been found to be a key parameter for

5 Desorption refers to the removal of an atom or cluster of atoms from the film or substrate surface by a means such as re-evaporation or ejection.

PLD; optimal depositions of oxides have been found using a deposition rate of ~ 1 Å per pulse [204]. Care must be taken when using the background gas pressure to control the deposition rate; an increase in background gas pressure will usually lead to a decrease in deposition rate, but in some cases there will be an increase in deposition rate to a maximum, before this subsequent decrease. A possible explanation for this phenomenon is the effect of desorption from the substrate [185] which will be discussed further in the next section.

The distribution of different constituents in the plume allows for some selection of what is deposited. Electrons attain the highest velocities and tend to be found at the outer edges of the plume, but are prevented from leaving the plume by the strong space-charge field produced by their collective movement away from the ions [199]. This effect also causes the ions to be accelerated towards the plume boundary with a strength relative to their charge value. Lighter species tend to be found mostly towards the front of the plume whilst heavier species, including particulates, travel more slowly at the back of the plume; this allows some control to be had over particulate deposition and this will be discussed further in the later section on particulates.

3.2.3 Film growth phase

The thickness distribution of the film is directly dependent upon the angular distribution of the plume, and as displayed in figure 3.2.4, a plume with a wide angle of expansion leads to more even growth, whereas a plume with a narrow angle of expansion leads to heaped growth in a smaller area of substrate.

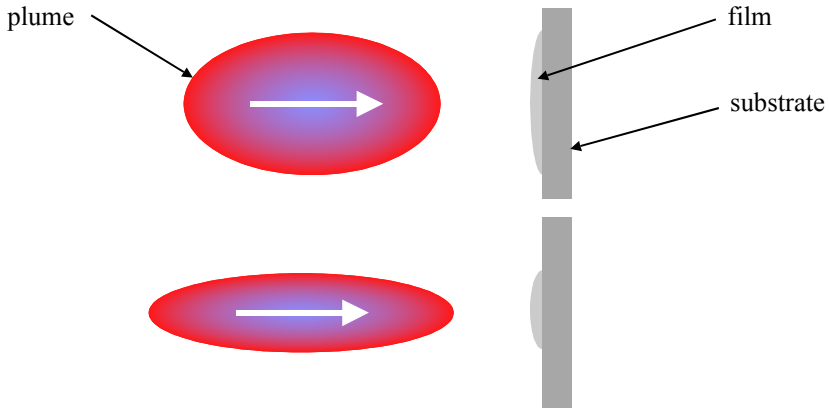

Figure 3.2.4: The relationship between plume angle of expansion and film thickness distribution.

The properties of the plume (as it arrives at the substrate) and the substrate temperature can predetermine the stoichiometry, crystalline phase, particulate size and density, and deposition rate of the deposited film. To obtain an ideal constant deposition rate, parameters such as laser fluence and background gas pressure must be balanced against the effect of desorption from the substrate [185]. Preferential desorption of particular film components will clearly affect the film composition [194], and this can occur because of the differing bond strengths of different film components. In particular, sputtering of the film surface by the plasma plume can occur if the substrate is placed close to the target, and may lead to non-stoichiometric growth. Substrate heating can help with the selection of the film crystalline phase and orientation, produce films with smoother surfaces [182], and increase the purity of the film grown because impurities can be desorbed preferentially [205]. However, raising the substrate temperature too high may also cause a higher rate of desorption of desired film components and lead to incorrect film stoichiometry.

Nucleation in films grown by PLD is different from other deposition techniques because of the relatively high peak deposition rate and high energy of the plume when it reaches the substrate [206; 207]. Nucleation is dependent upon the substrate and film materials, and parameters such as plume properties, background gas pressure and substrate temperature. The processes involved in film nucleation are summarised in figure 3.2.5 [206; 208].

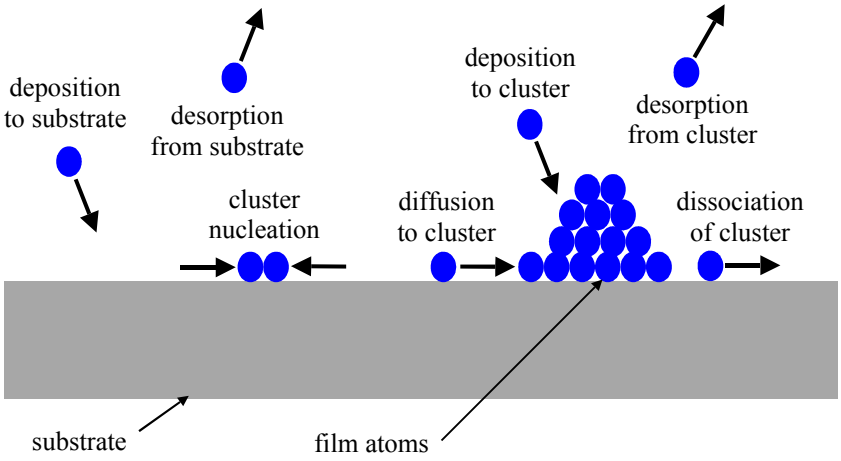

Figure 3.2.5: Summary of the processes involved in film nucleation.

Three different typical modes of film growth arise under different conditions of free energy on the substrate surface, and are shown in figures 3.2.6, 3.2.7 and 3.2.8, and described below:

Three-dimensional island growth (Volmer-Weber); three-dimensional islands are formed because the film components are more bound to each other than to the substrate [205]. In this case, on average, cluster free energy decreases as more atoms join, making the clusters stable.

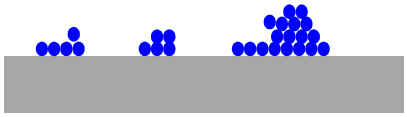

Figure 3.2.6: Three-dimensional island growth (Volmer-Weber).

Two-dimensional full monolayer growth (Frank-van der Merwe); the film grows in a two-dimensional planar layer-by-layer way because the film components are more bound to the substrate than to each other [205]. In this case, on average, cluster free energy increases as more atoms join, making the clusters unstable and leading to layer-by-layer growth.

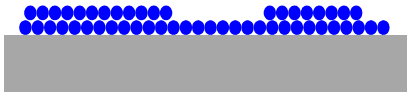

Figure 3.2.7: Two-dimensional full monolayer growth (Frank-van der Merwe).

Monolayers and islands (Stranski-Krastinov); the film grows in monolayers initially and islands start to occur as the surface conditions change as the film grows because of strain/stresses in the film [208]. In this case the free energy dynamics change as the film is deposited, causing a switch from layer-by-layer growth to three-dimensional island growth.

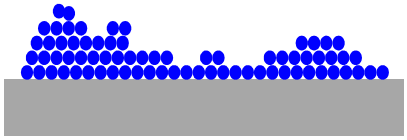

Figure 3.2.8: Monolayers and islands (Stranski-Krastinov).

3.2.4 Lattice mismatch

When films with a different lattice size to the substrate, but the same or similar crystal structure are grown, the first layers deposited will try to copy the substrate crystal structure and grow epitaxially, a critical condition for high crystal quality to be achieved. For

epitaxial growth to occur, a maximum of ~ 9% lattice mismatch can be accommodated [205], though it is possible that harmonic mismatches greater than 9% can allow epitaxial growth to occur. Figure 3.2.9 illustrates the conditions of matched lattice growth, strained growth, relaxed growth and harmonic mismatched growth [205].

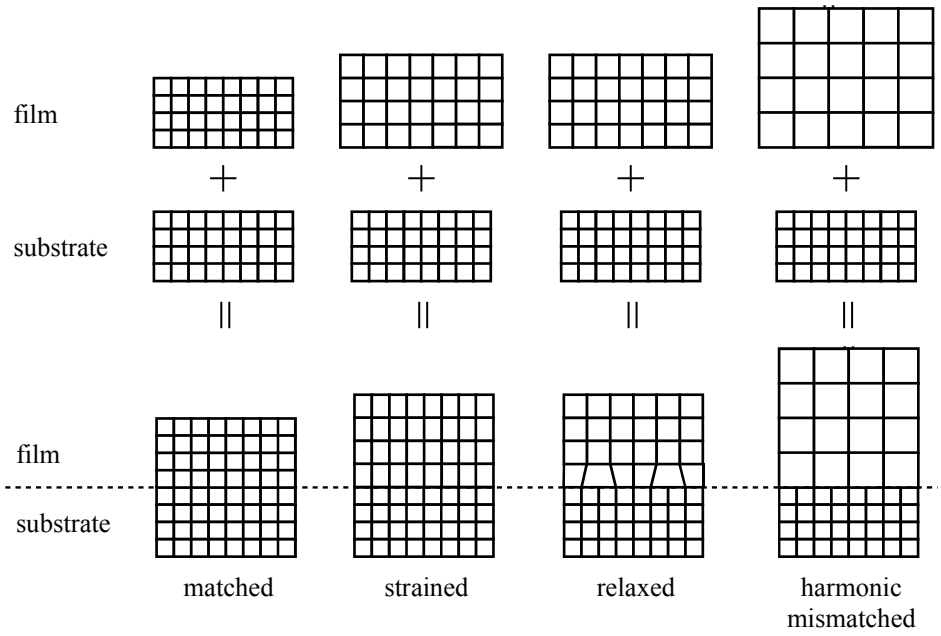

Figure 3.2.9: Matched lattice growth, strained growth, relaxed growth and harmonic mismatched growth.

After a few crystal layers have been deposited, the strain and stresses build up and may cause defects, or a different phase or orientation of crystal to be grown, particularly if the lattice sizes or crystal structures of the film and substrate are not well matched. Preferably, the stresses and strains will be accommodated by the occurrence of minor crystal defects such as dislocations and vacancies near the substrate-film boundary, allowing the film to relax to its bulk lattice size and grow further without any stresses, strains or defects.

3.2.5 Thermal expansion mismatch

In the case of thick films such as the ones discussed in this thesis, strains and stresses formed in the nucleation phase due to lattice mismatch will usually either relax away as a result of defects, or build up sufficiently to make the film grow differently. Stresses and strains that arise as a result of thermal expansion mismatch are not so easily avoided because they have the effect of making the film more susceptible to cracking as the thickness increases. If a thermal expansion mismatch exists in a substrate and film combination that

has been fabricated at high temperature, the film and substrate will shrink at different rates when cooled, producing one of the scenarios displayed in figure 3.2.10 [205]. In the scenario where $\alpha_{film} < \alpha_{substrate}$, the film is under compressive strain, whereas when $\alpha_{film} > \alpha_{substrate}$, the film is under tensile strain.

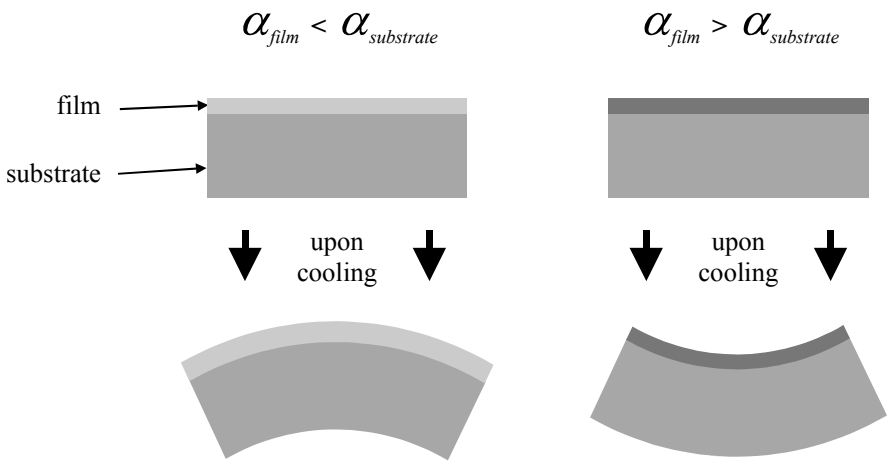

Figure 3.2.10: The effect of thermal expansion mismatch.

Thermal expansion mismatch can be difficult to predict because thermal expansion coefficients are usually quoted for a small temperature range and may not be valid for the range over which samples are heated. This problem is compounded by the fact that films don't always grow with the correct stoichiometry, leading to thermal expansion behaviour that differs from bulk crystal. Thermal expansion mismatch can lead to film fracturing and can cause the substrate to fracture in the case where the film has good adhesion to the substrate.

It is useful to be able to quantify the stress in a film. A comprehensive derivation and explanation of the quantification of stress in films has been presented elsewhere [205] so only the main formulas will be presented here. The Stoney formula can be used for calculating the stress that a film is under when the radius of curvature of the bending in the sample is known. For the case where the substrate thickness is much greater than the film, the Stoney formula can be simplified to the form shown as equation 3.2.11.

$$\sigma_f = \frac{1}{6R}\frac{E_S {d_S}^2}{(1-v_S)d_f} \quad \textbf{(3.2.11)}$$

σ_f = stress in the film, E_s = Young's modulus of the substrate, d_s and d_f = substrate and film thicknesses respectively, R = radius of curvature of bending, v_s = Poisson's ratio for the substrate.

The stress resulting from thermal expansion mismatch can be quantified using the formula shown as equation 3.2.12.

$$\sigma_{th} = \frac{(\alpha_{substrate} - \alpha_{film})E_f \Delta T}{(1-v_f)} \quad \textbf{(3.2.12)}$$

σ_{th} = stress in the film resulting from thermal expansion mismatch, E_f = Young's modulus of the film, ΔT = difference between the growth temperature and room temperature, v_f = Poisson's ratio for the film.

Stress in the film plane can result in contraction or expansion of the film in the axis perpendicular to the film plane. This will affect the crystal lattice spacing and provides another way of quantifying the stress, providing that the stressed and unstressed (bulk) crystal lattice sizes are known, as shown below in equation 3.2.13.

$$\sigma_f = -\frac{E_f}{2v_f}\left(\frac{\bar{a}_0 - a_0}{a_0}\right) \quad \textbf{(3.2.13)}$$

$\bar{a}_0$ = lattice parameter for the stressed film, a_0 = lattice parameter for bulk crystal.

3.2.6 Target damage and particulates

After the laser pulse has ended, the surface tension of the cooling ablated area can produce structures such as ripples and crater edges. The ablated area can also suffer from the following processes [192]:

- The redistribution of elements by diffusion whilst the ablated area is still cooling.
- The loss of more volatile constituents, resulting in a layer enriched with less volatile species.

- The segregation of less soluble constituents, resulting in an accumulation on the surface.
- Altered crystal structure; either the formation of a layer with altered phase/orientation or the partial or total loss of crystallinity.
- Altered composition by the background gas species.

Particulates are thought to arise due to the following processes [209]:

- The dislodging of existing or laser-produced protruding surface features.
- Subsurface superheating[6].
- Splashing of the molten surface layer.
- Condensation from vapour species due to supersaturation.

The extended use of a particular area on a target surface can lead to particulate production because of the formation of cone and trough structures [210]. The occurrence of increased vapour pressures behind cones can cause them to be ejected [178], but they do not directly form particulates without breaking up further because cones found on target surfaces are larger than typical particulate sizes found in films. The formation of cones can lead to higher particulate production due to an increased effective fluence caused by the channelling and focussing of the laser beam by the cone sides. Cones are thought to be formed due to sites of higher resistance to ablation that can exist in non-uniform targets, and as ablation continues, the area around cone sites is ablated normally leaving material behind in the form of cones. The cone apex angle is dependent upon the angle of incidence of the laser and its fluence, and the target material in use.

The gradual formation of cones slows the deposition rate until they are fully formed and the deposition rate relaxes to an asymptotic value [211]. In some instances it is useful to precondition the target surface to avoid the initial period of high deposition rate. Another more general effect that can occur on the target surface due to an extended period of laser exposure is LIPSS [211; 212]. Ripples with periodic structure and equal thickness have been observed on target surfaces after exposure to laser light, and again preconditioning is a good solution for stabilising the surface before deposition is commenced. Particulates that arise

6 Subsurface superheating refers to the situation where material below the target surface gets hotter than the evaporating surface above it, resulting in 'micro-explosions' on the surface

from target damage can be avoided by polishing the target at periodic intervals so that the target surface never gets damaged enough to make the occurrence of particulates increase significantly [213].

A disadvantage of using a higher laser fluence is that more particulates are produced [203], which is thought to be due to subsurface superheating [214][6]. Subsurface superheating is however also dependent upon other parameters such as the composition and structure of the target material. It has been shown that particulates are minimised by use of a lower fluence [215; 216], however it was found that lowering the fluence too much changed the stoichiometry of the films. A technique called rapid sequential PLD (RSPLD), which uses multiple elemental targets, has been presented as a possible solution to the use of low laser fluences without the loss of correct stoichiometry [215]. It has been shown that the laser fluence can be changed over a range, without significantly affecting the stoichiometry of the deposited film [203]. The reduction of particulates by use of a lower laser fluence is also indirectly supported by a separate report that concludes that particulates are reduced by use of a lower deposition rate [217].

The occurrence of particulates in the deposited film can be reduced by diverting the slow components of the plume after the rest of the plume has already reached the substrate. This can be achieved by the use of a pulsed oxygen jet or a shutter arrangement synchronised with the pulse rate of the ablation [21; 209; 210]. The positioning of the substrate can be utilised as another method for reducing particulate density in the film as particulates can be made to miss the substrate by placement of the substrate in an off-axis position [209]. The charged constituents of the plasma plume can be guided by a magnetic field around an arc, leaving neutrally charged particulates behind [218]. Secondary lasers have been used to reduce the occurrence of particulates by heating the plume and breaking them up [25]. The use of two crossing plumes in the crossed-beam pulsed laser deposition technique (CBPLD) has also been successful in reducing the effect of particulates [219; 220]. An alternative to the prevention of the occurrence of particulates is to bury them with a capping layer [21].

3.2.7 Summary of variables

Management of variables for the production of optimised high quality films is not trivial, since changing one variable often changes the ideal setting for other variables. The variables in PLD and their codependencies (in terms of what variable ideal settings are affected when another variable is changed) are summarised in figure 3.2.11. The effects of changing a

single variable can be identified by keeping all other variables constant, and variables such as target composition, laser characteristics (other than fluence) and background gas species are generally kept constant for simplicity. Some variables, such as laser fluence and target-substrate distance, can be tuned within a finite range without causing a significant change in the deposited films, and this allows the optimum value for these variables to be roughly tuned so that more time can be spent finding the optimum value of more critical variables. The process of changing variables one by one and leaving them at their optimal value when moving to a new variable allows optimum variable settings to be found with relative ease, though only local optimum variable settings can be found by this technique, since there may be more than one group of optimum variable settings.

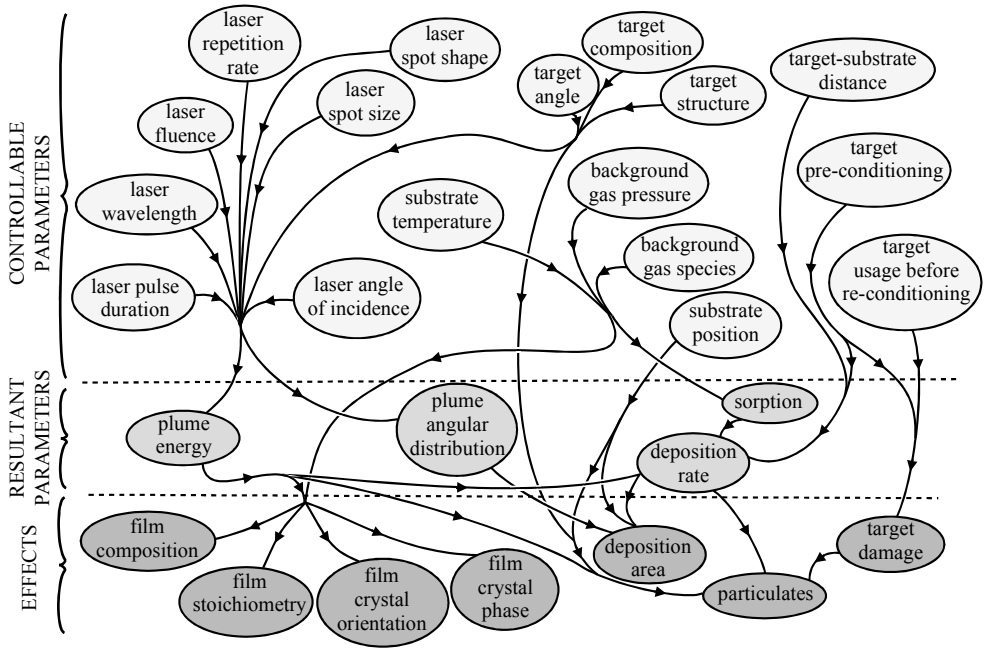

Figure 3.2.11: Summary of the various parameters and their effects in PLD.

3.3 Waveguide theory

Guidance of light can occur due to total internal reflection in a waveguide core when the refractive index of the core is higher than the refractive index of the substrate and superstrate. The condition for guidance of light inside an asymmetric waveguide geometry,

as shown in figure 3.3.1, is provided by Snell's law. Equation 3.3.1 shows the critical angle condition for guidance derived from Snell's law (the assumption that $n_3 \geq n_1$ has been used in the derivation). Light with an incident angle greater or equal to the critical angle is guided.

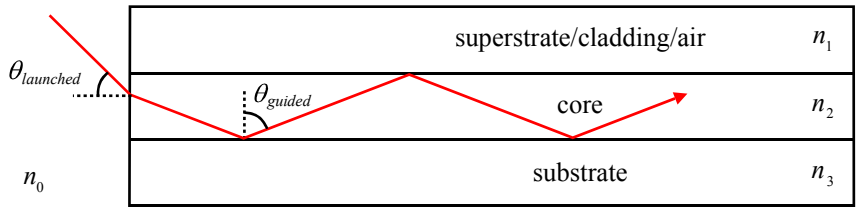

Figure 3.3.1: Waveguiding according to Snell's law in the core region.

$$\theta_{guided} \geq \theta_c = \sin^{-1}\left(\frac{n_3}{n_2}\right) \tag{3.3.1}$$

θ_{guided} = incident angle of guided light, θ_c = critical angle for waveguiding, n_1, n_2, n_3 = refractive indices of the superstrate/cladding/air, core and substrate respectively.

The maximum acceptance angle, θ_{NA}, for launching light into a waveguide is given by the NA and is also related to the refractive indices of the core and substrate (assuming $n_3 > n_1$) as shown in equation 3.3.2. Light launched with $\theta_{launched} \leq \theta_{NA}/2$ will be guided in the waveguide core.

$$\mathrm{NA} = \sqrt{{n_2}^2 - {n_3}^2} = n_0 \sin\left(\frac{\theta_{NA}}{2}\right) \tag{3.3.2}$$

θ_{NA} = maximum acceptance angle, n_0 = refractive index of the outer region.

3.3.1 Maxwell's equations

To consider how light propagates inside waveguides in more detail, it is necessary to use electromagnetic theory. We must look for solutions of the form shown in equations 3.3.3 and 3.3.4, whose transverse properties remain constant while propagating.

$$\mathbf{E}(x,y,z,t) = \mathbf{E}(x,y)e^{i(\omega t - \beta z)} \tag{3.3.3}$$

$$\mathbf{H}(x,y,z,t) = \mathbf{H}(x,y)e^{i(\omega t-\beta z)} \quad \textbf{(3.3.4)}$$

$\mathbf{E}(x, y, z, t)$ = full electric field function of a guided mode, $\mathbf{E}(x, y) = x$ and y dependence of the electric field function of a guided mode, $\mathbf{H}(x, y, z, t)$ = full magnetic field function of a guided mode, $\mathbf{H}(x, y) = x$ and y dependence of the magnetic field function of a guided mode, ω = angular frequency, β = z-component propagation constant, t = time dimension.

From equations 3.3.3 and 3.3.4, we can deduce that the operations $\partial/\partial z \equiv -i\beta$ and $\partial/\partial t \equiv i\omega$. Also from the condition of constant transverse properties, we can deduce that the operation $\partial/\partial y \equiv 0$. Implementing these conditions into Maxwell's equations (equations 3.3.5 and 3.3.6) for an isotropic, lossless and chargeless medium, we arrive at equations 3.3.7, 3.3.8, 3.3.9 and 3.3.10.

$$\nabla_\wedge \mathbf{E} = -\mu\frac{\partial \mathbf{H}}{\partial t}, \quad \nabla_\wedge \mathbf{H} = \varepsilon\frac{\partial \mathbf{E}}{\partial t} \quad \textbf{(3.3.5, 3.3.6)}$$

$$E_y = -\frac{\mu\omega}{\beta}H_x, \quad \frac{\partial E_y}{\partial x} = -i\mu\omega H_z \quad \textbf{(3.3.7, 3.3.8)}$$

$$H_y = \frac{\varepsilon\omega}{\beta}E_x, \quad \frac{\partial H_y}{\partial x} = i\varepsilon\omega E_z \quad \textbf{(3.3.9, 3.3.10)}$$

μ = magnetic permeability, ε = electric permittivity, E_x, E_y, $E_z = x$, y, and z-components of $\mathbf{E}$ respectively, H_x, H_y, $H_z = x$, y and z-components of $\mathbf{H}$ respectively.

Application of the standard vector identity for $\nabla_\wedge(\nabla_\wedge \mathbf{U})$ ($\mathbf{U}$ = any vector) to Maxwell's equations for an isotropic, lossless and chargeless medium yields equations 3.3.11 and 3.3.12.

$$\nabla^2\mathbf{E} = \varepsilon\mu\frac{\partial^2 \mathbf{E}}{\partial t^2}, \quad \nabla^2\mathbf{H} = \varepsilon\mu\frac{\partial^2 \mathbf{H}}{\partial t^2} \quad \textbf{(3.3.11, 3.3.12)}$$

We will propose solutions of the form shown in equations 3.3.13 and 3.3.14 for E_y and H_y respectively in the separate waveguide regions such that the solutions decay exponentially outside of the core region and form standing waves inside the core.

$$E_y(x,z,t) = \xi_y(x)e^{i(\omega t-\beta z)}, \quad H_y(x,z,t) = \zeta_y(x)e^{i(\omega t-\beta z)} \qquad \textbf{(3.3.13, 3.3.14)}$$

Equations 3.3.11 and 3.3.12 are thus simplified to equations 3.3.15 and 3.3.16.

$$\frac{\partial^2 \mathbf{E}}{\partial x^2} = \left(\beta^2 - \mu\varepsilon\omega^2\right)\mathbf{E}, \quad \frac{\partial^2 \mathbf{H}}{\partial x^2} = \left(\beta^2 - \mu\varepsilon\omega^2\right)\mathbf{H} \qquad \textbf{(3.3.15, 3.3.16)}$$

3.3.2 Asymmetric waveguides

There are derivations for transverse electric (TE) and transverse magnetic (TM) modes, but since the two derivations are similar, only the TE derivation will be continued from this point and the TM solution will be derived using similarity conditions at the end. Let us consider the solution for the asymmetric waveguide geometry illustrated in figure 3.3.2, which is the case for most of the devices reported in this thesis. We can propose the solutions shown as equation 3.3.17.

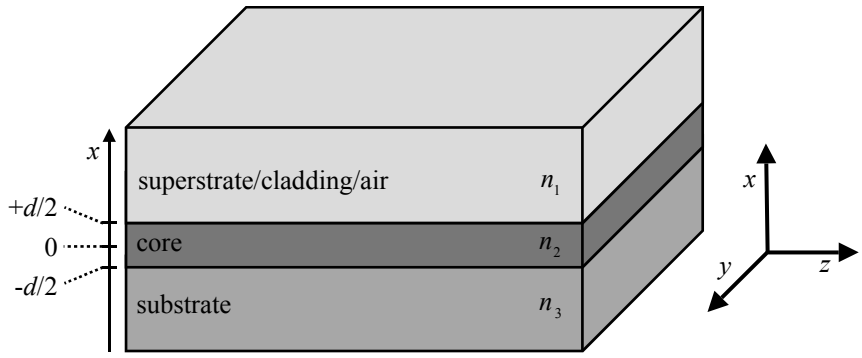

Figure 3.3.2: Asymmetric waveguide geometry.

$$\xi_y = \begin{cases} A_1 e^{-a_1 x} & +d/2 \le x \\ A_2 \cos(a_2 x + \varphi) & -d/2 \le x \le +d/2 \\ A_3 e^{a_3 x} & x \le -d/2 \end{cases} \qquad \textbf{(3.3.17)}$$

A_1, A_2 and A_3 = constants, a_1, a_2, a_3 = to be derived in a further step below,
φ = phase offset, d = core thickness.

ξ_y must be continuous at $x = +d/2$ and $x = -d/2$; these conditions allow it to be shown that $A_1 = A_2 = A_3 = A$ and the constant A can be removed from ξ_y for simplification. Insertion of the solutions into 3.3.15 reveals the definitions of the dispersion relations a_1, a_2 and a_3, shown below as equations 3.3.18, 3.3.19 and 3.3.20 respectively.

$$a_1 = \sqrt{\beta^2 - \mu_1 \varepsilon_1 \omega^2} \tag{3.3.18}$$

$$a_2 = \sqrt{\mu_2 \varepsilon_2 \omega^2 - \beta^2} \tag{3.3.19}$$

$$a_3 = \sqrt{\beta^2 - \mu_3 \varepsilon_3 \omega^2} \tag{3.3.20}$$

The tangential component of **H**, shown below as equation 3.3.21 can be obtained by inserting the solutions, equation 3.3.17, into equation 3.3.8.

$$H_z = A \begin{cases} -\dfrac{i}{\mu\omega} a_1 e^{-a_1 x} & +d/2 \le x \\ -\dfrac{i}{\mu\omega} a_2 \sin(a_2 x + \varphi) & -d/2 \le x \le +d/2 \\ \dfrac{i}{\mu\omega} a_3 e^{a_3 x} & x \le -d/2 \end{cases} \tag{3.3.21}$$

Finally, the condition that ξ_y and H_z must be continuous at $x = \pm d/2$ and the fact that tan (x) = tan ($x \pm m\pi$) (where m = an integer) yields equation 3.3.22, the TE guidance condition for asymmetric waveguides, after some rearrangement.

$$a_2 d - \tan^{-1}\left(\frac{\mu_2 a_1}{\mu_1 a_2}\right) - \tan^{-1}\left(\frac{\mu_2 a_3}{\mu_3 a_2}\right) = 2m\pi \tag{3.3.22}$$

The symmetry in Maxwell's equations allow us to now find equation 3.3.23, the TM guidance condition for asymmetric waveguides, by making the exchanges: **E** → **-H**, **H** → **E**, $\varepsilon \rightarrow \mu$ and $\mu \rightarrow \varepsilon$. Equation 3.3.24 shows the solutions to ζ_y (H_y x-dependence) in the different regions of the waveguide.

$$a_2 d - \tan^{-1}\left(\frac{\varepsilon_2 a_1}{\varepsilon_1 a_2}\right) - \tan^{-1}\left(\frac{\varepsilon_2 a_3}{\varepsilon_3 a_2}\right) = 2m\pi \qquad \textbf{(3.3.23)}$$

$$\zeta_y = A\begin{cases} \cos\left(\frac{a_2 d}{2} + \varphi'\right) e^{-a_1(x-d/2)} & +d/2 \le x \\ \cos(a_2 x + \varphi') & -d/2 \le x \le \\ \cos\left(\frac{a_2 d}{2} - \varphi'\right) e^{a_3(x+d/2)} & x \le -d/2 \end{cases} \qquad \textbf{(3.3.24)}$$

φ' = phase offset.

The guidance conditions are transcendental equations and must be plotted for solutions to be found, which can then be used to plot intensity profiles of guided modes. Figure 3.3.3 is an example of a TE mode intensity plot for an asymmetric waveguide consisting of a 4 μm thick Nd:GGG core on a YAG substrate with no cladding layer. The fundamental mode and first mode above fundamental are shown.

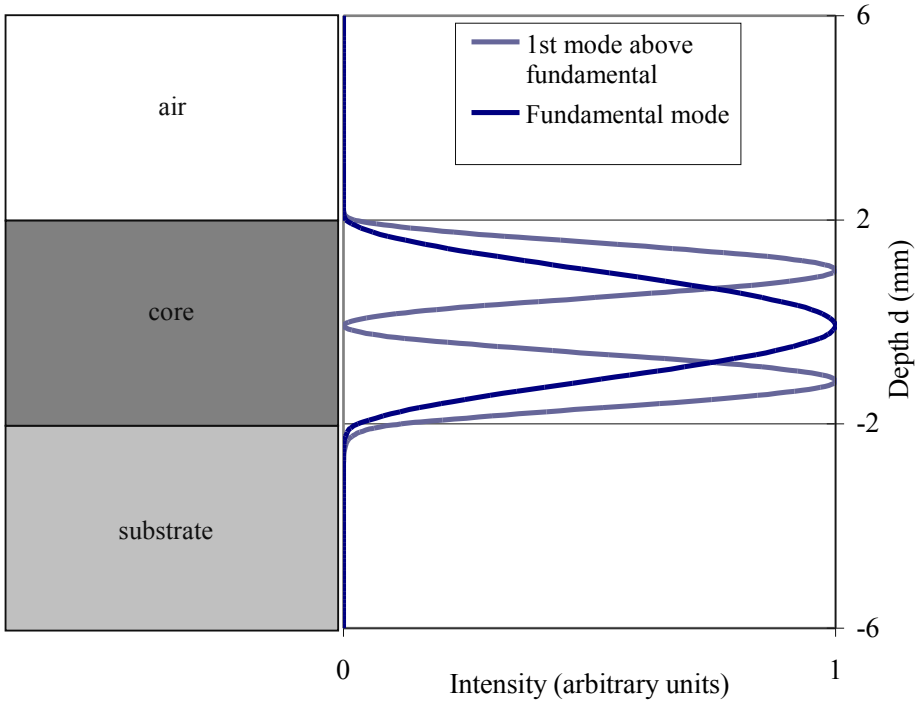

Figure 3.3.3: TE mode intensity plot of the fundamental mode and the first mode above fundamental for an asymmetric waveguide.

3.3.3 Symmetric waveguides

The waveguide is symmetric when the cladding layer is of the same material as the substrate. For symmetric waveguide geometries the guidance conditions for TE and TM modes simplify to equations 3.3.25 and 3.3.26 respectively, and represent even modes. It can also be shown that there are odd modes with the guidance conditions for TE and TM modes shown as equations 3.3.27 and 3.3.28 respectively.

$$\frac{a_2 d}{2} - \tan^{-1}\left(\frac{\mu_2 a_1}{\mu_1 a_2}\right) = m\pi, \quad \frac{a_2 d}{2} - \tan^{-1}\left(\frac{\varepsilon_2 a_1}{\varepsilon_1 a_2}\right) = m\pi \qquad \textbf{(3.3.25, 3.3.26)}$$

$$\frac{a_2 d}{2} - \cot^{-1}\left(\frac{\mu_2 a_1}{\mu_1 a_2}\right) = m\pi, \quad \frac{a_2 d}{2} - \cot^{-1}\left(\frac{\varepsilon_2 a_1}{\varepsilon_1 a_2}\right) = m\pi \qquad \textbf{(3.3.27, 3.3.28)}$$

Figure 3.3.4 is an example of a TE mode intensity plot for a symmetric waveguide consisting of a 20 μm thick Nd:GGG core on a YAG substrate with a 10 μm thick YAG cap, the fundamental mode and first mode above fundamental are shown.

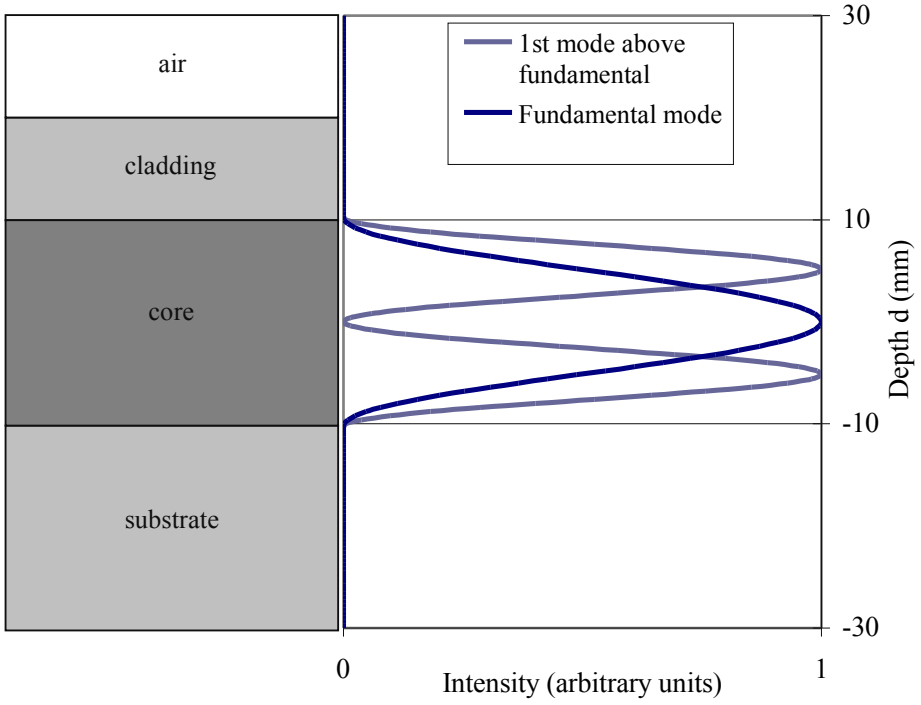

Figure 3.3.4: TE mode intensity plot of the fundamental mode and the first mode above fundamental for a symmetric waveguide.

It is useful to derive a formula for the maximum number of modes supported by a symmetric waveguide geometry. For a guided mode solution a_1 must be real and positive, meaning the cut-off condition for modes is reached when $a_1 = 0$. By applying this condition to the guidance conditions for even and odd TE modes we can deduce the condition shown as equation 3.3.29, where p is an integer whose maximum value will be the highest supported mode above the fundamental.

$$a_2 d = p\pi \tag{3.3.29}$$

We can eliminate a_2 from equation 3.3.29 using equation 3.3.30, and after some rearrangement is performed we can arrive at the formula for the maximum number of modes above the fundamental supported by a waveguide, equation 3.3.31.

$$a_1^{\,2} + a_2^{\,2} = \mu_2 \varepsilon_2 \omega^2 - \mu_1 \varepsilon_1 \omega^2 \tag{3.3.30}$$

$$M \leq \frac{2d}{\lambda} \mathrm{NA} \tag{3.3.31}$$

M = maximum number of modes above the fundamental supported by a waveguide (the largest integer that satisfies the equation must be found), λ = wavelength of light being guided, NA = numerical aperture.

3.3.4 Multilayer waveguides

The use of basic multilayer planar waveguide structures analogous to high NA optical fibres [30; 31] allows waveguides with a larger NA to be produced. Structures consisting of a substrate and superstrate (outer cladding), two more layers (inner cladding) and finally the core as shown in figure 3.3.5:A, allow the pump light to be coupled into the cladding and the core is then pumped as the pump radiation passes through it. In this configuration, a small core may not be able to lase because the absorption length may have been increased beyond the practical device length.

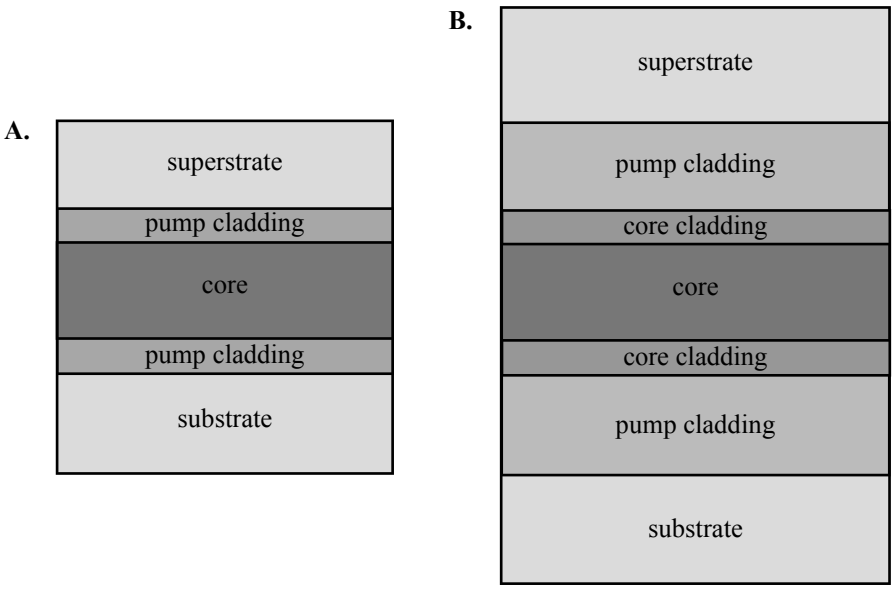

Figure 3.3.5: Multilayer planar waveguide structures.

Increasing the core size to avoid the problem of increased absorption length would normally lead to undesirable multimode operation, however this can be circumvented by the careful choice of cladding thickness, and use of an inner core cladding of the same material as the core, but undoped. With an appropriate choice of core to cladding thickness ratio, the higher order modes of the core will extend into the cladding. Laser operation of the fundamental mode will occur first, and will have a sufficient intensity to use enough of the available population inversion so that the operation of higher order modes is suppressed, making the device more analogous to LMA optical fibres [32; 33]. An example of the geometry of such a device is shown in figure 3.3.5:B. An example of a plot of the TE mode intensity profile for the fundamental and first mode above fundamental for a simpler five-layer geometry where the pump cladding is index-matched to the core making a LMA device is shown as figure 3.3.6 (core = 10 μm thick Nd:GGG, pump cladding layers = 5 μm thick index-matched GGG, outer cladding = 10 μm thick YAG, substrate = YAG). Further details concerning the potential and dynamics of advanced multilayer structured planar waveguide lasers have been presented elsewhere [34; 221-223].

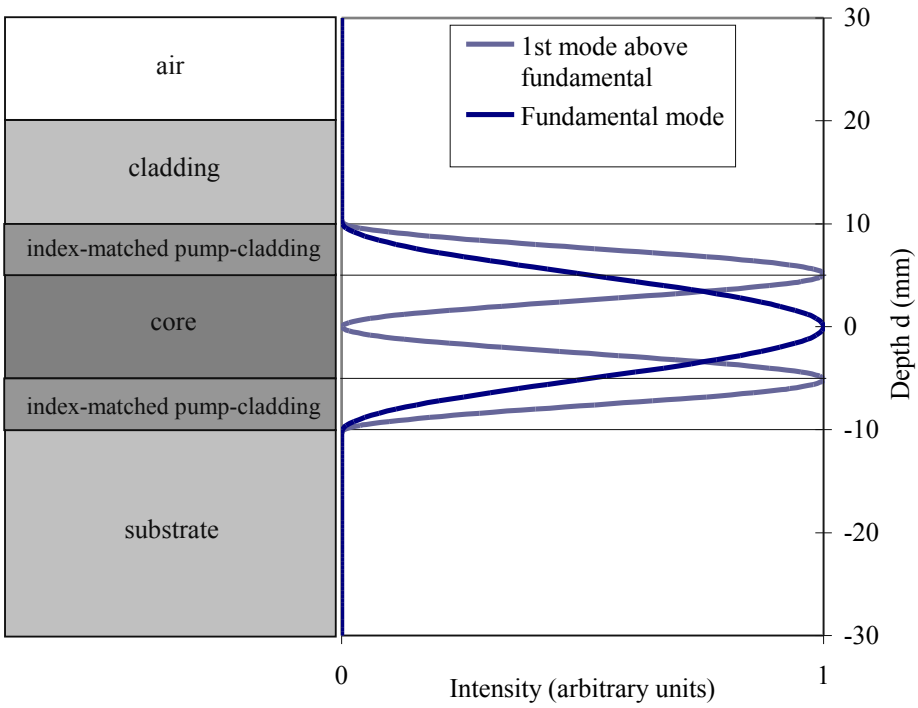

Figure 3.3.6: TE mode intensity plot of the fundamental mode and the first mode above fundamental for a symmetric multilayer waveguide.

3.3.5 Self-imaging

The interference of different modes in a multimode waveguide can produce imaging effects throughout the length of the waveguide. Equally separated multiple images occur periodically along a waveguide as a result of multimode interference (MMI), and this effect has been used extensively to make couplers and power splitters for the telecommunications industry [224; 225]. MMI also periodically causes the input profile to be fully reproduced, and this is known as self-imaging. The possibility of using the effect of self-imaging in planar waveguides was first suggested in 1973 [226] and explained in more detail in 1975 [227; 228]. The effect of self-imaging can be used to make thick multimode planar waveguide amplifiers that reproduce the input-face modal properties of a signal laser at the output-face [229; 230]. Thick planar waveguides that would normally have limited applications because of their multimode nature can be utilised and full advantage can be taken of high power diode laser arrays that are excellently suited for pumping planar waveguides. Equation 3.3.32 shows the length over which self-imaging will occur in a symmetric planar waveguide.

$$\Lambda = \frac{4nd^2}{\lambda} \tag{3.3.32}$$

Λ = length over which self-imaging occurs, n = refractive index of the waveguide core, d = waveguide thickness, λ = wavelength of the light being guided.

Self-imaging occurs periodically over a length of Λ, and also $\Lambda/4$ for the ideal case of a perfectly symmetric waveguide, an axially symmetric input profile and launching into the centre of the core along the optical axis of the waveguide. Light that is launched at an angle θ to the optical axis of the waveguide will exit at an angle $-\theta$ to the optical axis of the waveguide after a length Λ. Light launched with an offset of distance a from the optical axis of the waveguide will exit with an offset of distance $-a$ from the optical axis of the waveguide after a length Λ. Figure 3.3.7 shows an example of a mode intensity plot for self-imaging of a laser beam with a wavelength of 1.06 µm and a spot size of 5 µm. The plot was calculated using the beam propagation method software *Prometheus* (by D. P. Shepherd, ORC, University of Southampton) for a 50 µm thick Nd:GGG symmetric waveguide with a YAG substrate and a 10 µm thick YAG capping layer.

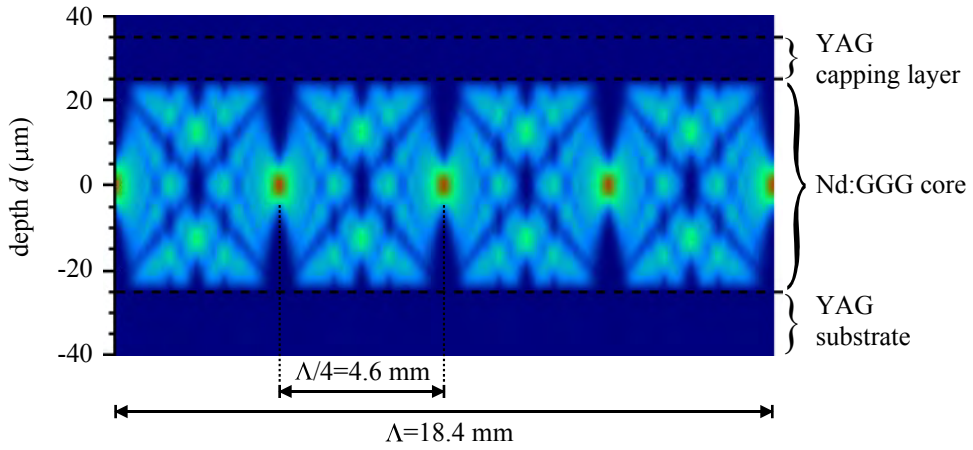

Figure 3.3.7: Mode intensity plot for self-imaging in a waveguide.

3.4 Laser theory

3.4.1 Three-level lasers

The two possible energy level schemes of a three-level laser system are shown in figure 3.4.1 and described below.

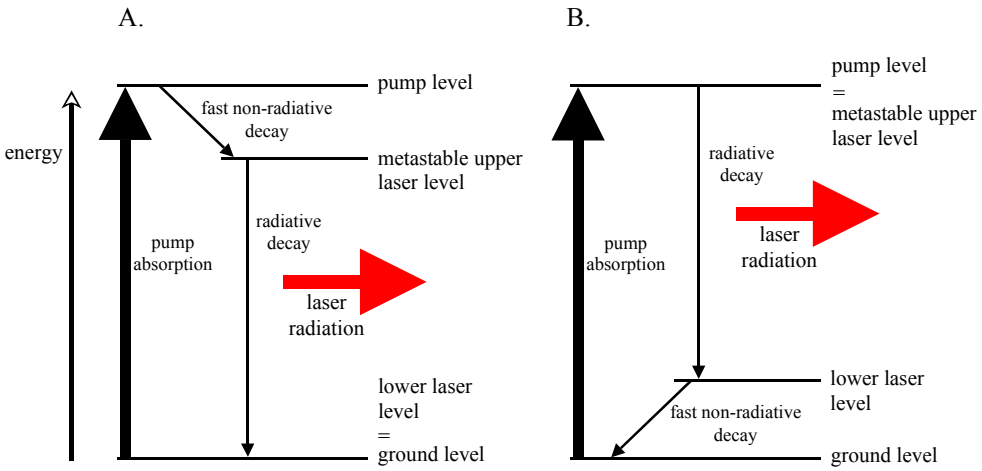

Figure 3.4.1: Energy level diagrams for a three-level laser.

A. Pump radiation is absorbed by ground level electrons that are excited to the pump level and then undergo rapid non-radiative decay to the metastable upper laser level. Electrons can then decay radiatively to the ground level by stimulated or spontaneous emission. The relatively long lifetime of the upper laser level allows a population inversion to occur and amplification of a signal beam can occur due to stimulated emission. This type of three-level laser system has to be highly pumped to obtain population inversion because the ground level is naturally highly populated. Pulsed mode is usually used for this type of three-level laser system because the population inversion is difficult to sustain.

B. Pump radiation is absorbed by ground level electrons that are excited to the pump level which in this case is also the metastable upper laser level. Electrons can then decay radiatively to the lower laser level by stimulated or spontaneous emission, and subsequently back to the ground level by rapid non-radiative decay. It is generally easier to achieve population inversion in this three-level laser system because the lower laser level has a very low population at room temperature. This three-level laser system

can be operated in continuous-wave (cw) mode because population inversion is relatively easy to sustain. A potential problem with this system is that pumping with high power levels can lead to stimulated emission of upper laser level electrons back to the ground level. This type of three-level laser system is sometimes referred to as a four-level laser because it essentially has the same properties as a four-level laser system when the lower laser level has a very low population at the laser operating temperature.

3.4.2 Four-level lasers

The energy level scheme of a four-level laser system is shown in figure 3.4.2. The four-level laser system benefits from the best properties of the two three-level laser systems. The lower laser level has a very low population, allowing population inversion to be achieved easily, and the system can be pumped with very high powers without causing stimulated emission from the upper laser level to the ground level. Four-level laser systems have low thresholds, and as long as the lifetime of the upper laser level is longer than the lower laser level, operation in cw mode is relatively easy to achieve because the population inversion is sustainable.

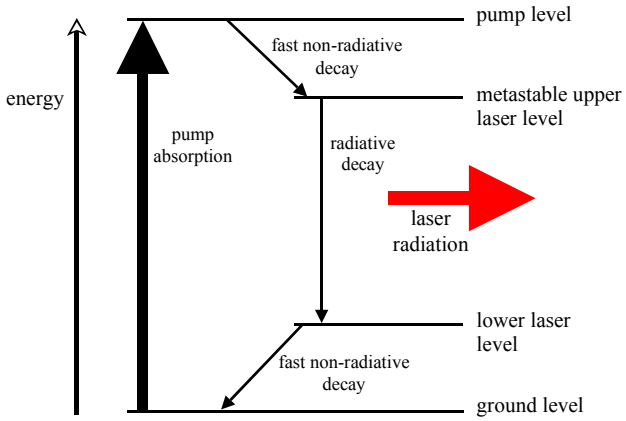

Figure 3.4.2: Energy level diagram for a four-level laser.

3.4.3 Quasi-three-level and quasi-four-level lasers

Quasi-three-level and quasi-four-level lasers take advantage of sub-levels; in the case of crystals, sub-levels arise due to Stark-splitting of the laser ion energy levels. The pump level and upper laser level can be Stark-split sub-levels from the same manifold[7] instead of a distinct pump level and an upper laser level, and/or the lower laser level and ground level can be Stark-split sub-levels from the same manifold instead of distinct levels. The possible energy level schemes for quasi-three-level and quasi-four-level lasers are summarised in figure 3.4.3.

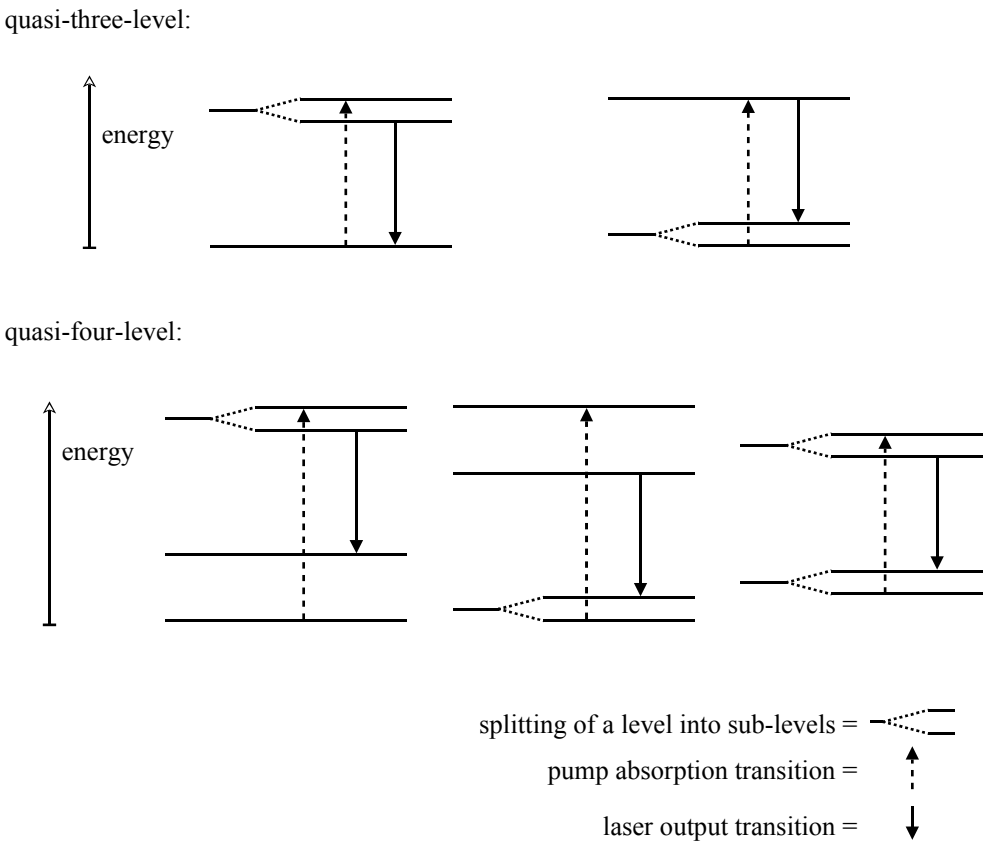

Figure 3.4.3: Summary of possible energy level schemes for quasi-three-level and quasi-four-level lasers.

In the case where the lower laser level and the ground level are part of the same manifold, reabsorption at the laser wavelength can become an issue because the lower laser level may have a high thermal population, meaning that the system has to be adequately cooled for laser operation to be possible, and this is also critical for efficient operation.

7 The term manifold is used to describe a group of sub-levels formed from a split energy level.

3.4.4 Nd:GGG lasers

The Nd^{3+} ions replace Gd^{3+} ions in GGG and substitution of about 1% of the Gd^{3+} ions is optimal since higher doping concentrations lead to crystal strain because of the difference in ionic radii of the two ions. The energy levels of a Nd^{3+} laser system are Stark-split into manifolds, but when the system is operated as a four-level laser the sub-levels aren't of significance and manifolds can be referred to as levels for simplicity. Figure 3.4.4 shows the energy level diagram for a four-level Nd:GGG laser system. The optimal wavelength of pump radiation is 808 nm and the transition $^4F_{3/2} \rightarrow {}^4I_{11/2}$ results in laser output of wavelength 1.06 μm. The lower laser level $^4I_{11/2}$ is not thermally populated so population inversion is relatively easy to achieve and maintain. The fluorescence lifetime of the upper laser level $^4F_{3/2}$ is approximately 280 μs [231].

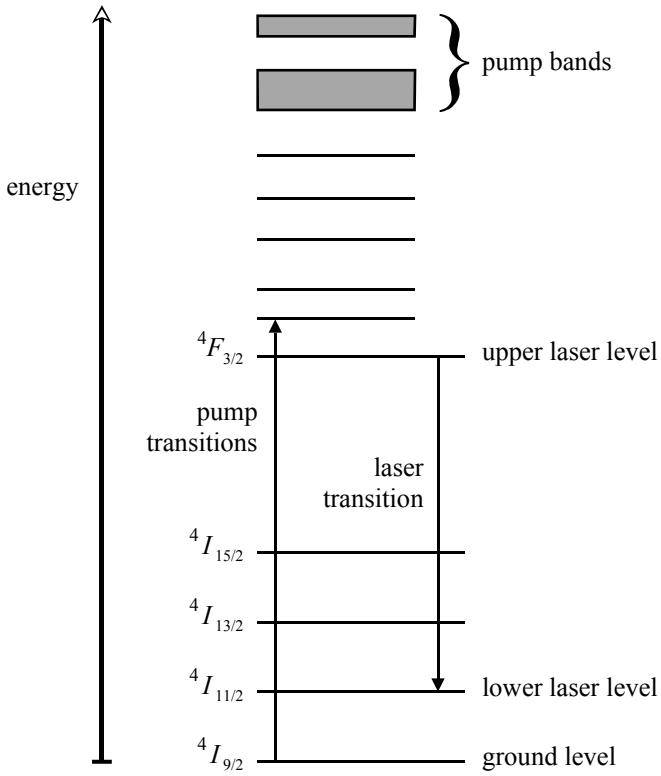

Figure 3.4.4: Energy level diagram of Nd:GGG.

3.4.4.1 Chromium co-doping

Co-doping of Cr^{3+} with Nd^{3+} can be performed to increase the pump absorption efficiency [232]. Energy is transferred from excited state Cr^{3+} ions to Nd^{3+} ions and since the Cr^{3+} ion has a broad absorption range the options for pumping of the system are widened.

Unfortunately, co-doping of Nd:GGG (and Nd:YAG) doesn't lead to efficient use of the Cr^{3+} ion, but co-doping of GSGG has been very successful and transfer of 100% of the energy from excited state Cr^{3+} ions to Nd^{3+} ions has been observed [232].

3.4.5 Yb:YAG lasers

The Yb^{3+} ions replace Y^{3+} ions in YAG, and it is possible to make crystals with anything up to 100% substitution because the ionic radii of Yb^{3+} and Y^{3+} are so similar; 100% substitution only changes the unit cell size of YAG by 1.5% [38]. The laser transition for $Yb3^{+}$ is ${}^2F_{5/2} \rightarrow {}^2F_{7/2}$ and is shown in figure 3.4.5.

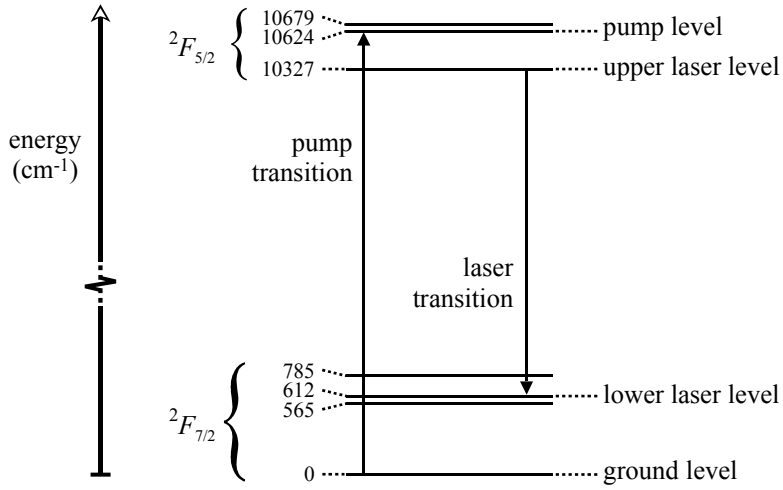

Figure 3.4.5: Energy level diagram of Yb:YAG.

The energy levels are split into manifolds so that laser transitions to the ground level terminate in a sub-level that is above the lowest lying ground sub-level. The pump transition is from the lowest lying ground sub-level to a sub-level in the manifold containing the upper laser level, and can be directly to the sub-level being used as the upper laser level, or to a sub-level above it. This means that the Yb^{3+} laser can be a quasi-three-level or quasi-four-level laser system, depending on the pump wavelength. A possible quasi-four-level scheme (the one whose operation was attempted) has an optimal wavelength of pump radiation at around 942 nm and the laser output from such a scheme has a wavelength of 1.03 μm. Population of the sub-level used for termination of the laser transition increases with temperature, making population inversion difficult to achieve without adequate cooling. Reabsorption at the laser wavelength can also be a problem and the system needs to be pumped with high power densities to reduce this effect [232]. The

fluorescence lifetime of the upper laser level $^2F_{5/2}$ is approximately 1 ms for lower dopant concentrations and decreases to as low as 270 μs for YbAG (100% ytterbium substituted) [38].

3.4.6 Longitudinally pumped lasers

Longitudinal modes exist because standing waves can be created in the cavity with wavelengths separated by half-integer numbers of the laser wavelength. The number of operational longitudinal modes is dependent upon the cavity length and the spectral width of the gain region. The wavelength separation of longitudinal modes can be found from equation 3.4.1.

$$\Delta\lambda = \frac{\lambda^2}{2nl} \tag{3.4.1}$$

$\Delta\lambda$ = longitudinal mode separation, λ = laser wavelength, n = refractive index of the cavity, l = cavity length.

The absorbed pump power threshold of a longitudinally pumped laser is given by equation 3.4.2 [233; 234].

$$P_{th} = \frac{\pi h\nu_p \left(L_{PL} + T_{OC} + 2\sigma_e N_1^0 l \right)}{4\sigma_e \eta_q \tau_{fl}} \left(\int_0^l \frac{1}{w_l(z)^2 + w_p(z)^2} dz \right)^{-1} \tag{3.4.2}$$

P_{th} = absorbed pump power threshold, h = Planck's constant, ν_p = frequency of the pump laser radiation, L_{PL} = round trip propagation loss exponent, T_{OC} = transmission exponent (of output and feedback mirrors), σ_e = emission cross-section, N_1^0 = population density of the lower laser level, l = cavity length, α_p = absorption coefficient of the pump laser radiation, z = direction of propagation, η_q = fraction of absorbed photons that lead to population of the upper laser level (quantum efficiency), τ_{fl} = lifetime of the upper laser level, $w_l(z)$ and $w_p(z)$ = spot sizes (as a function of z) of the output and pump lasers respectively.

The round trip propagation loss exponent[8] and transmission exponent are defined by equations 3.4.3 and 3.4.4 respectively.

$$L_{PL} = -\ln\left(e^{2\alpha_{PL} l} \right) = -2\alpha_{PL} l \tag{3.4.3}$$

$$T_{OC} = -\ln\left(R_1 R_2\right) \tag{3.4.4}$$

α_{PL} = propagation loss coefficient[8], R_1 and R_2 = reflectivity of feedback and output coupling mirrors respectively.

The absorbed pump power threshold can be related to the incident power threshold by equation 3.4.5.

$$P_{th} = P_{p\_th}\left(1 - e^{-\alpha_p l}\right) \tag{3.4.5}$$

P_{p_th} = incident pump power threshold.

The slope efficiency of a longitudinally pumped laser is given by equation 3.4.6 [234], where dS/dF is the normalised slope efficiency that accounts for spatial overlap of the output and pump lasers, and the efficiency of the conversion of absorbed pump photons (in excess of those required to reach threshold) into laser photons. The functions S and F are variables proportional to the laser output power and the pumping power respectively.

$$\eta = \eta_q \frac{\nu_l}{\nu_p} \frac{-\ln\left(R_2\right)}{\left(L_{PL} + T_{OC}\right)} \frac{\mathrm{d}S}{\mathrm{d}F} \tag{3.4.6}$$

η = slope efficiency, ν_l = frequency of the laser output.

The normalised slope efficiency dS/dF can be approximated by equation 3.4.7 at low powers close to threshold ($S \rightarrow 0$) if average spot sizes are used for the output and pump laser beams, and they are assumed to be fundamental Gaussian modes.

$$\left.\frac{\mathrm{d}S}{\mathrm{d}F}\right|_{S\rightarrow 0} = \frac{\left(1 + 2\dfrac{w_p^{\,2}}{w_l^{\,2}}\right)}{\left(1 + \dfrac{w_p^{\,2}}{w_l^{\,2}}\right)^2} \left(1 + \frac{N_1^{\,0}\sigma_e l}{\left(L_{PL} + T_{OC}\right)\left(1 + \dfrac{w_p^{\,2}}{w_l^{\,2}}\right)}\right)^{-1} \tag{3.4.7}$$

w_l, and w_p = average spot sizes of the output and pump laser beams respectively.

8 The convention that the propagation loss coefficient α_{PL} is negative is used here and throughout this thesis (this convention also applies to the substrate propagation loss coefficient α_{SL} used later).

Low losses and good spatial overlap of the output and pump beam are desired for the minimisation of threshold and maximisation of slope efficiency.

3.4.7 Waveguide lasers

In the case of waveguide lasers, the calculation of longitudinal mode separation must account for the effective refractive index of the laser mode by exchanging the cavity refractive index, as found in equation 3.4.1, for the effective modal refractive index.

The waveguide lasers discussed in this thesis are all Nd:GGG so the case of a four-level waveguide laser will be presented here. The absence of reabsorption losses in a four-level laser system and the special symmetry of a planar waveguide setup transform equation 3.4.2 into equation 3.4.8 [235].

$$P_{th} = \frac{\pi h\nu_p \left(L_{PL} + T_{OC} \right)}{4\sigma_e \eta_q \tau_{fl}} \left(\int_0^l \frac{1}{\left(w_{lx}(z)^2 + w_{px}(z)^2 \right)^{1/2} \left(w_{ly}(z)^2 + w_{py}(z)^2 \right)^{1/2}} dz \right)^{-1} \quad \textbf{(3.4.8)}$$

$w_{lx}(z)$, $w_{px}(z)$, $w_{ly}(z)$ and $w_{py}(z)$ = spot sizes (as a function of z) of output and pump lasers in x and y axis respectively.

If average spot sizes are used for the pump and laser beams, and the output and pump beams are assumed to be fundamental Gaussian modes, we can arrive at equation 3.4.9. The validity of these approximations depends on the properties of the waveguide being tested and the launch conditions of the pump light; they are generally acceptable for thick waveguides where tight focusing of the pump light isn't used, but are not acceptable for the case of thin waveguides where tight focussing of the pump light is used.

$$P_{th} = \frac{\pi h\nu_p \left(L_{PL} + T_{OC} \right)}{4\sigma_e \eta_q \tau_{fl}} \left(w_{px}{}^2 + w_{lx}{}^2 \right)^{1/2} \left(w_{py}{}^2 + w_{ly}{}^2 \right)^{1/2} \quad \textbf{(3.4.9)}$$

w_{lx}, w_{px}, w_{ly} and w_{py} = average spot sizes of output and pump laser beams in the x and y directions respectively.

Without reabsorption losses, dS/dF becomes a pure spatial overlap factor, η_{pl}, and equation 3.4.6 transforms to equation 3.4.10.

$$\eta = \eta_q \frac{\nu_l}{\nu_p} \frac{-\ln(R_2)}{(L_{PL} + T_{OC})} \eta_{pl} \tag{3.4.10}$$

η_{pl} = spatial overlap efficiency of output and pump laser beams.

For low powers ($4P_l \ll \pi w_l^2 I_s$, where P_l = laser output power, $I_s = h\nu_p/\sigma_e\tau_{fl}$ = saturation intensity of the laser transition (when the gain is reduced to half the small signal gain)), the spatial overlap for waveguide lasers can be approximated by 3.4.11 if average spot sizes are used for the output and pump laser beams and the output and pump beams are assumed to be fundamental Gaussian modes. We must also assume there is no spatial hole burning.

$$\eta_{pl} = \frac{w_{lx} w_{ly} \left(2w_{px}^2 + w_{lx}^2\right)^{1/2} \left(2w_{py}^2 + w_{ly}^2\right)^{1/2}}{\left(w_{px}^2 + w_{lx}^2\right)\left(w_{py}^2 + w_{ly}^2\right)} \tag{3.4.11}$$

The spot sizes of the output and pump laser beams will be restricted in the guided plane, but will obey the equation for propagation of a Gaussian beam shown as equation 3.4.12 in the unguided plane (under the assumption that they are both fundamental Gaussian modes). The average spot size of a Gaussian beam can be calculated from equation 3.4.13.

$$w(z)^2 = w_o^2 \left(1 + \left(\frac{\lambda(z - z_o)}{\pi w_o^2 n}\right)^2\right) \tag{3.4.12}$$

$$\overline{w^2} = \frac{1}{l}\int_0^l w(z)^2 \, dz \tag{3.4.13}$$

$w(z)$ = spot size (as a function of z), w_o = spot size at the focal point of the beam (z_o), λ = wavelength of the laser beam, z = direction of propagation, z_o = value of z at the focal point of the beam, n = refractive index of the core, l = cavity length.

3.4.8 Thin-disk lasers

The thin-disk laser discussed in this thesis is Yb:YAG so reabsorption losses are accounted for here. Pumping of thin-disk lasers is generally performed through the face of the disk at an angle. For calculation of threshold power and slope efficiency, equation 3.4.2 and the normalised slope efficiency dS/dF must be generalised to account for the actual volume of

the disk that is pumped [236]. If the output and pump laser beams are assumed to be fundamental Gaussian modes, and negligible diffraction is assumed inside the disk, the transverse coordinates x and y can be replaced by the radial coordinate r and the laser threshold and normalised slope efficiency dS/dF can be calculated from equations 3.4.14 and 3.4.15 respectively [236].

$$P_{th} = \frac{\pi h\nu_p \left(w_l^{\,2} + w_p^{\,2} \right)}{4\sigma_e \eta_q \tau_{fl} \left(f_1 + f_2 \right)} \left(L_{PL} + T_{OC} + 2\sigma_e N_1^{\,0} l \right) \qquad \textbf{(3.4.14)}$$

f_1 and f_2 = fractional population in the lower and upper laser levels respectively.

$$\frac{\mathrm{d}S}{\mathrm{d}F} = \frac{1 + \dfrac{B}{S/C} \ln\left(1 + S/C\right)}{\left(F/C\right) \displaystyle\int_0^{\infty} \frac{\left[\left(F/C\right) e^{-x'} - Ba^2 \right]}{\left[1 + \left(S/C\right) e^{-a^2 x'} \right]^2} e^{-2a^2 x'} dx'} \qquad \textbf{(3.4.15)}$$

$$a = \frac{w_p}{w_l}, \quad x' = \frac{2r^2}{w_p^{\,2}} \qquad \textbf{(3.4.16, 3.4.17)}$$

r = radial coordinate.

$$B = \frac{2\sigma_e N_1^{\,0} l}{\left(L_{PL} + T_{OC} \right)}, \quad C = \frac{\pi w_l^{\,2} \left(l_c + \left(n - 1 \right) l \right)}{2} \qquad \textbf{(3.4.18, 3.4.19)}$$

l_c = laser cavity length (as opposed to l which is the disk thickness in this case), n = refractive index of the disk.

$$S = P_l \left(l_c + \left(n - 1 \right) l \right) \frac{2\left(f_1 + f_2 \right) \sigma_e \tau_{fl}}{nh\nu_l T_{OC}} \qquad \textbf{(3.4.20)}$$

P_l = laser output power.

$$F = P_p \left(l_c + \left(n-1 \right) l \right) \frac{2\left(f_1 + f_2 \right) \eta_q \sigma_e \tau_{fl}}{nh\nu_p \left(L_{PL} + T_{OC} \right)} \tag{3.4.21}$$

P_p = incident pump power.

3.5 Conclusions

- An overview of PLD theory has been presented and the nature of the complex problem of finding optimal growth conditions has been highlighted.
- Some problems that arise with PLD, such as particulates and target damage, have been discussed.
- An overview of waveguide theory has been presented and the advantages of multilayer and self-imaging planar waveguide devices have been discussed.
- An overview of laser theory has been presented and some theory necessary for the analysis of results from planar waveguide lasers and thin-disk lasers have been highlighted.

Chapter 4

Experimental and Analytical Techniques

4.1 Introduction

The experimental and analytical techniques used to produce, analyse and operate the devices reported in this thesis are presented here. The technique of PLD is presented and problems such as substrate temperature measurement and the consequences of thick film growth are discussed in more detail. An overview of the substrate cleaning procedure and techniques used for the material and structural characterisation of films is provided. The strict requirements for waveguide preparation are discussed along with techniques used for optical analysis and lasing of devices. The experimental setup for pumping and cavity formation of thin-disk lasers is also presented.

4.2 Pulsed laser deposition

The PLD apparatus, which is subject to continual upgrade as possible enhancements are discovered or needed, is shown in its current form in figure 4.2.1 (some components are not shown, for simplicity) and described below:

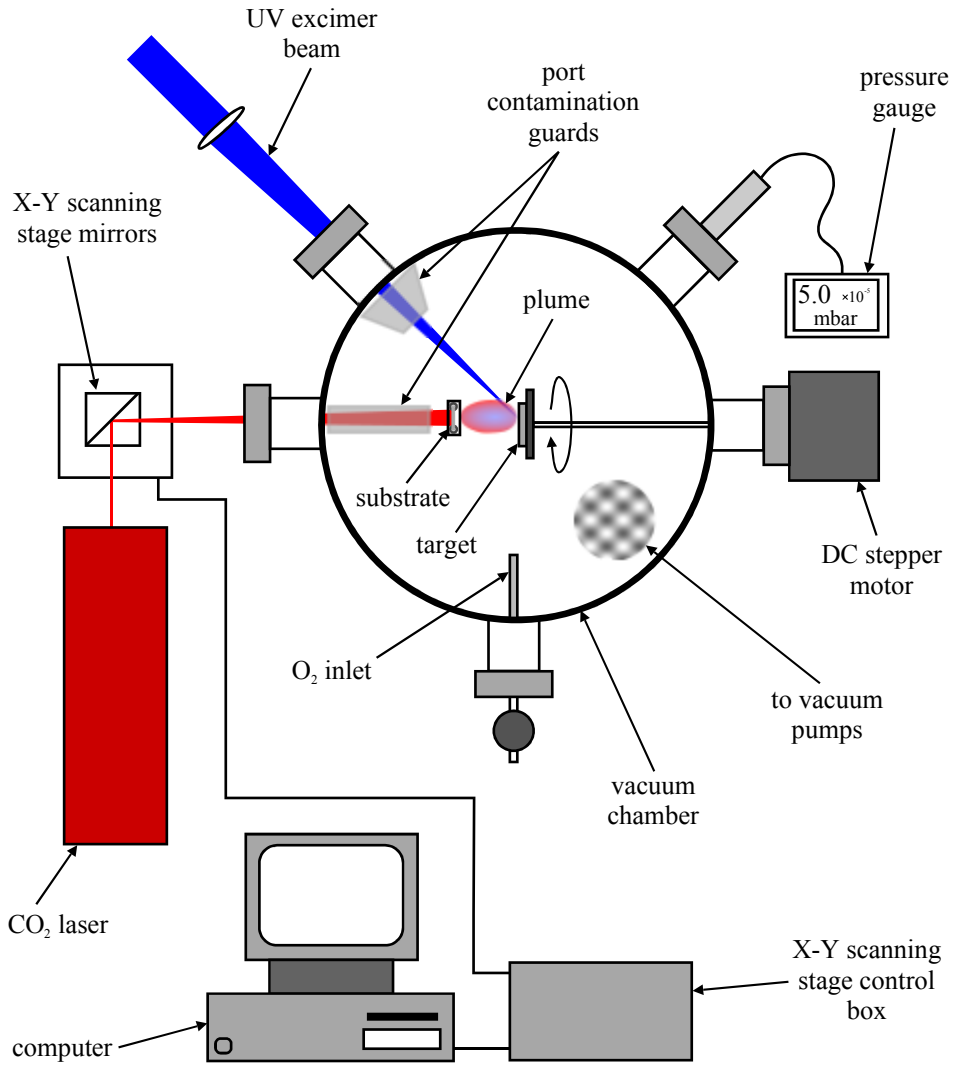

Figure 4.2.1: The PLD chamber apparatus.

- KrF excimer laser (248 nm wavelength, ~ 20 ns pulse length, capable of 1.0-4.0 Jcm^{-2} at the target surface when focussed, 1-20 Hz repetition rate) and appropriate optics for beam transport and focussing.
- Vacuum chamber with several ports including windows suitable for 248 nm and 10.6 µm wavelength radiation with minimal loss.
- Vacuum pumping system.
- Gas supply system with precise pressure control.
- Pressure gauge.
- Rotating target holder (stepper motor).

- Ceramic substrate holder.
- CCD camera and monitor for viewing the substrate when the chamber is under vacuum.
- Substrate blocker with remote control.
- Metal pipes for shielding the laser windows from unwanted material deposition.
- CO_2 laser (10.6 µm wavelength, up to 40 W cw output) and X-Y scanning optics with remote computer control.

The KrF excimer laser (Lambda Physik, Germany) was mainly used at a repetition rate of 10 Hz with an energy density of 1.5 Jcm^{-2} at the target surface. A two-stage vacuum pumping system consisting of a Leybold turbo molecular vacuum pump (Turbovac TW 300) backed by a Leybold rotary vane vacuum pump (Trivac D8B) was used with an oil trap to prevent back-streaming oil vapour and an exhaust filter to cut down on toxins released into the extract system. It was necessary to provide additional air cooling for the turbo molecular vacuum pump for operation at high chamber pressures with oxygen. The high pumping rate provided by using both vacuum pumps was found to lead to better films than were produced when only using the rotary pump. Metal pipes were introduced to the chamber to minimise the coating of laser port windows by stray deposit and lengthen their effective lifetime.

A rotating target holder was used to maximise target use between reconditioning and the direction of rotation was changed every minute to help prevent any directionally biased target damage from occurring. A raster scanned CO_2 laser (Synrad, USA) was used for substrate heating [22; 237]; this method is preferred because it provides homogeneous substrate heating without heating the chamber, which would increase desorption of contaminants from the chamber walls. A CCD camera and monitor was used for remote monitoring of the substrate temperature distribution via the relative intensity of light emitted from the substrate surface; this was critical for enabling in-situ adjustments to be made to the substrate temperature distribution. A remote controlled substrate blocker was used to allow preconditioning of the target without the substrate becoming contaminated and half-cylinder ceramic tubes were used to hold the substrate in place with minimal heat sinking. Simple half-cylinder ceramic tubes were found to be sufficient for use with 0.5 mm thick substrates but had to be modified as shown in figure 4.2.2 to be used with 1 mm thick substrates so as to minimise heat sinking.

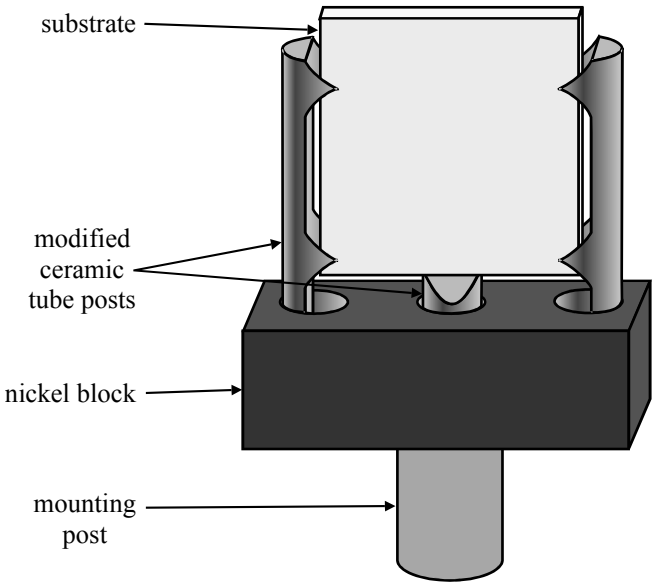

Figure 4.2.2: Modified ceramic tube based substrate holder to minimise heat sinking.

4.2.1 Substrate heating and temperature calibration

There are two types of methods for substrate heating; direct contact methods and indirect methods. Direct contact methods use a block of material that has good thermal conductance properties (for example copper) and is larger than the substrate; the substrate is then attached to the block and heated by conduction. An example of a direct heating method that is successful for many deposition configurations where only low temperatures are required (< 400 °C) is the resistive wire technique [238]. High temperatures are increasingly difficult to obtain with this technique because the resistive wires are prone to oxidise and burn out, and there are also problems with out-gassing. The resistive wire technique has been used with PLD [239], and the crystallinity of films grown using this heating method has been improved by post-annealing [62].

Radiation is used with indirect heating techniques, and filament bulb heating [238; 240] is an example of such a technique. Filament heating is very inefficient because most of the radiation misses the substrate and heats the chamber walls, increasing the rate of out-gassing of contaminants deposited on the chamber walls in previous depositions. The filament method can be improved by enclosing the bulb in a 'black box' and using the box as in a direct contact technique [238; 241-243] and infra-red (IR) radiation coupled into a piece of black quartz attached to a substrate has also been used in this way [65].

A far more efficient heat source is a laser [244], which allows substrates to be heated without the chamber heating up. Laser heating also allows more precise control over the heating power applied to the substrate, and the unloading process is faster because a substrate cools far quicker than a large heating block. The two difficulties with laser heating are measuring the substrate temperature without changing the substrate temperature due to heat sinking to the probe (discussed later), and spreading the power evenly over the substrate to produce a homogeneous temperature distribution. There are a few methods for overcoming the problem of spreading the power evenly, such as use of an intermediate quartz plate as in a direct contact technique [239], beam homogeniser pipes, and beam scanning [18; 22; 58; 60; 78; 237; 245]. The technique of substrate heating used for research discussed here was a raster scanned CO_2 laser, and computer control of the delay time at each scanning point allowed continuous updating of the substrate temperature distribution, meaning in-situ temperature homogeneity control was possible. In particular, control of the delay time at scanning points located around the edge of the substrate allowed compensation of the local drop in temperature (due to extra emission because of the higher surface area to volume ratio).

Temperature can be measured either directly or remotely [246], but in-situ direct contact temperature measurement of the substrate is not possible when a remote heating technique is used because the low thermal mass of the substrate would result in significant heat sinking to a direct contact probe, which would lead to an inhomogeneous temperature distribution. Direct contact temperature measurement also has problems with repeatability due to the difficulties of recreating a good contact. It is critical that the substrate temperature distribution is homogeneous, otherwise film qualities such as stoichiometry, crystal phase, crystal orientation and surface topography could vary at different points on the substrate, leading to films with poor overall optical quality and possibly resulting in cracking.

Indirect techniques of temperature measurement are difficult to calibrate and are generally more complex than direct contact methods. Two examples of remote temperature measurement that have been used with deposition techniques are pyrometry [246-248] and diffuse reflectance spectroscopy (DRS) [249-255]. Two pyrometers sensitive to different wavelength ranges of radiation can be used to detect the radiation emitted by the substrate, and comparison of the intensities measured by the pyrometers allows the temperature to be calculated without knowledge of the emissivity of the substrate (providing it is constant for both wavelength ranges). Two-colour pyrometry is less effective when the emissivity of the substrate is low and doesn't work when the emissivity varies as a function of wavelength and

temperature unless this variance is known precisely a priori. Care must also be taken when choosing the detection ranges of the pyrometers, so as to avoid the transparency windows of the substrate material in use.

DRS takes advantage of the temperature dependent absorption band-edge that some materials possess, making it ideal for use with semiconductors. A light source is directed at the substrate and the diffusely reflected light is collected so that the temperature can be calculated from the spectrum. The diffuse reflectance spectrum is used more commonly than the diffuse transmission spectrum because it is easier to probe and sample from the same side of the substrate. In deposition techniques, one side of the substrate is always unavailable for in-situ probing because the deposition plume would interfere with the measurement. An extra advantage with DRS is its ability to measure film thickness [255]. A disadvantage of remote temperature methods is their dependence upon port windows, which gradually get coated throughout depositions, making the use of absolute intensity measurements impractical.

The limitations of in-situ temperature measurement techniques make them unsuitable for use with the PLD setup used to conduct the research reported in this thesis. An in-situ technique is not strictly necessary with PLD anyway because the ideal temperature can usually be found empirically. The power output of the CO_2 laser is constant from day to day, allowing the substrate temperature to be calibrated to the output power setting of the CO_2 laser. Once such a calibration has been made, a temperature can be 'dialled in' by using the output power setting of the CO_2 laser.

An approximate calibration of substrate temperature to CO_2 laser output power was provided by a simple experiment. Some small samples of high purity metal foil were balanced on the substrate as it was heated, and the CO_2 laser power required to melt them was recorded. The foil samples were cut to approximately 1 mm × 3 mm in size and only one was used at a time to minimise heat sinking. It was found that this experiment had good repeatability when a good contact had been made, however when a bad contact had been made the foil samples melted at far higher temperatures (we believe due to the affect of oxidation), so when it became obvious that a bad contact had been made, that result was abandoned. Figure 4.2.3 shows the result of the calibration experiment.

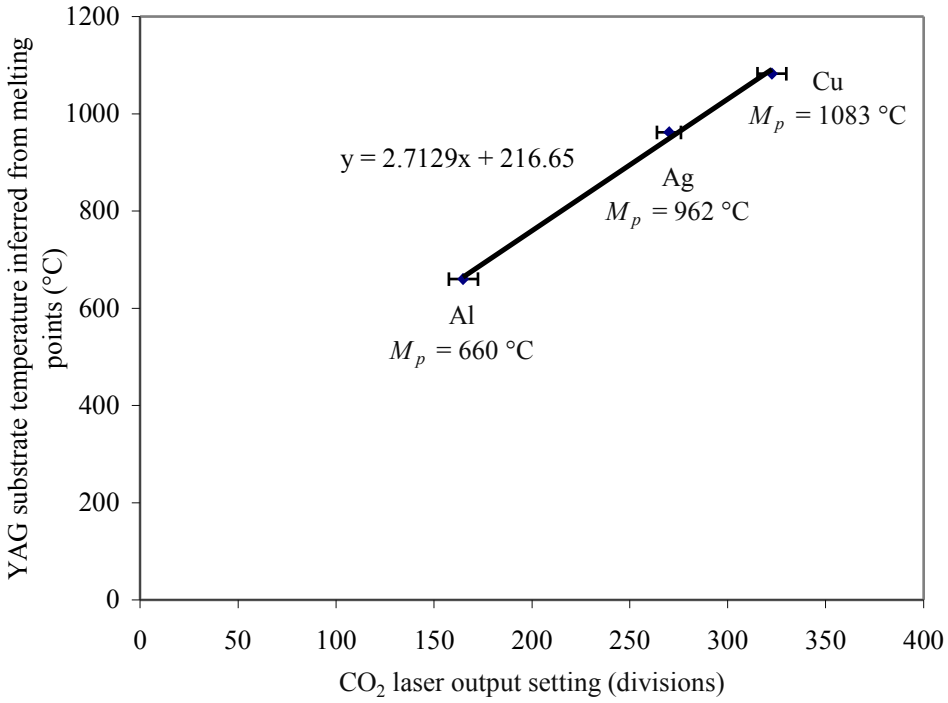

Figure 4.2.3: The results of the carbon dioxide laser power and substrate temperature calibration experiment.

Each data point is the average of the results from four experiments, and the error bars are representative of the repeatability of the measurements. The temperature increase appears to be roughly linear relative to the CO_2 laser output power setting, within the range examined. The temperature of a grey-body material (a material with a constant emissivity) can be found from Stefan's law shown as equation 4.2.1.

$$P_E = \varepsilon_E \sigma_S A_S T^4 \qquad \textbf{(4.2.1)}$$

P_E = power emitted, T = temperature, A_S = surface area, ε_E = emissivity, σ_S = Stefan-Boltzmann constant,.

Under the assumption that heated substrates in vacuum have minimal contact with the substrate holder and only lose heat via radiation, the incident CO_2 laser power will match the power emitted from the substrate and the temperature will be stable. We would therefore expect the temperature of a grey-body to scale as $P_{CO2}^{1/4}$ (P_{CO2} = output power of CO_2 laser), but since garnet crystals are not grey-bodies and their emissivity is wavelength and temperature dependent it is difficult to predict how the temperature should change with increasing incident CO_2 laser power.

4.2.2 Consequences of thick film growth

One of two things must be done for the growth of thick films to be possible; either the deposition time or rate must be increased. An attempt was made at thick film growth by increasing the deposition rate (by increasing the repetition rate of the laser), but the quality of the films was found to be heavily reduced, so the use of longer deposition times was chosen instead. The side effects that arise due to the use of long deposition times have to be managed so that the quality of films is not significantly affected.

Long deposition times require the target position to be changed regularly or reconditioned (polished) to prevent loss in quality as a result of poor target surface condition. It was found that the quality of films deposited over a period of more than two hours using the same target position decreased significantly, so growth runs of no more than one and a half hours were used. When repositioning or reconditioning the target, the chamber must be opened and care must be taken whilst this procedure is carried out to prevent intermediate layer contamination or disturbance of the substrate. Figures 4.2.4 and 4.2.5 show SEM pictures of the surface of a YbAG target crystal used for 1.5 hours and 9 hours respectively.

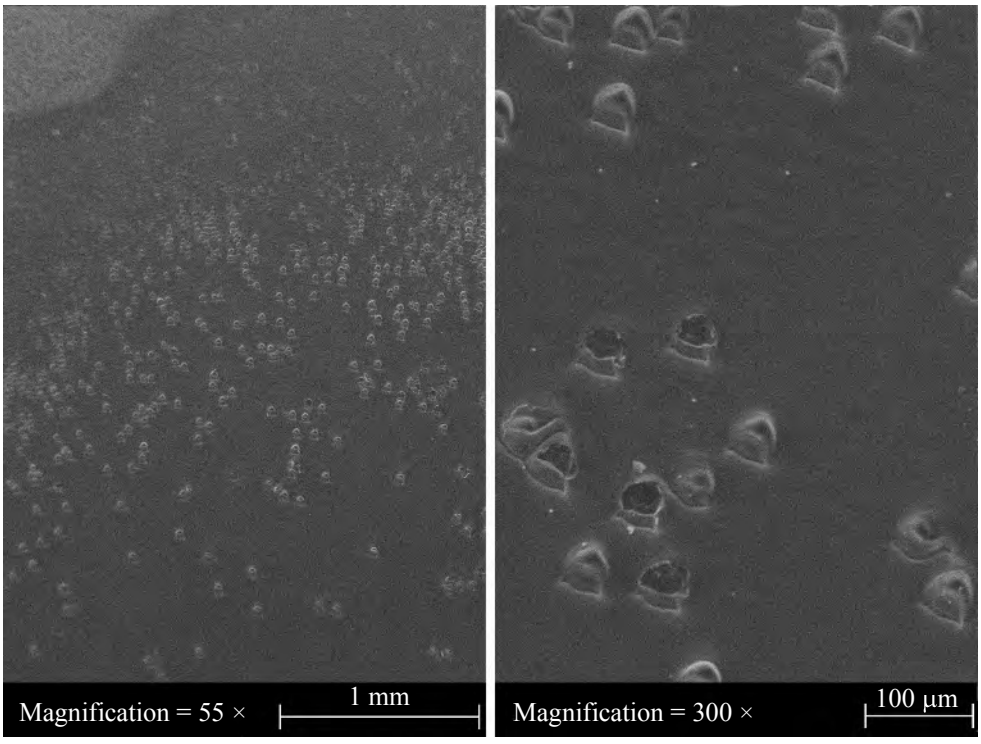

Figure 4.2.4: SEM image of a YbAG crystal target that has been used for 1.5 hours of deposition.

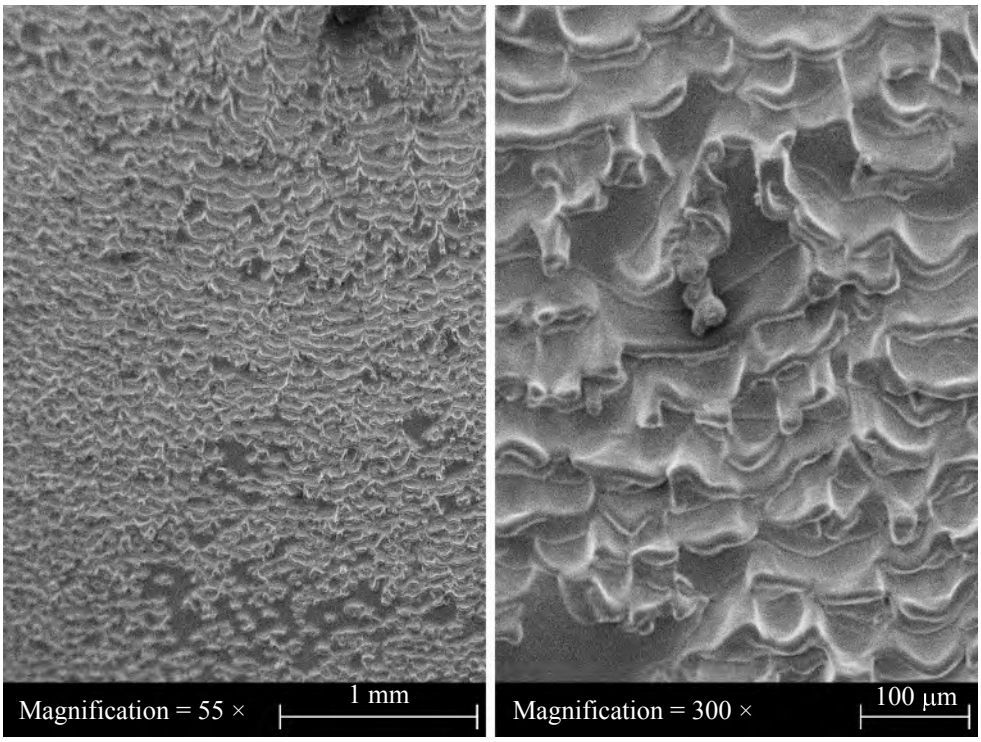

Figure 4.2.5: SEM image of a YbAG crystal target that has been used for 9 hours of deposition.

The difference in target damage can be seen clearly and the roughness that can be seen in figure 4.2.4 is known to increase the occurrence of particulates significantly. Degradation of the target surface quality means that rods (rotated so that the surface is ablated in a spiral pattern) are impractical targets because it is difficult to recondition the target surface. Another consequence of long deposition times is the gradual drift of deposition conditions, and it was found that deposition conditions must be constant over separate growth runs, or else the layers won't grow epitaxially. Evidence of non-epitaxial layers was observed under a microscope at the polishing stage of one sample in the form of a line separating the two layers. Figure 4.2.6 is an optical microscope image that shows an example of a film with a fault line separating two growth run layers. The film was deposited in eight growth runs, and from knowledge of the deposition rate, the fault line appears to be between the fifth and sixth growth runs. Cracks thought to be due to thermal expansion mismatch (to be discussed later) can also be seen in figure 4.2.6.

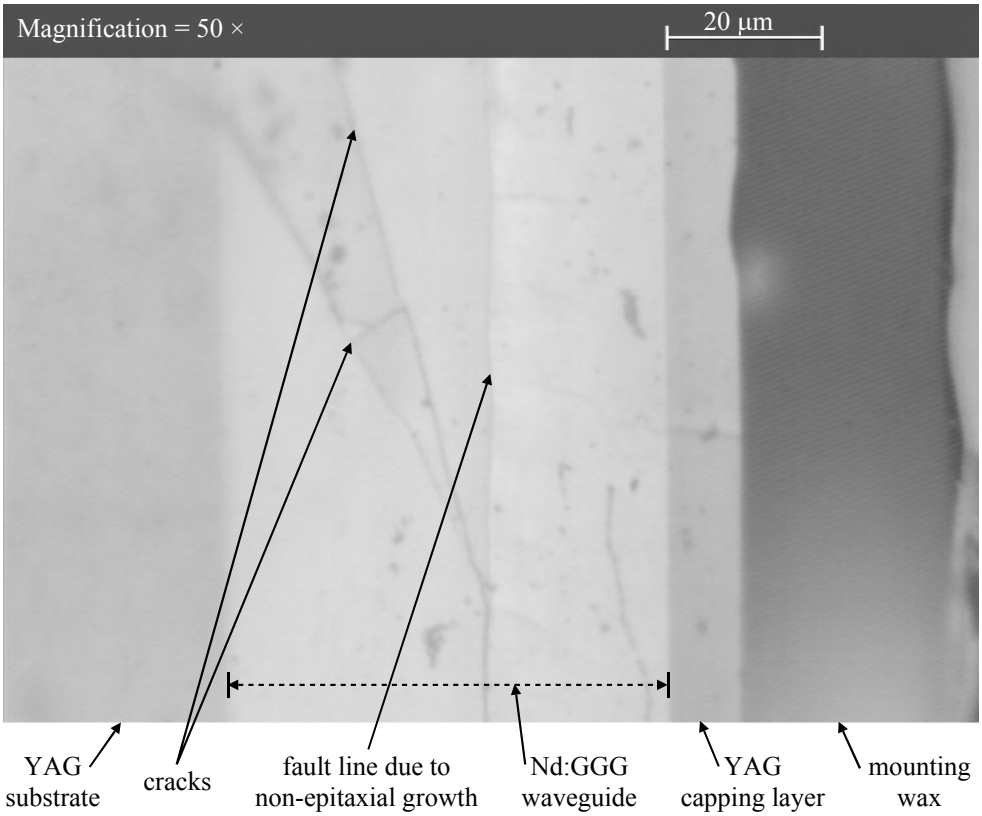

Figure 4.2.6: Optical microscope image of a sample with a fault line separating non-epitaxial layers.

Laser port windows can get coated, changing the laser power that enters the chamber throughout the depositions and causing a drift in film characteristics throughout thickness. Metal pipes were placed in the chamber to shield port windows and prevent this effect from becoming significant. The excimer laser gas mix gradually degrades over time and this can affect the beam shape, distribution and output power. The excimer gases must be changed regularly to avoid this causing different conditions in separate growth runs. General cleanliness in and around the chamber is more important when performing multiple growth runs so that no localised layer deficiencies occur.

The maximum thickness of films that could be successfully refined into devices by polishing was limited by cracking, thought to be due to thermal expansion mismatch. Films of thickness up to 135 μm were deposited in multiple growth runs, and they appeared to be stable until polishing was performed. We therefore surmise that the stresses and/or vibrations involved in the polishing process are a catalyst for cracking. The thickest film

(grown on a 0.5 mm thick substrate) to survive the polishing process was 40 μm. Figure 4.2.7 is an optical microscope image of a sample (with a 0.5 mm thick substrate) where the substrate has several cracks and will completely fall apart if demounted.

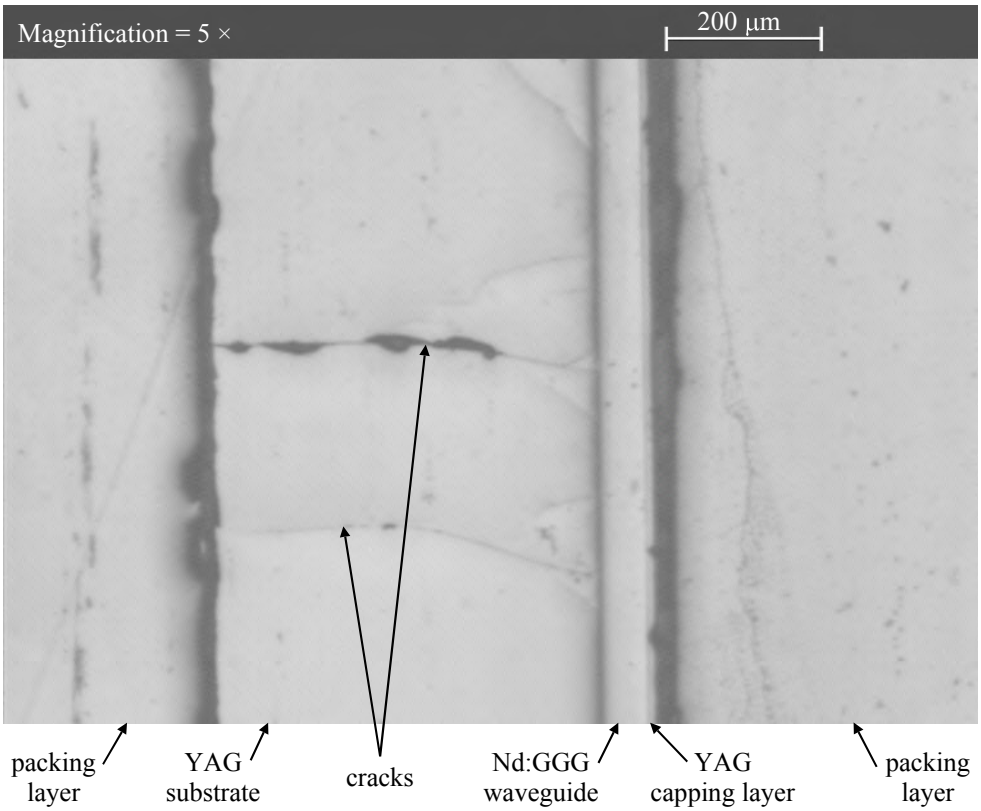

Figure 4.2.7: Optical microscope image of a sample with cracks in the substrate.

We changed from using 0.5 mm thick substrates to 1 mm thick substrates in an attempt at preventing the cracking from happening and this move was partially successful; the samples no longer shattered completely into pieces, but the film edges perpendicular to the ones being polished did persist in cracking away and it wasn't possible to polish all four sides for side-pumping. It was possible however to polish two opposing parallel sides, allowing the waveguides to be end-pumped. Figure 4.2.8 is an optical microscope image of a sample (with a 1 mm thick substrate) where the edges perpendicular to the ones being polished have cracks running down them and will come apart from the sample if demounted.

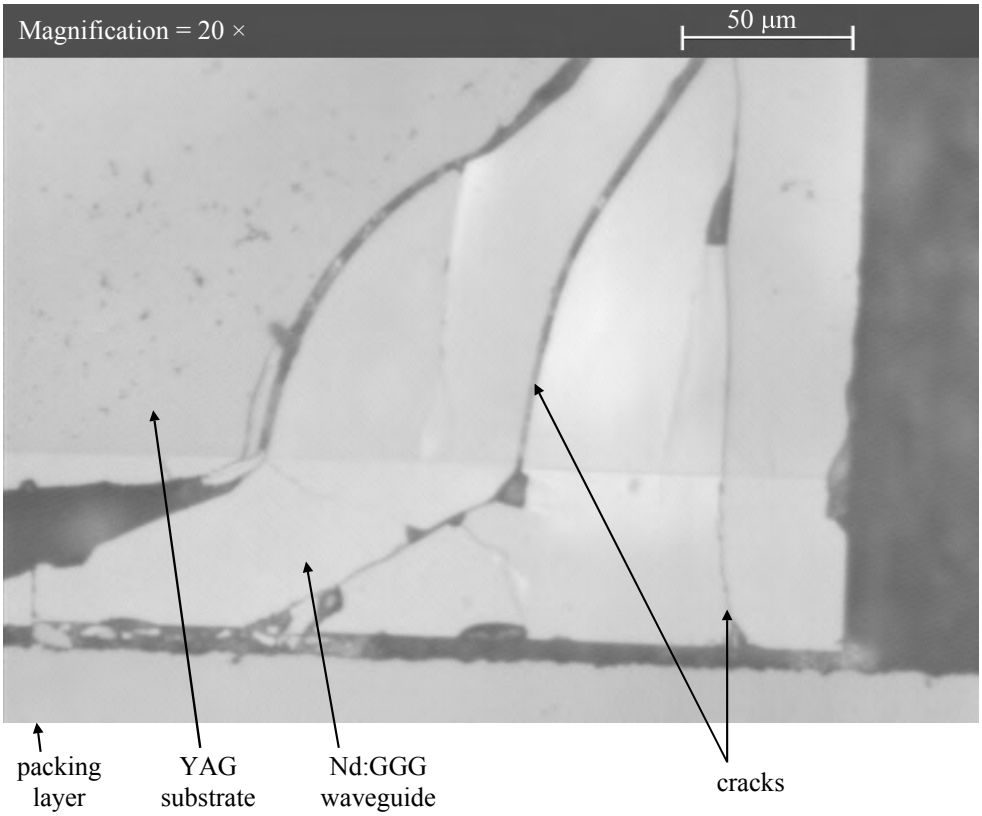

Figure 4.2.8: Optical microscope image of a sample with cracks in the edge perpendicular to the one being polished.

4.2.3 Deposition conditions

The excimer laser was set to produce an output of about 200 mJ per pulse at 10 Hz, resulting in an energy density of approximately 1.5 Jcm^{-2} at the target surface. Single crystals were used as targets, and the target to substrate distance was set to 4 cm. Substrate temperatures estimated to be between 650 °C and 750 °C were used and an oxygen pressure of 2.0 ± 0.1 Pa was used for the chamber atmosphere.

4.3 Substrate cleaning procedure

Substrates are supplied with a high grade 'epitaxial' polish on one side so that the surface is ready for depositing on; the cleanliness of the as-supplied substrates however is not good enough for immediate use. Substrates are therefore put through a micro-cleaning process to remove contaminants before use, involving the sequential steps:

A. Wiping with a cotton bud soaked in acetone to initially remove any large particles.

B. Immersion in a concentrated nitric acid solution for twenty minutes to remove any organic contaminants.

C. Rinsing with de-ionised water, transference into a beaker of de-ionised water and placement in an ultrasonic bath (at a temperature of 50 °C) for twenty minutes to remove any traces of acid.

D. Transference into a beaker of acetone and placement in an ultrasonic bath (at a temperature of 50 °C) for twenty minutes.

E. Rinsing with isopropanol, transference into a beaker of isopropanol and placement in an ultrasonic bath (at a temperature of 50 °C) for twenty minutes.

F. Rinsing with de-ionised water, transference into a beaker of de-ionised water and placement in an ultrasonic bath (at a temperature of 50 °C) for twenty minutes.

G. Removal from the ultrasonic bath and drying firstly with a jet of nitrogen gas, and then further in an oven (set to 120 °C) for thirty minutes.

4.4 Visual, optical microscopy and scanning electron microscopy

Visual inspection of films is the easiest type of analysis available for the determination of ideal growth conditions. An opaque film can indicate that the film stoichiometry is wrong and an incorrect phase has been grown, a 'frosted' film surface can indicate poorly tuned substrate temperature and plume properties, whilst poor temperature homogeneity can be indicated by cracks, lines or flaking in the films. Optical microscopy is useful for investigating surface defects in more detail and the location, frequency and relative sizes of particulates can be determined. The optical microscope image figure 4.4.1 shows an example of flaky and 'frosted' growth. The improved substrate holder design led to a more homogeneous substrate temperature distribution, but care still had to be taken to ensure that substrates were held with minimal contact with the posts, else fault lines of bad growth would occur on the film surface as shown in figure 4.4.2.

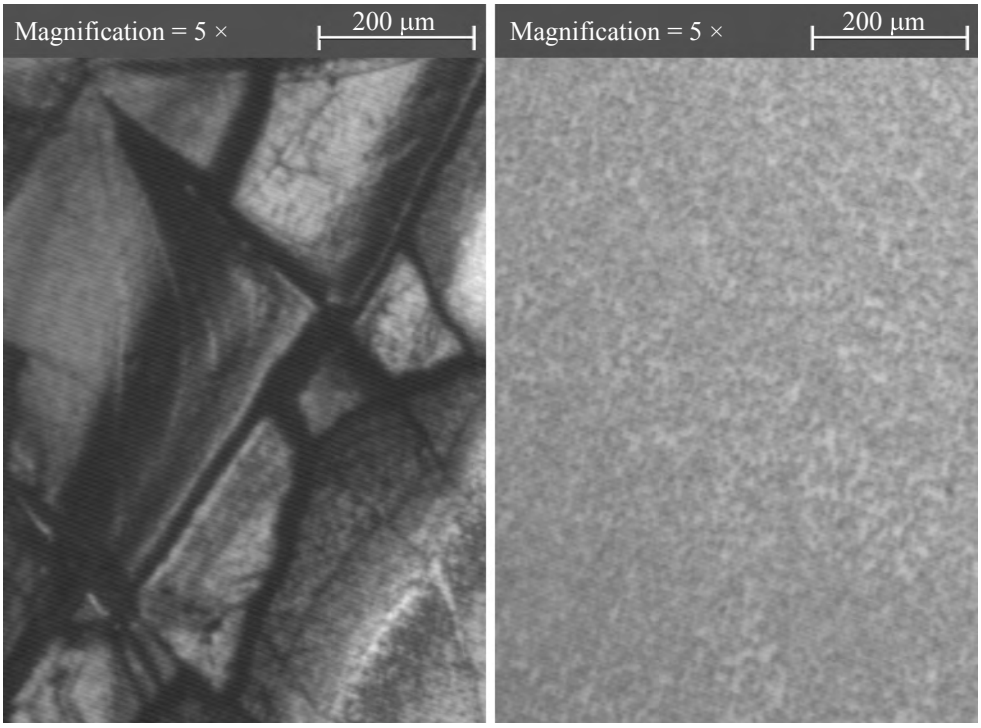

Figure 4.4.1: Optical microscope image of flaky and 'frosted' growth.

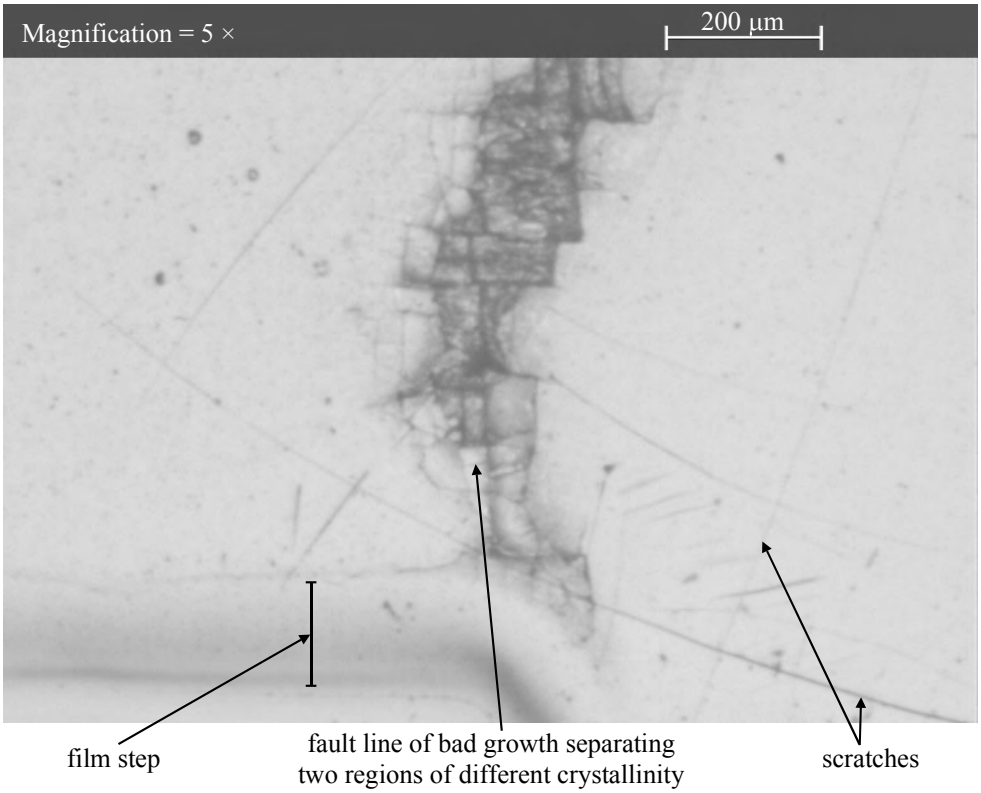

Figure 4.4.2: Optical microscope image of a surface defect caused by an inhomogeneous temperature distribution due to contact with the substrate holder.

SEM is used for an even closer look at the surface structure of films. SEM is a slightly destructive technique because to prevent electrical charging, films must be coated with gold, which can be difficult to remove after analysis without damaging the film surface. SEM can be used to determine if the surface structure is flat and smooth or made up of fine grains, and can also be used to explain the occurrence of differences in separate regions of the film surface.

4.5 Structural and compositional analysis

Determining the structural and compositional properties of films provides further feedback and allows the growth conditions to be optimised before the relatively time consuming process of optical testing is commenced. For high optical quality, single crystal films are desirable, and this makes the relatively fast technique of X-ray diffraction a critical test of film quality.

4.5.1 Surface height profiler

A Tencor Alpha-Step surface profiler was used for determining film thickness and profile. Film thickness measurement is possible because of the occurrence of bald areas on the substrate where no film is deposited, due to the substrate holder configuration. The surface profiler consists of a highly sensitive cantilever with a fine stylus on one end that rests on the sample. As the sample is moved underneath the profiler, the vertical movement of the stylus tip is measured and displayed on a monitor. When growing thick and multilayer films, the film thickness was also verified using a micrometer (accurate to ± 1 μm) before and after deposition.

4.5.2 X-ray diffraction

The planes of a crystal lattice can act as a diffraction grating for X-rays. The Bragg condition is shown below as equation 4.5.1.

$$2D\sin\theta = n_i\lambda \qquad \textbf{(4.5.1)}$$

D = crystal plane separation, θ = grazing angle of incident X-rays, n_i = integer, λ = X-ray wavelength.

The X-ray diffraction apparatus consists of an X-ray source and detector, both capable of rotating around the sample, mounted in the centre of their circles of rotation, as shown in figure 4.5.1 below.

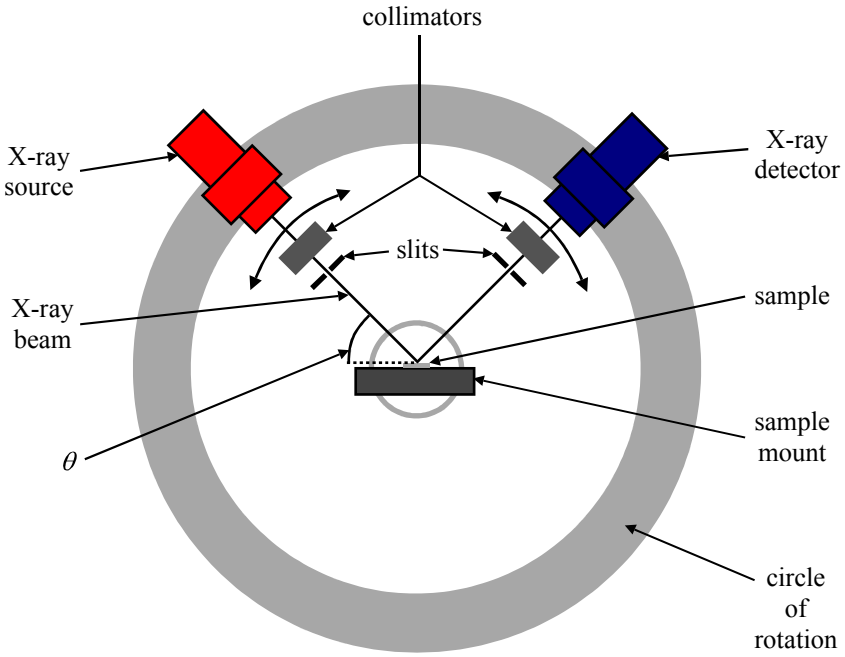

Figure 4.5.1: Schematic of an X-ray diffractometer.

The source and detector are started at an angle of 0° and 180° respectively, the source is then rotated around the sample as the detector is rotated in the opposite direction at the same rate. This produces an X-ray spectrum of X-ray yield (counts) versus 2θ angle. For an angle of incidence where constructive interference occurs, a significant peak will occur in the X-ray spectrum and the plane separation can be calculated from the Bragg condition.

The full width half maxima (FWHM) of peaks can give an indication of the crystal quality, and since substrates are of high crystal quality, their peaks can be used as a benchmark. Broadening of peaks is an indication of non-uniformity in the lattice, which can be produced by strain such as that caused by thermal expansion mismatch, or a randomly occurring deficiency in the film stoichiometry. The plane separation value can be compared to database values [256] and the crystal phase and orientation can be inferred. Small shifts of peak positions relative to their expected database values are an indication of a uniform difference in the lattice, which can be produced by strain such as that caused by lattice mismatch or thermal expansion mismatch, or a regular deficiency in the crystal structure that occurs across the whole crystal. The same sample holder couldn't always be used when performing XRD analysis, and this has caused some spectra to be slightly shifted; the YAG

substrate peaks have been used to account for this shift by comparing their positions to database values and applying the difference to other peaks to produce normalised peak positions and hence normalised values of plane separation.

Figure 4.5.2 shows the crystal structure of a unit cell of garnet crystal with the oxygen sites removed so that the metal sites can be seen clearly. In this example the garnet crystal lattice sites are labelled A, B and C (from the formula for garnet, $A_3B_2C_3O_{12}$), and the two types of planes that exist are referred to hereafter as p-planes and q-planes.

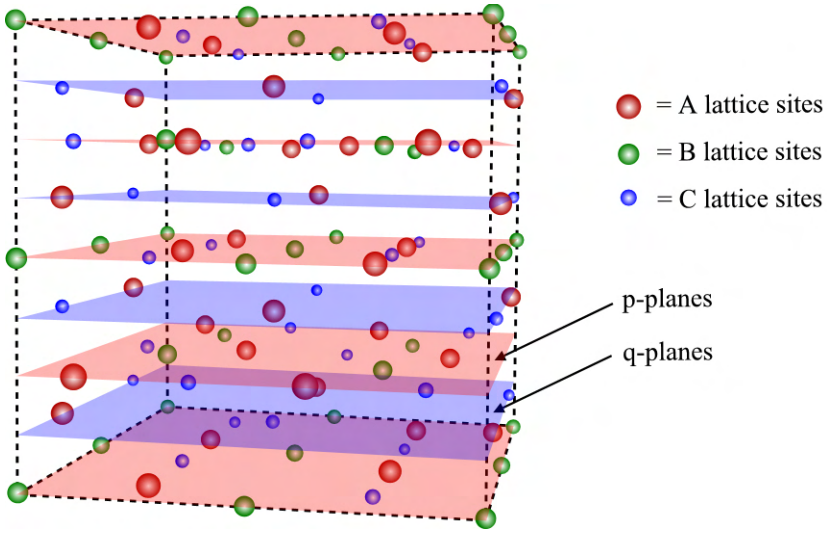

Figure 4.5.2: Crystal structure of a unit cell of garnet crystal.

Garnet crystal (800) planes alternate between two distinct types. In a unit cell sized square, a p-plane has four A lattice sites, four B lattice sites and four C lattices sites, whereas a q-plane only has two A lattice sites and two C lattice sites. This means that a deficiency in stoichiometry will affect (800) X-ray diffraction differently to (400) diffraction because (400) X-ray diffraction compares the spacing of p-planes and/or the spacing of q-planes (and is likely to be dominated by the denser p-planes), whereas (800) diffraction compares the spacing of p-planes to q-planes. The difference between (400) and (800) X-ray diffraction is illustrated in figures 4.5.3 and 4.5.4.

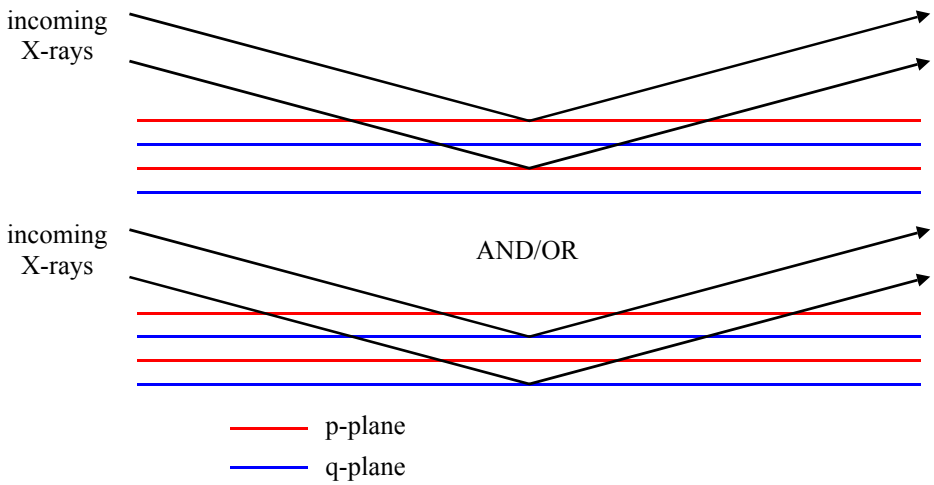

Figure 4.5.3: (400) X-ray diffraction from the spacings of p-planes and/or q-planes.

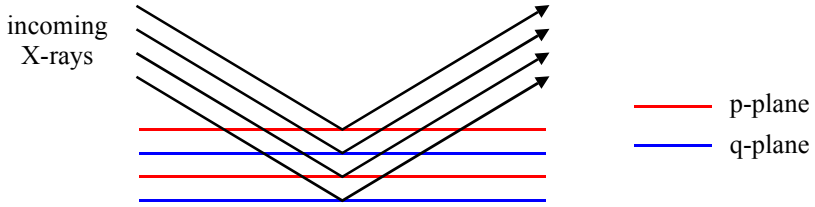

Figure 4.5.4: (800) X-ray diffraction from the spacings of p-planes to q-planes.

4.5.3 Energy dispersive X-ray analysis

Energy dispersive X-ray (EDX) analysis is an alternative mode of operation of a scanning electron microscope. The electron beam from the SEM is used to excite atoms within a small impact area (usually a few microns in diameter) just below the sample surface, causing the atoms within the impact area to emit X-rays of a unique wavelength depending upon their identity. A detector counts the X-ray yield at different wavelengths/energies emitted from the sample and a histogram is formed. A data sheet can be used to identify what elements the peaks correspond to, and software packages such as *SEMQuant* (the standard software package supplied with the SEM equipment) can be used to produce an estimate of the empirical formula for the sample. The EDX technique is subject to several problems detailed below:

- The detector window can absorb lower energy X-rays, making the detection of lighter elements such as oxygen inaccurate.
- Many X-rays are reabsorbed by the sample before they can reach the surface.

- The sample surface topography affects the volume of the impact area.
- The size of the impact area limits EDX analysis to the sample surface and makes the analysis of thick films difficult.
- The origin of broad peaks can be difficult to identify if the peak overlaps the energy values of more than one element.
- Samples must be coated with gold or carbon to prevent electrical charging.

4.5.4 Rutherford backscattering

Rutherford backscattering (RBS) analysis utilises the effect of Coulombic repulsion. An ion beam is directed at a sample and the scattered ions are detected at a constant angle. The ions undergo elastic scattering from the sample surface due to Coulombic repulsion from atomic nuclei within the sample. The energies of the scattered ions are dependent upon the masses of the atoms they were scattered from. Under the right conditions, RBS can be used to detect surface contaminants, measure layer thickness and sample stoichiometry, and profile the diffusion of a film element into the substrate.

To derive the stoichiometry of a sample material from RBS analysis, a comparison of the yield heights for different element peaks must be performed. A RBS spectrum from an unsupported monolayer sample will consist of sharp peaks corresponding to the elements in the monolayer, whereas a RBS spectrum from a thick sample will consist of plateaus due to the broadening of ion energies caused by scattering deeper within the sample. For yield height comparison, it is important that the yield from identical incident ion energies is used, and since it is difficult to identify the sample depth that different parts of the spectrum originated from, yield heights are usually taken at the plateau edges, which are representative of scattering from the sample surface. Figure 4.5.5 shows an example of an RBS spectrum from a thick sample with the features described below:

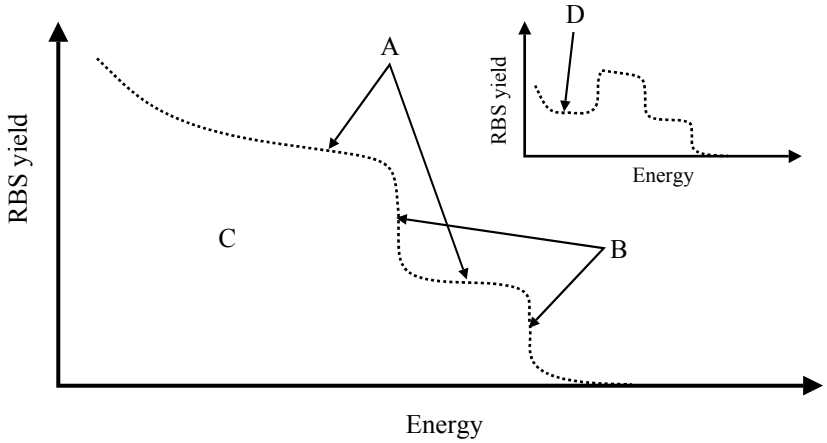

Figure 4.5.5: Example of an RBS spectrum with features A-D described in the text.

A. Different plateaus produced by different elements in the sample.

B. Plateau edges produced by scattering from the surface.

C. Inner part of spectrum produced by scattering from varying depths.

D. Low energy yield drop caused by a layer of different material to the surface (occurs when films with a thickness less than approximately half the penetration depth of ions are analysed).

The stoichiometry of a two-component compound A_XB_Y can be found using equation 4.5.2. The stoichiometry formula factor f_i can be calculated using equation 4.5.3 and the kinematic factor for an atomic species i, K_i, can be calculated using equation 4.5.4. The stopping power for an ion on path a, S_a, would usually have to be calculated by integrating over the path of the ion, but averages can be used instead, as is shown in equation 4.5.2.

$$\frac{X}{Y} = \frac{N_A}{N_B} = \frac{H_A}{H_B}\frac{{Z_B}^2}{{Z_A}^2}\frac{f_B}{f_A}\frac{\left(K_A S_1 + S_{2A}/\cos(\pi - \theta_s)\right)}{\left(K_B S_1 + S_{2B}/\cos(\pi - \theta_s)\right)} \qquad \textbf{(4.5.2)}$$

X = number of species A for every Y of species B, N_A = number density of species A, N_B = number density of species B, H_A = height of species A plateau, H_B = height of species B plateau, Z_A = nuclear charge of species A, Z_B = nuclear charge of species B, f_A and f_B can be found by replacing i with A or B in equation 4.5.3, K_A = kinematic factor for species A, K_B = kinematic factor for species B, S_1 = average stopping power for the ingoing path, S_{2A} = average stopping power for the outgoing path after scattering from species A, S_{2B} = average stopping power for the outgoing path after scattering from species B, θ_s = scattering angle of the ions.

$$f_i = \mathrm{cosec}^4\left(\frac{\theta_s}{2}\right) - 2\left(\frac{m_1}{m_i}\right)^2 \qquad \textbf{(4.5.3)}$$

f_i = stoichiometry formula factor for species i, m_1 = mass of the incident ions, m_i = mass of a sample atom of species i.

$$K_i = \left(\frac{m_1}{m_1 + m_i}\right)^2 \left(\cos\theta_s + \sqrt{\left(\frac{m_i}{m_1}\right)^2 - \sin^2\theta_s}\right)^2 \qquad (4.5.4)$$

The mass of the ions used with RBS determines the accuracy of stoichiometry measurements, and heavier ions are good at resolving heavy sample atoms but poor at resolving lighter sample atoms, whereas light ions are good at resolving light sample atoms but poor at resolving heavy sample atoms.

4.6 Polishing

Samples must be polished to a high quality optical finish before waveguiding and lasing analysis can be conducted. Samples were initially cut close to the desired dimensions using a slow speed circular saw, and were then mounted on a block with wax so that they could be attached to a jig. The jig holds the sample and allows the polishing pressure and angle to be controlled, and the polishing rate monitored. The polishing machine apparatus basically consists of a rotating flat circular plate, an arm that holds the jig on the plate and a drip supply, of grit mixed in de-ionised water, or polishing solution. Samples were polished in stages: firstly, lapping was performed with a relatively large sized grit (silicon carbide) to achieve rough flatness of the sample and packing layers, followed by further lapping with 9 µm sized particles (calcined aluminium oxide) to remove grit sized scratches, and then 3 µm sized particles (calcined aluminium oxide) to remove the 9 µm sized scratches, and finally polishing using a Leybold polishing solution (SF1 - alkaline colloidal silica) to achieve a high quality optical finish. Care must be taken to ensure that faces are polished as close to perpendicular to the plane of the film and the adjacent faces as possible. For lasing experiments to be successful it is also very important to make sure opposing faces are polished parallel to each other.

4.6.1 Face-polishing

Since the films are naturally domed, they must be face-polished before overgrowing new layers of a different material so that all of the layer interfaces are parallel to the substrate surface, making ideal planar waveguide geometries. A special mounting block was used with faces that are known to be parallel to a very high precision. One face of the mounting block is partially reflective, allowing it to be used in an autocollimator to align the mounting block face parallel to the polishing jig base. Substrate faces were polished parallel using this technique before deposition so that the back face of the substrate could be used as a reference after the films had been grown. Films were polished using this technique before overgrowing of further layers was performed, and the film thickness was measured between each stage.

4.6.2 End-polishing

A high degree of parallelism is required for films to be used as laser devices. The jig needs to be set to basic flatness and a mounting block that ensures the end being polished is roughly perpendicular to the two adjacent sides must be used. When one end is polished, the sample can be rotated on the mount so that the polished end can be used as a reference for the autocollimator. A high degree of parallelism was obtained for samples polished using this technique (the primary and secondary reflections of a HeNe laser overlapped exactly over a distance of 2 m).

4.7 Waveguide laser techniques and analysis

4.7.1 Waveguide laser cavity

Waveguide laser cavities were formed by butt-coupling lightweight mirrors to opposite end faces, as shown in figure 4.7.1 below. The mirrors were attached to the waveguide by the surface tension of a small amount of fluorinert liquid. Care must be taken to ensure that the mirrors get a good contact on the end faces, else it will be difficult to achieve lasing in the waveguide.

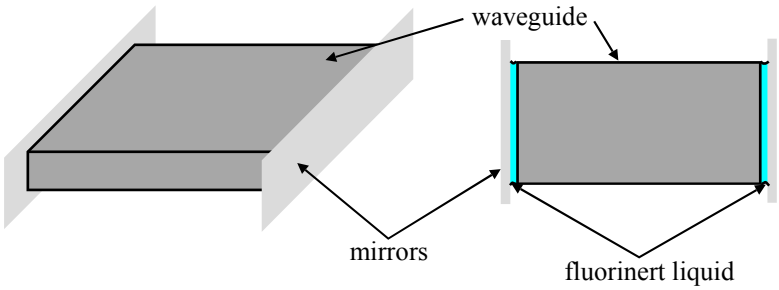

Figure 4.7.1: Waveguide laser cavity (fluorinert thickness has been exaggerated).

4.7.2 Ti:sapphire launching

The output from a Ti:sapphire laser (pumped by an Ar^+ laser) is well suited for waveguiding analysis because of its wide tunability range (wavelength range used: 790-830 nm). The modal output of the Ti:sapphire laser is generally stable when the pump power is kept constant at about 10 W, however the output power from the Ti:sapphire laser is higher than is required in this state, so a variable attenuator was used to select the power level for launching. The FWHM of the Ti:sapphire laser output was 0.1 nm when tuned to a wavelength of 808 nm. An input coupling lens was used to focus the Ti:sapphire beam into the waveguide samples, and an XYZ stage was used to manipulate the waveguide samples into the exact required position. The experimental arrangement used for launching the Ti:sapphire laser beam into waveguides, and various optical analysis is shown below in figure 4.7.2.

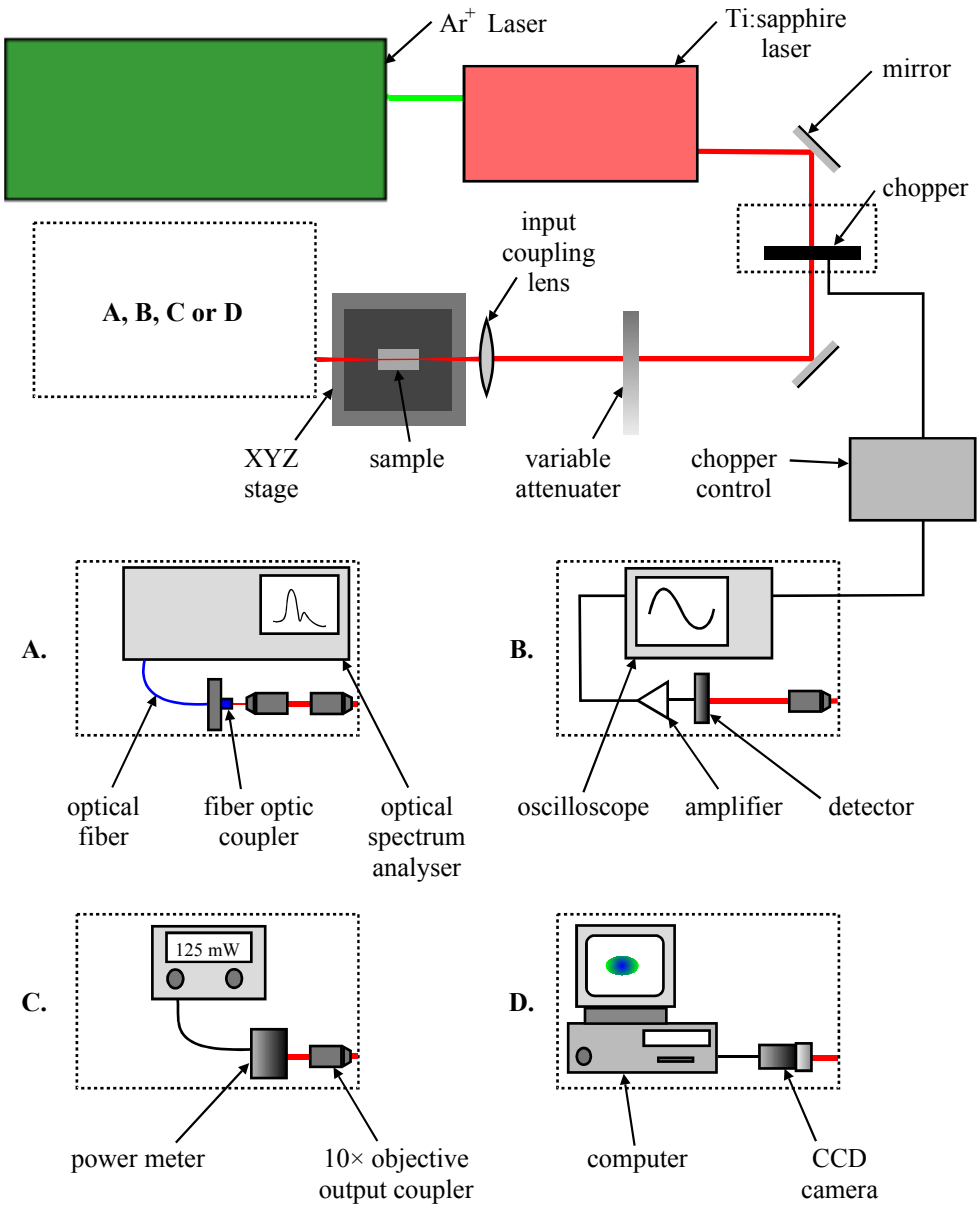

Figure 4.7.2: Experimental arrangement for launching and optical waveguiding based analysis with Ti:sapphire pumping.

4.7.3 Diode launching

The experimental arrangement used for launching diode laser light into waveguides, and various optical analysis is shown below in figure 4.7.3.

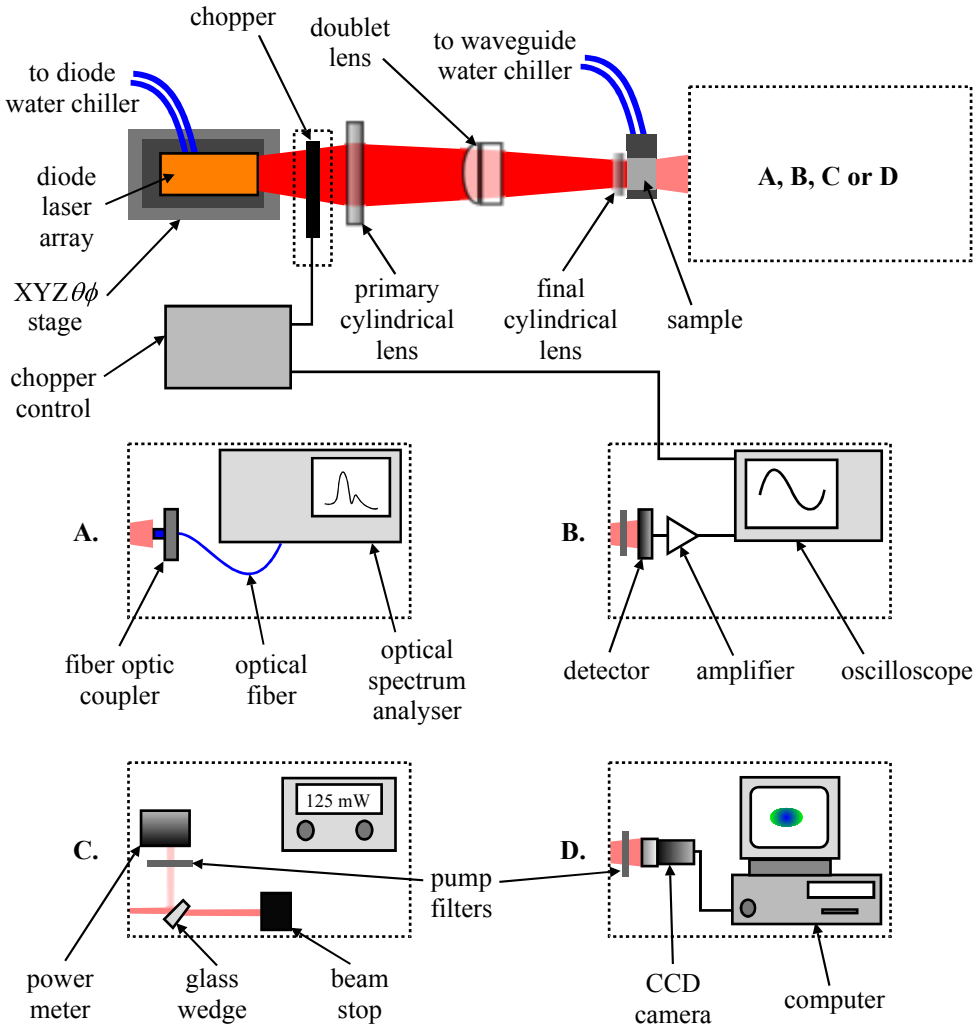

Figure 4.7.3: Experimental arrangement for launching and optical waveguiding based analysis with diode pumping.

Diode laser arrays are good pump sources for planar waveguide lasers because the stripe output profile is well matched to the end face of the waveguide. A diode laser array (stacked) consisting of three 60 W diode lasers supplied a potential of 180 W of pump power in total, and a series of lenses were used to focus the output into the waveguide. The output from the array had a FWHM of 2 nm and could be tuned within a small wavelength range around 808 nm by changing the temperature of the cooling water (the peak intensity of the array output was 807 nm at 20 °C). Rough alignment was performed with the primary cylindrical lens and doublet before the pump light was then tightly focused into the waveguide by a final cylindrical lens.

4.7.3.1 Launch efficiency

Focussing of diode laser array light efficiently into a waveguide is difficult and will directly affect the performance of a waveguide laser. It is useful therefore to be able to make estimations of the launch efficiency from measurements of the diode power that is collected just after the waveguide (with no cavity mirrors in place). The power collected just after the waveguide will be made up of launched light that has not been absorbed, and light that has not been launched but has gone through the substrate or the air above the waveguide. Equation 4.7.1 can be used to estimate the launch efficiency if the following assumptions are made:

- All of the light not launched actually reaches the power meter.
- Launching is symmetric so that half of the light not launched goes above the waveguide and half goes below.
- No light reaches the power meter by missing the sample and passing by its sides.

$$P_2 = P_1\left[L_{eff}\left(1-R_G\right)^2 e^{-\alpha_p l} e^{\alpha_{PL} l} + \frac{1-L_{eff}}{2}\left(1+\left(1-R_Y\right)^2 e^{\alpha_{SL} l}\right)\right] \quad \textbf{(4.7.1)}$$

P_2 = power after the waveguide output face, P_1 = power before the waveguide input face ($P_1 = P_p \times L_{lenses}$, P_p = pump power, L_{lenses} = loss factor for lenses before the waveguide input face), L_{eff} = Launch efficiency, R_G = GGG-air Fresnel reflectivity, α_p = pump absorption coefficient, α_{PL} = propagation loss coefficient, l = waveguide length, R_Y = YAG-air Fresnel reflectivity, α_{SL} = substrate loss coefficient.

After rearrangement of equation 4.7.1 we can arrive at equation 4.7.2 shown below.

$$L_{eff} = \frac{\left[\frac{P_2}{P_1} - \frac{1}{2}\left(1+\left(1-R_Y\right)^2 e^{\alpha_{SL} l}\right)\right]}{\left[\left(1-R_G\right)^2 e^{-\alpha_p l} e^{\alpha_{PL} l} - \frac{1}{2}\left(1+\left(1-R_Y\right)^2 e^{\alpha_{SL} l}\right)\right]} \quad \textbf{(4.7.2)}$$

4.7.4 Absorption spectra

The experimental arrangement shown in figure 4.7.2:A was used to measure the Ti:sapphire laser wavelength as it was tuned through a range of 790-830 nm and the Ti:sapphire laser power before and after a waveguide was measured at 0.5 nm intervals with the experimental

arrangement shown in figure 4.7.2:B. A reference power measurement straight through the substrate was used to make an approximation of the waveguide face Fresnel reflection losses, and a measurement of the power before and after other optical components was taken to estimate other losses. This allowed a spectrum of absorbed power as a function of wavelength to be plotted.

4.7.5 Fluorescence spectra

The experimental arrangement shown in figure 4.7.2:A was used to record fluorescence spectra when the Ti:sapphire laser was tuned to a wavelength of 808 nm (the wavelength of optimal absorption for a laser wavelength of 1.06 µm in Nd:GGG) and used to pump a waveguide. The experimental arrangement shown in figure 4.7.3:A was used to record the fluorescence spectra when a waveguide was pumped with diodes.

4.7.6 Threshold power for lasing, lasing spectra and slope efficiencies

High reflectivity (HR) mirrors are coated for high transmission at the pumping wavelength, and high reflectivity at the laser wavelength, whereas output coupling mirrors are coated for high reflectivity at the pumping wavelength and have various reflectivities at the laser wavelength. Several different output coupling mirrors were used to investigate the laser properties of the waveguides. The mirror positions were optimised by reducing the pump power just below threshold and moving the mirrors to see if lasing could be made to occur at a lower pump power.

The experimental arrangement shown in figure 4.7.2:C or figure 4.7.3:C was used to detect threshold lasing of waveguides when using Ti:sapphire pumping or diode pumping respectively. The threshold power for lasing was recorded when the cavity mirror positions had been satisfactorily optimised. The experimental arrangement shown in figure 4.7.2:A or figure 4.7.3:A was used to record laser spectra when using Ti:sapphire pumping or diode pumping respectively. For slope efficiencies, the experimental arrangement shown in figure 4.7.2:B or figure 4.7.3:B was used to measure the output power of waveguides at various different pumping powers when using Ti:sapphire pumping or diode pumping respectively. To prevent filters from cracking due to overheating when pumping with the diodes, a glass wedge was used to reflect the laser output at an angle of 45° so that only a

small amount of the laser output and any stray pump light was incident on the power meter setup (the reflectance of the wedge was calibrated experimentally). Equation 4.7.3 was used to calculate absorbed power when plotting slope efficiencies. The form of equation 4.7.3 shown below was used for calculation of absorbed power when both input and output coupling mirrors were HT coated for the pump wavelength, but had to be modified by changing $l \rightarrow 2l$ to approximate absorbed power when the output coupling mirror was HR coated for the pump wavelength.

$$P_{abs} = P_p L_{lenses} L_{eff} \left(1 - R_M\right) e^{\alpha_{PL} l} \left(1 - e^{-\alpha_p l}\right) \qquad \textbf{(4.7.3)}$$

P_{abs} = absorbed power, R_M = input mirror pump light reflectivity.

4.7.7 Beam profile measurements

The experimental arrangement shown in figure 4.7.2:D or figure 4.7.3:D was used to record pictures of the beam profile when waveguides were Ti:sapphire pumped or diode pumped respectively. The distance of the CCD camera from the waveguide output face must be taken into account when calculating the actual beam profile size.

4.7.8 Propagation losses

4.7.8.1 Findlay-Clay technique

The Findlay-Clay [257] technique of propagation loss estimation gives a 'worst case scenario' estimation and is suitable for the estimation of loss in a four-level laser system. A four-level laser does not suffer from significant depopulation of the ground level, and if losses due to reabsorption are assumed to be negligible, the absorbed power threshold for lasing in a waveguide laser is then only dependent upon the propagation loss and level of output coupling, as shown in equation 4.7.4. The value of the constant C included in equation 4.7.4 is found from equation 4.7.5.

$$P_{th} = C\left(L_{PL} + T_{OC}\right) = C\left(-2\alpha_{PL} l - \ln\left(R_1 R_2\right)\right) \qquad \textbf{(4.7.4)}$$

P_{th} = absorbed power threshold for lasing, C = a combined constant (see equation 4.7.5), L_{PL} = round trip propagation loss exponent, T_{OC} = transmission exponent, R_1 = reflectivity of the input coupling mirror (feedback mirror), R_2 = reflectivity of the output coupling mirror.

$$C = \frac{\pi h \nu_p}{4\sigma_e \eta_q \tau_{fl}} \left(w_{px}^{\ 2} + w_{lx}^{\ 2} \right)^{1/2} \left(w_{py}^{\ 2} + w_{ly}^{\ 2} \right)^{1/2} \qquad \textbf{(4.7.5)}$$

h = Planck's constant, ν_p = pump laser frequency, w_{lx}, w_{ly}, w_{px}, w_{py} = average spot sizes of the laser and pump modes in the horizontal and vertical directions respectively, σ_e = emission cross-section, η_q = fraction of absorbed photons that lead to population of the upper laser level, τ_{fl} = lifetime of the upper laser level.

The threshold power for lasing must be measured using output coupling mirrors with various different reflectivities. A graph of absorbed power threshold for lasing on the y-axis versus $-\ln(R_1R_2)/2l$ on the x-axis should then have a straight line trend, and since $-\ln(R_1R_2)/2l = \alpha_{PL}$ when $P_{th} = 0$ in equation 4.7.4, the x-axis intercept of the best fit line will be a good approximation of the propagation loss coefficient α_{PL}. A conversion calculation must then be made to achieve a value of loss in units of dBcm^{-1}, as shown in equation 4.7.6.

$$\text{Propagation Loss } \left(\text{dBcm}^{-1} \right) = -10 \log_{10} \left(e^{\alpha_{PL}} \right) \qquad \textbf{(4.7.6)}$$

4.7.8.2 Loss derivation from slope efficiencies

The measurement of two different slope efficiencies from two different output couplers (with different reflectivities) provides another means by which loss can be estimated in a four-level laser system. If the two output couplers are similar so that the pump powers used in each case are similar, we can assume that the spatial overlap efficiency and quantum efficiency will be approximately the same in each case as shown in equation 4.7.7, which is derived from equation 3.4.10.

$$\eta_A \frac{\left(-\ln\left(R_1 R_{2A} \right) + L_{PL} \right)}{-\ln\left(R_{2A} \right)} = \eta_{qA} \eta_{plA} \frac{\nu_l}{\nu_p} = \eta_{qB} \eta_{plB} \frac{\nu_l}{\nu_p} = \eta_B \frac{\left(-\ln\left(R_1 R_{2B} \right) + L_{PL} \right)}{-\ln\left(R_{2B} \right)} \qquad \textbf{(4.7.7)}$$

η_A and η_B = slope efficiencies for the output coupling mirrors A and B respectively, R_{2A} and R_{2B} = reflectivities of the output coupling mirrors A and B respectively, η_{qA} and η_{qB} = quantum efficiencies of the laser using output coupling mirrors A and B respectively, η_{plA} and η_{plB} = spatial overlap efficiency of the pump and laser beams using output coupling mirrors A and B respectively, ν_l = frequency of the laser radiation.

Equation 4.7.7 can be rearranged to find the propagation loss exponent L_{PL} shown below in equation 4.7.8.

$$L_{PL} = \frac{\eta_A \ln(R_{2B}) \ln(R_1 R_{2A}) - \eta_B \ln(R_{2A}) \ln(R_1 R_{2B})}{\eta_A \ln(R_{2B}) - \eta_B \ln(R_{2A})} \quad \textbf{(4.7.8)}$$

4.8 Thin-disk laser techniques and analysis

4.8.1 Diode pumping and thin-disk laser cavities

An indium gallium arsenide diode laser system was used to pump the YbAG film at a wavelength of 940 nm with a potential total power of 50 W. Two lenses were used to focus the pump light into a small volume of the film, forming a gain region. Two types of laser cavity were formed around the gain region to see if the film would lase. Both cavities are simple for testing purposes but the pump radiation can be used more efficiently by passing it through the disk several times as has been reported previously elsewhere [35]. The experimental arrangement used for pumping and optical analysis of the YbAG film is shown below in figure 4.8.1, and the two types of cavities attempted are shown in figure 4.8.2 and figure 4.8.3.

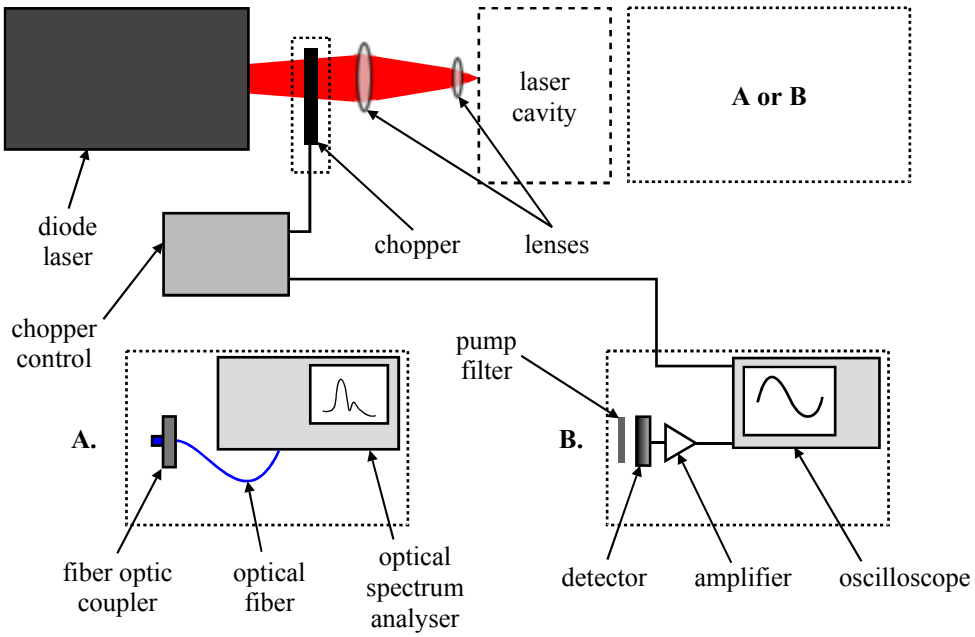

Figure 4.8.1: Experimental arrangement for pumping and optical analysis of the YbAG film.

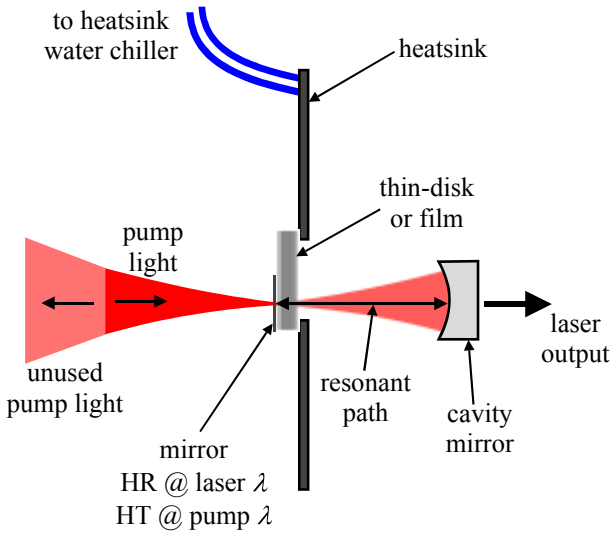

Figure 4.8.2: Coupled-cavity for a thin-disk laser.

The coupled-cavity arrangement utilises the occurrence of etalon cavities between the interfaces of the crystal. An external cavity is made using a flat mirror that transmits the pump wavelength but reflects the laser wavelength, and a curved mirror that reflects both the pump and laser wavelengths, but allows some of the laser wavelength to be transmitted as output. An advantage of such a cavity is that the pump light is passed through the device twice, but alignment is critical for it to overlap its original path through the crystal, and parallelism of the crystal interfaces is also critical for the etalon cavities to exist.

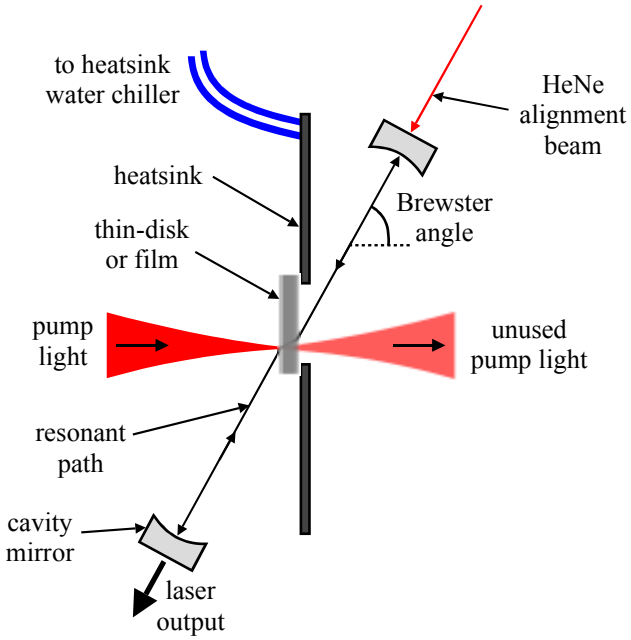

Figure 4.8.3: Brewster-angle-cavity for a thin-disk laser.

The Brewster-angle-cavity takes advantage of the fact that light polarised parallel to the plane of incidence is transmitted without any Fresnel reflection at the Brewster angle. The cavity is formed by two curved mirrors that must be set very precisely for lasing to be successful. A disadvantage of this cavity arrangement is that as the device thickness is scaled downwards, it becomes increasingly difficult to align the cavity mirrors. With smaller thicknesses, the pump light must be focussed more tightly for it to still be absorbed efficiently, and the volume of the gain region is therefore reduced. For lasing to occur, the resonant path between the two cavity mirrors must be aligned with the gain region and this task is much more difficult as the volume of the gain region is made smaller.

4.8.2 Absorption spectra and film losses

The absorption spectrum of the YbAG film was measured using a spectrophotometer and a polished blank YAG substrate was used as a reference. This allowed the absorption coefficient and an upper limit for the film transmission loss to be estimated.

4.8.3 Threshold power for lasing

The experimental arrangement shown in figure 4.8.1:B was used to detect the occurrence of lasing from the YbAG film. HeNe laser alignment beams were used to try and make the pumped volume and resonant path between the cavity mirrors coincide as closely as possible, before further adjustments were made to the alignment of the cavity mirrors.

4.9 Conclusions

- The technique of PLD has been described and some of the challenges involved in the growth of thick films have been discussed in detail. An improved substrate holder design allowed substrates to be heated with a homogeneous temperature distribution, and deposition using multiple growth runs and target reconditioning was found to be a route to thick film growth without the occurrence of particulates increasing significantly.

- The techniques used for the characterisation and preparation of films have been described and a limit was found for the thickness of waveguiding films, due to cracking at the polishing stage of preparation. The use of 1 mm thick substrates allowed thicker films to be polished without the substrate cracking, but difficulties were still experienced with films cracking.
- The experimental setups for waveguide and thin-disk laser cavities, and the techniques used for their qualitative analysis have been described. Some theory necessary for the derivation of properties such as propagation loss and launch efficiency has been discussed.

Chapter 5

Nd:GGG Film Results

5.1 Introduction

All of the results obtained from Nd:GGG films are presented in this chapter. Firstly, there is an overview of the results from basic material analysis that are the same or similar for each film. The lasing results from a 40 μm thick Nd:GGG film deposited in a single growth run and pumped with a Ti:sapphire laser are presented and discussed, along with the results from a 50 μm thick Nd:GGG film deposited using multiple growth runs and pumped with a Ti:sapphire laser, and subsequently with a laser diode array. Finally, the results obtained from self-imaging in a Nd:GGG film are presented and conclusions are drawn from all of the results.

5.2 General Nd:GGG film properties

5.2.1 Visual and optical microscopy comments

The deposition conditions were tuned sufficiently to allow perfectly clear films to be grown routinely. With increased target usage, particulates normally become large enough to be seen easily with the naked eye, however, restriction of growth runs to < 1.5 hours, and

reconditioning of the target surface allowed films to be grown without a significant amount of visible particulates on the film surface. The improved design of the substrate holder allowed the growth of high quality film across the whole substrate without any defect lines.

5.2.2 Structural and compositional results

5.2.2.1 Film thickness profiles

Figure 5.2.1 shows the thickness profile of a 135 µm thick film deposited in thirteen growth runs (the thickest Nd:GGG film grown). Figure 5.2.2 shows an example of a 2D thickness profile of a thin film (the 2D profiler wasn't available for the 135 µm thick film).

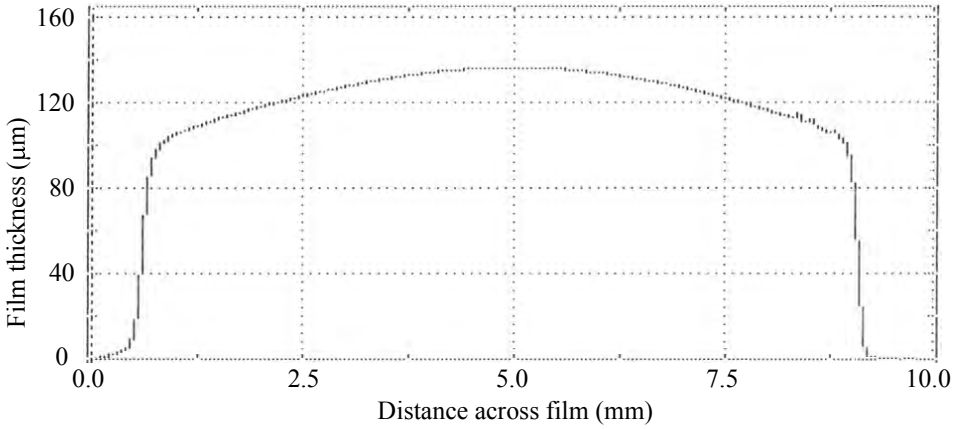

Figure 5.2.1: 1D thickness profile of a 135 µm thick Nd:GGG film.

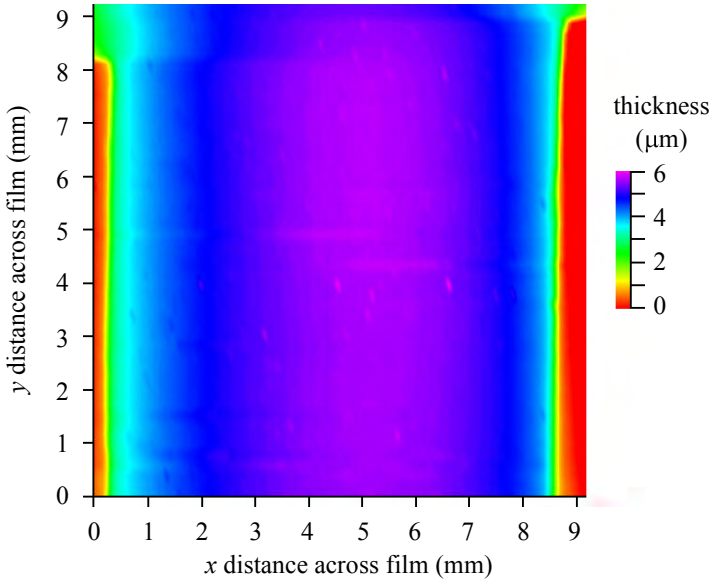

Figure 5.2.2: 2D thickness profile of a thin film.

5.2.2.2 X-ray diffraction spectra

Figure 5.2.3 shows an XRD spectrum of a typical thin Nd:GGG film where the substrate peaks are in evidence, and figure 5.2.4 shows some expanded views of the peaks so that the FWHM can be seen clearly. The peaks found from the XRD analysis represent the Nd:GGG (400), YAG (400), Nd:GGG (800) and YAG (800) orientations, and the absence of any other peaks confirms that the thick Nd:GGG films are highly textured crystal. Various properties of the spectrum are summarised in table 5.2.1 and the *D*-spacing values have been normalised using the positions of the YAG substrate peaks.

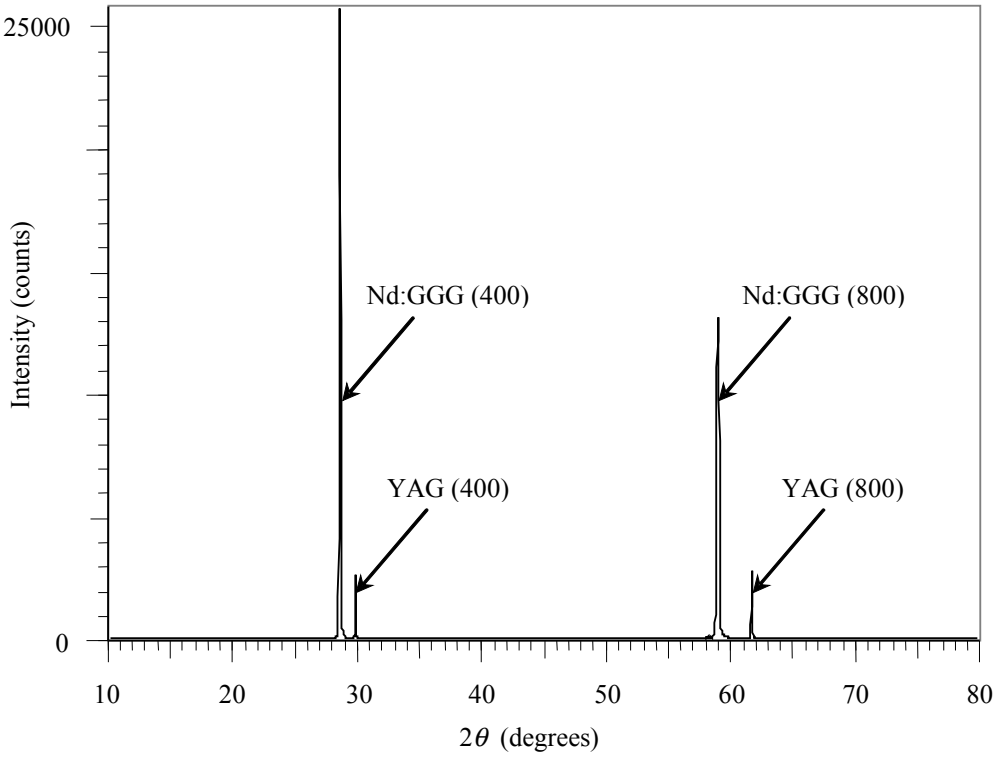

Figure 5.2.3: XRD spectrum of a typical thin Nd:GGG film where the YAG substrate peaks are in evidence.

Crystal (orientation)	2θ (degrees)	FWHM (degrees)	*D*-spacing (Å)	Normalised *D*-spacing (Å)	Database *D*-spacing (Å)
Nd:GGG (400)	28.578	0.11	3.121	3.126	3.0957 [50]
Nd:GGG (800)	59.063	0.23	1.563	1.562	1.5479 [50]
YAG substrate (400)	29.805	0.06	2.995	-	3.0015 [42]
YAG substrate (800)	61.798	0.08	1.500	-	1.5008 [42]

Table 5.2.1: Summary of the typical thin Nd:GGG film XRD spectrum properties.

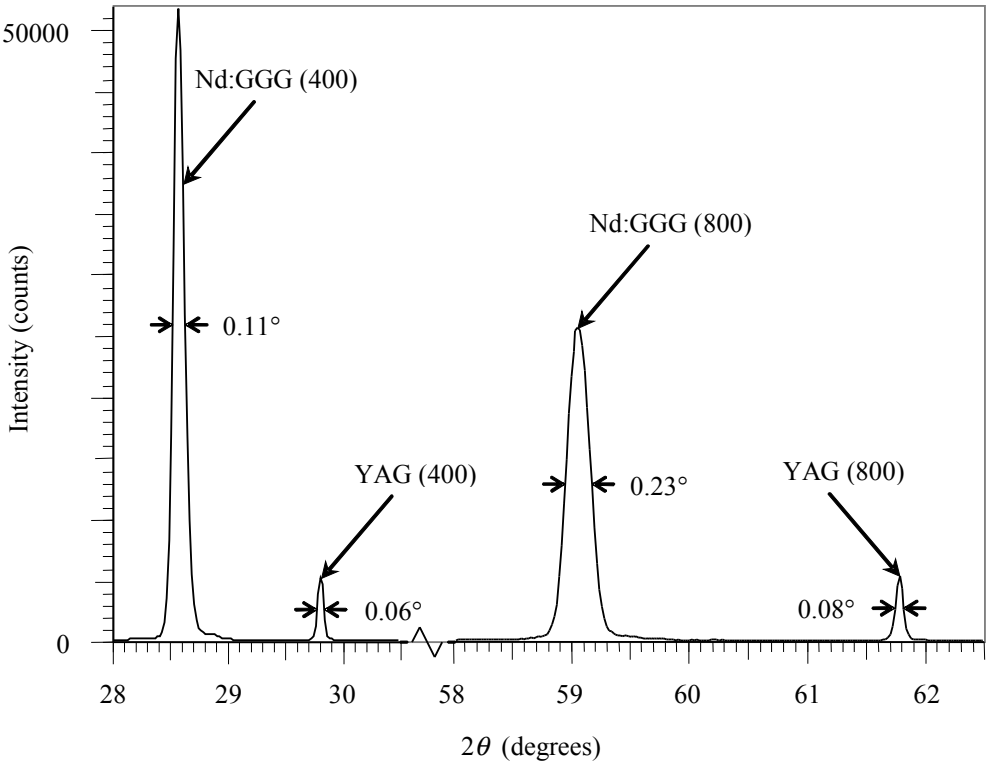

Figure 5.2.4: Expanded views of the XRD peaks of a typical thin Nd:GGG film where the substrate peaks are in evidence.

The normalised *D*-spacing values for the thin Nd:GGG film compare well to database values but are slightly shifted by 0.97% and 0.90% for the (400) and (800) orientations respectively. This shift is attributed to the effects of thermal expansion mismatch and slightly deficient stoichiometry. As the sample is cooled after deposition is completed, the YAG substrate shrinks at a different rate to the Nd:GGG film. We can use equation 3.2.12 to produce a rough value for the stress we expect to be produced by thermal expansion mismatch. Using the thermal expansion coefficients for bulk crystals shown in table 1.4.1, a temperature difference of -700 K and values for Young's modulus and Poisson's ratio of 300 GPa and 0.30 respectively (these values are actually for YAG because no data could be found for GGG, but the properties of GGG are expected to be similar and this substitution allows progress to be made with at least an order of magnitude estimate), a value of 0.3 GPa can be produced as an estimate for the stress induced by thermal expansion mismatch.

We can use equation 3.2.13 to produce an estimate of the actual stress in the film as measured by the shift in *D*-spacing values. Using values for Young's modulus and Poisson's ratio as above, a value of -5 GPa can be obtained for the actual stress in the film when the *D*-spacing value of the film is shifted by about 1% compared to bulk crystal. This is approximately an order of magnitude more than predicted by thermal expansion mismatch

and is also the opposite type of stress predicted by thermal expansion mismatch. It is difficult to know for sure what the origin of this stress is without further analysis of the films, but if the stress is all to be attributed to thermal expansion mismatch, we must conclude that the film does not have the same thermal expansion coefficient as bulk crystal. Otherwise we must conclude that another factor is involved with the occurrence of stress in the films, such as deficient stoichiometry to be discussed further in the next section.

The thin Nd:GGG (400) film peak FWHM compares well to the YAG (400) substrate but the Nd:GGG (800) peak FWHM is significantly worse. This is thought to be due to the interception of defects at the film-substrate boundary, and the garnet crystal structure; diffraction from the (800) planes is dependent on the *D*-spacing of adjacent p-planes and q-planes, whereas diffraction from the (400) planes is dependent on the *D*-spacing of p-planes and q-planes separately.

Figure 5.2.5 shows an XRD spectrum of a typical thick Nd:GGG film and figure 5.2.6 shows some expanded views of the peaks so that the FWHM can be seen clearly. Various properties of the spectrum are summarised in table 5.2.2 and the *D*-spacing values have been normalised using the positions of the YAG substrate peaks from a scan of a blank YAG substrate that was analysed under the same conditions as the thick Nd:GGG film.

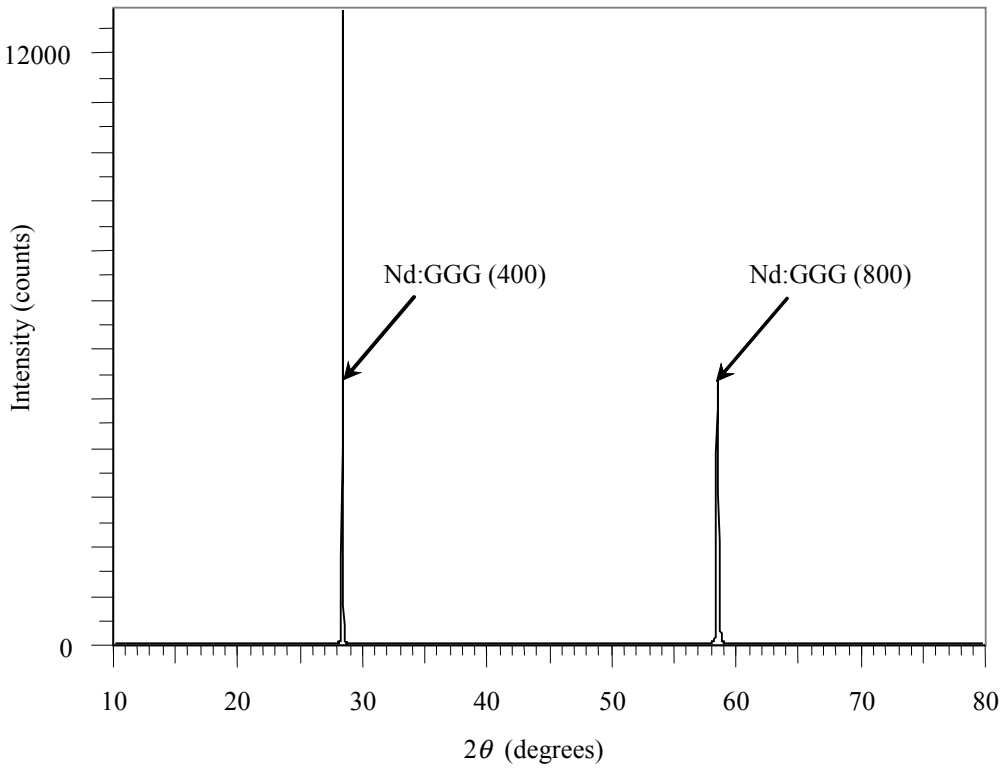

Figure 5.2.5: XRD spectrum of a typical thick Nd:GGG film.

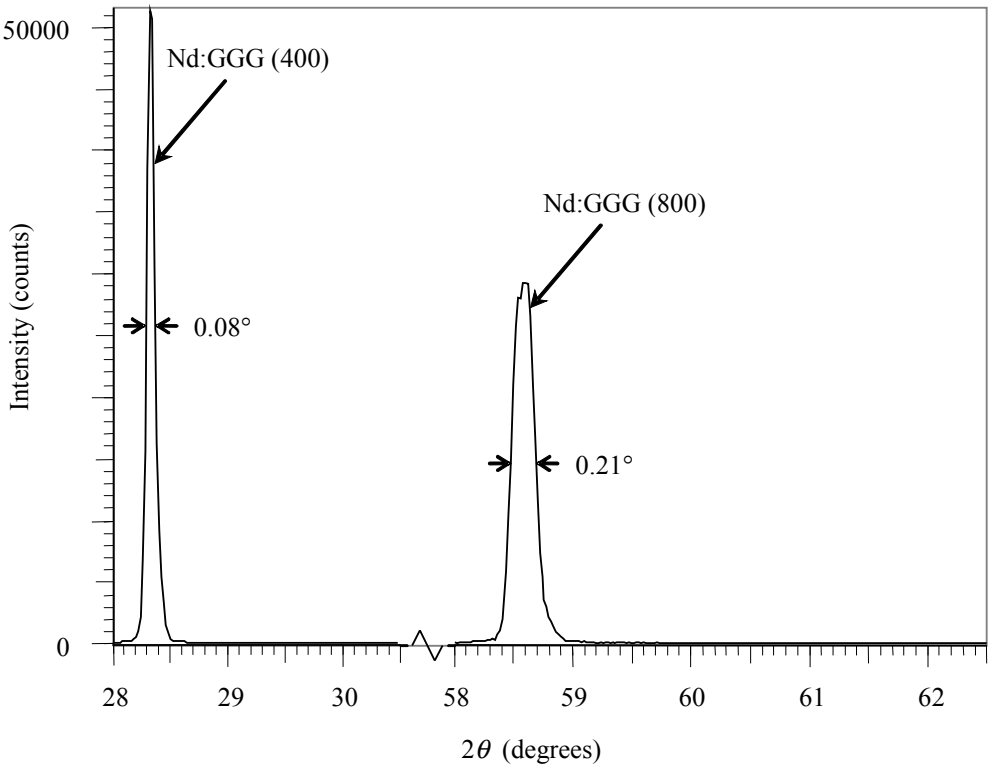

Figure 5.2.6: Expanded views of the XRD peaks of a typical thick Nd:GGG film.

Crystal (orientation)	2θ (degrees)	FWHM (degrees)	*D*-spacing (Å)	Normalised *D*-spacing (Å)	Database *D*-spacing (Å)
Nd:GGG (400)	28.318	0.08	3.149	3.150	3.0957 [50]
Nd:GGG (800)	58.582	0.21	1.574	1.573	1.5479 [50]
YAG substrate (400)	29.772	0.06	2.998	-	3.0015 [42]
YAG substrate (800)	61.776	0.07	1.501	-	1.5008 [42]

Table 5.2.2: Summary of the thick Nd:GGG film XRD spectrum properties.

The thick Nd:GGG film was grown on a 1 mm thick YAG substrate, whereas the thin film discussed previously was grown on a 0.5 mm thick YAG substrate. This seems to have changed the stress in the film, as the normalised *D*-spacing values for the thick Nd:GGG film are shifted by 1.7% and 1.6% for the (400) and (800) orientations respectively. The thick Nd:GGG film peak FWHM are improved and this is thought to be due to lattice relaxation and fewer defects away from the film-substrate boundary.

Figure 5.2.7 shows an XRD spectrum of a thick Nd:GGG film with a YAG cap, and figure 5.2.8 shows some expanded views of the peaks so that the FWHM can be seen clearly. Various properties of the spectrum are summarised in table 5.2.3 and the *D*-spacing values have been normalised using the positions of the YAG substrate peaks.

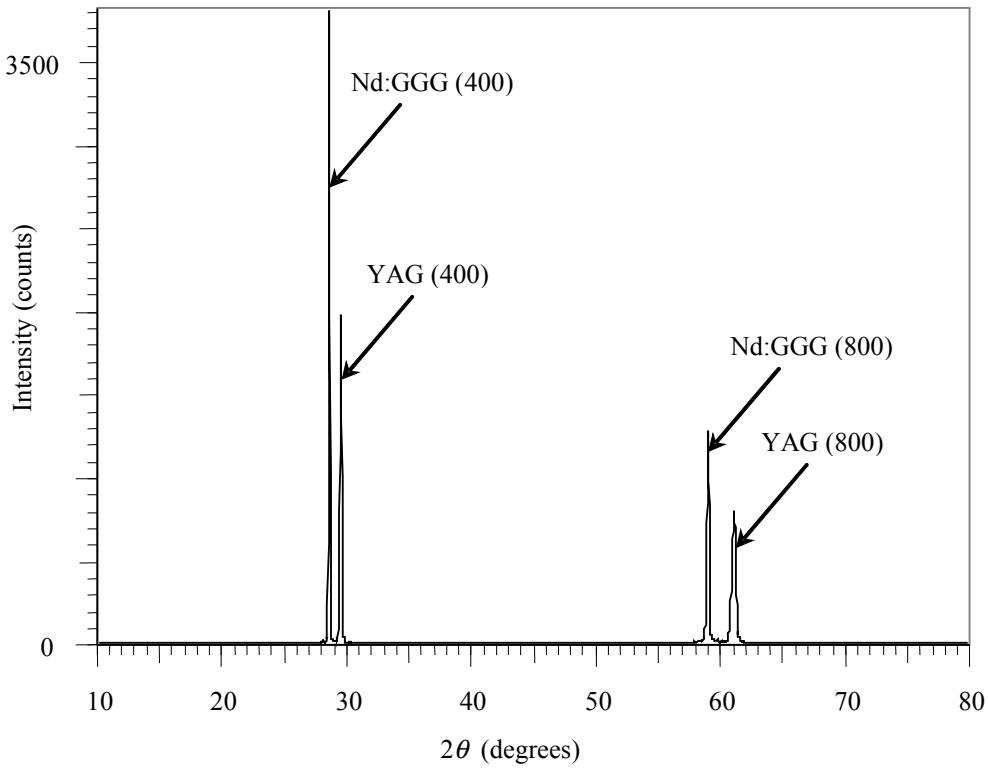

Figure 5.2.7: XRD spectrum of a YAG capped Nd:GGG film.

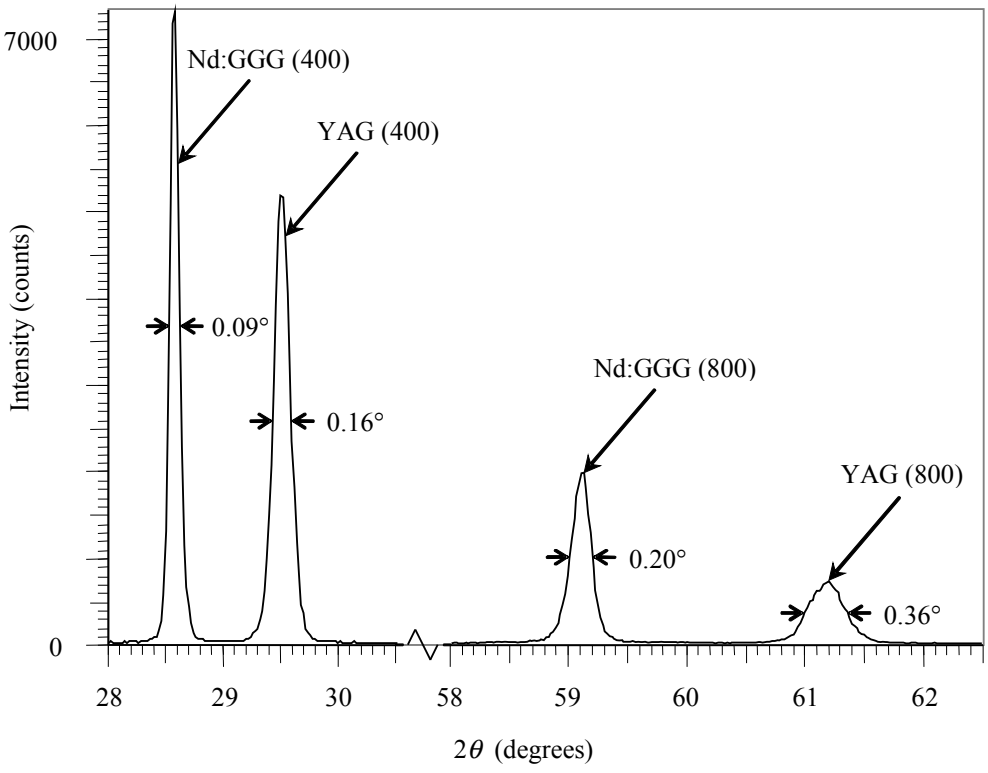

Figure 5.2.8: Expanded views of the XRD peaks of a YAG capped Nd:GGG film.

Crystal (orientation)	2θ (degrees)	FWHM (degrees)	*D*-spacing (Å)	Normalised *D*-spacing (Å)	Database *D*-spacing (Å)
Nd:GGG (400)	28.550	0.09	3.124	3.122	3.0957 [50]
Nd:GGG (800)	59.093	0.20	1.562	1.560	1.5479 [50]
YAG cap (400)	29.493	0.16	3.026	3.024	3.0015 [42]
YAG cap (800)	61.188	0.36	1.514	1.512	1.5008 [42]
YAG substrate (400)	29.740	0.06	3.002	-	3.0015 [42]
YAG substrate (800)	61.754	0.07	1.501	-	1.5008 [42]

Table 5.2.3: Summary of the YAG capped Nd:GGG film XRD spectrum properties.

The thick Nd:GGG film with a YAG cap was grown on a 0.5 mm thick YAG substrate and is therefore a good test of the consistency of observations made about the previous two films. The normalised *D*-spacing values for the Nd:GGG layer are shifted by 0.84% and 0.78% for the (400) and (800) orientations respectively, and this supports the proposition that the shifting of these values is dependent on the substrate thickness. The shift of the Nd:GGG *D*-spacings is slightly less than for the thin Nd:GGG film grown on a 0.5 mm thick substrate, and this may be an indication that stress in the film is easing and the film lattice is relaxing away from the film-substrate boundary. The normalised *D*-spacing values for the YAG layer are shifted by 0.73% for both the (400) and (800) orientations. The Nd:GGG layer peak FWHM are very similar to the previously discussed thick film, and this supports the proposition that lattice relaxation and fewer defects away from the film-substrate boundary are being observed when thick films are analysed. The YAG layer peak FWHM are significantly worse and this is due to the interception of defects at the YAG cap-Nd:GGG layer boundary, and a deficient stoichiometry.

5.2.2.3 Energy dispersive X-ray analysis

Thin, thick and YAG capped Nd:GGG films were analysed using the EDX technique, and pieces of bulk crystal were analysed at the same time under the same conditions to allow the error in the technique to be estimated. Unfortunately, the results for oxygen content proved to be too inaccurate to be of use; this is understandable because there was only one peak at a relatively low energy for the software package to use to estimate the stoichiometry. Figures 5.2.9 and 5.2.10 show examples of typical EDX spectra of Nd:GGG and YAG respectively. Some of the gadolinium peak positions overlap gallium peak positions.

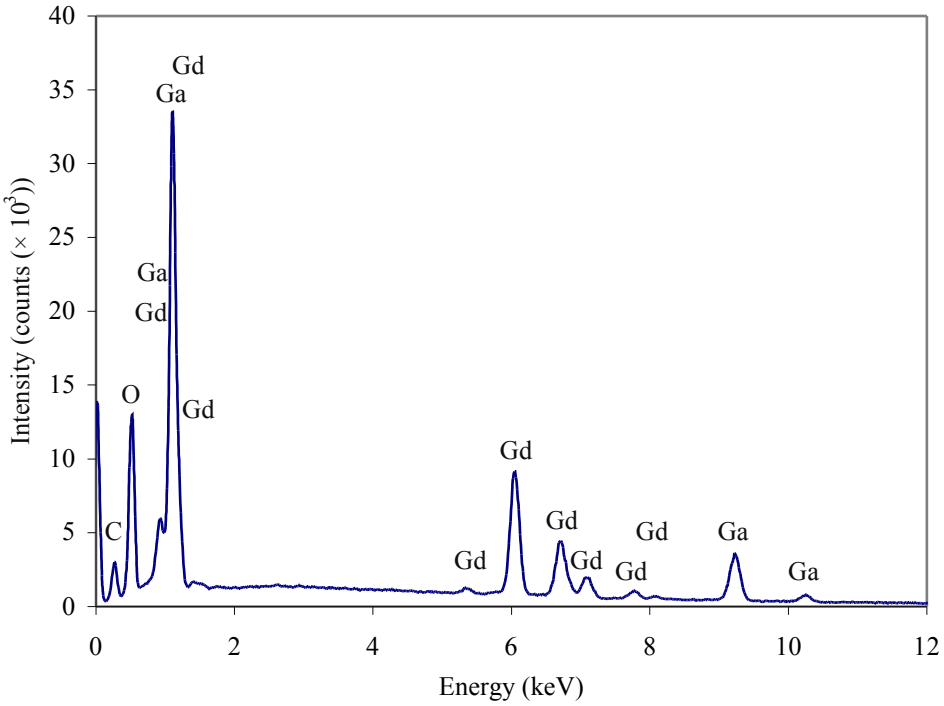

Figure 5.2.9: EDX spectrum of Nd:GGG.

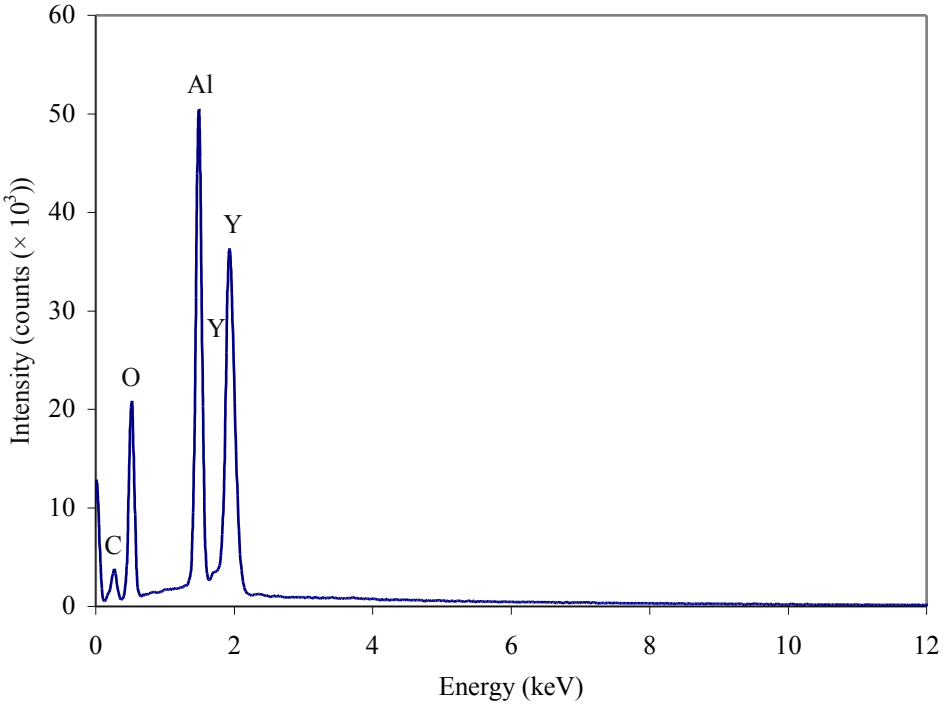

Figure 5.2.10: EDX spectrum of YAG.

Each sample was analysed five times at different locations on the sample surface and an average was taken of the results. Since the oxygen content results were unreliable, only the ratios of the elements other than oxygen are presented below in table 5.2.4. The error was estimated from the results of the analysis of bulk crystals.

Sample analysed	Ratio of elements other than oxygen
Thin Nd:GGG film	$Gd_3Ga_{3.8 \pm 0.2}$
Thick Nd:GGG film	$Gd_3Ga_{3.9 \pm 0.2}$
YAG capping layer	$Y_3Al_{4.0 \pm 0.2}$
Bulk Nd:GGG	$Gd_3Ga_{4.8 \pm 0.2}$
Bulk YAG	$Y_3Al_{5.2 \pm 0.2}$

Table 5.2.4: EDX results for the Nd:GGG films.

The Nd:GGG films are both gallium deficient by a similar amount, and this shows that the deposition of thick films using multiple growth runs doesn't appear to affect the stoichiometry significantly. Also, the YAG capping layer is aluminium deficient. It is thought that the deficiency in the stoichiometry of both the Nd:GGG and YAG causes the broadening of the peaks observed from XRD analysis, and that the deficient lattice sites intrinsically affect diffraction from the (800) planes more than the (400) planes.

5.2.2.4 Rutherford backscattering analysis

Backscattering analysis was performed (by M. J. F. Healy, Ion Beam Analysis Facility, Cranfield University) on a wedge-polished Nd:GGG film sample that was deposited in multiple growth runs, to determine the stoichiometry uniformity of the film throughout its thickness. Figure 5.2.11 shows the thickness profile of the sample used for RBS analysis.

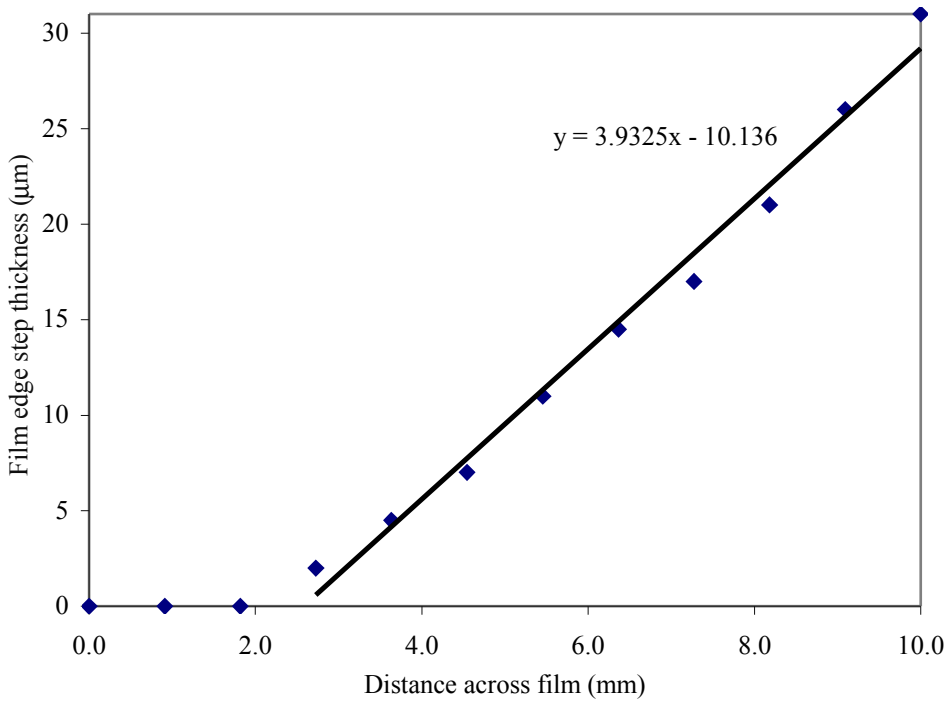

Figure 5.2.11: Thickness profile of the sample used for RBS analysis.

Figures 5.2.12 and 5.2.13 respectively show the helium and proton backscattering spectra at seven points at 1 mm intervals along the film. The three leading edges in the spectra correspond to gadolinium, gallium and oxygen present at the surface, the edge heights give surface concentration, and the plateau height below the energy of each edge gives shallow depth information. Gd:Ga ratios were derived from the top 0.2 µm of the exposed surface whereas oxygen concentrations were derived over 3 µm, due to the greater range of protons. The slight shift in energy of the front edges with increased thickness is consistent with surface charging of the sample. The proton yields for the 3 mm and 4 mm data in figure 5.2.13 drop off at low energies, which is due to the substrate and is an indication that the protons' range is great enough that they reach the substrate at these points.

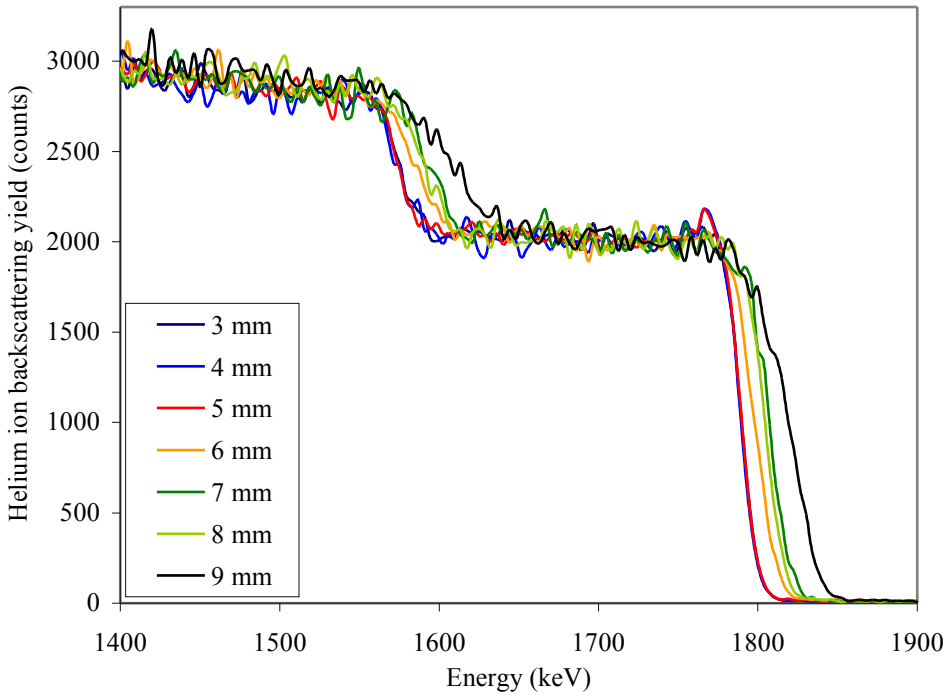

Figure 5.2.12: Helium ion backscattering spectra for analysis performed at various different points along the sample which correspond to different thicknesses.

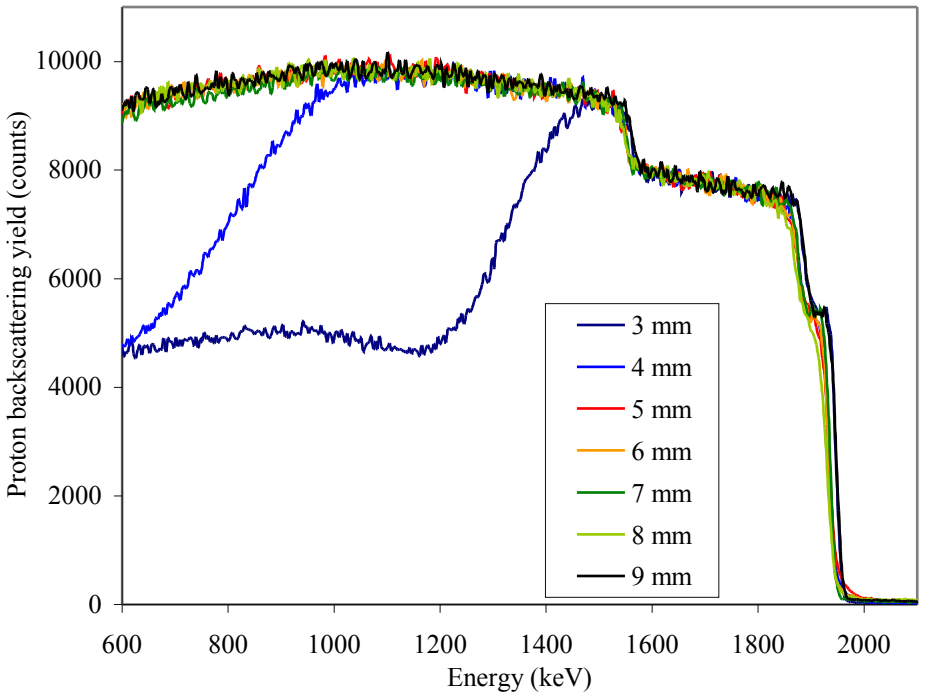

Figure 5.2.13: Proton backscattering spectra for analysis performed at various different points along the sample which correspond to different thicknesses.

Figure 5.2.14 shows the Gd:Ga ratio and figure 5.2.15 shows the oxygen content in atomic percent calculated from the backscattering analysis as a function of distance along the film.

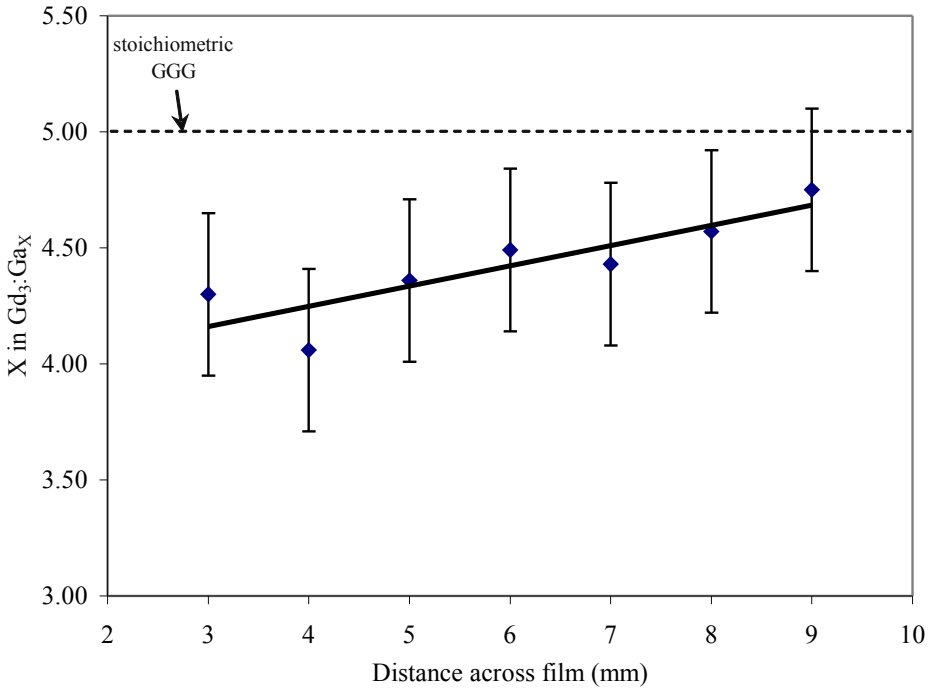

Figure 5.2.14: Gd:Ga ratios derived from the helium ion backscattering spectra.

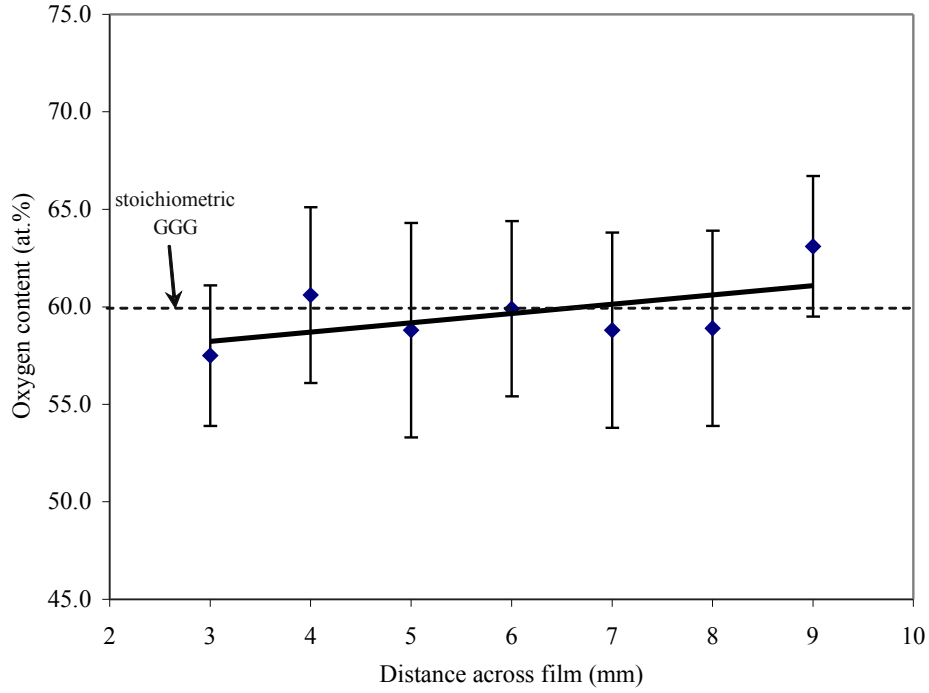

Figure 5.2.15: Oxygen contents derived from the proton backscattering spectra.

The Gd:Ga ratio and the oxygen content are both consistent throughout the film thickness and growth run layers. If X = 4.4 is taken as an average value of the X in $Gd_3:Ga_X$ and 60% is taken as an average value for the oxygen content in atomic percent, we can estimate an empirical formula of (Nd:)$Gd_3Ga_{4.4}O_{11.1}$ for the thick Nd:GGG film. There appears to be a slight positive trend in the Gd:Ga ratio results which may indicate that the Nd:GGG film grows gallium deficient close to the YAG substrate-Nd:GGG film boundary to accommodate for the lattice mismatch and then the gallium content recovers as the lattice relaxes further away from the substrate.

Both EDX and RBS analysis have shown that the films are gallium deficient, yet XRD results suggest that the films have still grown as an $A_3B_2C_3O_{12}$ (where B = C) garnet phase. This could mean that some gadolinium ions are located in gallium lattice sites, making a stoichiometry such as $Gd_{3.4}Ga_{4.6}O_{12}$. Gadolinium has a larger ionic radius than gallium, and such a stoichiometry would produce a large amount of strain in the crystal. This would explain the discrepancy between the stress measured in the film and the stress expected due to thermal expansion mismatch. Another possibility is that there are vacancies in the crystal lattice where the missing gallium would have been located. It may be the case that vacancies are tolerated by the crystal more easily than gadolinium ions in alternative lattice sites. These kinds of deficiencies in the crystal structure mean that laser ions in the crystal experience slightly different crystal fields, and this leads to broadening of the spectroscopic properties of the films.

5.2.3 Optical properties

5.2.3.1 Absorption spectra

Figure 5.2.16 shows the absorption spectrum of a thick Nd:GGG film compared to that of bulk Nd:GGG for the wavelength region 790-830 nm; the absorption coefficient α_p can be read directly from the graph. The maximum of the absorption coefficient at a wavelength of 808 nm has been found to be typically 2.64 cm^{-1} for the thick Nd:GGG films. This is significantly lower than the value of 4.53 cm^{-1} at a wavelength of 808 nm measured for the Nd:GGG target, and therefore it can be concluded that the cross-section and/or the Nd^{3+} concentration of the thick Nd:GGG films is not the same as the Nd:GGG target. This can likely be attributed to imperfect crystal structure and stoichiometry as already suggested from the results of the structural and compositional analysis. It is also likely that some Nd^{3+} may have been lost in the deposition process, an effect that has been observed for previous

depositions incorporating the dopants Nd^{3+} and Ti^{3+} [78]. Some of the thick Nd:GGG film absorption peaks are shifted relative to bulk. This is due to the slightly different crystal field seen by laser ions as a result of the deficient crystal structure and stoichiometry.

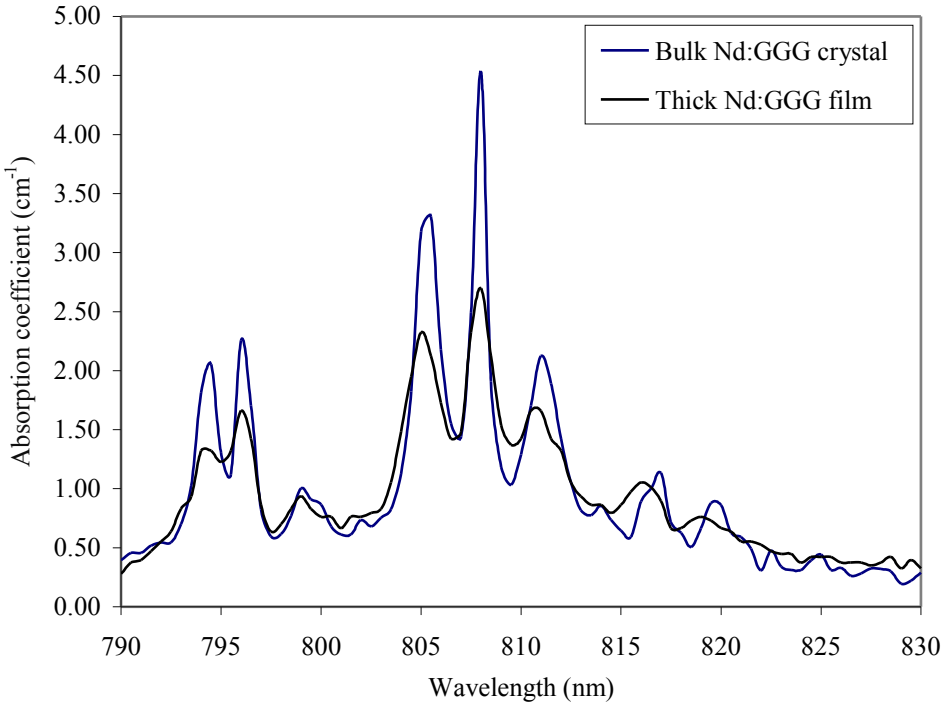

Figure 5.2.16: Absorption spectrum of a thick Nd:GGG film compared to that of bulk Nd:GGG crystal for the wavelength region 790-830 nm.

5.2.3.2 Fluorescence spectra

Figures 5.2.17 and 5.2.18 show typical fluorescence spectra of the thick Nd:GGG films compared to a thin Nd:GGG film grown previously [18] and bulk Nd:GGG crystal for the wavelength region 1045-1080 nm, and compared to bulk Nd:GGG crystal for the wavelength region 920-950 nm. The fluorescence spectra are normalised to have the same area under the curves so that the comparison is effectively based on the same number of laser ions in each case. The fluorescence spectra obtained from our thick Nd:GGG films appear slightly broadened and some peaks are shifted relative to bulk. This is due to the different crystal field present at different laser ion lattice sites caused by the deficient crystal structure and stoichiometry. Our thick Nd:GGG film fluorescence spectra however are much closer to bulk than the previously reported thin Nd:GGG film grown by PLD [18].

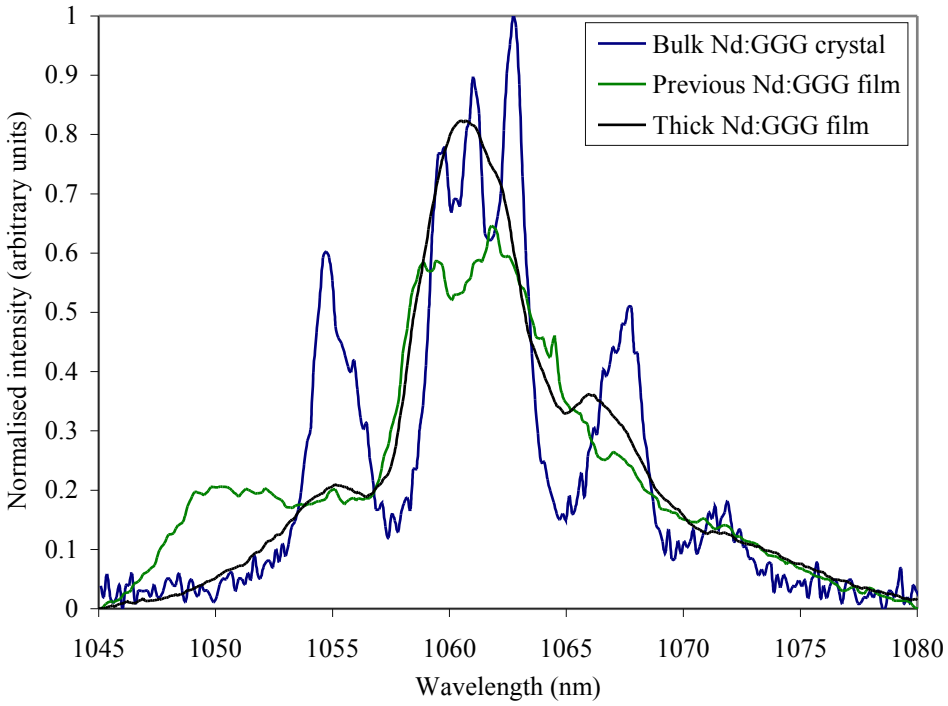

Figure 5.2.17: Typical thick Nd:GGG film fluorescence spectrum compared to bulk Nd:GGG crystal and a previously reported thin Nd:GGG film [18] for the wavelength region 1045-1080 nm.

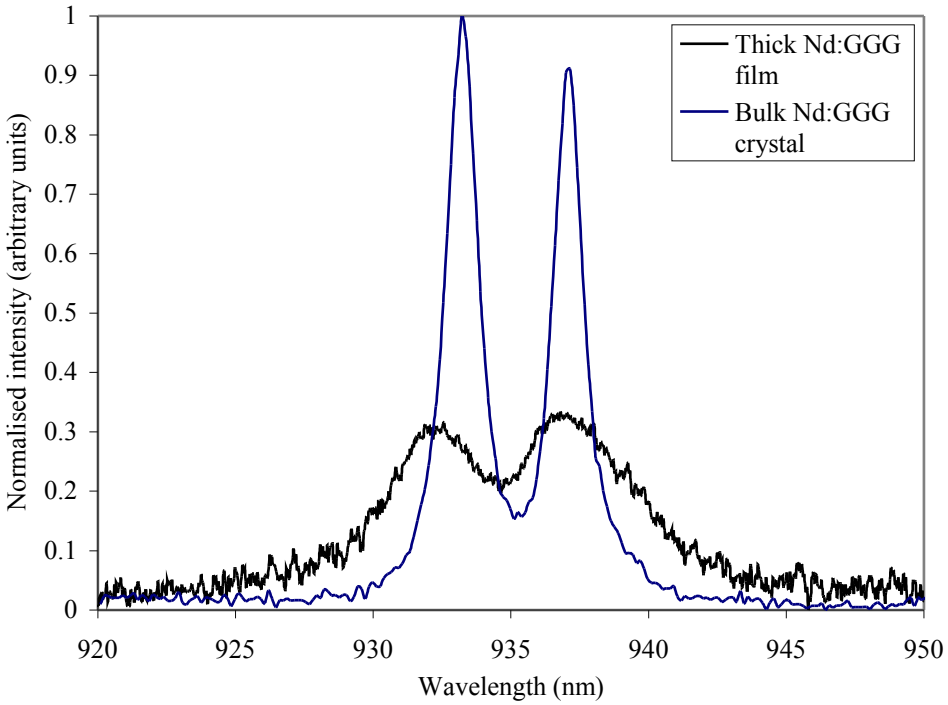

Figure 5.2.18: Typical thick Nd:GGG film fluorescence spectrum compared to bulk Nd:GGG crystal for the wavelength region 920-950 nm.

5.2.4 Conclusions

- The deposition conditions have been tuned sufficiently for the growth of 'water clear' films to be routine.
- XRD analysis has found that the crystal lattice relaxes slightly as films get thicker and X-rays can no longer penetrate deep enough to reach the film-substrate boundary where the occurrence of defects is likely to be higher than elsewhere.
- The crystal lattice size of films has been found to be shifted depending on the thickness of the substrate used, and this is thought to be due to the effect of thermal expansion mismatch and/or stress produced by the deficient stoichiometry.
- EDX and RBS analysis have found the composition of Nd:GGG films to be slightly gallium deficient and YAG capping layers to be slightly aluminium deficient.
- Optical analysis has found the film absorption and fluorescence peaks to be broadened and sometimes shifted and this is thought to be due to the slightly deficient crystal structure and stoichiometry.
- The method of depositing thick films by multiple growth runs is now established and it has been shown by structural and compositional analysis that this method is not detrimental to film quality.

5.3 Ti:sapphire pumping

A 40 μm thick film made in a single growth run and a 50 μm thick film made in multiple growth runs were pumped by a Ti:sapphire laser and lasing was observed from both devices (laser experiments with the 40 μm thick film were performed in collaboration with C. Grivas, ORC, University of Southampton). The 40 μm thick film was end-polished (in collaboration with C. Grivas, ORC, University of Southampton) to allow launching of the Ti:sapphire laser beam, whereas the 50 μm thick film was end-polished and face-polished to create an ideal parallel slab geometry. The 40 μm thick film was polished to 4.1 mm in length to make it optimal for end-pumping by the Ti:sapphire laser, whereas the 50 μm thick

film was polished to 7.0 mm in width to make it optimal for double side-pumping by diode laser arrays. Minimal polishing of the 50 μm thick film length was desirable to match the waveguide faces as closely as possible to the 1 mm wide diode laser array output, but while attempting to polish out several cracks the length was reduced to 7.1 mm and polishing of these third and fourth sides had to be abandoned because cracking could not be prevented.

5.3.1 Threshold power for lasing

Table 5.3.1 shows the absorbed pump power thresholds for lasing of the 40 μm thick device with different transmittance output coupling mirrors.

Output coupler transmittance (at the laser wavelength)	**Absorbed power threshold for lasing (mW)**
0.15% (HR)	17.8
1.90%	40.9
2.00%	36.1
4.75%	54.0
12.86%	134.0

Table 5.3.1: Absorbed pump power thresholds for the 40 μm thick device with different transmittance output coupling mirrors and Ti:sapphire pumping.

The threshold obtained with a 1.90% transmittance output coupling mirror is higher than expected. Table 5.3.2 shows the absorbed pump power thresholds for lasing of the 50 μm thick device with different transmittance output coupling mirrors.

Output coupler transmittance (at the laser wavelength)	**Absorbed power threshold for lasing (mW)**
0.15%	27.4
1.90%	60.9
2.00%	52.8
4.75%	35.6
12.86%	64.3
21.80%	74.6
24.30%	98.8
29.30%	110.2
30.70%	104.5

Table 5.3.2: Absorbed pump power thresholds for the 50 μm thick device with different transmittance output coupling mirrors and Ti:sapphire pumping.

The thresholds obtained with 1.90%, 2.00% and 29.30% transmittance output coupling mirrors are higher than expected. It is thought that higher thresholds than expected are due to poor mirror alignment, and lower thresholds would have eventually been observed if more attempts were made at lasing with these mirrors. The thresholds obtained with higher output coupling mirrors for the 50 μm thick film are lower than for the 40 μm thick film, whereas the thresholds for low output coupling mirrors are higher for the 50 μm thick film than for the 40 μm thick film. This is a further indication that an optimal alignment may not have been obtained with the low transmittance output coupling mirrors in the case of the 50 μm thick film, since the difference in the round-trip losses (discussed later) of the two devices is not sufficient enough to be responsible for this effect. Also, this suggests there was a significant difference in the material or modal properties of the devices.

5.3.2 Laser spectra

Figures 5.3.1 and 5.3.2 show typical laser spectra for a pump power close to threshold and pump powers well above threshold respectively.

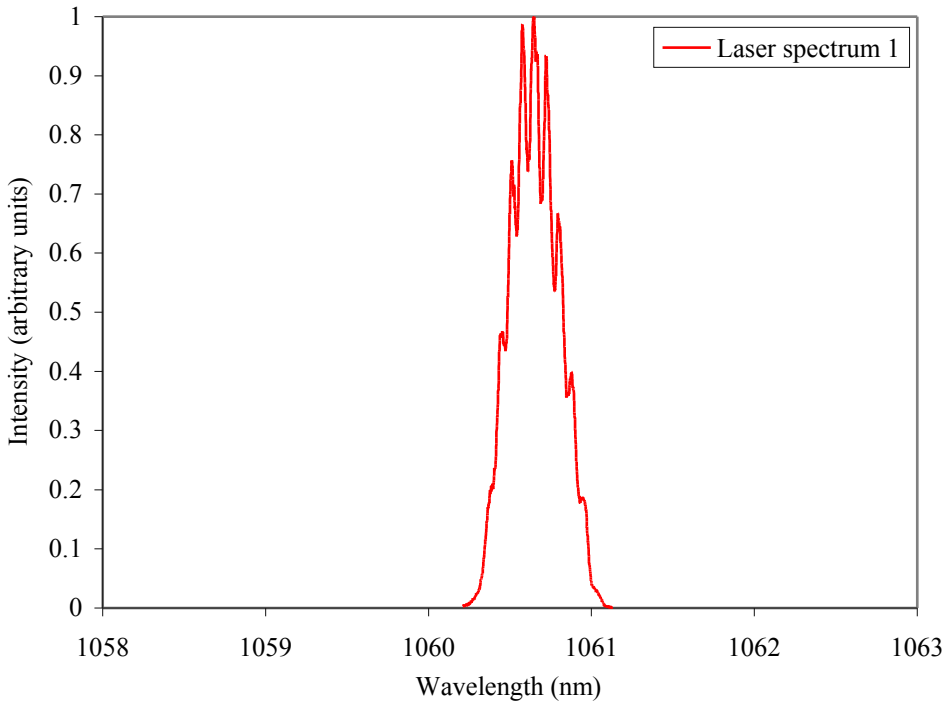

Figure 5.3.1: Typical laser spectrum obtained from the thick Nd:GGG films at just above the threshold for lasing using Ti:sapphire pumping.

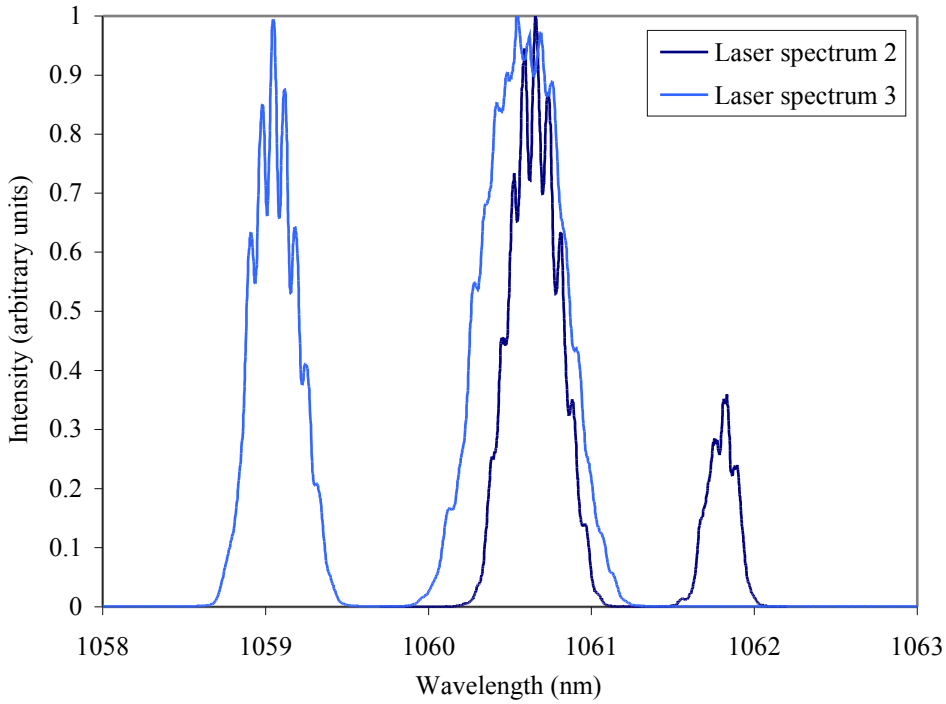

Figure 5.3.2: Typical laser spectra obtained from the thick Nd:GGG films for pump powers well above threshold using Ti:sapphire pumping.

Three distinct spectral gain regions can be observed. Lasing action has occurred centred at a wavelength of 1060.6 nm for pump powers close to threshold, and this central gain region is aligned with the centre of the peak fluorescence observed previously. At pump power levels well above threshold, lasing occurred centred at wavelengths of 1059.1 nm, 1060.6 nm and 1061.8 nm, and the existence of the two other gain regions suggests that the central fluorescence peak at a wavelength of 1060.6 is actually made up of three peaks as in the bulk Nd:GGG crystal case, but this finer detail wasn't observed in the fluorescence spectrum. Ripples can be observed in all of the laser spectra of periodicity 0.07 nm, which is consistent with the calculated expected longitudinal mode spacing of 0.0702 nm.

5.3.3 Slope efficiencies

Figures 5.3.3 and 5.3.4 show the slope efficiencies obtained with the 40 µm thick film and the 50 µm thick film respectively. Slope efficiencies of 12.5% and 17.5% were obtained for the 40 µm thick film with the 2.00%T and 4.75%T output coupling mirrors respectively, and slope efficiencies of 14.6% and 32.0% were obtained for the 50 µm thick film with the 4.75%T and 21.8%T output coupling mirrors respectively.

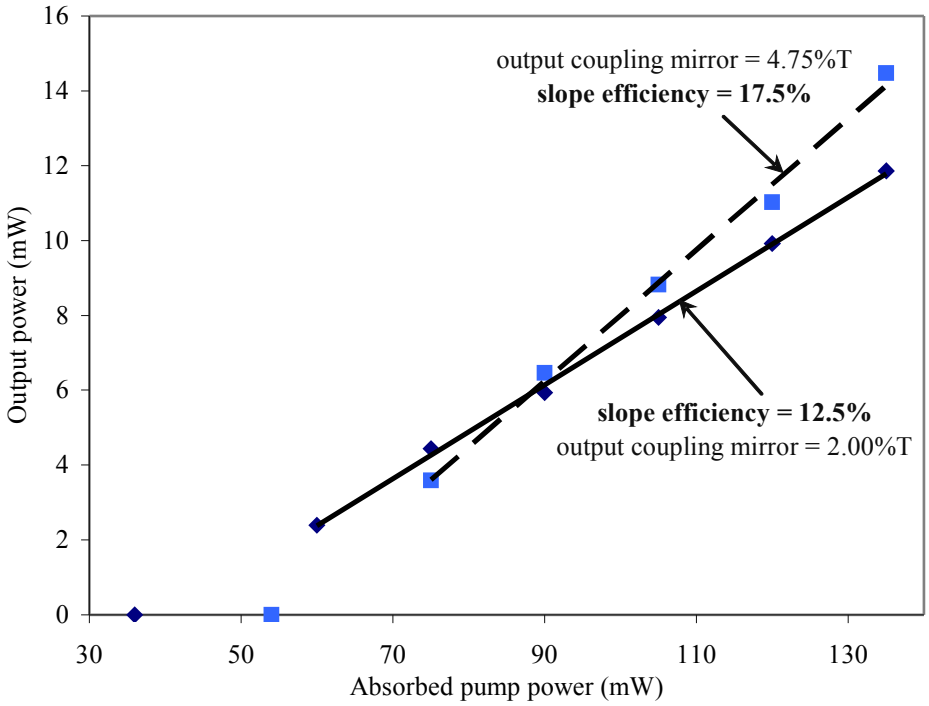

Figure 5.3.3: Slope efficiencies obtained with Ti:sapphire pumping of the 40 µm thick device.

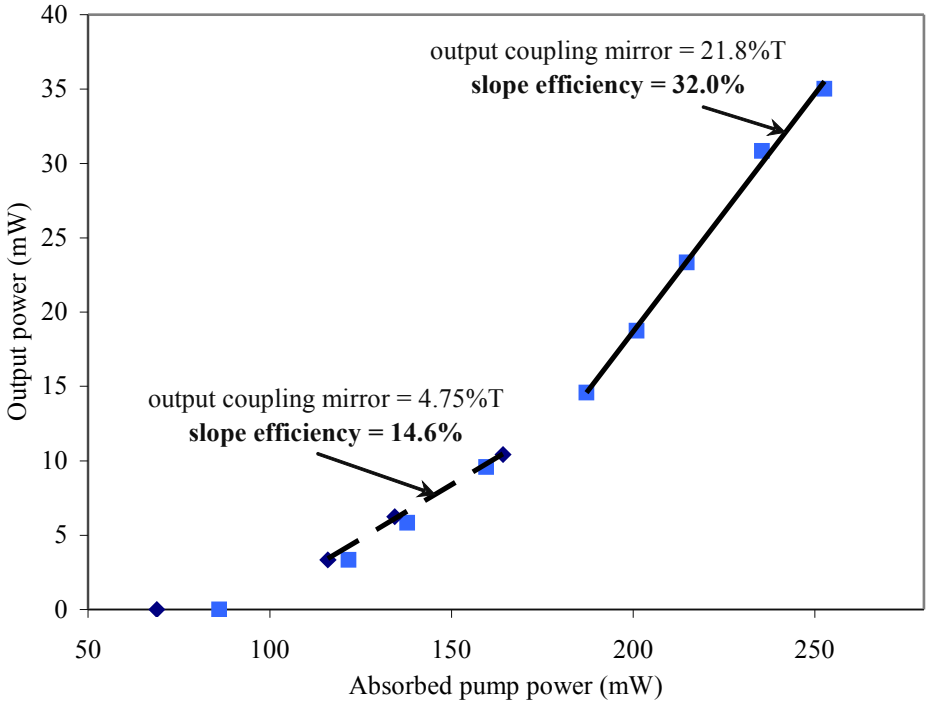

Figure 5.3.4: Slope efficiencies obtained with Ti:sapphire pumping of the 50 µm thick device.

The slope efficiencies obtained for the two devices with the 4.75%T output coupling mirror are different. We can therefore deduce (from equation 3.4.10) that one, some or all of the following properties must be different in the two devices: propagation loss, quantum efficiency, or spatial overlap of the pump and laser beam. The quantum efficiency is expected to be similar for the two devices since the same pump laser was used and the films were grown with similar deposition conditions which seems to agree with the results from laser thresholds; the modal properties therefore of lasing in the two devices must provide the reason for this difference.

5.3.4 Beam profiles

Figure 5.3.5 shows an image of the laser output beam profile from the 40 μm thick device, taken with the pump power well above threshold. The laser output is clearly multimode in the guided direction, with three lobes parallel to the unguided plane, and may also be multimode in the unguided direction. The laser output has filled the thickness of the film and has a diameter of about 40 μm in the guided direction.

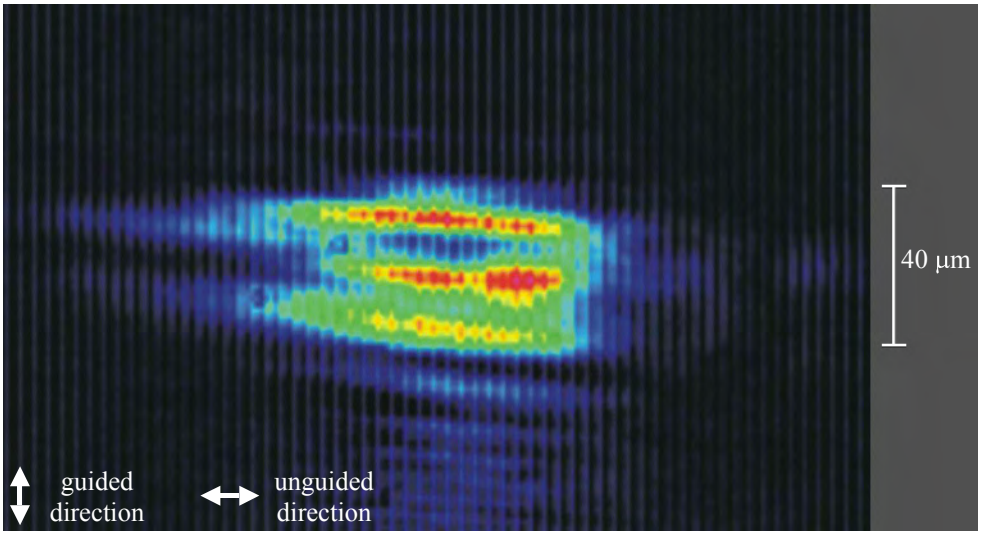

Figure 5.3.5: Laser output beam profile obtained from the 40 μm thick device using Ti:sapphire pumping.

Figure 5.3.6 shows an image of the laser output beam profile from the 50 μm thick device, taken with the pump power well above threshold. The laser output appears to be single-mode in both the guided and unguided directions, and has not filled the full thickness of the film, having a diameter of about 20 μm in the guided direction. The output could be made to convert to multimode by changing the launch height of the pump beam. The

difference in the modal output is in agreement with the observations made from the results with threshold powers for lasing and slope efficiencies of the two devices. It is thought that single-mode operation was possible in the case of the 50 μm thick device because the increased thickness and more ideal parallel interfaces allowed the pump beam to be guided without its modal properties becoming as distorted as in the case of the 40 μm thick device.

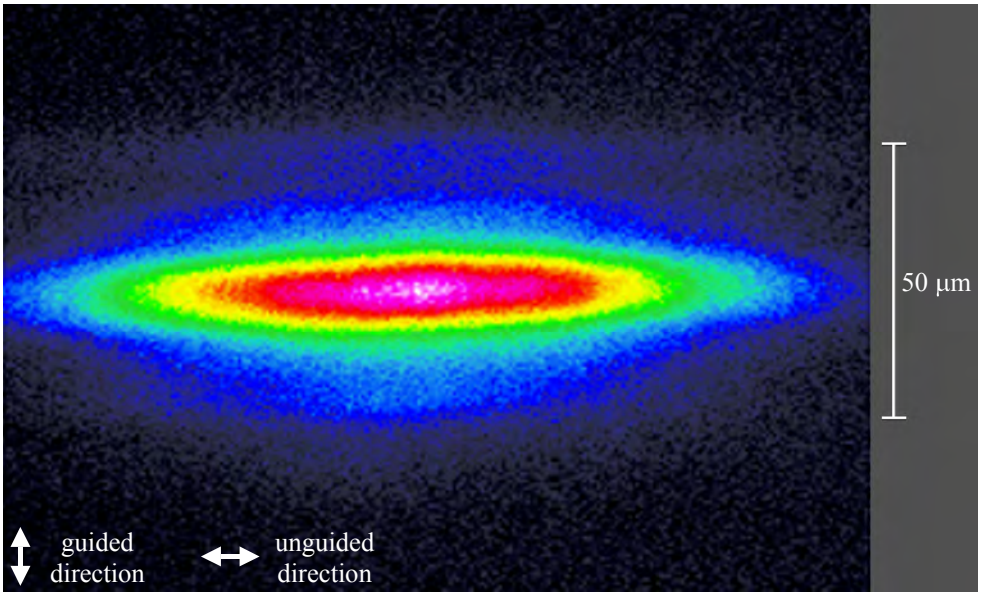

Figure 5.3.6: Laser output beam profile obtained from the 50 μm thick device using Ti:sapphire pumping.

5.3.5 Propagation losses

Figures 5.3.7 and 5.3.8 show the results of the Findlay-Clay loss experiments with the 40 μm thick and 50 μm thick films respectively. The Findlay-Clay loss experiments yield estimations of 0.095 $dBcm^{-1}$ and 0.37 $dBcm^{-1}$ for the propagation losses of the 40 μm thick and 50 μm thick devices respectively.

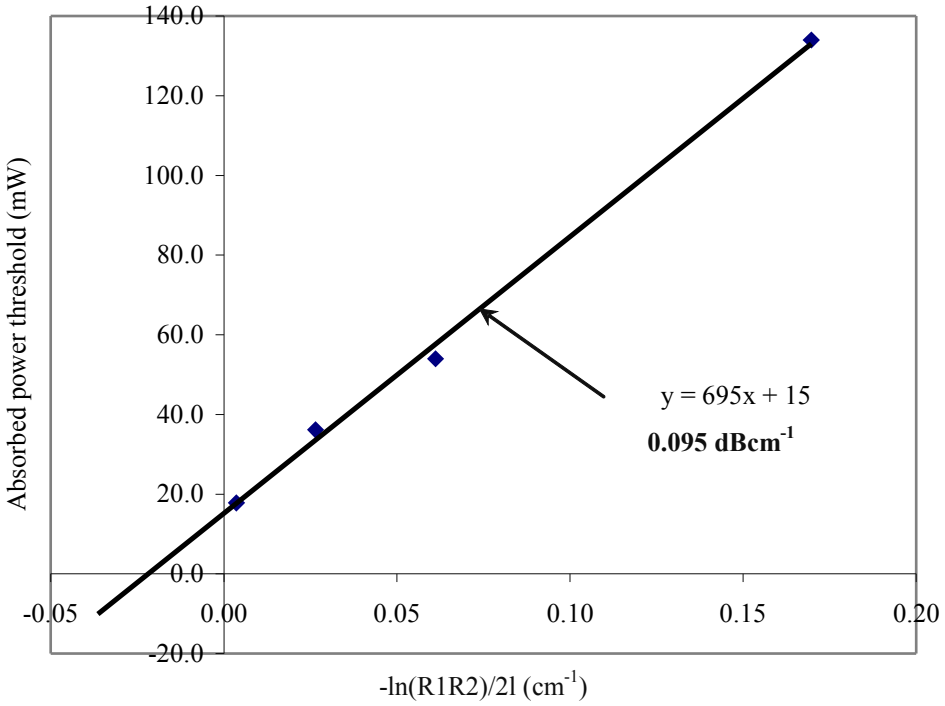

Figure 5.3.7: Findlay-Clay loss experiment results for the 40 µm thick device using Ti:sapphire pumping.

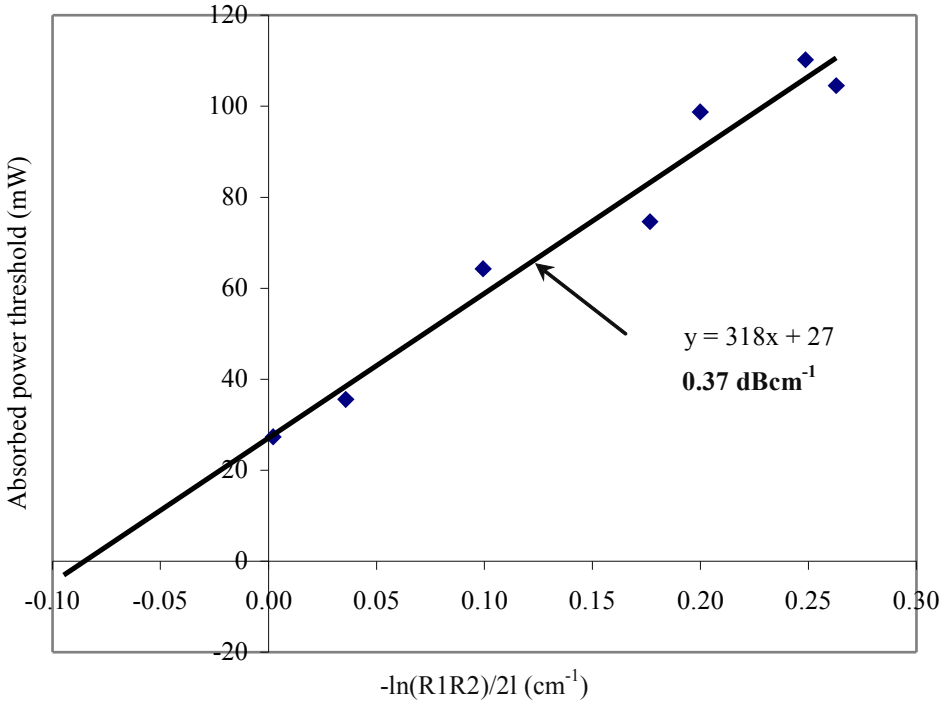

Figure 5.3.8: Findlay-Clay loss experiment results for the 50 µm thick device using Ti:sapphire pumping.

Since two different slope efficiencies were obtained for each device, the estimation of loss from slope efficiencies using equation 4.7.8 was possible. The slope efficiencies obtained for the 40 μm thick device produce an estimate of 0.094 $dBcm^{-1}$, suggesting that the spatial overlap of the pump and laser beams was very similar when using the two different output coupling mirrors. The slope efficiencies obtained for the 50 μm thick device produce an estimate of 0.31 $dBcm^{-1}$, suggesting that the spatial overlap of the pump and laser beams may have been slightly different using the two different output coupling mirrors, or the Findlay-Clay loss estimation may have been an overestimate of the loss.

The values of loss obtained with the two devices approach the value of loss for bulk garnet crystals, which is reported to be ~ 0.03 $dBcm^{-1}$ [258], and the loss of 0.094 $dBcm^{-1}$ obtained with the 40 μm thick film is the lowest loss reported to date for a waveguide grown by PLD, to the best of our knowledge. It is unclear why the loss of the 50 μm thick film is higher than the 40 μm thick film. This may be because the films were deposited with slightly different growth conditions.

Using equation 4.7.7, the two values for slope efficiency can be combined to eliminate the loss and calculate the other unknowns, quantum and overlap efficiency. This calculation was performed and the combined quantum and overlap efficiency was found to be 32% and 59% for the 40 and 50 μm thick devices respectively. Since we expect the quantum efficiencies to be similar, this is in agreement with results discussed previously that suggested the spatial overlap of the pump and laser beams was very different for the two devices.

5.3.6 Conclusions

- Lasing was achieved in two devices using Ti:sapphire pumping; minimum threshold pump powers of 17.8 mW and 27.4 mW were observed for the 40 μm thick and 50 μm thick devices respectively.
- Three distinct spectral gain regions were observed, indicating that the central fluorescence peak at a wavelength of 1060.6 nm is actually made up of three peaks as in the bulk Nd:GGG crystal case.
- Slope efficiencies of 12.5% and 17.5% were obtained for the 40 μm thick device, and 14.6% and 32.0% were obtained for the 50 μm thick device.
- Multimode output was observed from the 40 μm thick device, whereas single-mode output was observed from the 50 μm thick device.

- Loss estimates of 0.095 $dBcm^{-1}$ and 0.094 $dBcm^{-1}$ were obtained for the 40 μm thick device, and 0.37 $dBcm^{-1}$ and 0.31 $dBcm^{-1}$ were obtained for the 50 μm thick device.

5.4 Diode pumping

Problems with cracking only allowed one set of opposing sides of the 50 μm thick device to be polished. This meant that side-pumping could not be performed and instead, as an initial test of diode launching, the device was end-pumped using a diode laser array (in collaboration with J. Wang, ORC, University of Southampton). Once lasing was achieved, the wavelength of the pump source was tuned to optimise the threshold for lasing by changing the temperature of the cooling water.

5.4.1 Threshold power for lasing

Table 5.4.1 shows the absorbed pump power thresholds for lasing of the 50 μm thick device with different transmittance output coupling mirrors.

Output coupler transmittance (at the laser wavelength)	**Absorbed power threshold for lasing (W)**
0.15% (HR)	12.2
2.00%	7.44
4.75%	7.97
12.86%	8.32
24.30%	11.8
46.07%	21.5

Table 5.4.1: Absorbed pump power thresholds for the 50 μm thick device with different transmittance output coupling mirrors and a diode pumping.

It is likely that the threshold obtained with a HR mirror is higher than expected because an optimal alignment was not obtained. The threshold is expected to scale from the Ti:sapphire pumped case approximately with the increase in pumped area, neglecting the effects of the difference in the pumping geometry and spectral properties. If we use 0.001 mm^2 (area of a 35 μm diameter spot) and 0.35 mm^2 (7 mm × 50 μm) as approximations of the pumped areas when pumping with the Ti:sapphire laser and diode laser array respectively, we would expect the threshold to increase from 35.6 mW to 12.5 W when pumping with the diode

laser array, and using the 4.75%T output coupling mirror. This estimate of the expected threshold is in agreement with the threshold found experimentally, considering the approximations made.

5.4.2 Laser spectra

Lasing has been observed centred at wavelengths of 1060.6 nm and 1061.3 nm, and was spectrally unstable; the strongest output was always centred on a wavelength of 1060.6 nm. Lasing in distinct bands is similar to the behaviour observed when pumping with the Ti:sapphire laser, but the bands are much narrower in this case. Figure 5.4.1 shows a typical laser spectrum. The group of peaks centred at a wavelength of 1060.6 nm are separated consistently with an expected longitudinal mode spacing of 0.0412 nm, though there is a peak missing between the strongest peak and the two weaker peaks.

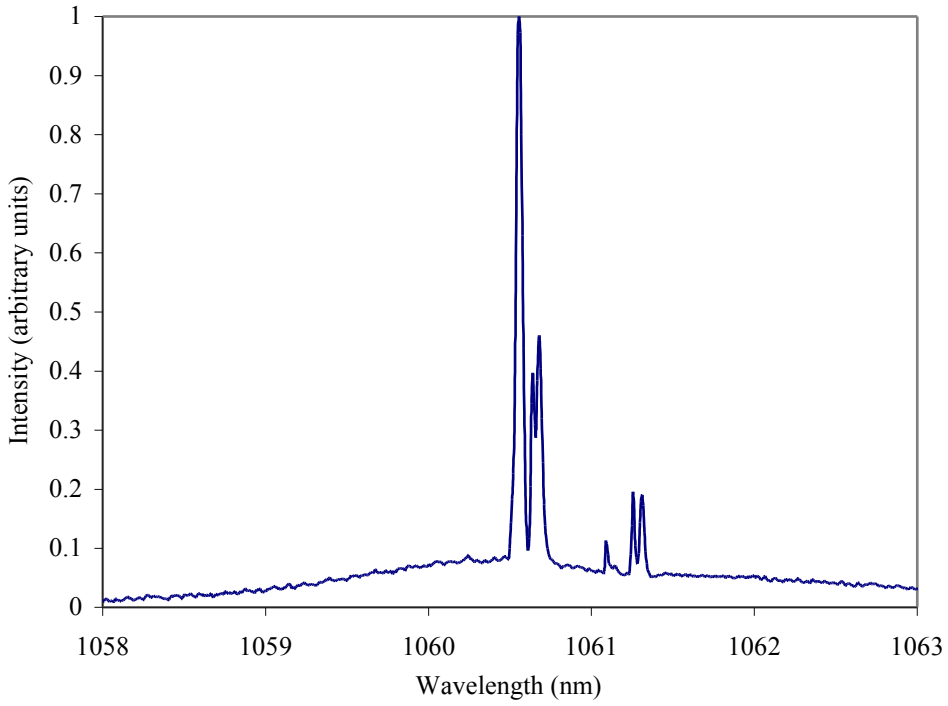

Figure 5.4.1: Typical laser spectrum obtained from the 50 μm thick device using diode pumping.

5.4.3 Slope efficiency

End-pumping through the laser cavity mirrors with the diode laser array was not ideal; at high pump powers the fluorinert fluid holding the mirrors was prone to boiling, causing the mirrors to slip or drop off. As a result of the complications introduced by end-pumping with high power levels, only one value of slope efficiency was obtained for diode pumping of the 50 μm thick device. Figure 5.4.2 shows the slope efficiency plot obtained with a 12.86%T output coupling mirror. The laser output was dropping as the value of the last point was taken, indicating that the mirror was in the process of slipping off and explaining why the point is not in line with others as expected. A slope efficiency of 11.2% was obtained with the 12.86%T output coupling mirror. From results with Ti:sapphire pumping, this value was expected to be higher, but is explainable by the differences in pumping geometry and spectral properties. In particular, the spatial overlap of the pump and laser beams was quite good when pumping with the Ti:sapphire laser, whereas both the pump and laser beams are expected to be highly multimode in the case of diode pumping.

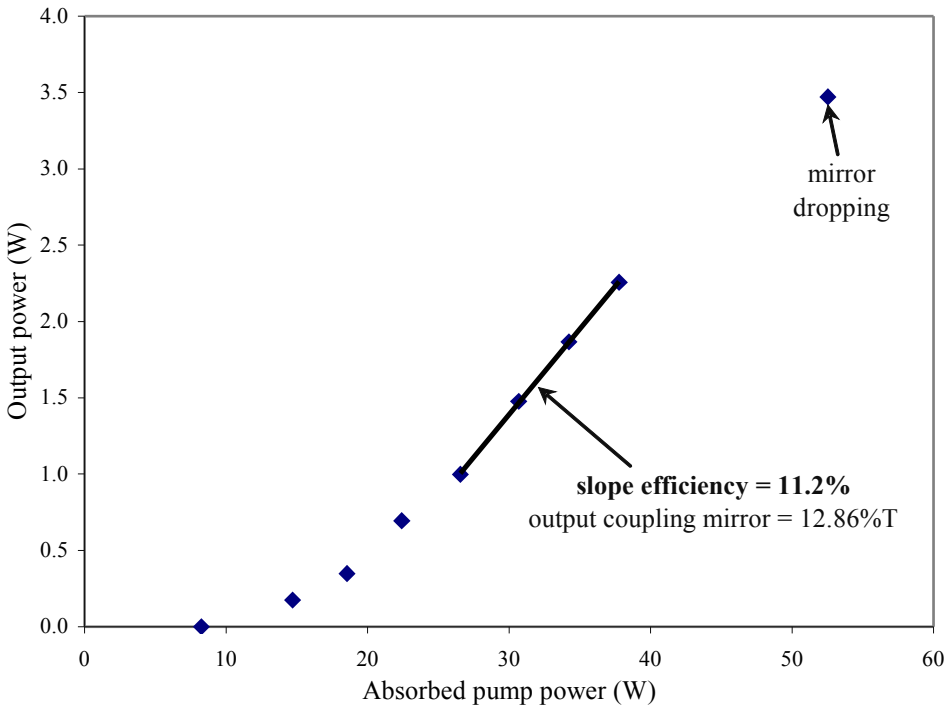

Figure 5.4.2: Slope efficiency obtained with diode pumping of the 50 μm thick device.

5.4.4 Beam profile

Figure 5.4.3 shows a typical image of the laser output beam profile recorded with a pump power level close to threshold (use of higher pump powers would have lead to saturation of the camera or overheating of filters). The laser output was highly multimode as expected, and filled the full thickness of the film in the guided direction. The beam profile was found to be unstable, and was also very sensitive to the launching position of the diode pump light.

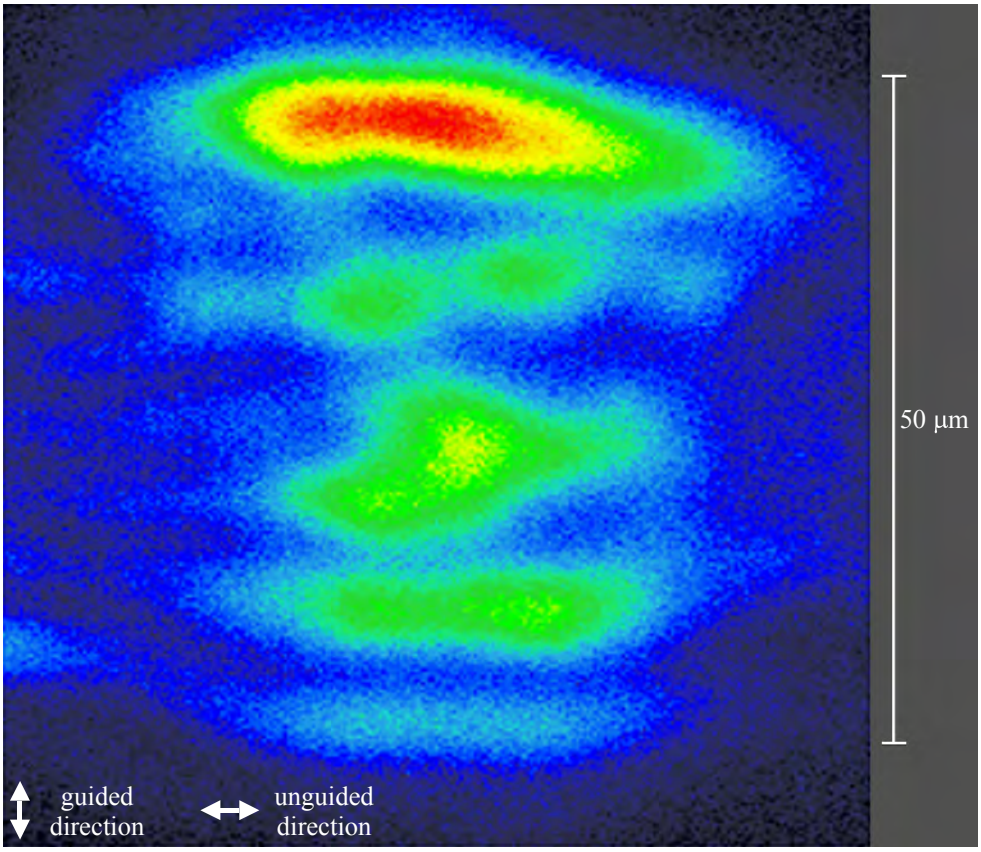

Figure 5.4.3: Laser output beam profile obtained from the 50 μm thick device using diode pumping.

5.4.5 Propagation losses

Figure 5.4.4 shows the results of the Findlay-Clay loss experiment, which produces an estimate of 0.79 $dBcm^{-1}$ for the 50 μm thick device. This is twice the loss estimate obtained from Ti:sapphire pumping, and may indicate that the average loss of the entire film is higher than in some select areas. If only the last three points are used in the Findlay-Clay plot, an

estimate of 0.47 dBcm^{-1} is obtained for the loss, which is in much better agreement with the result obtained from Ti:sapphire pumping, and indicates that 0.79 dBcm^{-1} can be taken as an upper limit of the 50 μm thick device loss.

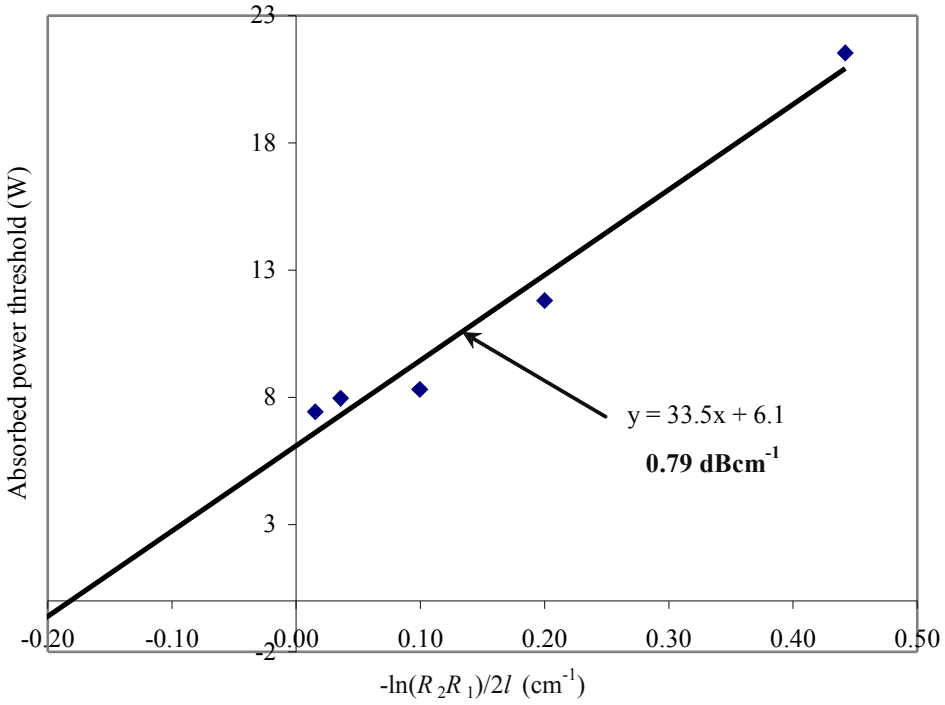

Figure 5.4.4: Findlay-Clay loss experiment results for the 50 μm thick device using diode pumping.

5.4.6 Conclusions

- Unfortunately, the 50 μm thick device could not be double side-pumped with diode laser arrays. However, the less ideal end-pumping geometry has been used and lasing has been observed with a minimum threshold of 7.44 W obtained with a 2.00% transmittance output coupling mirror.
- Lasing in distinct spectral regions occurred, as was the case with Ti:sapphire pumping.
- A slope efficiency of 11.2% was obtained with a 12.86% transmittance output coupling mirror.

- The laser output was highly multimode and the spatial overlap of the pump and laser beams is expected to have been poor. Future work involving multilayered film geometries is expected to overcome this problem.
- An upper limit of 0.79 $dBcm^{-1}$ was obtained for the average loss over the entire film.

5.5 Self-imaging

A Nd:GGG film was fabricated with a YAG capping layer to observe the effect of self-imaging in a symmetric waveguide. The Nd:GGG film was face-polished at a slight angle before deposition of the YAG capping layer, to allow different thicknesses to be tested in one device; the film thickness was about 27 μm after polishing. Subsequent to deposition of the YAG capping layer, the sample end faces were polished at a slight angle to allow slightly different lengths to be tested in one device.

5.5.1 Beam profiles

A Ti:sapphire laser beam was used to test the self-imaging properties of the device (in collaboration with J. Wang, ORC, University of Southampton); the beam was focussed tightly with a microscope objective lens to ensure that highly multimode propagation occurred. The launching position was changed so that propagation occurred through different thicknesses and across different lengths of the waveguide, and the wavelength of the Ti:sapphire laser was tuned. The output profile of the transmitted Ti:sapphire laser beam changed as these three parameters were adjusted. Figure 5.5.1 shows an example output profile of the Ti:sapphire laser beam when the conditions were not suitable for self-imaging to occur, in this case the output was highly multimode in the guided direction. Figure 5.5.2 shows an example output profile of the Ti:sapphire laser beam when the conditions for self-imaging were met, in this case the output was single-mode in the guided direction and a launched spot size of 6 μm in diameter was reproduced (in terms of the self-imaged guided direction) at the output face.

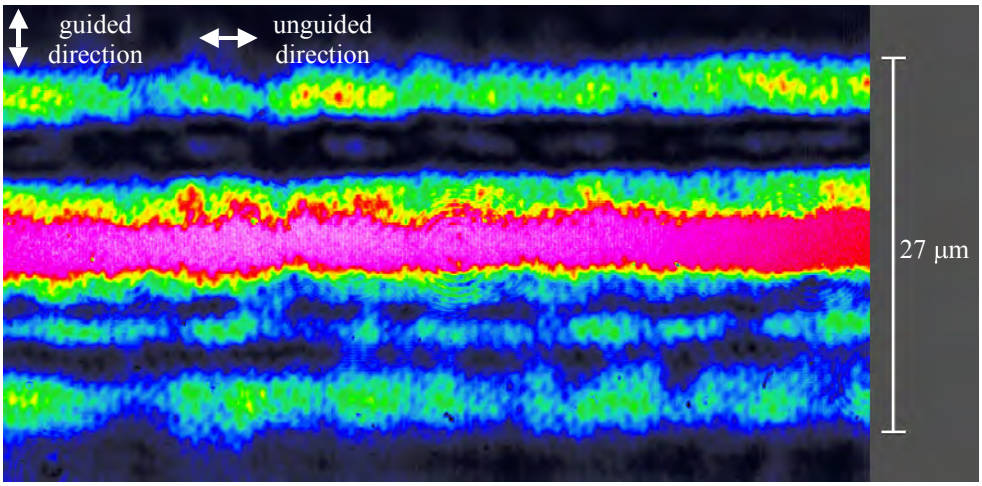

Figure 5.5.1: Beam profile of multimode propagation of a Ti:sapphire laser beam through the YAG capped device.

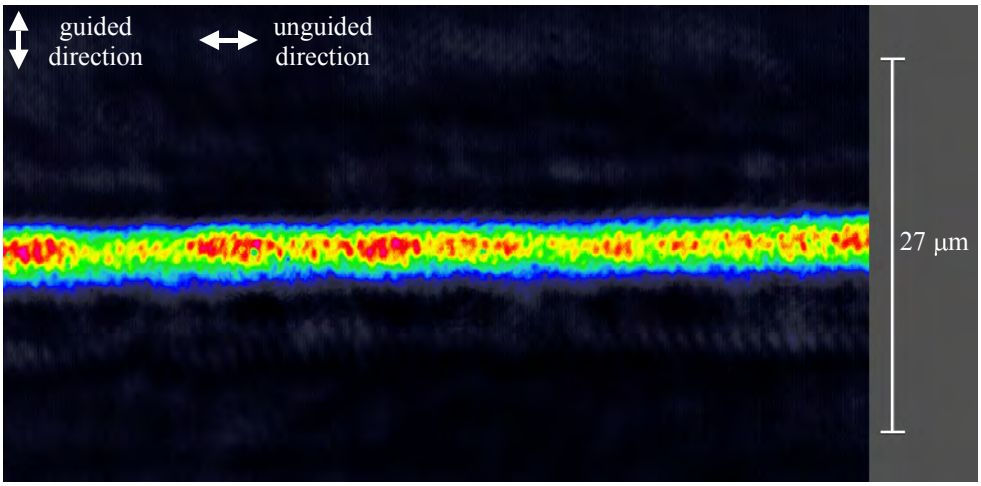

Figure 5.5.2: Beam profile of self-imaged propagation of a Ti:sapphire laser beam through the YAG capped device.

5.5.2 Conclusions

- The effect of self-imaging was observed in a YAG capped device.
- A device with the correct length and thickness for self-imaging at a wavelength of 1060.6 nm (for example, 8 mm in length and a thickness of 66 μm) may be used as an amplifier that can be pumped by high-power diode laser arrays and reproduce the modal properties of the signal beam at the output face.

5.6 Conclusions summary

- A series of Nd:GGG films have been grown and successfully used as devices, proving the potential of garnet films deposited by PLD.
- Structural, compositional and optical analysis of the films have shown that they have qualities approaching bulk crystal.
- Lasing was achieved in two devices using Ti:sapphire pumping, and lasing was achieved in one of the devices that was subsequently pumped with a laser diode array.
- Both laser devices displayed very low propagation losses, among the lowest obtained to date for films fabricated using a deposition based technique.
- The effect of self-imaging was observed in a YAG capped device.

Chapter 6

YbAG and other Garnet Film Results

6.1 Introduction

The growth of YbAG and several other garnets is discussed in this chapter. The YbAG film was grown to test the possibility of using highly doped thick garnet films as thin-disk lasers. A material analysis of the YbAG is presented along with the results from laser trial experiments. A material analysis of some other garnet films is also discussed here; the growth of other garnets (using the same deposition conditions as used for Nd:GGG) has proven the potential of the current setup and opens up possibilities for future work. Finally, the results from a first attempt at a four-layer geometry are presented and the conclusions that can be drawn from all of the films discussed in this chapter are summarised.

6.2 YbAG film results

The YbAG crystal target was too thin to risk polishing so the YbAG film was deposited in a single 6 hour growth run. The rate and size of particulate deposition could be seen to increase significantly after about 3 hours of deposition. Unfortunately, the thick YbAG film cracked into two pieces halfway through deposition, but since it remained in the holder the

growth run was continued. The two pieces were at different temperatures for the second half of the growth run and are referred to hereafter as piece A and B (piece A was hotter than piece B for the remainder of the growth run after cracking occurred). The YbAG film thickness was 18 ± 2 μm after parallel polishing was performed.

6.2.1 X-ray diffraction spectra

Figures 6.2.1, 6.2.3 and 6.2.5 show XRD spectra of a thin YbAG film, piece A of the thick YbAG film and piece B of the thick YbAG film respectively. Figures 6.2.2 and 6.2.4 show some expanded views of the peaks from the XRD spectra of the thin YbAG film and piece A of the thick YbAG film respectively so that the FWHM can be seen clearly. Tables 6.2.1, 6.2.2 and 6.2.3 summarise various properties of the spectra. In the case of the thick YbAG film spectra, *D*-spacing values have been normalised using the positions of the YAG substrate peaks from a scan of a blank YAG substrate that was analysed under the same conditions as the thick YbAG film.

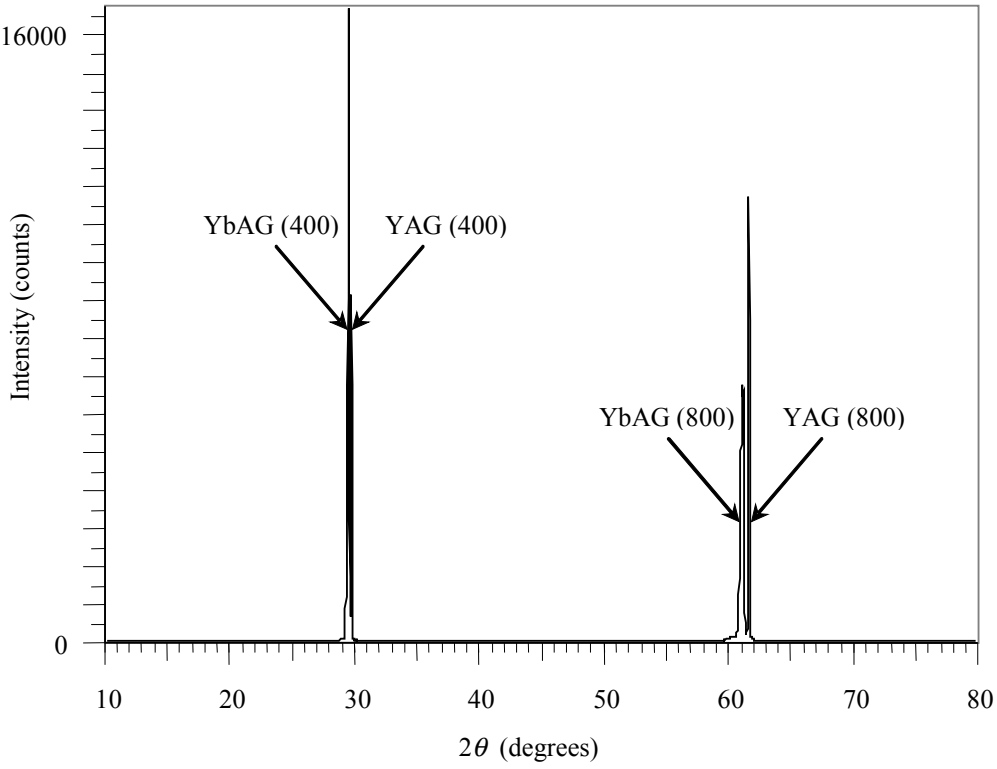

Figure 6.2.1: XRD spectrum of a thin YbAG film.

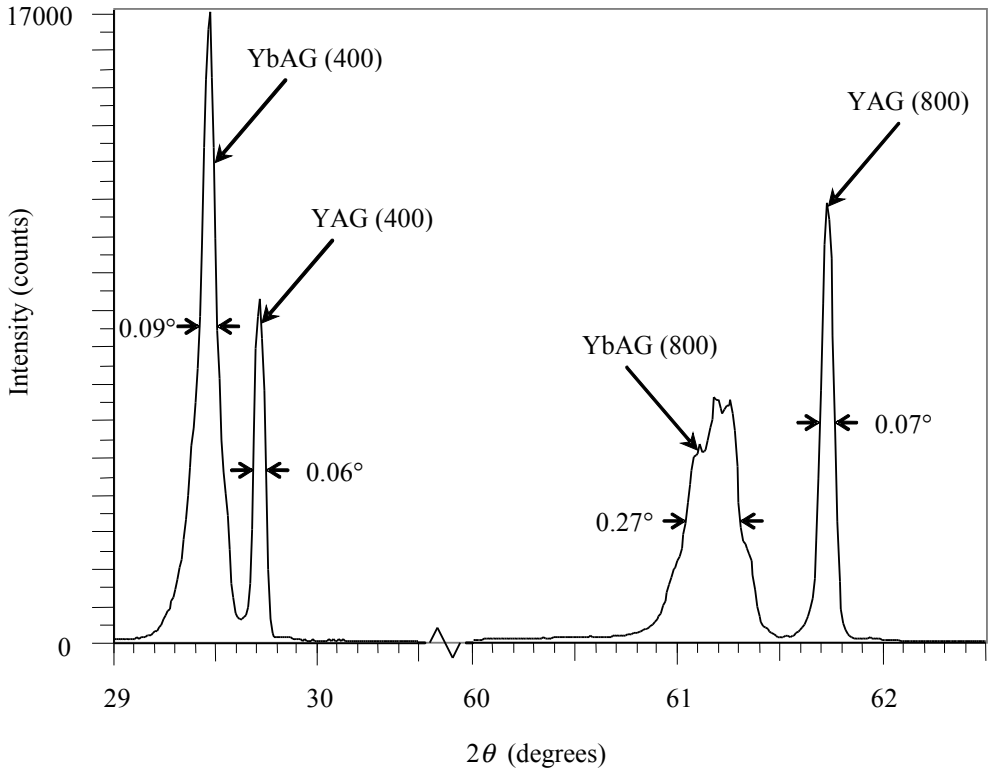

Figure 6.2.2: Expanded views of the XRD peaks of a thin YbAG film.

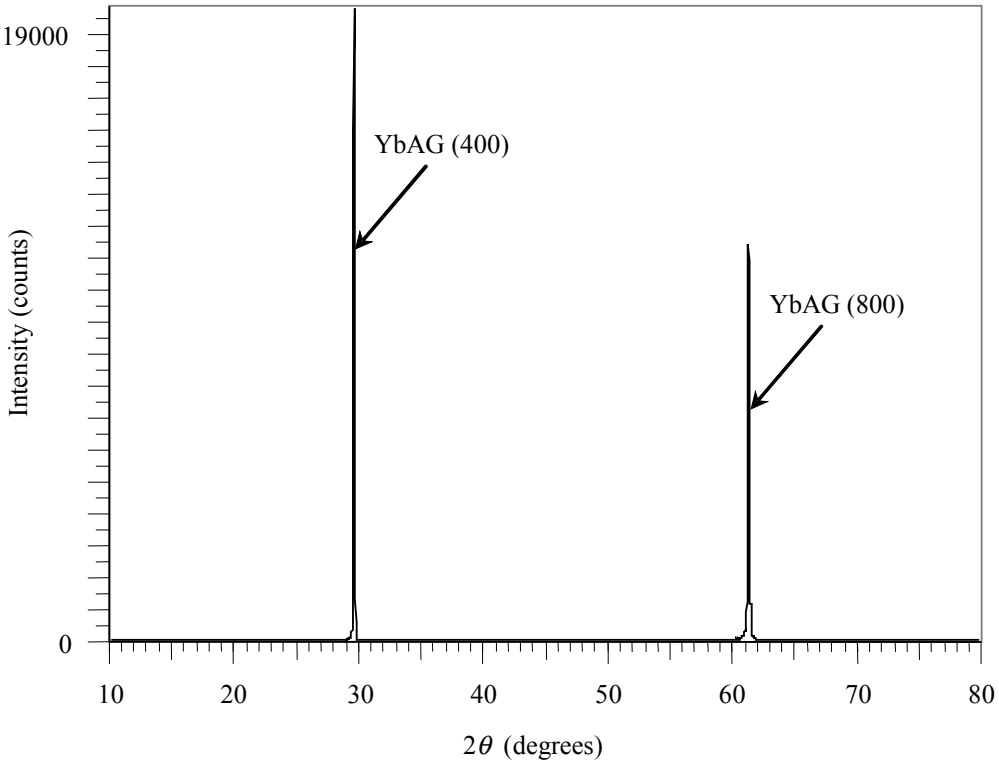

Figure 6.2.3: XRD spectrum of a thick YbAG film (piece A).

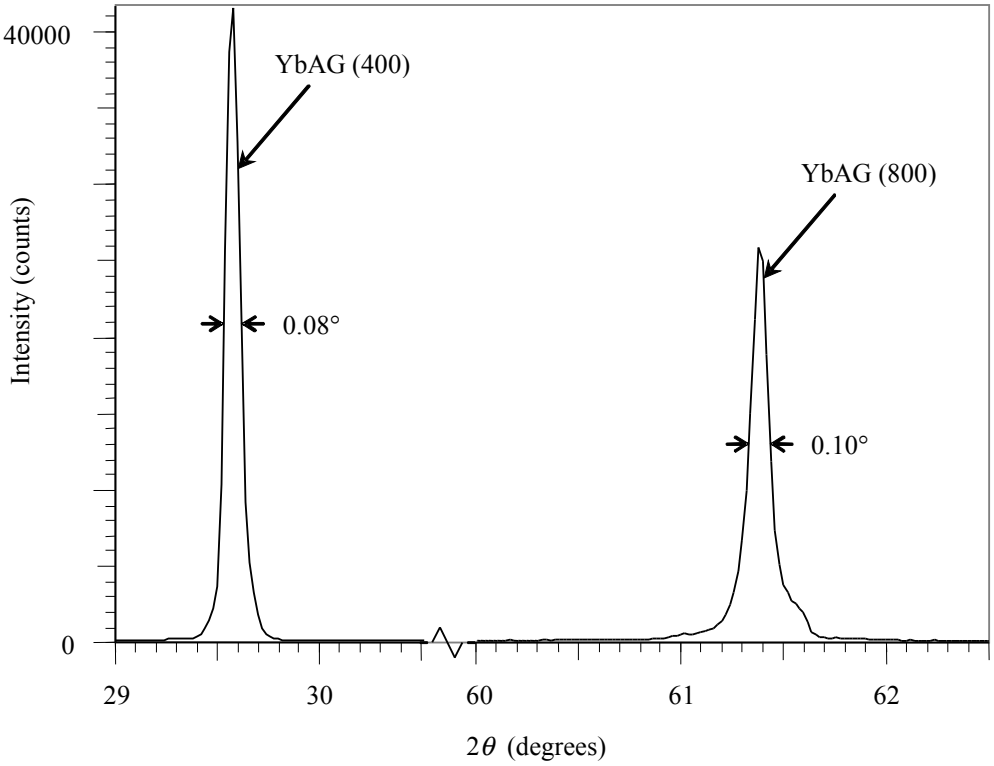

Figure 6.2.4: Expanded views of the XRD peaks of the thick YbAG film (piece A).

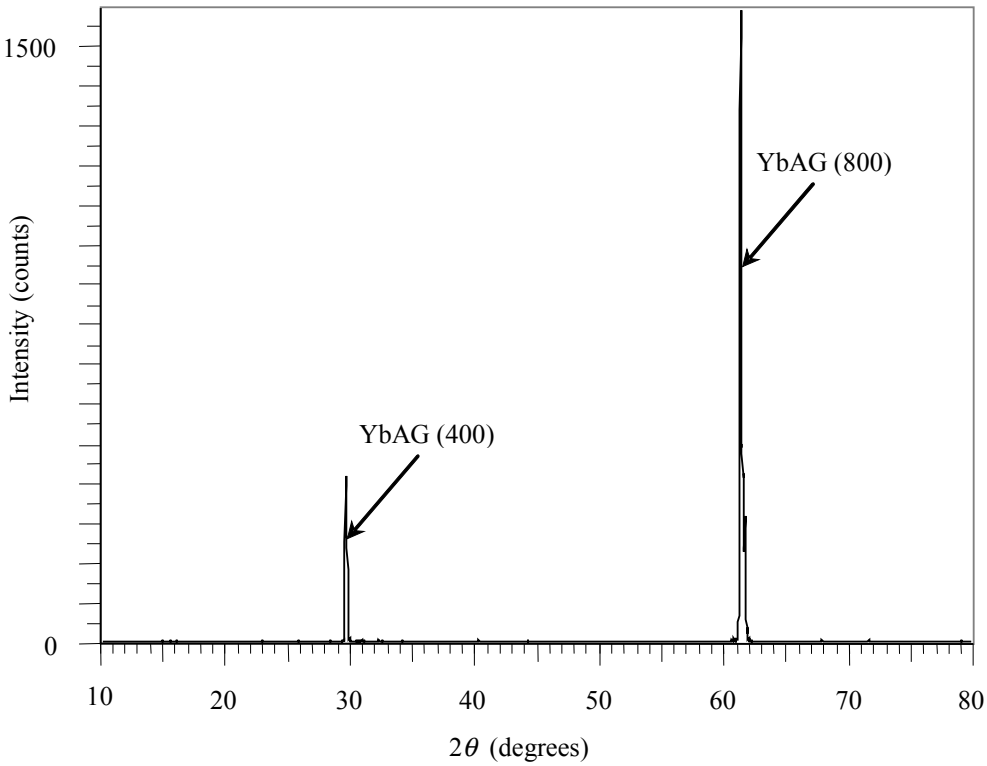

Figure 6.2.5: XRD spectrum of the thick YbAG film (piece B**)**.

Crystal (orientation)	2θ (degrees)	FWHM (degrees)	*D*-spacing (Å)	Normalised *D*-spacing (Å)	Database *D*-spacing (Å)
YbAG (400)	29.462	0.09	3.029	3.024	2.9847 [56]
YbAG (800)	61.202	0.27	1.513	1.511	1.4923 [56]
YAG substrate (400)	29.710	0.06	3.005	-	3.0015 [42]
YAG substrate (800)	61.718	0.07	1.502	-	1.5008 [42]

Table 6.2.1: Summary of the thin YbAG film XRD spectrum properties.

Crystal (orientation)	2θ (degrees)	FWHM (degrees)	*D*-spacing (Å)	Normalised *D*-spacing (Å)	Database *D*-spacing (Å)
YbAG (400)	29.589	0.08	3.017	3.013	2.9847 [56]
YbAG (800)	61.388	0.10	1.509	1.507	1.4923 [56]
YAG substrate (400)	29.719	0.07	3.004	-	3.0015 [42]
YAG substrate (800)	61.743	0.08	1.501	-	1.5008 [42]

Table 6.2.2: Summary of the thick YbAG film (piece A) XRD spectrum properties.

Crystal (orientation)	2θ (degrees)	*D*-spacing (Å)	Normalised *D*-spacing (Å)	Database *D*-spacing (Å)
YbAG (400)	29.632	3.012	3.008	2.9847 [56]
YbAG (800)	61.413	1.508	1.507	1.4923 [56]
YAG substrate (400)	29.719	3.004	-	3.0015 [42]
YAG substrate (800)	61.743	1.501	-	1.5008 [42]

Table 6.2.3: Summary of the thick YbAG film (piece B) XRD spectrum properties.

As in the case of the Nd:GGG films, the shift of the normalised *D*-spacings is attributed to the effects of deficient stoichiometry, and is significantly greater than would be expected from predictions using thermal expansion mismatch. The normalised *D*-spacing values for the thin YbAG film are shifted by 1.3% for both the (400) and (800) orientations, whereas the values for piece A of the thick YbAG film are shifted by 0.94% and 1.0% for the (400) and (800) orientations respectively. This difference in shift between the thin and thick YbAG films is thought to be due to relaxation of the lattice away from the film-substrate boundary. The thin YbAG film (400) peak FWHM compares well to the YAG substrate (400) peak but the thin YbAG film (800) peak FWHM is significantly worse. The (400) and (800) peak FWHM of piece A of the thick YbAG film however both compare very well to the blank YAG substrate peak FWHM. This strongly suggests that increasing film thickness allows the crystal lattice to relax, and also suggests that the stoichiometry is close to bulk for piece A of the thick YbAG film.

The significant decrease in the intensity of X-ray diffraction from piece B of the thick YbAG film compared to piece A indicates that the decrease in temperature in the second half of the growth run was enough to prevent good quality crystal growth. It is possible that the main peaks observed are due to diffraction from the layer of crystal grown before the sample cracked.

6.2.2 Energy dispersive X-ray analysis

A thin YbAG film was analysed using the EDX technique, and a piece of bulk crystal was analysed at the same time under the same conditions. Figure 6.2.6 shows an example of an EDX spectrum of a YbAG film.

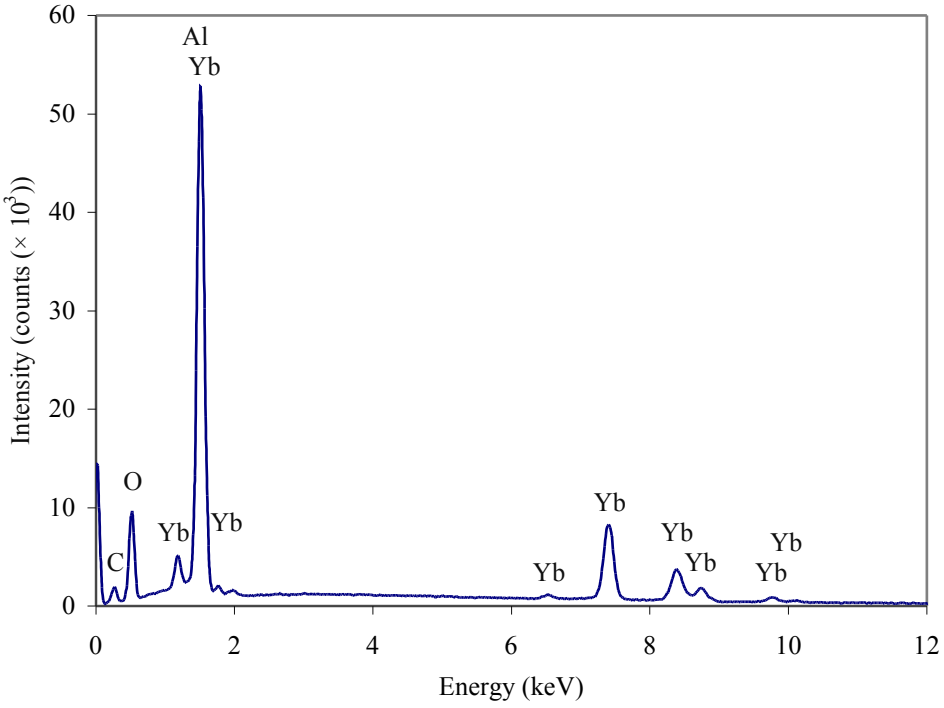

Figure 6.2.6: EDX spectrum of YbAG.

It was not possible to analyse the thick YbAG film because the carbon coating would have affected its performance as a device. As was the case for EDX analysis of Nd:GGG and YAG, the results for oxygen content were too inaccurate to be of use. The sample was analysed five times at different locations on the sample surface and an average was taken of

the results. Since the oxygen content results were unreliable, only the ratios of the elements ytterbium and aluminium are presented below in table 6.2.4. The error was estimated from the results of the analysis of bulk crystals.

Sample analysed	Ratio of elements other than oxygen
Thin YbAG film	$Yb_3Al_{4.6 \pm 0.2}$
Bulk YbAG	$Yb_3Al_{5.2 \pm 0.2}$

Table 6.2.4: EDX results for the thin YbAG film.

The ratio of ytterbium to aluminium in the thin YbAG film is very close to bulk crystal. If it is assumed that the stoichiometry of the film does not change significantly with thickness (as was the case for Nd:GGG films), this suggests that as film thickness is increased, the film (800) XRD peak only narrows to have a FWHM close to the substrate (800) peak if the stoichiometry is close to bulk (i.e. nearly all of the crystal lattice sites are occupied).

6.2.3 Absorption spectra

Both pieces of the thick YbAG film and the backs of the substrate were face-polished in preparation for lasing experiments; this also allowed them to be analysed with a spectrophotometer. Figure 6.2.7 shows the absorption spectra for the two pieces of YbAG film in the IR wavelength range, and figure 6.2.8 shows the absorption spectrum of the thick YbAG film in the visible range (which was the same for both pieces). The absorption spectra are plotted so that the absorption coefficient can be read directly from the graph, however since it depends on the thickness measurement it carries the same error of ± 11%. A polished blank YAG substrate was also scanned to allow the Fresnel reflections and small absorption in the YAG substrate to be taken into account. Both spectra include a comparison to bulk YbAG crystal and the visible spectrum includes a comparison to bulk YbAG crystal with the ytterbium in the 2+ and 3+ valence states. The absorption spectra for bulk YbAG crystal have been taken from a report of a crystal that was grown by the Czochralski method [38]. It was found that annealing was required to change the valence state of the ytterbium in this crystal from the 2+ to the 3+ valence state.

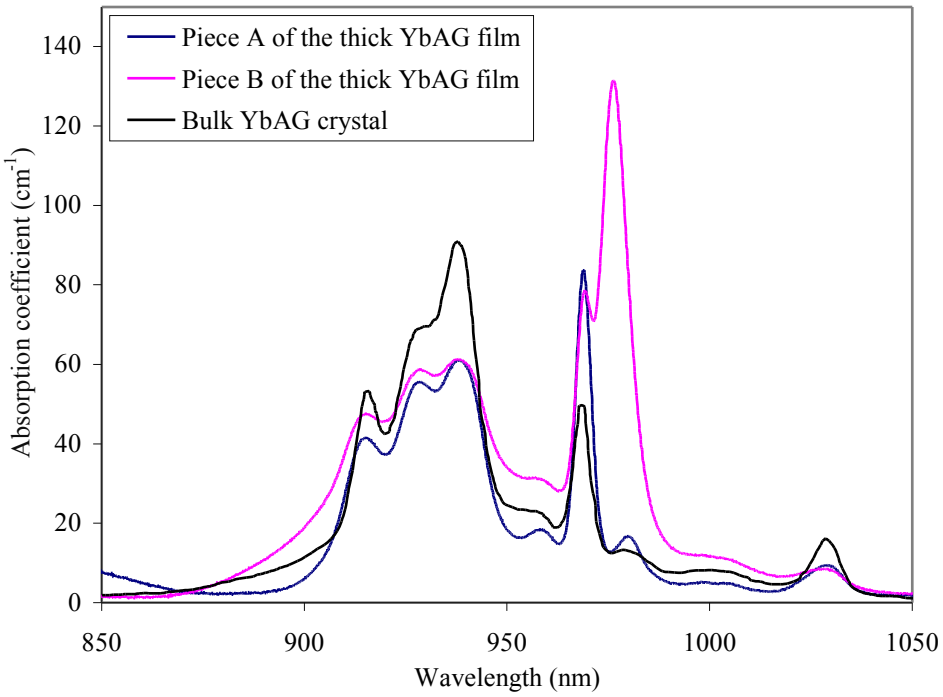

Figure 6.2.7: IR wavelength range absorption spectrum of the two pieces of thick YbAG film compared to bulk YbAG crystal [38].

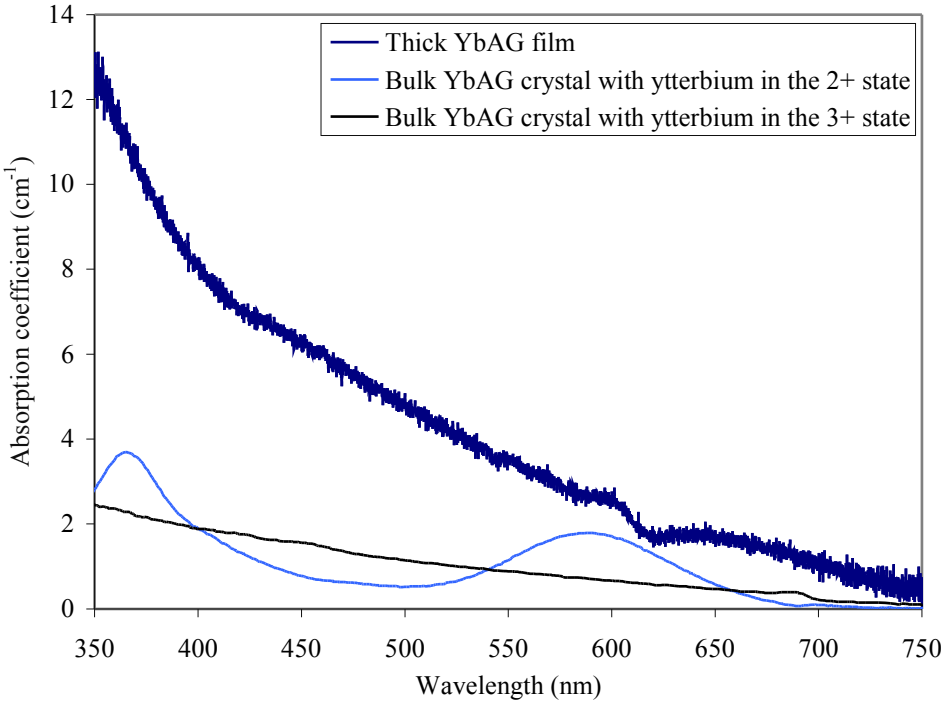

Figure 6.2.8: Visible wavelength range absorption spectrum of the two pieces of thick YbAG film compared to bulk YbAG crystal with the ytterbium in the 2+ and the 3+ valence states [38].

None of the thick YbAG film IR absorption peaks appear to be shifted, but the relative height of the peaks is not the same as bulk. The height of the absorption peak for piece B of the thick YbAG film at 975.5 nm is significantly different from bulk. This is attributed to the incorrect substrate temperature in the second half of the growth run after cracking had occurred. The incorrect growth temperature has caused the crystal to grow differently so that the crystal field around the ytterbium ions is significantly different from bulk crystal and the spectroscopic properties have been altered.

The height of the absorption peak at 968.5 nm is also significantly higher than bulk for both pieces of thick YbAG film. The absorption peaks at 1030 nm and around 940 nm are all lower than bulk, and these are of particular significance because they represent the laser and pump transitions respectively (for the laser energy level scheme whose operation was attempted). The difference in the heights of these peaks may be an indication that the film is ytterbium deficient, or some of the ytterbium may be in the 2+ valence state. Absorption in the visible wavelength range is higher than bulk and the small peak at 600 nm supports the proposition that some of the ytterbium ions may be in the 2+ valence state. The occurrence of ytterbium ions in the 2+ valence state could be caused by an oxygen deficiency in the film, and the spectroscopy of future YbAG films may be improved by increasing the oxygen pressure used when depositing.

6.2.4 Laser experiments

Laser trial experiments were performed (in collaboration with P. Wang, ORC, University of Southampton) with both pieces of the thick YbAG film. The parallelism of the interfaces of both pieces wasn't good enough for the coupled-cavity setup to be effective. Numerous attempts were made with the Brewster-angle-cavity setup but lasing was not achieved in either piece of the thick YbAG film. The possibilities for why lasing could not be achieved are summarised below. It is also worth noting at this point that it was not possible to obtain a fluorescence spectrum from either of the YbAG film pieces. This was partly due to limiting factors in the experimental setup (care had to be taken not to allow the intense pump light into the optical spectrum analyser), but may also be a symptom of a non-optimal setup.

- The threshold for lasing may be above the level of pump power available. The threshold was estimated (by P. Wang, ORC, University of Southampton) and thought to be about 10 W of incident power, meaning there should have been enough power available. But, unknown properties of the film had to be replaced by bulk properties to get an estimate and this may make the estimate unreliable.
- Cooling of the films may not have been sufficient to prevent significant reabsorption loss. The size of the films made them difficult to attach to heat sinks and the Brewster-angle-cavity setup meant that the films only had contact with the heat sink at the edges. This may have allowed a hot-spot to develop where the pump light was focussed into the films.
- Some of the ytterbium might be in the 2+ valence state as suggested by the absorption spectra. Annealing has been shown to convert ytterbium ions to the 3+ valence state [38], but annealing of films may lead to cracking.
- The alignment of the cavity mirrors may not have been good enough to allow lasing to occur. When focussing tightly into the film, producing a gain region about 20 μm in diameter, it is hard to align the cavity mirrors so that a resonant path crosses such a small area. Optimisation of a cavity is easiest to do when a sample is lasing because the threshold can be used as a measure of optimisation.

6.2.5 Conclusions

- A YbAG film with a thickness of 18 ± 2 μm was fabricated.
- The film displayed excellent quality crystallinity and the ratio of ytterbium to aluminium in a thin film grown with the same conditions was close to the ratio in bulk YbAG crystal.
- The absorption properties of the film differed from bulk YbAG crystal and this may be an indication that some of the ytterbium is not in the 3+ valence state.
- Lasing attempts were unsuccessful to date, and some of the possibilities for why lasing could not be achieved have been discussed.

6.3 Other garnet film results

A selection of other garnet crystals were grown to prove the potential of the current setup and growth conditions. All of the films were deposited on 1 mm thick YAG substrates in single growth runs lasting 30 minutes each.

6.3.1 X-ray diffraction spectra

Figures 6.3.1, 6.3.3, 6.3.5 and 6.3.7 show XRD spectra of thin films of YGG, Nd,Cr:YSAG, Cr:GSAG and Nd,Cr:GSGG respectively, and figures 6.3.2, 6.3.4, 6.3.6 and 6.3.8 show some expanded views of the peaks from the spectra so that the FWHM can be seen clearly. Various properties of the spectra are summarised in table 6.3.1 and the *D*-spacing values have been normalised using the positions of the YAG substrate peaks.

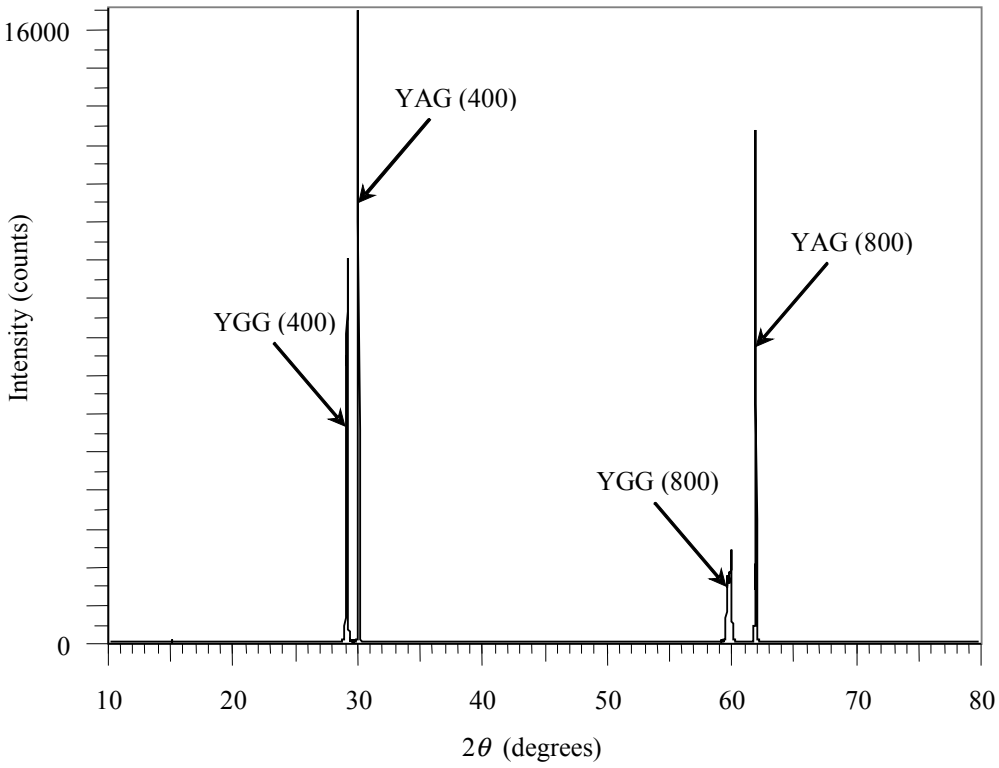

Figure 6.3.1: XRD spectrum of a thin YGG film.

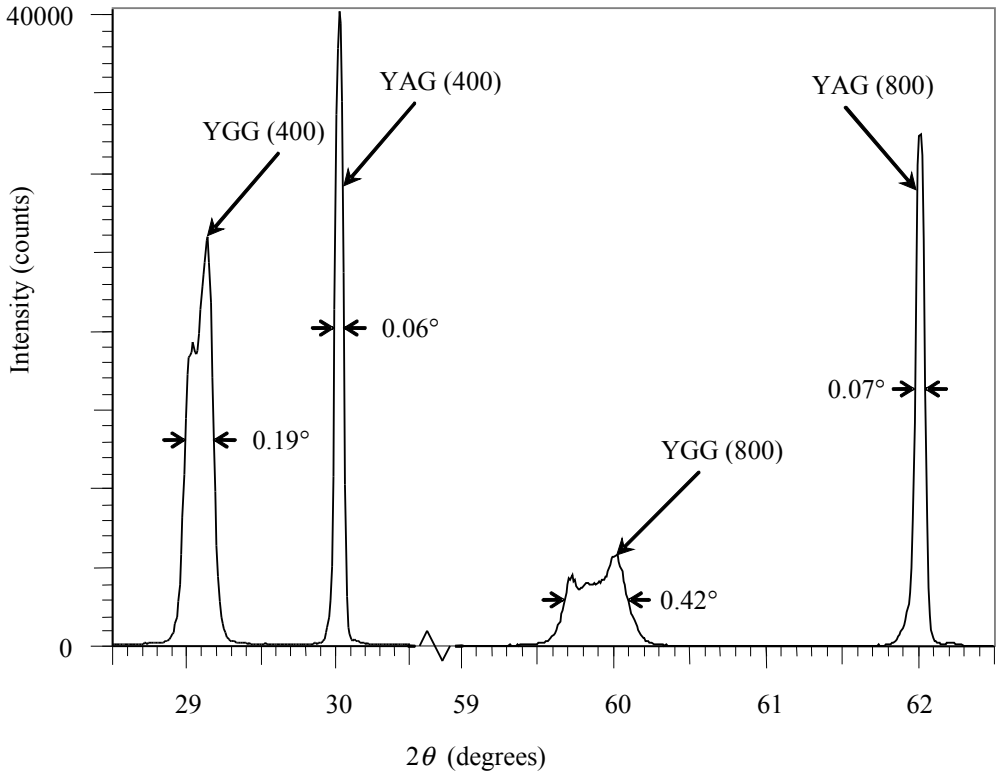

Figure 6.3.2: Expanded views of the XRD peaks of a thin YGG film.

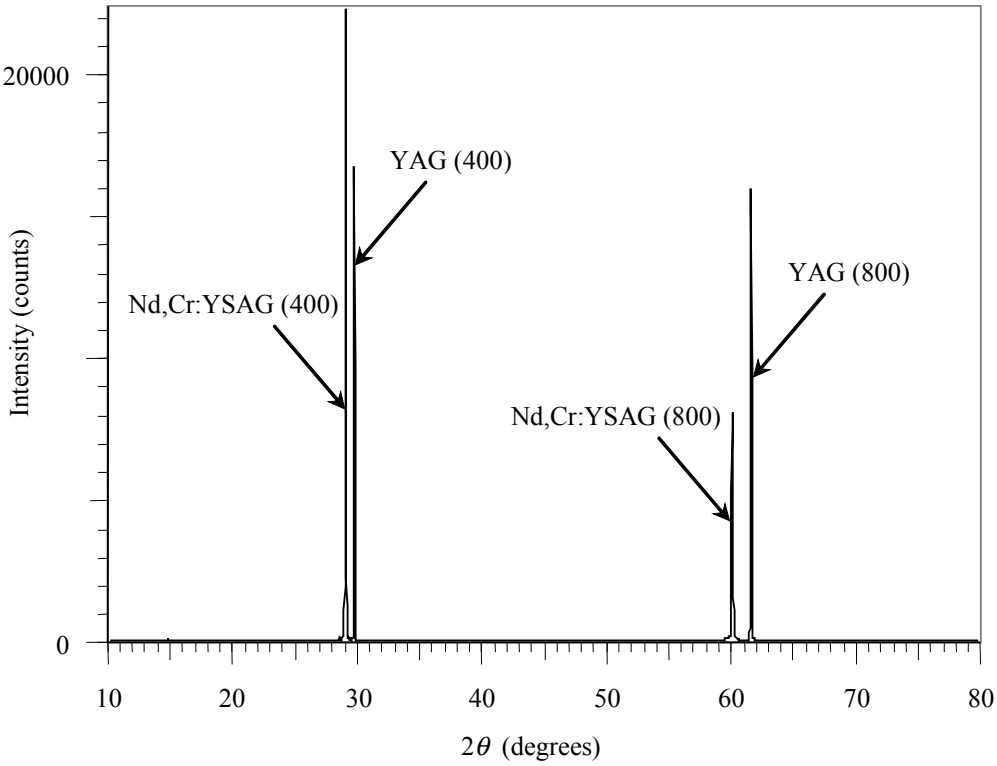

Figure 6.3.3: XRD spectrum of a thin Nd,Cr:YSAG film.

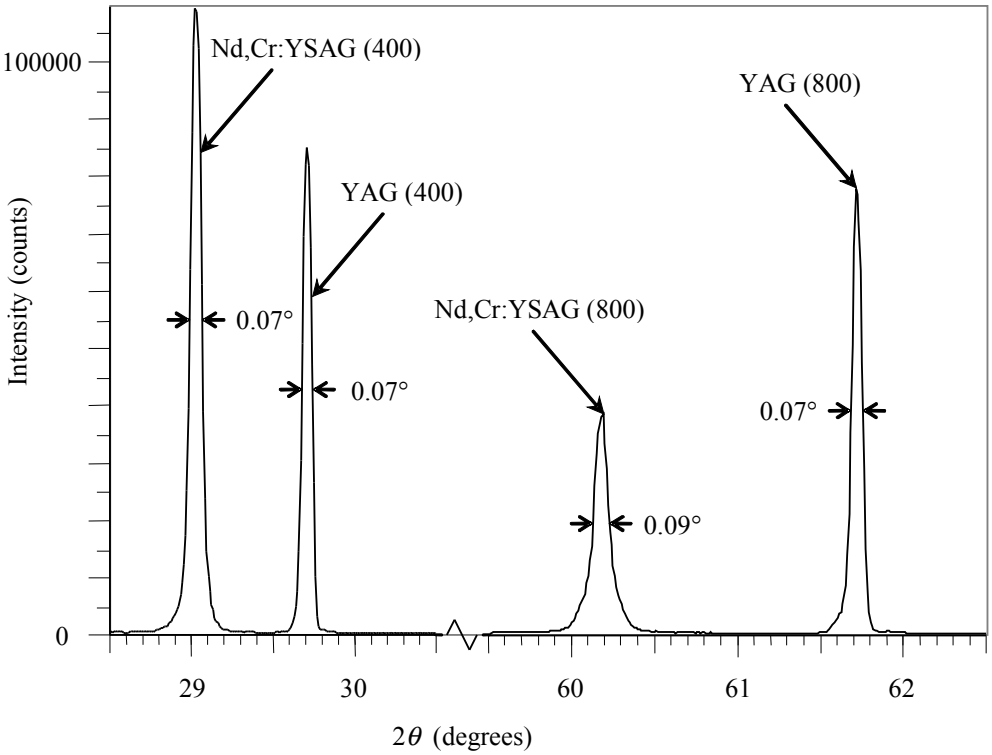

Figure 6.3.4: Expanded views of the XRD peaks of a thin Nd,Cr:YSAG film.

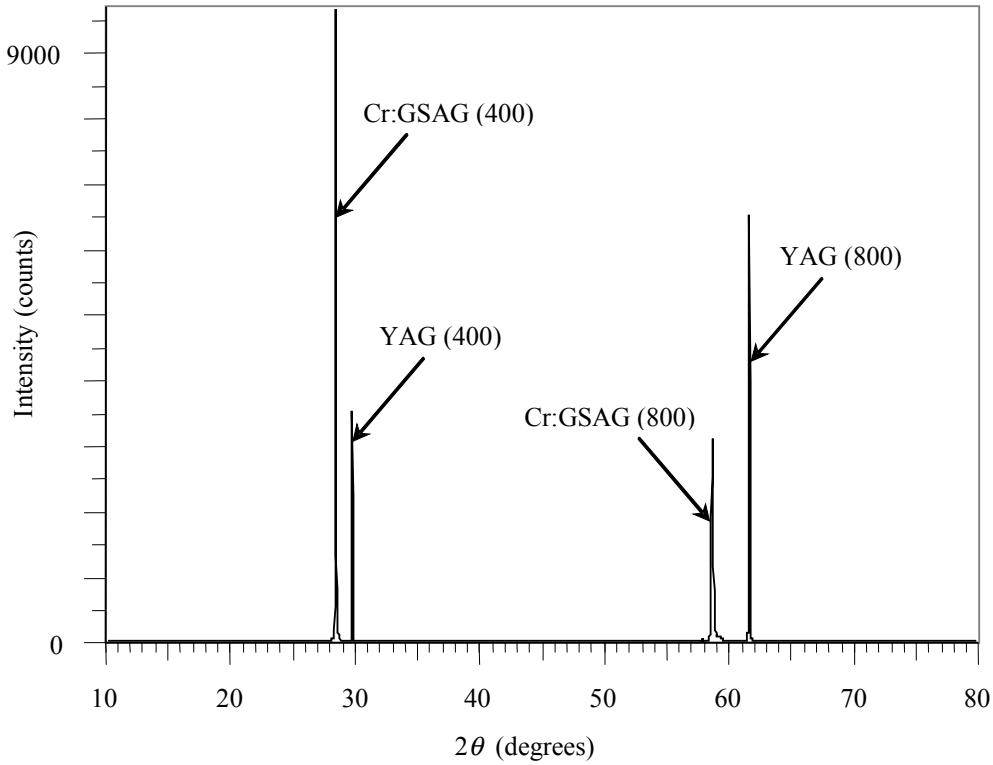

Figure 6.3.5: XRD spectrum of a thin Cr:GSAG film.

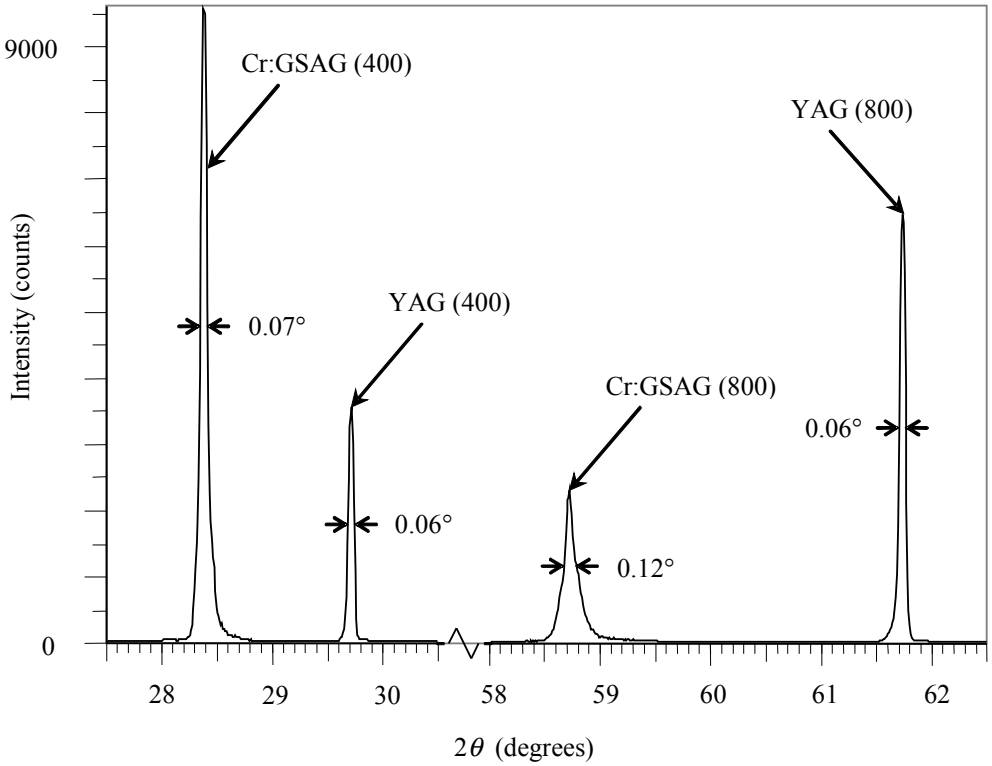

Figure 6.3.6: Expanded views of the XRD peaks of a thin Cr:GSAG film.

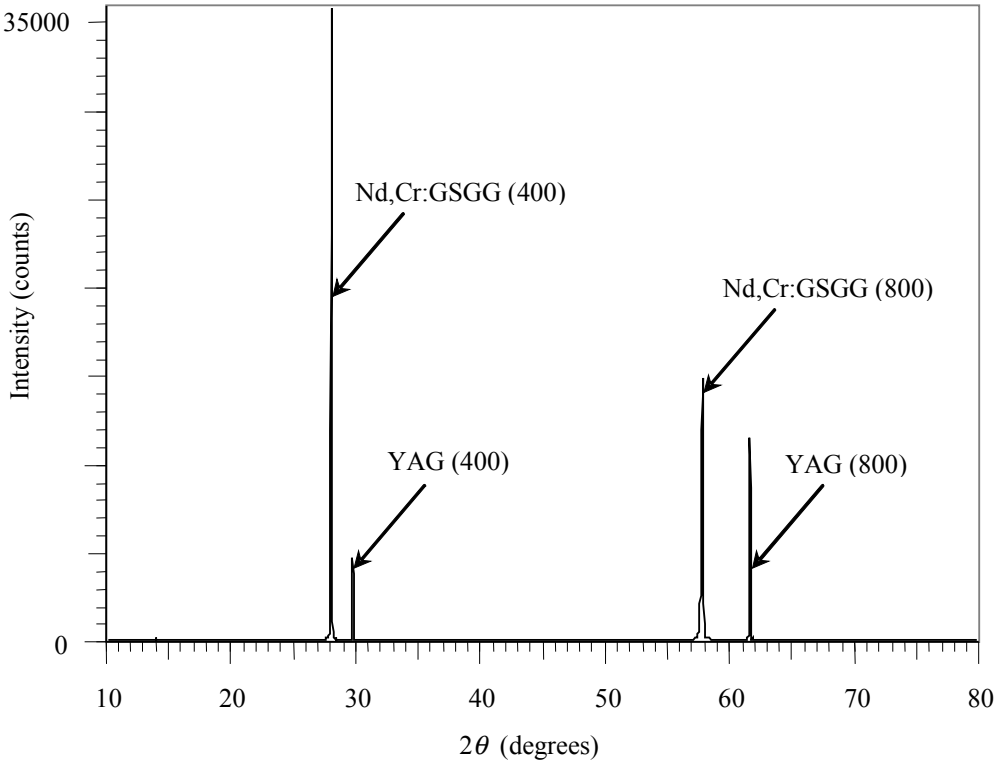

Figure 6.3.7: XRD spectrum of a thin Nd,Cr:GSGG film.

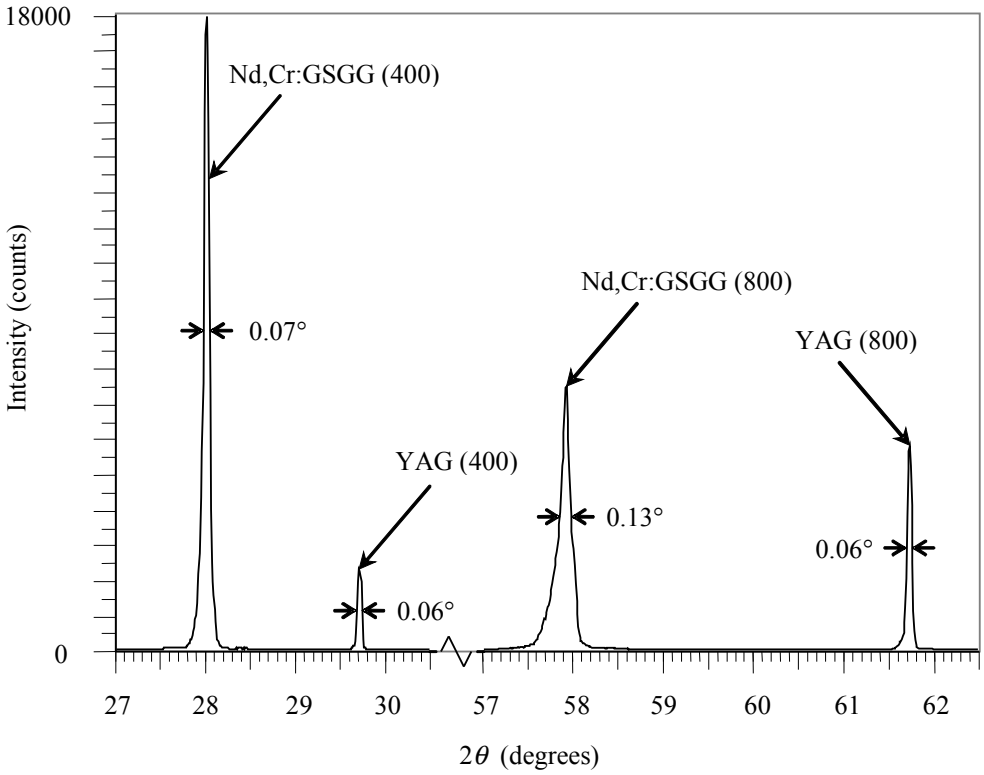

Figure 6.3.8: Expanded views of the XRD peaks of a thin Nd,Cr:GSGG film.

Crystal (orientation)	2θ (degrees)	FWHM (degrees)	*D*-spacing (Å)	Normalised *D*-spacing (Å)	Database *D*-spacing (Å)
YGG (400)	29.095	0.19	3.067	3.095	3.0682 [43]
YGG (800)	59.762	0.42	1.546	1.551	1.5341 [43]
YAG substrate (400)	30.036	0.06	2.973	-	3.0015 [42]
YAG substrate (800)	62.017	0.07	1.495	-	1.5008 [42]
Nd,Cr:YSAG (400)	29.031	0.07	3.073	3.069	3.0677 [44]
Nd,Cr:YSAG (800)	60.176	0.09	1.537	1.535	1.5339 [44]
YAG substrate (400)	29.720	0.07	3.004	-	3.0015 [42]
YAG substrate (800)	61.733	0.07	1.501	-	1.5008 [42]
Cr:GSAG (400)	28.378	0.07	3.143	3.136	3.0972 [53][9]
Cr:GSAG (800)	58.730	0.12	1.571	1.569	1.5486 [53][9]
YAG substrate (400)	29.700	0.06	3.006	-	3.0015 [42]
YAG substrate (800)	61.740	0.06	1.501	-	1.5008 [42]
Nd,Cr:GSGG (400)	28.014	0.07	3.183	3.178	3.1360 [54]
Nd,Cr:GSGG (800)	57.917	0.13	1.591	1.589	1.5680 [54]
YAG substrate (400)	29.716	0.06	3.004	-	3.0015 [42]
YAG substrate (800)	61.725	0.06	1.502	-	1.5008 [42]

Table 6.3.1: Summary of the different thin garnet film XRD spectra properties.

9 The only crystallographic data available was for $Gd_{2.91}Sc_{1.80}Al_{3.15}O_{11.80}$ and this has been used as an approximation of GSAG.

The shifts of the normalised *D*-spacings relative to database values for each film are shown in table 6.3.2. The shift of the Nd,Cr:YSAG *D*-spacings is the smallest shift seen for any film grown so far, and this makes sense because YSAG has the closest composition to YAG and is likely to have the smallest thermal expansion mismatch (no data was available for the thermal expansion coefficient of YSAG at the time of writing) and the highest compatibility with growth on YAG.

Crystal (orientation)	**Shift of normalised *D*-spacing relative to the database value**
YGG (400)	0.88%
YGG (800)	1.1%
Nd,Cr:YSAG (400)	0.033%
Nd,Cr:YSAG (800)	0.065%
Cr:GSAG (400)	1.3%
Cr:GSAG (800)	1.3%
Nd,Cr:GSGG (400)	1.3%
Nd,Cr:GSGG (800)	1.3%

Table 6.3.2: Summary of the shifts of the normalised *D*-spacings relative to database values for the alternative garnet films.

The YGG XRD film peaks are significantly broadened and the (800) peak is worse affected. This indicates the stoichiometry is more deficient than previously discussed films and could also be due to the interception of defects at the film-substrate boundary. The Nd,Cr:YSAG peak FWHM are the smallest observed for a film so far and are very close to the YAG substrate peaks. This is an indication that the Nd,Cr:YSAG film is relatively free of defects at the film-substrate boundary and has a stoichiometry very close to bulk YSAG. The Nd,Cr:GSAG and Nd,Cr:GSGG peak FWHM are close to the YAG substrate peaks, but the (800) peak FWHM are slightly worse than the (400) peak FWHM, indicating that the film stoichiometries are slightly deficient.

6.3.2 Energy dispersive X-ray analysis

EDX analysis was performed on all of the films. Figures 6.3.9, 6.3.10, 6.3.11 and 6.3.12 show example EDX spectra of YGG, Nd,Cr:YSAG, Cr:GSAG and Nd,Cr:GSGG respectively.

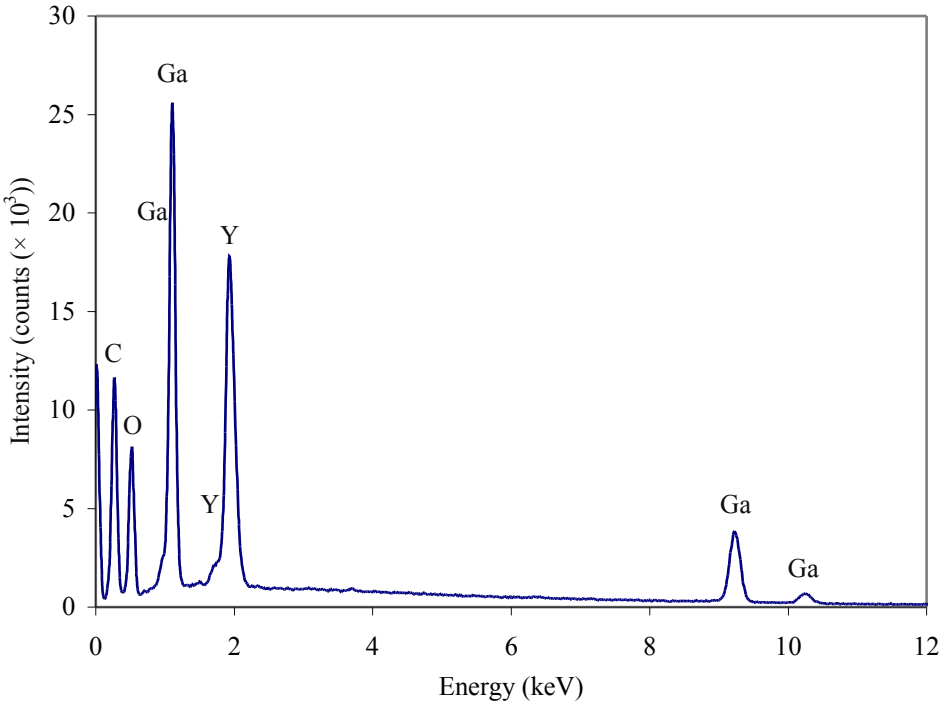

Figure 6.3.9: EDX spectrum of YGG.

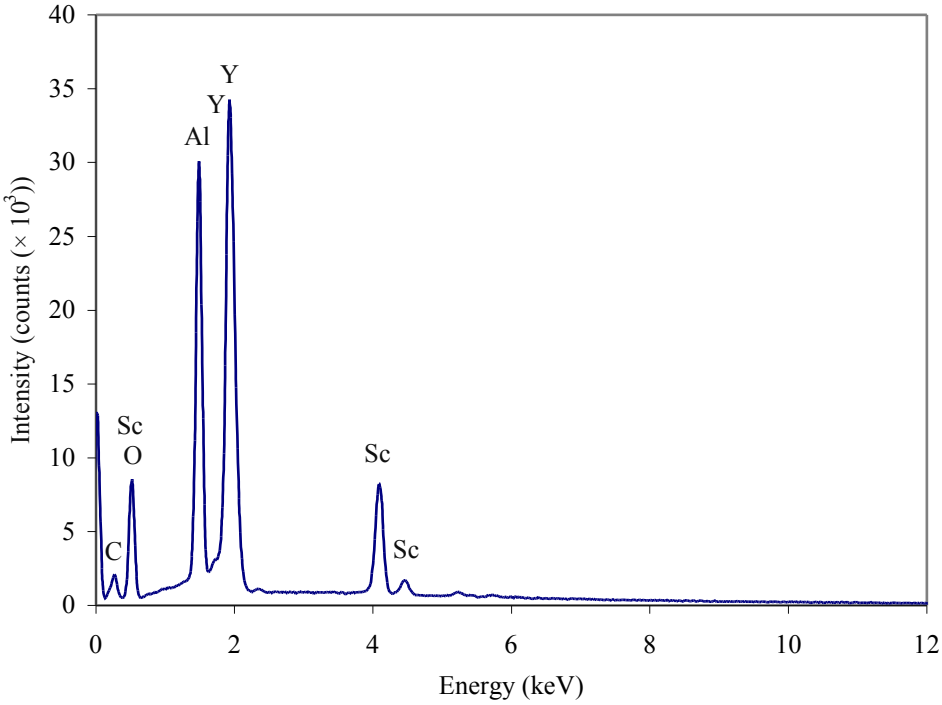

Figure 6.3.10: EDX spectrum of Nd,Cr:YSAG.

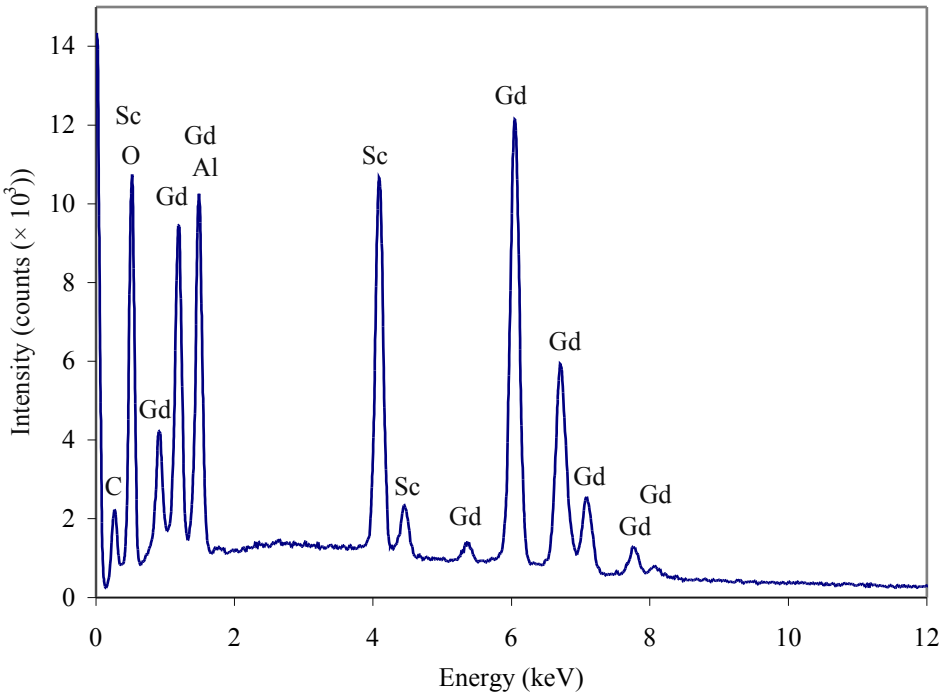

Figure 6.3.11: EDX spectrum of Cr:GSAG.

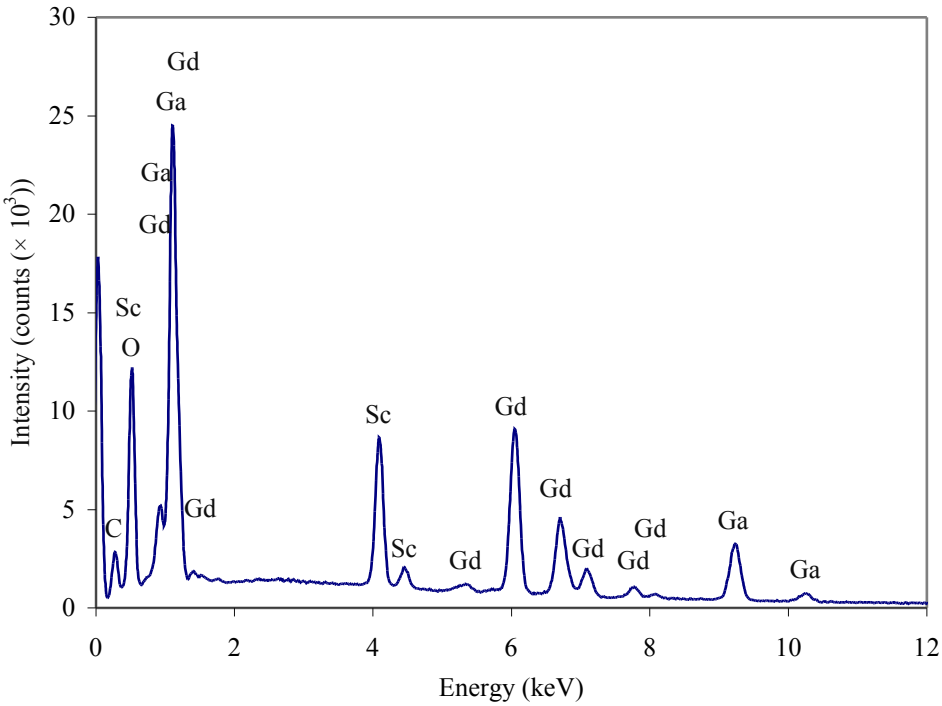

Figure 6.3.12: EDX spectrum of Nd,Cr:GSGG.

As was the case for previously displayed EDX analysis, the results for oxygen content were too inaccurate to be of use. The samples were analysed five times at different locations on the sample surfaces and an average was taken of the results. Since the oxygen content results were unreliable, only the ratios of the elements other than oxygen are presented below in table 6.3.3. The error was estimated from the results of the analysis of bulk crystals.

Sample analysed	Ratio of elements other than oxygen
YGG film	$Y_3Ga_{3.1 \pm 0.2}$
Bulk YGG	$Y_3Ga_{3.4 \pm 0.2}$
Nd,Cr:YSAG film	$Y_3Sc_{1.1 \pm 0.2}Al_{3.4 \pm 0.2}$
Bulk Nd,Cr:YSAG	$Y_3Sc_{1.3 \pm 0.2}Al_{4.1 \pm 0.2}$
Cr:GSAG film	$Gd_3Sc_{1.9 \pm 0.2}Al_{2.9 \pm 0.2}$
Bulk Cr:GSAG	$Gd_3Sc_{2.0 \pm 0.2}Al_{3.3 \pm 0.2}$
Nd,Cr:GSGG film	$Gd_3Sc_{1.9 \pm 0.2}Ga_{2.2 \pm 0.2}$
Bulk Nd,Cr:GSGG	$Gd_3Sc_{2.1 \pm 0.2}Ga_{3.1 \pm 0.2}$

Table 6.3.3: EDX results for the thin YbAG film.

The YGG film is gallium deficient, but the bulk crystal also appears to be gallium deficient so the target is likely to be partly to blame. The YSAG target is scandium deficient, but it appears that the stoichiometry has been made up with extra aluminium instead so that the crystal still has a garnet stoichiometry. With this in mind, it appears that the Nd,Cr:YSAG film is slightly aluminium deficient. The stoichiometry of elements other than oxygen in Cr:GSAG film is very close to bulk and in terms of composition, represents the best film grown so far. The Nd,Cr:GSGG film is slightly gallium deficient relative to the bulk crystal. The relative deficiencies in film stoichiometries fit with the relative broadening of XRD peaks; YGG was the worst affected, followed by GSGG, GSAG and YSAG. Scandium seems to be retained through the deposition process more than aluminium or gallium, and from all of the EDX analysis it appears that aluminium is retained more than gallium.

6.3.3 Conclusions

- The potential of the current setup and growth conditions has been proven by the growth of several different garnet crystal films.
- The films were all found to be highly textured crystal and had compositions close to bulk crystals (allowing for some deficient target crystals).

- The results from XRD and EDX analysis may suggest that quaternary garnets grow with a higher quality than ternary garnets.

6.4 Multilayer film results

A four-layer film geometry was grown in preparation for future work. The layers were deposited in single 20 minute growth runs, and the thickness of each layer varied as a result of the slightly different absorption properties of the garnets deposited. To simulate a cladding-pumped geometry, a core layer of Nd,Cr:GSGG was grown with YGG cladding layers and a YAG capping layer. Laser trial experiments have not been attempted yet.

6.4.1 Scanning electron microscopy

Figure 6.4.1 shows a SEM image of the multilayers where the layers can be clearly distinguished. The YGG has grown with a slightly higher deposition rate than the Nd,Cr:GSGG and YAG layers. The YGG layers are both about 2.1 μm thick whereas the Nd,Cr:GSGG and YAG layers are about 1.4 μm thick.

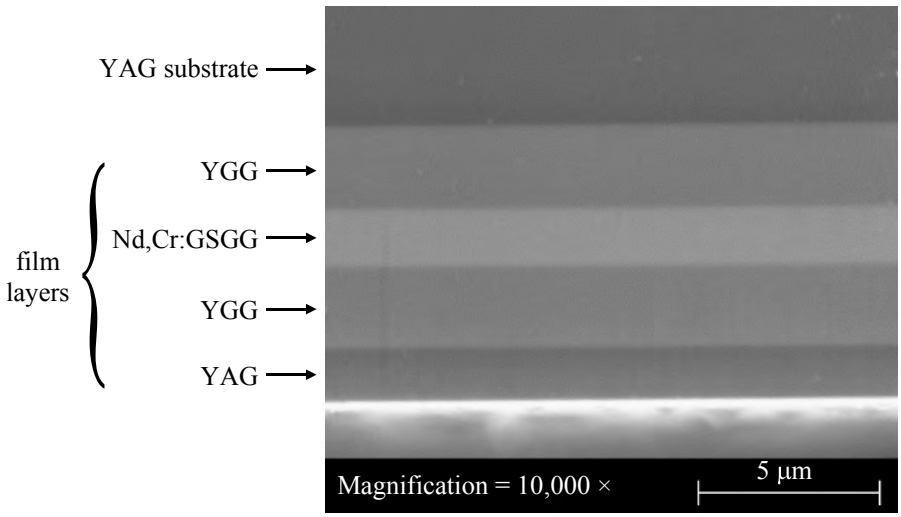

Figure 6.4.1: SEM image of the multilayers.

6.4.2 X-ray diffraction spectra

Figures 6.4.2 and 6.4.3 shows an XRD spectrum and some expanded views of the peaks respectively of the multilayer film of YGG, Nd,Cr:GSGG and YAG.

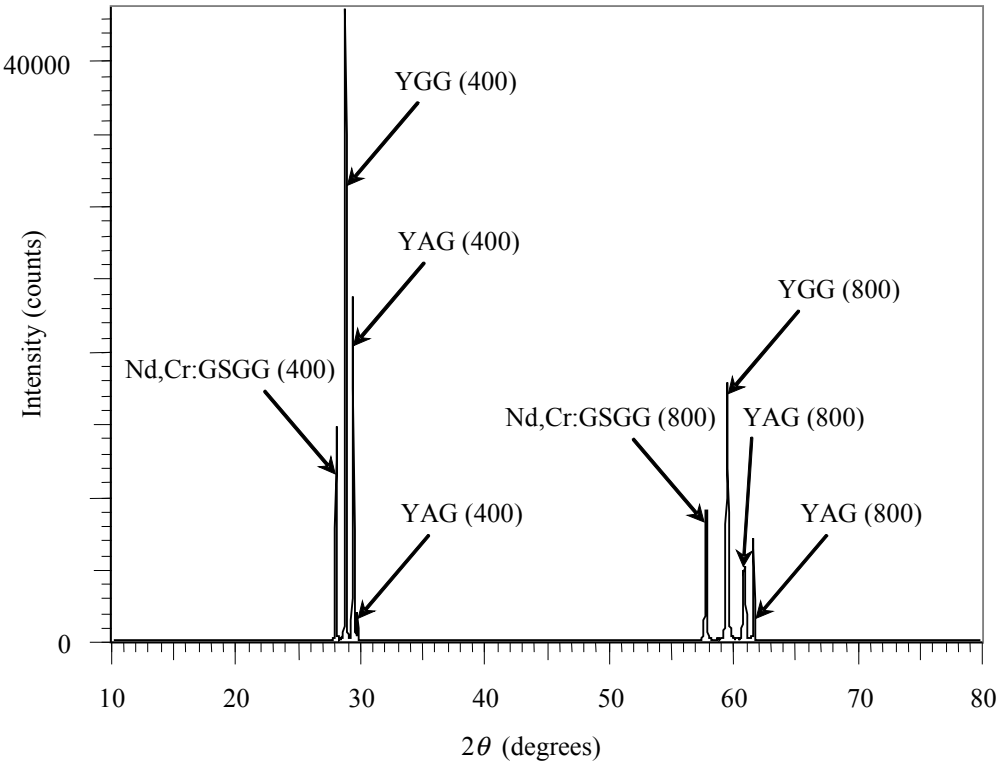

Figure 6.4.2: XRD spectrum of a multilayer film of YGG, Nd,Cr:GSGG and YAG.

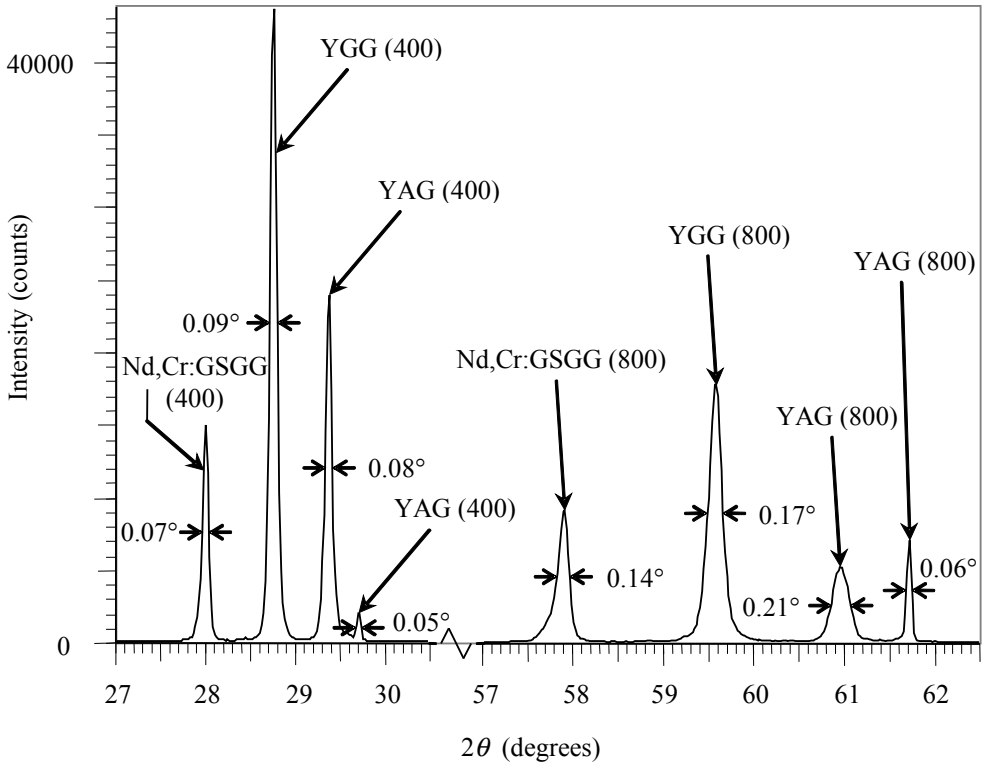

Figure 6.4.3: Expanded views of the XRD peaks of a multilayer film of YGG, Nd,Cr:GSGG and YAG.

Various properties of the spectrum are summarised in table 6.4.1 and the *D*-spacing values have been normalised using the positions of the YAG substrate peaks.

Crystal (orientation)	**2θ (degrees)**	**FWHM (degrees)**	***D*-spacing (Å)**	**Normalised *D*-spacing (Å)**	**Database *D*-spacing (Å)**
Nd,Cr:GSGG (400)	27.982	0.07	3.186	3.179	3.1360 [54]
Nd,Cr:GSGG (800)	57.894	0.14	1.592	1.589	1.5680 [54]
YGG cladding (400)	28.746	0.09	3.103	3.097	3.0682 [43]
YGG cladding (800)	59.573	0.17	1.551	1.548	1.5341 [43]
YAG cap (400)	29.382	0.08	3.037	3.031	3.0015 [42]
YAG cap (800)	60.968	0.21	1.518	1.516	1.5008 [42]
YAG substrate (400)	29.700	0.05	3.006	-	3.0015 [42]
YAG substrate (800)	61.723	0.06	1.502	-	1.5008 [42]

Table 6.4.1: Summary of the multilayer film of YGG, Nd,Cr:GSGG and YAG XRD spectrum properties.

The shifts of the normalised *D*-spacings relative to database values for each layer are shown in table 6.4.2.

Crystal (orientation)	Shift of normalised *D*-spacing relative to the database value
Nd,Cr:GSGG (400)	1.4%
Nd,Cr:GSGG (800)	1.3%
YGG cladding (400)	0.95%
YGG cladding (800)	0.91%
YAG cap (400)	0.97%
YAG cap (800)	1.0%

Table 6.4.2: Summary of the shifts of the normalised *D*-spacings relative to database values for the multilayer film.

The shifts of the normalised *D*-spacings for each layer of the multilayer film are similar to the shifts observed for single-layer films of the same crystals. This indicates that the layers have grown similarly to the previous single-layer thin films. The areas under the peaks are representative of the total intensity of X-rays diffracted from each type of garnet and should be proportional to the thickness of each type of garnet and the depth below other layers. Each group of peaks fit this proposition; the YGG has caused the most intense diffraction because there are two layers and they are both thicker than the YAG and Nd,Cr:GSGG layers, whereas the YAG capping layer and the Nd,Cr:GSGG core layer have caused the next highest intensity of diffraction and finally the YAG substrate has caused the least intense diffraction because it is close to half the maximum penetration depth of X-rays.

The FWHM of the (400) peaks are all comparable to the YAG substrate peak but as has been observed for previous films the (800) peaks are broader than the YAG substrate peak. This is due to the interception of defects at the layer boundaries and also indicates that the layers are likely to have slightly deficient stoichiometries as was observed for previous single-layer thin films. The YGG layers appear to be of a higher quality than the previously grown single-layer YGG thin film, this may be due to a small difference in the target alignment between the depositions.

6.4.3 Energy dispersive X-ray analysis

The YAG capping layer was analysed and found to have the same ratio of ytterbium to aluminium as the previously analysed thick Nd:GGG film YAG capping layer, $Y_3Al_{4.0 \pm 0.2}$. The resolution of the EDX apparatus was not fine enough to analyse the layers separately, but an alternative mode of operation, line-scan mode, allowed the layers to be analysed and

the relative occurrence of each element across the layers to be seen (though the line-scan is still resolution limited). Figure 6.4.4 shows the results from the EDX line-scan across the multilayers (perpendicular to the layer planes).

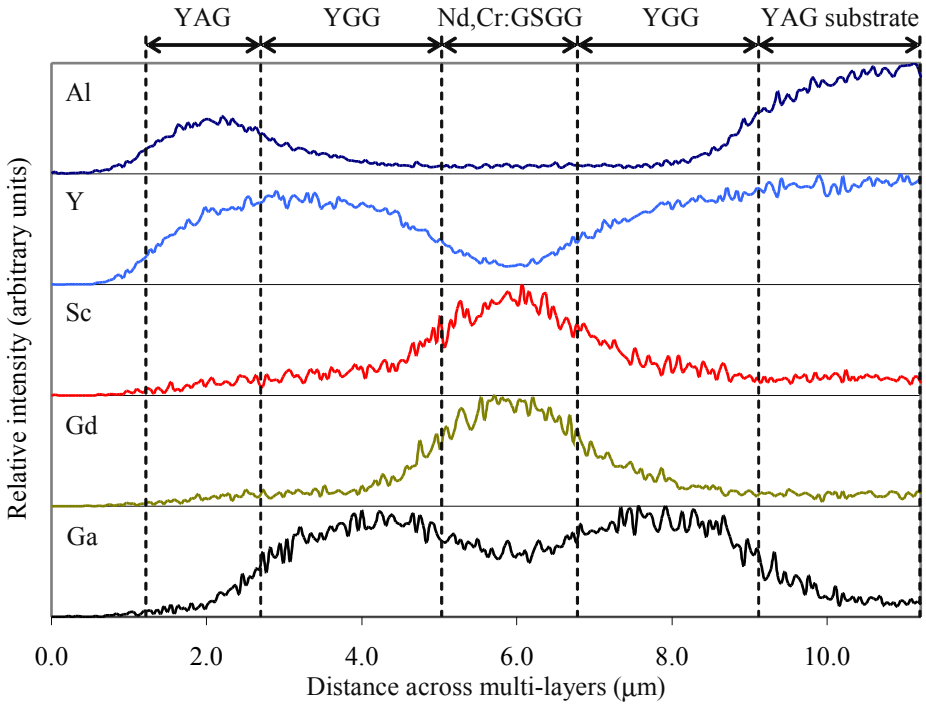

Figure 6.4.4: EDX line-scan perpendicular to the multilayer film planes.

The layer thicknesses appear to be slightly bigger than the SEM image of the multilayers suggested, this is due to a small amount of sample movement (caused by charging) which has stretched the line-scan data. Aluminium has been found in the YAG capping layer and the YAG substrate, and the response from the capping layer is less than from the substrate, in line with the slightly deficient stoichiometry of the capping layer. Yttrium has been found in the YAG capping layer, the YGG cladding layers and the YAG substrate, and the response from the layers is slightly less than from the substrate, indicating that the layers may be slightly yttrium deficient. Scandium and gadolinium has only been found in the Nd,Cr:GSGG layer, as expected. Gallium has been found in the YGG cladding layers and the Nd,Cr:GSGG core layer, and the response is slightly less in the Nd,Cr:GSGG layer, as expected.

6.4.4 Conclusions

- A four-layer garnet crystal geometry has been fabricated by PLD, the first to date to the best of our knowledge.
- The layers were all found to be highly textured crystal and had compositions close to bulk.

6.5 Conclusions summary

- The fabrication of a thick YbAG film, a four-layer garnet crystal geometry and a range of different garnet crystals has opened up the potential for device applications from garnet films grown by PLD.
- The films were all found to be highly textured crystal and had stoichiometries (of elements other than oxygen) close to bulk crystals.
- It is thought that the difficulties with laser experiments with the thick YbAG film may be remedied by the growth of a thicker film (effectively desensitising the laser operation to alignment), the use of a dopant other than ytterbium, such as erbium, or operation in pulsed mode to reduce thermal effects.
- The results from XRD and EDX analysis may suggest that quaternary garnets are a brighter prospect than ternary garnets in terms of crystal quality.

Chapter 7

Conclusions and Future Work

7.1 Introduction

A summary of the conclusions made throughout this thesis is presented here along with a discussion of future work that may be undertaken with garnet films fabricated by PLD, and the future directions of the PLD research group.

7.2 Conclusions summary

7.2.1 Conclusions from introductory chapters

In Chapter 2, an overview of the results obtained to date from optically waveguiding films grown by PLD was presented, and the benchmark for measuring the quality of current films was set in terms of film thickness, propagation loss and device capability. Also, a discussion of alternative fabrication techniques highlighted the advantages and disadvantages of using PLD, and set the benchmarks for measuring the quality of current films relative to some of

the best results obtained using other fabrication techniques. The main competitors to PLD, for the fabrication of thick garnet crystal films and multilayers, were found to be LPE and direct bonding.

In Chapter 3, an overview of the theoretical aspects of PLD, planar waveguides and lasers was presented. Some of the problems that must be overcome to realise high quality films from PLD, and the reasoning behind the various different device geometries reported in this thesis were discussed.

In Chapter 4, the experimental techniques required for PLD, the preparation of waveguides and subsequent laser experiments were presented. An improved substrate holder design was described, and deposition using multiple growth runs and target reconditioning was found to be a route to thick film growth without the occurrence of particulates increasing significantly. The use of 1 mm thick substrates was found to allow thicker films to be polished without the problems of substrate cracking.

7.2.2 Conclusions from results chapters

In Chapter 5, the results from a series of Nd:GGG devices were presented. Structural, compositional and optical analysis of the Nd:GGG films have shown that they have qualities approaching bulk crystal. XRD analysis has found that the films are all highly textured crystal, and suggests that the crystal lattice relaxes slightly and the occurrence of defects decreases as films get thicker. The (800) XRD peaks were found to be a more sensitive measure of crystal quality than the (400) XRD peaks. The crystal lattice size of films was found to be shifted depending on the thickness of the substrate used. This is thought to be due to stress in the film as a result of the slightly deficient crystal structure and stoichiometry, and the effect of thermal expansion mismatch may also be adding to this stress, though the stress observed in the films is significantly greater than predicted by thermal expansion mismatch alone. Cracking at the polishing stage of waveguide preparation (thought to be due to the stress in the films) was the limiting factor for the successful preparation of devices fabricated throughout the course of the project. EDX and RBS analysis have found the composition of Nd:GGG films to be slightly gallium deficient and EDX analysis has found the composition of the YAG capping layers to be slightly aluminium deficient. The Nd:GGG film absorption and fluorescence peaks were broadened and sometimes shifted, and this is thought to be due to the slightly deficient crystal structure and stoichiometry.

Lasing was achieved in 40 μm thick and 50 μm thick Nd:GGG films using Ti:sapphire pumping, and subsequently, lasing was achieved in the 50 μm thick film when it was pumped by a diode laser array. The minimum threshold pump powers were 17.8 mW and 27.4 mW for the 40 μm thick and 50 μm thick devices respectively, when using Ti:sapphire pumping, and a minimum threshold of 7.44 W was found for the 50 μm thick device pumped by the diode laser array. Slope efficiencies of 12.5% and 17.5% were obtained for the 40 μm thick device, and 14.6% and 32.0% were obtained for the 50 μm thick device when using Ti:sapphire pumping. A slope efficiency of 11.2% was obtained for the 50 μm thick device pumped by the diode laser array.

Multimode output was observed from the 40 μm thick device, whereas single-mode and multimode output was observed from the 50 μm thick device when using Ti:sapphire pumping and diode pumping respectively. Loss estimates of 0.095 $dBcm^{-1}$ and 0.094 $dBcm^{-1}$ were obtained for the 40 μm thick device, and 0.37 $dBcm^{-1}$ and 0.31 $dBcm^{-1}$ were obtained for the 50 μm thick device, from the results with Ti:sapphire pumping. An upper limit of 0.79 $dBcm^{-1}$ was obtained for the average loss over the entire film, from the results with diode pumping. Also, a YAG capped device allowed the effect of self-imaging to be observed. The results from the thick Nd:GGG films have shown that the method of fabricating thick films by multiple growth runs is capable of producing devices with properties approaching bulk crystal.

In Chapter 6, the results from a thick YbAG film, a four-layer garnet crystal geometry, and a range of different garnet crystals were discussed. A YbAG film with a thickness of 18 ± 2 μm was fabricated. The film displayed excellent quality crystallinity and the ratio of ytterbium to aluminium in a thin film grown with the same conditions was close to the ratio in bulk YbAG crystal. The absorption properties of the thick film differed from bulk YbAG crystal, and this may be an indication that some of the ytterbium is not in the 3+ valence state. Lasing attempts to date have been unsuccessful with the YbAG film, and some of the possibilities for why lasing could not be achieved were discussed.

All of the alternative garnet crystals were found to be highly textured crystal and had stoichiometries (of elements other than oxygen) close to bulk crystals. The results from XRD and EDX analysis may suggest that quaternary garnets grow with properties closer to bulk crystal than ternary garnets. Growth of all of the garnet films further to Nd:GGG have proven the potential of the current setup and deposition conditions, showing that PLD is a very attractive choice as a technique for the fabrication of thick and multilayer garnet crystal films.

7.3 Future work with garnet crystal films

7.3.1 Multilayers and more ideal geometries

The structures of devices fabricated to date were not ideal geometries, and lasing was not attempted in the multilayer film; from a device point of view therefore, further work and optimisation is required before the full potential of garnet crystal films is realised. Due to the apparent limit in Nd:GGG film thickness imposed by cracking at the polishing stage of waveguide preparation, experiments with large thicknesses of alternative garnets (with smaller thermal expansion mismatches to YAG) need to be conducted. Alternatively, the deposition of buffer layers of alternative garnets before the growth of a thick Nd:GGG layer may allow the combination of YAG substrates and thick Nd:GGG films to still be used. These experiments are essential if the large film thicknesses (60-70 μm) required for an ideal self-imaging device are to survive the polishing process. The thin four-layer film reported here needs to undergo laser trial experiments, and multilayer structures with more ideal layer thicknesses are required to truly utilise the advantages presented by the use of diode laser arrays as pumps. A further step will be to go to six-layer geometries, but more experimentation will be required for this step if the desirable sapphire substrates are to be used.

7.3.2 Thick films used as thin-disk lasers

A first step for a possible improvement of the lasing capability of the thick YbAG film is to anneal it, though this may lead to complications with cracking. A set of YbAG films need to be grown at different temperatures and the absorption spectra compared to isolate what is happening with the valence state of the ytterbium ions. Other options are to attempt pulsed operation, which will suffer less from detrimental thermal effects, grow a thicker film with a lower concentration of ytterbium, making lasing less sensitive to alignment, or attempt growth of an Er:YAG device, which may lase more easily because it can be operated as a four-level laser. The use of multilayers can also be applied to thin-disk lasers; a layer doped with a saturable absorber ion such as Cr^{4+} would allow Q-switching of a ytterbium based laser film [39].

7.3.3 Novel doping structures and distributions

Rib waveguide lasers offer attractive advantages because light can be coupled to and from optical fibres with relative ease. Lasing has been observed in buried Ti:sapphire rib waveguides fabricated on films grown by PLD [28], and in Nd:GGG rib waveguides fabricated on films grown by LPE [160]. It should be possible to fabricate buried rib waveguide lasers from neodymium-doped garnet films. An investigation of other ways of creating useful doping structures and distributions, or variation of the dopant concentration with film thickness is also a possibility. For example, the use of a mask in front of the substrate may allow ribs or sections of film with a saturable absorber dopant such as Cr^{4+} to be fabricated without the need for post-deposition processing. In such an experiment the definition of the patterns of film deposited will depend on the distance of the mask from the substrate, making the experiment quite challenging.

7.4 Future work and directions for the pulsed laser deposition research group

7.4.1 New materials to be considered

The potential of glass coatings and films has not yet been fully realised due to problems with the quality of film growth. Glass could be used as a coating for various different applications such as capping layers, and with optimal growth conditions, PLD could be a good way of depositing glass layers quickly and with relative ease. Glass could also be used as a thin film material for planar waveguide devices such as amplifiers and lasers, and the isotropic properties of glass should make it an easy material to grow because of the absence of the constraints presented by crystal properties.

Growth of ferroelectric films on silicon is an interesting prospect, and may have many applications if it can be perfected. Silicon has been widely used to fabricate MEMS devices. However, actuation of silicon based devices is not ideal because of the dependence on the Coulombic force. Coulomb's law has an inverse square dependence upon distance/radius, making very small actuating devices based on silicon difficult to control without crashing the devices and rendering them stuck. Actuating devices based upon a ferroelectric material,

such as lithium niobate, depend upon the piezoelectric effect, which is linear and hence far simpler to control. However, since lithium niobate has poor electrical conduction properties, electrical circuitry of a different material is required to support and control devices. A combination of the electrical properties of silicon with the vast range of exploitable properties of lithium niobate may be perfect for the fabrication of MEMS devices, and the technique of PLD may be a suitable technique for the growth of the lithium niobate layers.

7.4.2 Femtosecond pulsed laser deposition

PLD using ultra-short femtosecond pulses is thought to be a route to the elimination of particulates that arise due to thermal effects because the absorption of ultra-short pulses is by multi-photon absorption [259]. Also, the dynamics of plasmas produced by femtosecond pulses may have favourable differences to plasmas generated by nanosecond pulses [260], allowing new materials to be grown that may have only had limited success with conventional excimer laser based PLD. To date, reports of films grown using femtosecond PLD have been limited to simple compounds such as nitrides [261], carbon [262], zinc oxide [263; 264], gallium arsenide (GaAs) [265] and barium titanate [266], and mixed success has been experienced. From the films reported so far, it is unclear if femtosecond PLD always leads to particulate free films, and it is not known if materials with complex stoichiometries can be grown with femtosecond PLD. The new femtosecond laser facility at the ORC will allow the PLD research group to investigate the advantages and disadvantages offered by femtosecond PLD, and compare the deposition of materials such as garnets, for which we have previously experienced success, using femtosecond and nanosecond pulses.

Appendix I

Publications

I.I Publications from results reported in this thesis

Journal articles:

On the growth and lasing characteristics of thick Nd:GGG waveguiding films fabricated by pulsed laser deposition. C. Grivas, T. C. May-Smith, D. P. Shepherd & R. W. Eason. Applied Physics A-Materials Science & Processing **79** p1203-1206 (2004).

Laser operation of a low loss (0.1 dBcm^{-1}) Nd:$Gd_3Ga_5O_{12}$ thick (40 µm) planar waveguide grown by pulsed laser deposition. C. Grivas, T. C. May-Smith, D. P. Shepherd & R. W. Eason. Optics Communications **229** p355-361 (2004).

Thick film growth of high optical quality low loss (0.1 dBcm^{-1}) Nd:$Gd_3Ga_5O_{12}$ on $Y_3Al_5O_{12}$ by pulsed laser deposition. T. C. May-Smith, C. Grivas, D. P. Shepherd, R. W. Eason & M. J. F. Healy. Applied Surface Science **223** p361-371 (2004).

Conferences:

A low-loss PLD fabricated garnet planar waveguide laser. C. Grivas, T. C. May-Smith, J. Wang, M. S. B. Darby, D. P. Shepherd & R. W. Eason. EPS-QEOD Europhoton, Lausanne, August-September (2004).

Pulsed laser deposition of thick multilayer garnet films for cladding-pumped planar waveguide laser devices. T. C. May-Smith, C. Grivas, D. P. Shepherd, M. S. B. Darby & R. W. Eason. CLEO/IQEC, San Francisco, May (2004).

Laser operation of a low loss (0.1 dBcm^{-1}) Nd:$Gd_3Ga_5O_{12}$ thick film (40 µm) waveguide grown by pulsed laser deposition. C. Grivas, T. C. May-Smith, D. P. Shepherd & R. W. Eason. COLA, Crete, October (2003).

I.II Other publications from the pulsed laser deposition research group

Journal articles:

Single-transverse-mode Ti:sapphire rib waveguide laser. C. Grivas, D. P. Shepherd, T. C. May-Smith & R. W. Eason. Optics Express **13** p210-215 (2005).

Broadband single-transverse-mode fluorescence sources based on ribs fabricated in pulsed laser deposited Ti:sapphire waveguides. C. Grivas, T. C. May-Smith, D. P. Shepherd, R. W. Eason, M. Pollnau & M. Jelinek. Applied Physics A-Materials Science & Processing **79** p1195-1198 (2004).

Performance of Ar^+-milled Ti:sapphire rib waveguides as single-transverse-mode broadband fluorescence sources. C. Grivas, D. P. Shepherd, T. C. May-Smith, R. W. Eason, M. Pollnau, A. Crunteanu & M. Jelinek. IEEE Journal of Quantum Electronics **39** p501-507 (2003).

Book chapter:

Optical waveguides. R. W. Eason, S. J. Barrington, C. Grivas, T. C. May-Smith & D. P. Shepherd. In Pulsed Laser Deposition of Thin Films: Applications in Electronics, Sensors, and Biomaterials. Eason, R. W. & D. B. Chrisey (Eds.). (to be released in 2006).

Conferences:

Single-transverse-mode laser operation of Ti:sapphire rib waveguides. C. Grivas, D. P. Shepherd, T. C. May-Smith, R. W. Eason & M. Pollnau. EPS-QEOD Europhoton, Lausanne, August-September (2004).

Ar^+ beam etched Ti:sapphire rib waveguides: a route for the development of broadband fluorescence and channel laser sources. C. Grivas, D. P. Shepherd, T. C. May-Smith, M. S. B. Darby, R. W. Eason & M. Pollnau. CLEO/IQEC, San Francisco, May (2004).

Single-transverse-mode broadband luminescence source based on a PLD grown Ti:sapphire waveguide in rib geometry. C. Grivas, D. P. Shepherd, T. C. May-Smith, R. W. Eason, M. Pollnau & A. Crunteanu. COLA, Crete, October (2003).

Ti:sapphire rib waveguides as single-transverse-mode broadband fluorescence sources for optical coherence tomography applications. C. Grivas, D. P. Shepherd, T. C. May-Smith, R. W. Eason, M. Pollnau, A. Crunteanu & M. Jelinek. CLEO/Europe EQEC, Munich, June (2003).

Invited talk:

Optical waveguides grown by pulsed laser deposition for applications in lasing and photosensitivity. R. W. Eason, D. P. Shepherd, S. J. Barrington, C. Grivas, T. C. Smith [name changed to May-Smith] & M. Pollnau. Doctoral School Programme - Swiss Federal Institute of Technology, Lausanne, March (2002).

List of References

[1] Smith, H. M. & A. F. Turner. *Vacuum deposited thin films using a ruby laser*. Applied Optics **4** p147-148 (1965).

[2] Dijkkamp, D., T. Venkatesan, X. D. Wu, S. A. Shaheen, N. Jisrawi, Y. H. Min-Lee, W. L. McLean & M. Croft. *Preparation of Y-Ba-Cu oxide superconductor thin films using pulsed laser evaporation from high T_c bulk material*. Applied Physics Letters **51** p619-621 (1987).

[3] Wu, X. D., D. Dijkkamp, S. B. Ogale, A. Inam, E. W. Chase, P. F. Miceli, C. C. Chang, J. M. Tarascon & T. Venkatesan. *Epitaxial ordering of oxide superconductor thin-films on (100) $SrTiO_3$ prepared by pulsed laser evaporation*. Applied Physics Letters **51** p861-863 (1987).

[4] Schwartz, H. & H. A. Tourtellotte. *Vacuum deposition by high-energy laser with emphasis on barium titanate films*. Journal of Vacuum Science and Technology **6** p373-378 (1969).

[5] Dubowski, J. J., D. F. Williams, P. B. Sewell & P. Norman. *Epitaxial-growth of (100) CdTe on (100) GaAs induced by pulsed laser evaporation*. Applied Physics Letters **46** p1081-1083 (1985).

[6] Vogel, E. M., E. W. Chase, J. L. Jackel & B. J. Wilkens. *Fabrication of thin-film nonlinear optical-glasses using pulsed excimer laser deposition*. Applied Optics **28** p649-651 (1989).

[7] Joshi, S., R. Nawathey, V. N. Koinkar, V. P. Godbole, S. M. Chaudhari, S. B. Ogale & S. K. Date. *Pulsed laser deposition of iron-oxide and ferrite films*. Journal of Applied Physics **64** p5647-5649 (1988).

[8] Ramesh, R., K. Luther, B. Wilkens, D. L. Hart, E. Wang, J. M. Tarascon, A. Inam, X. D. Wu & T. Venkatesan. *Epitaxial growth of ferroelectric bismuth titanate thin films by pulsed laser deposition*. Applied Physics Letters **57** p1505-1507 (1990).

[9] Singh, R. K. & J. Narayan. *Pulsed-laser evaporation technique for deposition of thin-films - physics and theoretical-model*. Physical Review B **41** p8843-8859 (1990).

[10] Singh, R. K., O. W. Holland & J. Narayan. *Theoretical-model for deposition of superconducting thin-films using pulsed laser evaporation technique*. Journal of Applied Physics **68** p233-247 (1990).

[11] Bhattacharya, D., R. K. Singh & P. H. Holloway. *Laser-target interactions during pulsed laser deposition of superconducting thin films*. Journal of Applied Physics **70** p5433-5439 (1991).

[12] Ventzek, P. L. G., R. M. Gilgenbach, D. M. Heffelfinger & J. A. Sell. *Laser-beam deflection measurements and modeling of pulsed laser ablation rate and near-surface plume densities in vacuum*. Journal of Applied Physics **70** p587-593 (1991).

[13] Davis, M. F., J. Wosik, K. Forster, S. C. Deshmukh, H. R. Rampersad, S. Shah, P. Siemsen, J. C. Wolfe & D. J. Economou. *Deposition of high-quality $YBa_2Cu_3O_{7-delta}$ thin-films over large areas by pulsed laser ablation with substrate scanning*. Journal of Applied Physics **69** p7182-7188 (1991).

[14] Gupta, A. & B. W. Hussey. *Laser deposition of $YBa_2Cu_3O_{7-delta}$ films using a pulsed oxygen source*. Applied Physics Letters **58** p1211-1213 (1991).

[15] Youden, K. E., T. Grevatt, R. W. Eason, H. N. Rutt, R. S. Deol & G. Wylangowski. *Pulsed laser deposition of Ga-La-S chalcogenide glass thin film optical waveguides*. Applied Physics Letters **63** p1601-1603 (1993).

[16] Dorsey, P. C., S. E. Bushnell, R. G. Seed & C. Vittoria. *Epitaxial yttrium-iron-garnet films grown by pulsed-laser deposition*. Journal of Applied Physics **74** p1242-1246 (1993).

[17] Gill, D. S., A. A. Anderson, R. W. Eason, T. J. Warburton & D. P. Shepherd. *Laser operation of an Nd:$Gd_3Ga_5O_{12}$ thin-film optical waveguide fabricated by pulsed laser deposition*. Applied Physics Letters **69** p10-12 (1996).

[18] Anderson, A. A., C. L. Bonner, D. P. Shepherd, R. W. Eason, C. Grivas, D. S. Gill & N. Vainos. *Low loss (0.5 dB/cm) Nd:$Gd_3Ga_5O_{12}$ waveguide layers grown by pulsed laser deposition*. Optics Communications **144** p183-186 (1997).

[19] Schenck, P. K., M. D. Vaudin, D. W. Bonnell, J. W. Hastie & A. J. Paul. *Particulate reduction in the pulsed laser deposition of barium titanate thin films*. Applied Surface Science **127-129** p655-661 (1998).

[20] Schey, B., W. Biegel, M. Kuhn & B. Stritzker. *Large area pulsed laser deposition of YBCO thin films*. IEEE Transactions on Applied Superconductivity **9** p2359-2362 (1999).

[21] Barrington, S. J., T. Bhutta, D. P. Shepherd & R. W. Eason. *The effect of particulate density on performance of Nd : $Gd_3Ga_5O_{12}$ waveguide lasers grown by pulsed laser deposition*. Optics Communications **185** p145-152 (2000).

[22] Barrington, S. J.. *Planar waveguide devices fabricated by pulsed laser deposition*. Ph.D. Thesis, Physics & Astronomy, University of Southampton, Southampton (2001).

[23] Kuzanyan, A. S., G. R. Badalyan, V. R. Nikoghosyan, A. L. Gyulamiryan & A. M. Gulian. *Three simple methods to obtain large area thin films by pulsed laser deposition*. IEEE Transactions on Applied Superconductivity **11** p3852-3855 (2001).

[24] Crunteanu, A., M. Pollnau, G. Janchen, C. Hibert, P. Hoffmann, R. P. Salathe, R. W. Eason, C. Grivas & D. P. Shepherd. *Ti : sapphire rib channel waveguide fabricated by reactive ion etching of a planar waveguide*. Applied Physics B-Lasers and Optics **75** p15-17 (2002).

[25] Gyorgy, E., I. N. Mihailescu, M. Kompitsas & A. Giannoudakos. *Particulates-free Ta thin films obtained by pulsed laser deposition: the role of a second laser in the laser-induced plasma heating*. Applied Surface Science **195** p270-276 (2002).

[26] May-Smith, T. C., C. Grivas, D. P. Shepherd, R. W. Eason & M. J. F. Healy. *Thick film growth of high optical quality low loss (0.1 dBcm^{-1}) Nd:$Gd_3Ga_5O_{12}$ on $Y_3Al_5O_{12}$ by pulsed laser deposition*. Applied Surface Science **223** p361-371 (2004).

[27] Grivas, C., T. C. May-Smith, D. P. Shepherd & R. W. Eason. *Laser operation of a low loss (0.1 dB/cm) Nd : $Gd_3Ga_5O_{12}$ thick (40 mu m) planar waveguide grown by pulsed laser deposition*. Optics Communications **229** p355-361 (2004).

[28] Grivas, C., D. P. Shepherd, T. C. May-Smith & R. W. Eason. *Single-transverse-mode Ti:sapphire rib waveguide laser*. Optics Express **13** p210-215 (2005).

[29] ISI Web of Science. http://wos.mimas.ac.uk. (Last accessed: April 2005).

[30] Zenteno, L.. *High-power double-clad fiber lasers*. Journal of Lightwave Technology **11** p1435-1446 (1993).

[31] Jackson, S. D. & T. A. King. *High-power diode-cladding-pumped Tm-doped silica fiber laser*. Optics Letters **23** p1462-1464 (1998).

[32] Furusawa, K., A. Malinowski, J. H. V. Price, T. M. Monro, J. K. Sahu, J. Nilsson & D. J. Richardson. *Cladding pumped Ytterbium-doped fiber laser with holey inner and outer cladding*. Optics Express **9** p714-720 (2001).

[33] Limpert, J., T. Schreiber, S. Nolte, H. Zellmer, A. Tunnermann, R. Iliew, F. Lederer, J. Broeng, G. Vienne, A. Petersson & C. Jakobsen. *High-power air-clad large-mode-area photonic crystal fiber laser*. Optics Express **11** p818-823 (2003).

[34] Shepherd, D. P., S. J. Hettrick, C. Li, J. I. Mackenzie, R. J. Beach, S. C. Mitchell & H. E. Meissner. *High-power planar dielectric waveguide lasers*. Journal of Physics D-Applied Physics **34** p2420-2432 (2001).

[35] Stewen, C., K. Contag, M. Larionov, A. Giesen & H. Hugel. *A 1-kW cw thin disc laser*. IEEE Journal of Selected Topics in Quantum Electronics **6** p650-656 (2000).

[36] Patel, F. D., E. C. Honea, J. Speth, S. A. Payne, R. Hutcheson & R. Equall. *Laser demonstration of $Yb_3Al_5O_{12}$ (YbAG) and materials properties of highly doped Yb:YAG*. IEEE Journal of Quantum Electronics **37** p135-143 (2001).

[37] Taira, T., J. Saikawa, T. Kobayashi & R. L. Byer. *Diode-pumped tunable Yb:YAG miniature lasers at room temperature: modeling and experiment*. IEEE Journal of Selected Topics in Quantum Electronics **3** p100-104 (1997).

[38] Xu, X. D., Z. W. Zhao, J. Xu & P. Z. Deng. *Crystal growth and spectral properties of $Yb_3Al_5O_{12}$*. Journal of Crystal Growth **257** p272-275 (2003).

[39] Buryy, O. A., S. B. Ubiszkii, S. S. Melnyk & A. O. Matkovskii. *The Q-switched Nd:YAG and Yb:YAG microchip lasers optimization and comparative analysis*. Applied Physics B-Lasers and Optics **78** p291-297 (2004).

[40] Adair, R., L. L. Chase & S. A. Payne. *Nonlinear refractive index of optical crystals*. Physical Review B **39** p3337-3350 (1989).

[41] Foster, J. D. & L. M. Osterink. *Index of refraction and expansion thermal coefficients of Nd:YAG*. Applied Optics **7** p2428-2429 (1968).

[42] Nakatsuka, A., A. Yoshiasa & T. Yamanaka. *Cation distribution and crystal chemistry of Y_3 Al_{5-x} Ga_x O_{12} (0<=x<=5) garnet solid solution*. Acta Crystallographica Section B **55** p266-272 (1999).

[43] Nakatsuka, A., A. Yoshiasa & S. Takeno. *Site preference of cations and structural variation in Y_3 Fe_{5-x} Ga_x O_{12}*. Acta Crystallographica Section B **51** p737-745 (1995).

[44] Allik, T. H., C. A. Morrison, J. B. Gruber & M. R. Kokta. *Crystallography, spectroscopic analysis, and lasing properties of Nd3+:$Y_3Sc_2Al_3O_{12}$*. Physical Review B **41** p21-30 (1990).

[45] Molecular Technology GmbH, Berlin, Germany (crystal supplier). http://www.mt-berlin.com/frames_cryst/descriptions/ysgg.htm. (Last accessed: April 2005).

[46] Efremov, V. A., N. D. Zakharov, G. M. Kuz'micheva, B. V. Mukhin & V. V. Chernyshev. *Yttrium-scandium-gallium garnet: the crystal structure*. Zhurnal Neorganicheskoi Khimii **38** p220-225 (1993).

[47] Euler, F. & J. A. Bruce. *Oxygen coordinates of compounds with garnet structure*. Acta Crystallographica **19** p971-978 (1965).

[48] Wood, D. L. & K. Nassav. *Optical properties of gadolinium gallium garnet*. Applied Optics **29** p3704-3707 (1990).

[49] Gloshkova, V. B., Y. V. Zharikov, S. Y. Zinovev, V. A. Krzhizhanovskaya, V. V. Osiko & P. A. Stodenikin. *Thermal expansion of rare-earth gallium garnets*. Rep. 289, General Physics Institute, Moscow, (1986).

[50] Sawada, H.. *Electron density study of garnets: Z_3 Ga_5 O_{12}; Z = Nd, Sm, Gd, Tb*. Journal of Solid State Chemistry **132** p302-307 (1997).

[51] Hoefer, C. S., K. W. Kirby & L. G. DeShazer. *Thermo-optic properties of gadolinium garnet laser crystals*. Journal of the Optical Society of America B-Optical Physics **5** p2327-2332 (1988).

[52] Sumida, D. S., M. S. Mangir, D. A. Rockwell & M. D. Shinn. *Laser-related properties of chromium and neodymium-doped gadolinium scandium aluminum garnet (Cr-Nd-GSAG)*. Journal of the Optical Society of America B-Optical Physics **11** p2066-2078 (1994).

[53] Yamazaki, S., F. Marumo, K. Tanaka, H. Morikawa, N. Kodama, K. Kitamura & Y. Miyazawa. *A structural study of facet and off-facet parts of rare-earth garnets, $Gd_3Sc_2Al_3O_{12}$, $Gd_3Sc_2Ga_3O_{12}$, and $La_3Lu_2Ga_3O_{12}$*. Journal of Solid State Chemistry **108** p94-98 (1994).

[54] Kondratyuk, I. P., E. V. Zharikov & V. I. Simonov. *Refinement of atomic structures of Gd_3 Sc_2 Ga_3 O_{12} and ($Gd_{0.8}$ $Nd_{0.2}$) Sc_2 Ga_3 O_{12}*. Kristallografiya **31** p51-56 (1988).

[55] Xu, X. D., Z. W. Zhao, X. M. He, P. X. Song, G. Q. Zhou, J. Xu & P. Z. Deng. *Growth and thermal properties of Cr^{4+}: YbAG single crystal*. Materials Letters **58** p3153-3155 (2004).

[56] Etschmann, B. E., V. A. Strel'tsov, N. Ishizawa & E. N. Maslen. *Synchrotron X-ray study of Er_3 Al_5 O_{12} and Yb_3 Al_5 O_{12} garnets*. Acta Crystallographica Section B **57** p136-141 (2001).

[57] Singh, S., R. G. Smith & L. G. Van Uitert. *Stimulated-emission cross section and fluorescent quantum efficiency of Nd^{3+} in yttrium aluminium garnet at room temperature*. Physical Review B **10** p2566-2572 (1974).

[58] Gill, D. S., R. W. Eason, J. Mendiola & P. J. Chandler. *Growth of crystalline $Gd_3Ga_5O_{12}$ thin-film optical wave-guides by pulsed-laser deposition*. Materials Letters **25** p1-4 (1995).

[59] Bonner, C. L., A. A. Anderson, R. W. Eason, D. P. Shepherd, D. S. Gill, C. Grivas & N. Vainos. *Performance of a low-loss pulsed-laser deposited Nd:$Gd_3Ga_5O_{12}$ waveguide laser at 1.06 and 0.94 mu m*. Optics Letters **22** p988-990 (1997).

[60] Vainos, N. A., C. Grivas, C. Fotakis, R. W. Eason, A. A. Anderson, D. S. Gill, D. P. Shepherd, M. Jelinek, J. Lancok & J. Sonsky. *Planar laser waveguides of Ti : sapphire, Nd : GGG and Nd : YAG grown by pulsed laser deposition*. Applied Surface Science **129** p514-519 (1998).

[61] Fukaya, S., K. Adachi, M. Obara & H. Kumagai. *The growth of Cr^{4+}: YAG and Cr^{4+}: GGG thin films by pulsed laser deposition*. Optics Communications **187** p373-377 (2001).

[62] Fukaya, S., T. Hasegawa, Y. Ishida, T. Shimoda & M. Obara. *Fabrication of Nd^{3+}, Cr^{4+} co-doped $Gd_3Ga_5O_{12}$ thin film waveguide by two-target pulsed laser deposition*. Applied Surface Science **177** p147-151 (2001).

[63] Ezaki, M., H. Kumagai, K. Kobayashi, K. Toyoda & M. Obara. *Crystal growth of Nd:YAG laser films on various substrates by pulsed laser deposition*. Japanese Journal of Applied Physics Part 1-Regular Papers Short Notes & Review Papers **34** p6838-6841 (1995).

[64] Ezaki, M., M. Obara, H. Kumagai & K. Toyoda. *Characterization of Nd:$Y_3Al_5O_{12}$ thin films grown on various substrates by pulsed laser deposition*. Applied Physics Letters **69** p2977-2979 (1996).

[65] Kumagai, H., K. Adachi, M. Ezaki, K. Toyoda & M. Obara. *Epitaxial growth of Nd:YAG thin films by pulsed laser deposition*. Applied Surface Science **109-110** p528-532 (1997).

[66] Sonsky, J., M. Jelinek, P. Hribek, J. Oswald, L. Jastrabik, V. Studnicka, C. Fotakis & C. Grivas. *The experience with pulsed laser deposition of Nd : YAG and Nd : YAP thin films for planar laser waveguides*. Laser Physics **8** p285-290 (1998).

[67] Hirata, G. A., O. A. Lopez, L. E. Shea, J. Y. Yi, T. Cheeks, J. McKittrick, J. Siqueiros, M. AvalosBorja, A. Esparza & C. Falcony. *Pulsed laser deposition of $Y_3Al_5O_{12}$:Tb photoluminescent thin films*. Journal of Vacuum Science & Technology a-Vacuum Surfaces and Films **14** p1694-1696 (1996).

[68] Shimoda, T., Y. Ishida, K. Adachi & M. Obara. *Fabrication of highly ytterbium (Yb^{3+})-doped YAG thin film by pulsed laser deposition*. Optics Communications **194** p175-179 (2001).

[69] Jelinek, M., A. Klini, C. Grivas, J. Lancok, V. Studnicka, J. Chval, A. Mackova & C. Fotakis. *Deposition of Er : YAG (YAP) layers by subpicosecond and nanosecond KrF excimer laser ablation*. Applied Surface Science **197** p416-420 (2002).

[70] Willmott, P. R., P. Manoravi & K. Holliday. *Production and characterization of Nd,Cr : GSGG thin films on Si(001) grown by pulsed laser ablation*. Applied Physics A-Materials Science & Processing **70** p425-429 (2000).

[71] Kidoh, H., A. Morimoto & T. Shimizu. *Synthesis of ferromagnetic Bi-substituted yttrium iron garnet films by laser ablation*. Applied Physics Letters **59** p237-239 (1991).

[72] Katoh, Y., N. Sugimoto, A. Tate & A. Shibukawa. *110 -directed ridge formation of epitaxial $Y_3Fe_5O_{12}$ film grown on 111 -oriented $Gd_3Ga_5O_{12}$*. Japanese Journal of Applied Physics Part 2-Letters **31** pL652-L654 (1992).

[73] Katoh, Y., N. Sugimoto, A. Tate & A. Shibukawa. *Preparation of substituted $Y_3Fe_5O_{12}$ single-mode buried wave- guides on a 1 0 0 oriented $Gd_3Ga_5O_{12}$ substrate*. Japanese Journal of Applied Physics Part 2-Letters **32** pL508-L510 (1993).

[74] Kim, H. J., A. M. Grishin, K. V. Rao, S. C. Yu, R. Sbiaa & H. La Gall. *Ce-substituted YIG films grown by pulsed laser deposition for magneto-optic waveguide devices*. IEEE Transactions on Magnetics **35** p3163-3165 (1999).

[75] Higuchi, S., K. Ueda, F. Yahiro, Y. Nakata, H. Uetsuhara, T. Okada & M. Maeda. *Fabrications of cerium-substituted YIG thin films for magnetic field sensor by pulsed-laser deposition*. IEEE Transactions on Magnetics **37** p2451-2453 (2001).

[76] Hayashi, H., S. Iwasa, N. J. Vasa, T. Yoshitake, K. Ueda, S. Yokoyama & S. Higuchi. *Characteristics of Bi : YIG magneto-optic thin films fabricated by pulsed laser deposition method for an optical current transformer*. Japanese Journal of Applied Physics Part 1-Regular Papers Short Notes & Review Papers **41** p410-411 (2002).

[77] Hayashi, H., S. Iwasa, N. J. Vas, T. Yoshitake, K. Ueda, S. Yokoyama, S. Higuchi, H. Takeshita & M. Nakahara. *Fabrication of Bi-doped YIG optical thin film for electric current sensor by pulsed laser deposition*. Applied Surface Science **197** p463-466 (2002).

[78] Anderson, A. A., R. W. Eason, M. Jelinek, C. Grivas, D. Lane, K. Rogers, L. M. B. Hickey & C. Fotakis. *Growth of Ti:sapphire single crystal thin films by pulsed laser deposition*. Thin Solid Films **300** p68-71 (1997).

[79] Anderson, A. A., R. W. Eason, L. M. B. Hickey, M. Jelinek, C. Grivas, D. S. Gill & N. A. Vainos. *Ti:sapphire planar waveguide laser grown by pulsed laser deposition*. Optics Letters **22** p1556-1558 (1997).

[80] Jelinek, M., R. W. Eason, J. Lancok, A. A. Anderson, C. Grivas, C. Fotakis, L. Jastrabik, F. Flory & H. Rigneault. *Waveguiding pulsed laser deposited Ti : sapphire layers on quartz*. Thin Solid Films **322** p259-262 (1998).

[81] Uetsuhara, H., S. Goto, Y. Nakata, N. Vasa, T. Okada & M. Maeda. *Fabrication of a Ti : sapphire planar waveguide by pulsed laser deposition*. Applied Physics A-Materials Science & Processing **69** pS719-S722 (1999).

[82] Serna, R. & C. N. Afonso. *In situ growth of optically active erbium doped Al_2O_3 thin films by pulsed laser deposition*. Applied Physics Letters **69** p1541-1543 (1996).

[83] Pillonnet, A., C. Garapon, C. Champeaux, C. Bovier, R. Brenier, H. Jaffrezic & J. Mugnier. *Influence of oxygen pressure on structural and optical properties of Al_2O_3 optical waveguides prepared by pulsed laser deposition*. Applied Physics A-Materials Science & Processing **69** pS735-S738 (1999).

[84] Serna, R., M. J. de Castro, J. A. Chaos, A. Suarez-Garcia, C. N. Afonso, M. Fernandez & I. Vickridge. *Photoluminescence performance of pulsed-laser deposited Al_2O_3 thin films with large erbium concentrations*. Journal of Applied Physics **90** p5120-5125 (2001).

[85] Grivas, C., D. P. Shepherd, T. C. May-Smith, R. W. Eason, M. Pollnau, A. Crunteanu & M. Jelinek. *Performance of Ar^+-milled Ti : sapphire rib waveguides as single transverse-mode broadband fluorescence sources*. IEEE Journal of Quantum Electronics **39** p501-507 (2003).

[86] Craciun, V., J. Howard, E. S. Lambers, R. K. Singh, D. Craciun & J. Perriere. *Low-temperature growth of Y_2O_3 thin films by ultraviolet- assisted pulsed laser deposition*. Applied Physics A-Materials Science & Processing **69** pS535-S538 (1999).

[87] Korzenski, M. B., P. Lecoeur, B. Mercey, P. Camy & J. L. Doualan. *Low propagation losses of an Er : Y_2O_3 planar waveguide grown by alternate-target pulsed laser deposition*. Applied Physics Letters **78** p1210-1212 (2001).

[88] Lecoeur, P., M. B. Korzenski, A. Ambrosini, B. Mercey, P. Camy & J. L. Doualan. *Growth of Er : Y_2O_3 thin films by pulsed laser ablation from metallic targets*. Applied Surface Science **186** p403-407 (2002).

[89] Pons-Y-Moll, O., J. Perriere, E. Millon, R. M. Defourneau, D. Defourneau, B. Vincent, A. Essahlaoui, A. Boudrioua & W. Seiler. *Structural and optical properties of rare-earth-doped Y_2O_3 waveguides grown by pulsed-laser deposition*. Journal of Applied Physics **92** p4885-4890 (2002).

[90] Burmester, P. B. W., T. Ishii, G. Huber, M. Kurfiss & M. Schilling. *Characterization of crystalline europium doped alpha-Y_2O_3 PLD- films grown on alpha-Al_2O_3.* Materials Science and Engineering B-Solid State Materials for Advanced Technology **105** p25-29 (2003).

[91] Bar, S., G. Huber, J. Gonzalo, A. Perea, A. Climent & F. Paszti. *Europium-doped sesquioxide thin films grown on sapphire by PLD*. Materials Science and Engineering B-Solid State Materials for Advanced Technology **105** p30-33 (2003).

[92] Burmester, P. B. W., G. Huber, M. Kurfiss & M. Schilling. *Crystalline growth of cubic (Eu, Nd): Y_2O_3 thin films on alpha- Al_2O_3 by pulsed laser deposition*. Applied Physics A-Materials Science & Processing **80** p627-630 (2005).

[93] Lancok, J., C. Garapon, C. Martinet, J. Mugnier & R. Brenier. *Influence of the PLD parameters on the crystalline phases and fluorescence of Eu : Y_2O_3 planar waveguides*. Applied Physics A-Materials Science & Processing **79** p1263-1265 (2004).

[94] Lancok, J., M. Jelinek, C. Grivas, F. Flory, E. Lebrasseur & C. Garapon. *Structural and optical characterisation of Nd doped $YAlO_3$ films deposited on sapphire substrate by pulsed laser deposition*. Thin Solid Films **346** p284-289 (1999).

[95] Noh, T. W., S. H. Lee, D. W. Kim, S. M. Oh, M. J. Lim, S. D. Lee, S. H. Han & J. W. Wu. *Growth of epitaxial $LiNbO_3$ films on sapphire substrates and their nonlinear optical properties*. Journal of the Korean Physical Society **32** pS1307-S1310 (1998).

[96] Kim, D. W., S. M. Oh, S. H. Lee & T. W. Noh. *Structural and optical properties of $LiNbO_3$ films grown by pulsed laser deposition with a shadow mask.* Japanese Journal of

Applied Physics Part 1-Regular Papers Short Notes & Review Papers **37** p2016-2020 (1998).

[97] Kim, D. W., S. H. Lee & T. W. Noh. *Structural and nonlinear optical properties of epitaxial $LiNbO_3$ films grown by pulsed laser deposition*. Materials Science and Engineering B-Solid State Materials for Advanced Technology **56** p251-255 (1998).

[98] Tomov, R. I., T. K. Kabadjova, P. A. Atanasov, S. Tonchev, M. Kaneva, A. Zherikhin & R. W. Eason. *$LiNbO_3$ optical waveguides deposited on sapphire by electric- field-assisted pulsed laser deposition*. Vacuum **58** p396-403 (2000).

[99] Chaos, J. A., V. Pruneri, J. Gonzalo & C. N. Afonso. *Second-harmonic generation in highly textured $LiNbO_3$ films prepared by pulsed laser deposition*. Journal of Applied Physics **88** p3768-3770 (2000).

[100] Kakehi, Y., A. Okamato, Y. Sakurai, Y. Nishikawa, T. Yotsuya & S. Ogawa. *Epitaxial growth of $LiNbO_3$ thin films using pulsed laser deposition*. Applied Surface Science **169** p560-563 (2001).

[101] Nakata, Y., S. Gunji, T. Okada & M. Maeda. *Fabrication of $LiNbO_3$ thin films by pulsed laser deposition and investigation of nonlinear properties*. Applied Physics A-Materials Science & Processing **79** p1279-1282 (2004).

[102] Guo, X. L., Z. G. Liu, S. N. Zhu, T. Yu, S. B. Xiong & W. S. Hu. *Pulsed laser deposition of c-oriented $LiNbO_3$/$LiTaO_3$ optical waveguiding bilayered films on silicon wafers*. Journal of Crystal Growth **165** p187-190 (1996).

[103] Wang, X. C., Z. Z. Ye, J. H. He, L. L. Cao & B. H. Zhao. *The role of SiO_2 buffer layer in the growth of highly textured $LiNbO_3$ thin film upon SiO_2/Si by pulsed laser deposition*. Materials Letters **58** p3597-3600 (2004).

[104] Alfonso, J. E., M. J. Martin & C. Zaldo. *Photoluminescence of Nd-doped $LiNbO_3$ films prepared by pulsed laser deposition*. Applied Physics Letters **71** p2904-2906 (1997).

[105] Gonzalo, J., J. A. Chaos, A. Suarez-Garcia, C. N. Afonso & V. Pruneri. *Enhanced second-order nonlinear optical response of $LiNbO_3$ films upon Er doping*. Applied Physics Letters **81** p2532-2534 (2002).

[106] Zaldo, C., D. S. Gill, R. W. Eason, J. Mendiola & P. J. Chandler. *Growth of $KNbO_3$ thin films on MgO by pulsed laser deposition*. Applied Physics Letters **65** p502-504 (1994).

[107] Martin, M. J., J. E. Alfonso, J. Mendiola, C. Zaldo, D. S. Gill, R. W. Eason & P. J. Chandler. *Pulsed laser deposition of $KNbO_3$ films*. Journal of Materials Research **12** p2699-2706 (1997).

[108] Beckers, L., C. Buchal, D. Fluck, T. Pliska & P. Gunter. *Potassium niobate waveguides: He^+ implantation in bulk single crystals and pulsed laser deposition of thin films*. Materials Science and Engineering A **253** p292-295 (1998).

[109] Higuchi, T., T. Aoyama, S. Iwashita, T. Kijima & T. Shimoda. *Fabrication of $KNbO_3$ epitaxial thin films on sapphire substrates by pulsed laser deposition*. Japanese Journal of Applied Physics Part 1-Regular Papers Short Notes & Review Papers **43** p6622-6626 (2004).

[110] Thony, S. S., K. E. Youden, J. J. S. Harris & L. Hesselink. *Growth of epitaxial strontium barium niobate thin films by pulsed laser deposition*. Applied Physics Letters **65** p2018-2020 (1994).

[111] Fernandez, F. E., Y. Gonzalez, H. M. Liu, A. Martinez, V. Rodriguez & W. Y. Jia. *Structure, morphology, and properties of strontium barium niobate thin films grown by pulsed laser deposition*. Integrated Ferroelectrics **42** p219-233 (2002).

[112] Liu, H., S. T. Li, G. K. Liu, W. Jia & F. E. Fernandez. *Optical properties of undoped and Eu^{3+}-doped SBN thin film grown by pulsed laser deposition*. Journal of Luminescence **83-4** p367-371 (1999).

[113] Liu, H., G. K. Liu, S. T. Li, J. V. Beitz & F. E. Fernandez. *Nonlinear optical dynamics and Eu^{3+} spectral holeburning in strontium barium niobate thin film grown by pulsed laser deposition*. Journal of Applied Physics **91** p129-135 (2001).

[114] Shibata, Y., K. Kaya, K. Akashi, M. Kanai, T. Kawai & S. Kawai. *Epitaxial-growth and surface-acoustic-wave properties of $LiTaO_3$ films grown by pulsed-laser deposition*. Applied Physics Letters **62** p3046-3048 (1993).

[115] Agostinelli, J. A., G. H. Braunstein & T. N. Blanton. *Epitaxial $LiTaO_3$ thin films by pulsed laser deposition*. Applied Physics Letters **63** p123-125 (1993).

[116] Davis, G. M. & M. C. Gower. *Epitaxial growth of thin films of $BaTiO_3$ using excimer laser ablation*. Applied Physics Letters **55** p112-114 (1989).

[117] Wang, F. X., W. Li, F. Lu, H. Hu, J. M. Wang, Z. G. Liu & Z. Yong. *$BaTiO_3$ film optical-waveguide prepared by pulsed laser deposition*. Nuclear Instruments & Methods in Physics Research Section B- Beam Interactions with Materials and Atoms **191** p778-782 (2002).

[118] Beckers, L., J. Schubert, W. Zander, J. Ziesmann, A. Eckau, P. Leinenbach & C. Buchal. *Structural and optical characterization of epitaxial waveguiding $BaTiO_3$ thin films on MgO*. Journal of Applied Physics **83** p3305-3310 (1998).

[119] Buchal, C., L. Beckers, A. Eckau, J. Schubert & W. Zander. *Epitaxial $BaTiO_3$ thin films on MgO*. Materials Science and Engineering B-Solid State Materials for Advanced Technology **56** p234-238 (1998).

[120] Petraru, A., J. Schubert, M. Schmid & C. Buchal. *Ferroelectric $BaTiO_3$ thin-film optical waveguide modulators*. Applied Physics Letters **81** p1375-1377 (2002).

[121] Ito, A., A. Machida & M. Obara. *Cobalt doping in $BaTiO_3$ thin films by two-target pulsed KrF laser ablation with in situ laser annealing*. Applied Physics Letters **70** p3338-3340 (1997).

[122] Xiong, S. B., W. P. Ding, Z. G. Liu, X. Y. Chen, X. L. Guo, T. Yu, Y. Y. Zhu & W. S. Hu. *Layered defective lanthanum titanate thin films prepared by pulsed laser ablation of potassium lanthanum titanate ceramics*. Applied Physics Letters **69** p191-193 (1996).

[123] Liao, H. B., R. F. Xiao, P. Yu & G. K. L. Wong. *Growth of beta barium borate (beta-BaB_2O_4) thin films for nonlinear optical applications*. Journal of Crystal Growth **174** p434-439 (1997).

[124] Xiong, F., R. P. H. Chang, M. E. Hagerman, V. L. Kozhevnikov, K. R. Poeppelmeier, H. Zhou, G. K. Wong, J. B. Ketterson & C. W. White. *Pulsed excimer laser deposition of potassium titanyl phosphate films*. Applied Physics Letters **64** p161-163 (1993).

[125] Xiong, F. L., M. Hagerman, H. Zhou, V. Kozhevnikov, G. K. Wong, K. Poeppelmeier, J. B. Ketterson, R. P. H. Chang & C. W. White. *Deposition of nonlinear-optical films of potassium titanyl phosphate ($KTiOPO_4$) by pulsed excimer-laser ablation*. Journal of Vacuum Science & Technology a-Vacuum Surfaces and Films **12** p1446-1450 (1994).

[126] Wang, K., B. Shi, N. Cue, Y. Zhu, R. Xiao, F. Lu, W. Li & Y. Liu. *Waveguide laser film in erbium-doped $KTiOPO_4$ by pulsed laser deposition*. Applied Physics Letters **73** p1020-1022 (1998).

[127] Wang, K. M., B. R. Shi, N. Cue, Y. Y. Zhu, R. F. Xiao, F. Lu, H. Hu & Y. G. Liu. *Waveguide structure of Er-doped $KTiOPO_4$ films on different substrates by pulsed-laser deposition*. Journal of Vacuum Science & Technology a-Vacuum Surfaces and Films **19** p394-397 (2001).

[128] Liu, J. M., F. Zhang, Z. G. Liu, S. N. Zhu, L. J. Shi, Z. C. Wu & N. B. Ming. *Epitaxial-growth of optical $Ba_2NaNb_5O_{15}$ wave-guide film by pulsed-laser deposition*. Applied Physics Letters **65** p1995-1997 (1994).

[129] Liu, J. M., Z. G. Liu, S. N. Zhu, Y. Y. Zhu & N. B. Ming. *Excimer laser ablating preparation of $Ba_2NaNb_5O_{15}$ thin films on $KTiOPO_4$ substrate and its guide wave property*. Applied Surface Science **96-98** p819-822 (1996).

[130] Zhang, M. S., P. Zhang, Z. Yin & J. Liu. *Study of optical waveguide of barium sodium niobate films on potassium titanyl phosphate*. Applied Physics A-Materials Science & Processing **69** p389-395 (1999).

[131] Afonso, C. N., J. M. Ballesteros, J. Gonzalo, G. C. Righini & S. Pelli. *Rare-earth doped glass waveguides prepared by pulsed laser deposition*. Applied Surface Science **96-98** p760-763 (1996).

[132] Serna, R., J. M. Ballesteros, M. J. de Castro, J. Solis & C. N. Afonso. *Optically active Er-Yb doped glass films prepared by pulsed laser deposition*. Journal of Applied Physics **84** p2352-2354 (1998).

[133] Gill, D. S., R. W. Eason, H. N. Rutt, C. Zaldo & N. A. Vainos. *Characterisation of Ga-La-S chalcogenide glass thin-film optical waveguides, fabricated by pulsed laser deposition*. Journal of Non-Crystalline Solids **191** p321-326 (1995).

[134] Peng, C. J., D. Roy & S. B. Krupanidhi. *Oriented lead germanate thin films by excimer laser ablation*. Applied Physics Letters **60** p827-829 (1991).

[135] Mailis, S., A. A. Anderson, S. J. Barrington, W. S. Brocklesby, R. Greef, H. N. Rutt & R. W. Eason. *Photosensitivity of lead germanate glass waveguides grown by pulsed laser deposition*. Optics Letters **23** p1751-1753 (1998).

[136] Mailis, S., C. Riziotis, J. Wang, E. Taylor, A. A. Anderson, S. J. Barrington, H. N. Rutt, R. W. Eason, N. A. Vainos & C. Grivas. *Growth and characterization of pulsed laser deposited lead germanate glass optical waveguides*. Optical Materials **12** p27-33 (1999).

[137] Perna, G., V. Capozzi, S. Pagliara, M. Ambrico & D. Lojacono. *Reflectance and photoluminescence characterization of CdS and CdSe heteroepitaxial films deposited by laser ablation technique*. Thin Solid Films **387** p208-211 (2001).

[138] Bagnall, D. M., B. Ullrich, H. Sakai & Y. Segawa. *Micro-cavity lasing of optically excited CdS thin films at room temperature*. Journal of Crystal Growth **214** p1015-1018 (2000).

[139] Ullrich, B., D. M. Bagnall, H. Sakai & Y. Segawa. *Photoluminescence and lasing of thin CdS films on glass formed by pulsed-laser-deposition*. Journal of Luminescence **87-9** p1162-1164 (2000).

[140] Hu, W. S., Z. G. Liu, X. L. Guo, C. Lin, S. N. Zhu & D. Feng. *Preparation of c-axis oriented ZnO optical wave-guiding films on fused-silica by pulsed-laser reactive ablation*. Materials Letters **25** p5-8 (1995).

[141] Hu, W. S., Z. G. Liu, J. Sun, X. L. Guo, Z. J. Yang, L. J. Shi & D. Feng. *Pulsed laser reactive ablation of (0001)-textured ZnO optical waveguiding films on alpha-SiO_2*. Materials Science and Engineering B-Solid State Materials for Advanced Technology **40** p165-169 (1996).

[142] Ryu, Y. R., S. Zhu, J. D. Budai, H. R. Chandrasekhar, P. F. Miceli & H. W. White. *Optical and structural properties of ZnO films deposited on GaAs by pulsed laser deposition*. Journal of Applied Physics **88** p201-204 (2000).

[143] Bae, S. H., S. Y. Lee, B. J. Jin & S. Im. *Pulsed laser deposition of ZnO thin films for applications of light emission*. Applied Surface Science **154** p458-461 (2000).

[144] Bae, S. H., S. Y. Lee, H. Y. Kim & S. Im. *Comparison of the optical properties of ZnO thin films grown on various substrates by pulsed laser deposition*. Applied Surface Science **168** p332-334 (2000).

[145] Kim, T. W., D. U. Lee, D. C. Choo, J. H. Lee, M. Jung, J. Cho, K. Y. Seo & Y. S. Yoon. *Microstructural and optical properties of ZnO thin films grown on InSb (111) substrates*. Journal of Physics and Chemistry of Solids **62** p1199-1203 (2001).

[146] Hu, W. S., Z. G. Liu, J. Sun, S. N. Zhu, Q. Q. Xu, D. Feng & Z. M. Ji. *Optical properties of pulsed laser deposited ZnO thin films*. Journal of Physics and Chemistry of Solids **58** p853-857 (1997).

[147] Tang, Z. K., G. K. L. Wong, P. Yu, M. Kawasaki, A. Ohtomo, H. Koinuma & Y. Segawa. *Room-temperature ultraviolet laser emission from self-assembled ZnO micro-crystallite thin films*. Applied Physics Letters **72** p3270 (1998).

[148] Jelinek, M., J. Lancok, M. Pavelka, P. A. Atanasov, A. Mackova, F. Flory & C. Garapon. *Optical and waveguiding properties of Nd : KGW films grown by pulsed laser deposition*. Applied Physics A-Materials Science & Processing **74** p481-485 (2002).

[149] Blomqvist, M., S. Khartsev, A. Grishin, A. Petraru & C. Buchal. *Optical waveguiding in magnetron-sputtered $Na_{0.5}K_{0.5}NbO_3$ thin films on sapphire substrates*. Applied Physics Letters **82** p439-441 (2003).

[150] Lansiaux, X., E. Dogheche, D. Remiens, M. Guilloux-viry, A. Perrin & P. Ruterana. *$LiNbO_3$ thick films grown on sapphire by using a multistep sputtering process*. Journal of Applied Physics **90** p5274-5277 (2001).

[151] Bai, G. R., H. L. M. Chang & C. M. Foster. *Preparation of single-crystal $Y_3Al_5O_{12}$ thin-film by metalorganic chemical-vapor-deposition*. Applied Physics Letters **64** p1777-1779 (1994).

[152] Gornert, P. & F. Voigt. *High temperature solution growth of garnets: theoretical models and experimental results*. In Current Topics in Material Science. Kaldis, E. (Ed.). p1 (1984).

[153] Park, J. H., J. K. Cho, K. Nishimura, H. Uchida & M. Inoue. *Growth of epitaxial garnet film by LPE for application to integrated magneto-optic light switch arrays*. Physica Status Solidi A-Applied Research **201** p1976-1979 (2004).

[154] Aichele, T., A. Lorenz, R. Hergt & P. Gornert. *Garnet layers prepared by liquid phase epitaxy for microwave and magneto-optical applications - a review*. Crystal Research and Technology **38** p575-587 (2003).

[155] Pelenc, D., B. Chambaz, I. Chartier, B. Ferrand & J. C. Vial. *Epitaxial-growth of garnets for thin-film lasers*. Journal De Physique IV **1** p311-314 (1991).

[156] Ferrand, B., D. Pelenc, I. Chartier & C. Wyon. *Growth by LPE of Nd-YAG single-crystal layers for wave-guide laser applications*. Journal of Crystal Growth **128** p966-969 (1993).

[157] Bonner, C. L., C. T. A. Brown, D. P. Shepherd, W. A. Clarkson, A. C. Tropper, D. C. Hanna & B. Ferrand. *Diode-bar end-pumped high-power $NdY_3Al_5O_{12}$ planar waveguide laser*. Optics Letters **23** p942-944 (1998).

[158] Ubizskii, S. B., A. O. Matkovskii, S. S. Melnyk, I. M. Syvorotka, V. Muller, V. Peters, K. Petermann, A. Beyertt & A. Giesen. *Optical properties of epitaxial YAG : Yb films*. Physica Status Solidi A-Applied Research **201** p791-797 (2004).

[159] Sarnecki, J., K. Kopczynski, Z. Mierczyk, J. Skwarcz & J. Mlynczak. *Liquid-phase epitaxy growth and characterization of Co,Si : YAG thin film saturable absorber*. Optical Materials **27** p445-448 (2004).

[160] Gerhardt, R., J. Kleine-Borger, L. Beilschmidt, M. Frommeyer, H. Dotsch & B. Gather. *Efficient channel-waveguide laser in Nd:GGG at 1.062 mu m wavelength*. Applied Physics Letters **75** p1210-1212 (1999).

[161] Balaji, T., G. Lifante, E. Daran, R. Legros & G. Lacoste. *Growth by molecular beam epitaxy and characterization of $CaF_2 : Pr^{3+}$ planar waveguides*. Thin Solid Films **339** p187-193 (1999).

[162] Bhutta, T., A. M. Chardon, D. P. Shepherd, E. Daran, C. Serrano & A. Munoz-Yague. *Low phonon energy, Nd : LaF_3 channel waveguide lasers fabricated by molecular beam epitaxy*. IEEE Journal of Quantum Electronics **37** p1469-1477 (2001).

[163] Lou, L., W. Zhang, A. Brioude, C. L. Luyer & J. Mugnier. *Preparation and characterisation of sol-gel Y_2O_3 planar waveguides*. Optical Materials **18** p331-336 (2001).

[164] Guo, H., W. Zhang, L. Lou, A. Brioude & J. Mugnier. *Structure and optical properties of rare earth doped Y_2O_3 waveguide films derived by sol-gel process*. Thin Solid Films **458** p274-280 (2004).

[165] Que, W. X., Y. Zhou, Y. L. Lam, Y. C. Chan, H. T. Tan, T. H. Tan & C. H. Kam. *Sol-gel processed silica/titania/y- glycidoxypropyltrimethoxysilane composite materials for photonic applications*. Journal of Electronic Materials **29** p1052-1058 (2000).

[166] Que, W. X. & C. H. Kam. *Sol-gel fabrication and properties of optical channel waveguides and gratings made from composites of titania and organically modified silane*. Optical Engineering **41** p1733-1737 (2002).

[167] Brown, C. T. A., C. L. Bonner, T. J. Warburton, D. P. Shepherd, A. C. Tropper, D. C. Hanna & H. E. Meissner. *Thermally bonded planar waveguide lasers*. Applied Physics Letters **71** p1139-1141 (1997).

[168] Sugiyama, A., H. Fukuyama, T. Sasuga, T. Arisawa & H. Takuma. *Direct bonding of Ti : sapphire laser crystals*. Applied Optics **37** p2407-2410 (1998).

[169] Shepherd, D. P., C. L. Bonner, C. T. A. Brown, W. A. Clarkson, A. C. Tropper, D. C. Hanna & H. E. Meissner. *High-numerical-aperture, contact-bonded, planar waveguides for diode-bar-pumped lasers*. Optics Communications **160** p47-50 (1999).

[170] Hempstead, M., J. S. Wilkinson & L. Reekie. *Wave-guide lasers operating at 1084 nm in neodymium-diffused lithium-niobate*. IEEE Photonics Technology Letters **4** p852-855 (1992).

[171] Wei, P. K. & W. S. Wang. *Fabrication of lithium-niobate optical channel waveguides by nickel indiffusion*. Microwave and Optical Technology Letters **7** p219-221 (1994).

[172] Aust, J. A., K. J. Malone, D. L. Veasey, N. A. Sanford & A. Roshko. *Passively Q-switched Nd-doped wave-guide laser*. Optics Letters **19** p1849-1851 (1994).

[173] Hettrick, S. J., J. I. Mackenzie, R. D. Harris, J. S. Wilkinson, D. P. Shepherd & A. C. Tropper. *Ion-exchanged tapered-waveguide laser in neodymium-doped BK7 glass*. Optics Letters **25** p1433-1435 (2000).

[174] Huang, X., N. Cutinha, A. A. de Velasco, P. J. Chandler & P. D. Townsend. *Upconversion in erbium doped YAG ion-implanted waveguides*. Nuclear Instruments & Methods in Physics Research Section B- Beam Interactions with Materials and Atoms **142** p50-60 (1998).

[175] Vazquez, G. V., J. Rickards, H. Marquez, G. Lifante, E. Cantelar & M. Domenech. *Optical waveguides in Nd : YAG by proton implantation*. Optics Communications **218** p141-146 (2003).

[176] Mairaj, A. K., P. Hua, H. N. Rutt & D. W. Hewak. *Fabrication and characterization of continuous wave direct UV (lambda=244 nm) written channel waveguides in chalcogenide (Ga : La : S) glass*. Journal of Lightwave Technology **20** p1578-1584 (2002).

[177] Faerch, K. & M. Svalgaard. *Symmetrical waveguide devices fabricated by direct UV writing*. IEEE Photonics Technology Letters **14** p173-175 (2002).

[178] Wood, R. F., G. A. Geist & C. L. Liu. *Two-dimensional modeling of pulsed-laser irradiated alpha-Si and other materials*. Physical Review B **53** p15863-15870 (1996).

[179] Amoruso, S.. *Modeling of UV pulsed-laser ablation of metallic targets*. Applied Physics A-Materials Science & Processing **69** p323-332 (1999).

[180] Tosto, S.. *Modeling and computer simulation of pulsed-laser-induced ablation*. Applied Physics A-Materials Science & Processing **68** p439-446 (1999).

[181] Granse, G., S. Vollmar, A. Lenk, A. Rupp & K. Rohr. *Modeling of laser induced plasma, spectroscopic and time of flight experiments in pulsed laser deposition*. Applied Surface Science **96-98** p97-101 (1996).

[182] Mayr, S. G., M. Moske, K. Samwer, M. E. Taylor & H. A. Atwater. *The role of particle energy and pulsed particle flux in physical vapor deposition and pulsed-laser deposition*. Applied Physics Letters **75** p4091-4093 (1999).

[183] Kuzma, M., M. Bester, L. Pyziak, I. Stefaniuk & I. Virt. *Modelling of growth of thin solid films obtained by pulsed laser deposition*. Applied Surface Science **168** p132-135 (2000).

[184] Itina, T. E., W. Marine & M. Autric. *Mathematical modelling of pulsed laser ablated flows*. Applied Surface Science **154-155** p60-65 (2000).

[185] Tyunina, M., J. Levoska & S. Leppavuori. *Sorption in pulsed laser deposition of multicomponent materials: Experiment versus modeling*. Journal of Applied Physics **86** p2901-2908 (1999).

[186] Lo, E. Y., W. T. Laughlin & E. R. Pugh. *A numerical model of the pulsed-laser deposition coating process*. Miller, J. C. & D. B. Geohegan (Eds.). Laser Ablation: Mechanisms and Applications - II, Knoxville, TN (1993).

[187] Cheung, J. T.. *History and fundamentals of pulsed laser deposition*. In Pulsed laser deposition of thin films. Chrisey, D. B. & G. K. Hubler (Eds.). p1 (1994).

[188] Jackson, S. R., W. J. Metheringham & P. E. Dyer. *Excimer laser ablation of Nd:YAG and Nd:Glass*. Applied Surface Science **86** p223-227 (1995).

[189] Laser ablation. http://epsc.wustl.edu/admin/resources/icpms/laser.html. (Last accessed: November 2004).

[190] Bloembergen, N.. *Laser Solid Interaction and Laser Processing*. Leamy, H. J. & J. M. Poate (Eds.). AIP Press, (1979).

[191] Ready, J. F.. *Effect of High Power Laser Radiation*. Academic Press, (1971).

[192] Allmen, M. V.. *Laser ablation of solids: basic principles and physical effects*. In Laser Ablation of Electronic Materials - Basic Mechanisms and Applications. Fogarassy, E. & S. Lazare (Eds.). p55-59 (1992).

[193] Guidoni, A. G., R. Kelly, A. Mele & A. Miotello. *Heating effects and gas-dynamic expansion of the plasma plume produced by irradiating a solid with laser pulses*. Plasma Sources Science & Technology **6** p260-269 (1997).

[194] Tyunina, M. & S. Leppavuori. *Effects of laser fluence, size, and shape of the laser focal spot in pulsed laser deposition using a multielemental target*. Journal of Applied Physics **87** p8132-8142 (2000).

[195] Singh, R. K.. *Spatial thickness variations in laser-deposited thin films*. Materials Science and Engineering B-Solid State Materials for Advanced Technology **45** p180-185 (1997).

[196] Anisimov, S. I., B. S. Lukyanchuk & A. Luches. *An analytical model for three-dimensional laser plume expansion into vacuum in hydrodynamic regime*. Applied Surface Science **96-98** p24-32 (1996).

[197] Lunney, J. G. & R. Jordan. *Pulsed laser ablation of metals*. Applied Surface Science **127-129** p941-946 (1998).

[198] Singh, R. K. & J. Viatella. *Estimation of plasma absorption effects during pulsed-laser ablation of high-critical-temperature superconductors*. Journal of Applied Physics **75** p1204-1206 (1994).

[199] Geohegan, D. B.. *Diagnostics and characteristics of laser-produced plasmas*. In Pulsed Laser Deposition of Thin Films. Chrisey, D. B. & G. K. Hubler (Eds.). p115 (1994).

[200] Kelly, R. & A. Miotello. *On the mechanisms of target modification by ion beams and laser pulses*. Nuclear Instruments & Methods in Physics Research Section B- Beam Interactions with Materials and Atoms **122** p374-400 (1997).

[201] Geohegan, D. B.. *Effects of ambient background gases on YBCO plume propagation under film growth conditions: spectroscopic, ion probe, and fast photographic studies*. In Laser Ablation of Electronic Materials - Basic Mechanisms and Applications. Fogarassy, E. & S. Lazare (Eds.). p73-88 (1992).

[202] Champeaux, C., D. Damiani, C. Girault, P. Marchet, J. Aubreton, J. P. Mecurio & A. Catherinot. *Plasma formation from laser-target interaction; basic phenomena and applications to superconducting thin film deposition*. In Laser Ablation of Electronic Materials - Basic Mechanisms and Applications. Fogarassy, E. & S. Lazare (Eds.). p141-165 (1992).

[203] Foote, M. C., B. B. Jones, B. D. Hunt, J. B. Barner, R. P. Vasquez & L. J. Bajuk. *Composition variations in pulsed-laser-deposited Y-Ba-Cu-O thin-films as a function of deposition parameters*. Physica C **201** p176-182 (1992).

[204] Strikovski, M., J. H. Miller Jr & J. Wosik. *Deposition rate as the key parameter in pulsed laser deposition of oxide films: a practical model and experiment*. Physica C **341-348** p2349-2350 (2000).

[205] Ohring, M.. *The Materials Science of Thin Films*. Academic Press, (1992).

[206] Horwitz, J. S. & J. A. Sprague. *Film nucleation and film growth in pulsed laser deposition of ceramics*. In Pulsed Laser Deposition of Thin Films. Chrisey, D. B. & G. K. Hubler (Eds.). p229 (1994).

[207] Willmott, P. R.. *Deposition of complex multielemental thin films*. Progress in Surface Science **76** p163-217 (2004).

[208] Venables, J. A.. *Atomic processes in crystal growth*. Surface Science **299/300** p798-817 (1994).

[209] Chen, L. C.. *Particulates generated by pulsed laser ablation*. In Pulsed Laser Deposition of Thin Films. Chrisey, D. B. & G. K. Hubler (Eds.). p167 (1994).

[210] Tomov, R. I., V. P. Manolov, P. A. Atanasov, V. N. Tsaneva, D. G. Ouzounov & V. I. Tsanev. *Experimental and theoretical investigation of cumulative laser irradiation effects in YBCO thin film pulsed laser deposition*. Physica C **274** p187-196 (1997).

[211] Foltyn, S. R.. *Surface modification of materials by cumalitive laser irradiation*. In Pulsed Laser Deposition of Thin Films. Chrisey, D. B. & G. K. Hubler (Eds.). p98 (1994).

[212] Lowndes, D. H., M. J. Godbole, G. E. Jellison & A. J. Pedraza. *Ablation, surface activation and electroless metallization of insulating materials by pulsed excimer laser*

irradiation. Miller, J. C. & D. B. Geohegan (Eds.). Laser Ablation: Mechanisms and Applications - II, Knoxville, TN (1993).

[213] Chang, C. C., X. D. Wu, R. Ramesh, X. X. Xi, T. S. Ravi, T. Venkatesan, D. M. Hwang, R. E. Muenchausen, S. Foltyn & N. S. Nogar. *Origin of surface roughness for c-axis oriented Y-Ba-Cu-O superconducting films*. Applied Physics Letters **57** p1814-1816 (1990).

[214] Bhattacharya, D., R. K. Singh & P. H. Holloway. *Laser-target interactions during pulsed laser deposition of superconducting thin-films*. Journal of Applied Physics **70** p5433-5439 (1991).

[215] Watanabe, Y., Y. Seo, M. Tanamura, H. Asami & Y. Matsumoto. *Compositional distribution of laser-deposited films and rapid sequential pulsed-laser deposition*. Journal of Applied Physics **78** p5126-5135 (1995).

[216] Watanabe, Y., M. Tanamura, Y. Matsumoto & Y. Seki. *Laser power dependence of particulate formation on pulse laser deposited films*. Journal of Applied Physics **78** p2029-2036 (1995).

[217] Zhu, S., D. H. Lowndes, B. C. Chakoumakos, D. K. Christen, J. D. Budai, X. Y. Zheng & R. J. Warmack. *Effects of deposition rate on $Bi_2Sr_2CaCu_2O_{8+x}$ and $Bi_2Sr_{1.6}La_{0.4}CuO_{6+x}$ epitaxial thin-film growth by pulsed-laser deposition*. Miller, J. C. & D. B. Geohegan (Eds.). Laser Ablation: Mechanisms and Applications - II, Knoxville, TN (1993).

[218] Jordan, R., D. Cole & J. G. Lunney. *Pulsed laser deposition of particulate-free thin films using a curved magnetic filter*. Applied Surface Science **109/110** p403-407 (1997).

[219] Gorbunov, A. A., W. Pompe, A. Sewing, S. V. Gaponov, A. D. Akhsakhalyan, I. G. Zabrodin, L. A. Kas'kov, E. B. Klyenkov, A. P. Morozov, N. N. Salaschenko, R. Dietsch, H. Mai & S. Vollmar. *Ultrathin fim deposition by pulsed laser ablation using crossed beams*. Applied Surface Science **96-98** p649-655 (1996).

[220] Willmott, P. R., H. Spillmann & J. R. Huber. *Design and synthesis of novel thin films and structures by reactive crossed-beam laser ablation*. Journal of Materials Chemistry **12** p397-402 (2002).

[221] Mackenzie, J. I., C. Li & D. P. Shepherd. *Multi-watt, high efficiency, diffraction-limited Nd:YAG planar waveguide laser*. IEEE Journal of Quantum Electronics **39** p493-500 (2003).

[222] Mackenzie, J. I., C. Li, D. P. Shepherd, R. J. Beach & S. C. Mitchell. *Modeling of high-power continuous-wave Tm:YAG side-pumped double-clad waveguide lasers*. IEEE Journal of Quantum Electronics **38** p222-230 (2002).

[223] Mackenzie, J. I., C. Li, D. P. Shepherd, H. E. Meissner & S. C. Mitchell. *Longitudinally diode-pumped Nd : YAG double-clad planar waveguide laser*. Optics Letters **26** p698-700 (2001).

[224] Soldano, L. B., F. B. Veerman, M. K. Smit, B. H. Verbeek, A. H. Dubost & E. C. M. Pennings. *Planar monomode optical couplers based on multimode interference effects*. Journal of Lightwave Technology **10** p1843-1850 (1992).

[225] Heaton, J. M., R. M. Jenkins, D. R. Wight, J. T. Parker, J. C. H. Birbeck & K. P. Hilton. *Novel 1-to-N way integrated optical beam splitters using symmetric mode mixing in GaAs/AlGaAs multimode waveguides*. Applied Physics Letters **61** p1754-1756 (1992).

[226] Bryngdahl, O.. *Image formation using self-imaging techniques*. Journal of the Optical Society of America **63** p416-419 (1973).

[227] Ulrich, R. & G. Ankele. *Self-imaging in homogeneous planar optical waveguides*. Applied Physics Letters **27** p337-339 (1975).

[228] Ulrich, R.. *Image formation by phase coincidences in optical waveguides*. Optics Communications **13** p259-262 (1975).

[229] Baker, H. J., J. R. Lee & D. R. Hall. *Self-imaging and high-beam-quality operation in multi-mode planar waveguide optical amplifiers*. Optics Express **10** p297-301 (2002).

[230] Pelouch, W. S., D. D. Smith, J. E. Koroshetz, I. T. McKinnie, J. R. Unternahrer, S. W. Henderson & W. R. Scharpf. *Self-imaging in waveguide lasers and amplifiers*. ASSL (Technical Digest), Quebec City, February (2002).

[231] Comaskey, B., B. D. Moran, G. F. Albrecht & R. J. Beach. *Characterisation of the heat loading of Nd-doped YAG, YOS, YLF, and GGG excited at diode pumping wavelengths*. IEEE Journal of Quantum Electronics **31** p1261-1264 (1995).

[232] Koechner, W.. *Solid-State Laser Engineering*. Schawlow, A. L., A. E. Siegman & T. Tamir (Eds.). Springer, (1999).

[233] Digonnet, M. J. F. & C. J. Gaeta. *Theoretical analysis of optical fiber laser amplifiers and oscillators*. Applied Optics **24** p333-341 (1985).

[234] Risk, W. P.. *Modelling of longitudinally pumped solid-state lasers exhibiting reabsorption losses*. Journal of the Optical Society of America B-Optical Physics **5** p1412 (1988).

[235] Clarkson, W. A. & D. C. Hanna. *Effects of transverse-mode profile on slope efficiency and relaxation oscillations in a longitudinally-pumped laser*. Journal of Modern Optics **36** p483-498 (1989).

[236] Taira, T., W. M. Tulloch & R. L. Byer. *Modeling of quasi-three-level lasers and operation of cw Yb:YAG lasers*. Applied Optics **36** p1867-1874 (1997).

[237] Barrington, S. J. & R. W. Eason. *Homogeneous substrate heating using a CO2 laser with feedback, rastering, and temperature monitoring*. Review of Scientific Instruments **71** p4223-4225 (2000).

[238] Gill, D. S.. *Fabrication and characterisation of thin film optical waveguides by pulsed laser deposition*. Ph.D. Thesis, Physics & Astronomy, University of Southampton, Southampton (1996).

[239] Wu, K. H., C. L. Lee, J. Y. Juang, T. M. Uen & Y. S. Gou. *Insitu growth of $Y_1Ba_2Cu_3O_{7-x}$ superconducting thin-films using a pulsed neodymium yttrium-aluminium-garnet laser with CO_2-laser heated substrates*. Applied Physics Letters **58** p1089-1091 (1991).

[240] Youden, K. E.. *Fabrication and characterisation of photorefractive thin films and waveguides*. Ph.D. Thesis, Physics & Astronomy, University of Southampton, Southampton (1993).

[241] Campion, R., R. G. Ormson, C. A. Bashford & P. J. King. *Design and performance of a reliable and low-cost substrate heater for superconducting thin-film deposition*. Vacuum **46** p195-197 (1995).

[242] Cillessen, J. F. M., M. J. M. deJong & X. Croize. *Improved uniformity of multielement thin films prepared by off- axis pulsed laser deposition using a new heater design*. Review of Scientific Instruments **67** p3229-3237 (1996).

[243] Zhou, Y. L., X. M. Xiong, H. B. Lu, D. F. Cui, Z. H. Chen, C. L. Li, Y. W. Liu, M. He & G. Z. Yang. *Double-sided $YBa_2Cu_3O_{7-delta}$ superconducting films prepared by laser ablation with a Si radiation heater*. Journal of Superconductivity **9** p625-627 (1996).

[244] Ohashi, S., M. Lippmaa, N. Nakagawa, H. Nagasawa, H. Koinuma & M. Kawasaki. *Compact laser molecular beam epitaxy system using laser heating of substrate for oxide film growth*. Review of Scientific Instruments **70** p178-183 (1999).

[245] Anderson, A. A.. *Crystalline planar waveguide lasers fabricated by pulsed laser deposition*. Ph.D. Thesis, Physics & Astronomy, University of Southampton, Southampton (1998).

[246] McGee, T. D.. *Principles and Methods of Temperature Measurement*. John Wiley & Sons, (1988).

[247] Buzea, C., H. Myoren, H. B. Wang, K. Nakajima & T. Yamashita. *Variation of LaSrCuO film temperature during pulsed laser deposition on LaSrGaO substrate*. IEEE Transactions on Applied Superconductivity **9** p2398-2401 (1999).

[248] Buzea, C., H. B. Wang, K. Nakajima, S. J. Kim & T. Yamashita. *Comprehensive study of the film surface temperature and plasma thermokinetics during $La_{1.85}Sr_{0.15}CuO_4$ deposition by laser ablation*. Journal of Applied Physics **86** p2856-2864 (1999).

[249] Thompson, P., Y. Li, J. J. Zhou, D. L. Sato, L. Flanders & H. P. Lee. *Diffuse reflectance spectroscopy measurement of substrate temperature and temperature transient during molecular beam epitaxy and implications for low-temperature III-V epitaxy*. Applied Physics Letters **70** p1605-1607 (1997).

[250] Zhao, R. A., M. J. Cich, P. Specht & E. R. Weber. *In situ diffuse reflectance spectroscopy investigation of low- temperature-grown GaAs*. Applied Physics Letters **80** p2060-2062 (2002).

[251] Johnson, S. R. & T. Tiedje. *Effect of substrate thickness, back surface texture, reflectivity, and thin film interference on optical band-gap thermometry*. Journal of Crystal Growth **175** p273-280 (1997).

[252] Guyer, J. E., W. F. Tseng & J. G. Pellegrino. *Diffuse reflectance spectroscopy for in situ process monitoring and control during molecular beam epitaxy growth of InGaAs/AlGaAs pseudomorphic high electron mobility transistors*. Journal of Vacuum Science & Technology B **18** p2518-2522 (2000).

[253] Wang, Z. Z., S. L. Kwan, T. P. Pearsall, J. L. Booth, B. T. Beard & S. R. Johnson. *Real-time, noninvasive temperature control of wafer processing based on diffusive reflectance spectroscopy*. Journal of Vacuum Science & Technology B **15** p116-121 (1997).

[254] Johnson, S. R., C. Lavoie, T. Tiedje & J. A. Mackenzie. *Semiconductor substrate-temperature measurement by diffuse reflectance spectroscopy in molecular-beam epitaxy*. Journal of Vacuum Science & Technology B **11** p1007-1010 (1993).

[255] Li, Y., J. J. Zhou, P. Thompson, D. Pacheco, D. L. Sato, O. Arain & H. P. Lee. *Simultaneous in situ measurement of substrate temperature and layer thickness using diffuse reflectance spectroscopy (DRS) during molecular beam epitaxy*. Journal of Crystal Growth **175-176** p250-255 (1997).

[256] Inorganic crystal structure database (ICSD), part of the chemical database service (CDS) based at Daresbury Laboratory UK. http://cds3.dl.ac.uk/dif/icsd. (Last accessed: March 2005).

[257] Findlay, D. & R. A. Clay. *The measurement of internal losses in 4-level lasers*. Physics Letters **20** p277 (1966).

[258] Nishimura, T. & T. Omi. *Relation between laser characteristics and Nd ion concentration in Nd: YAG crystals*. Japanese Journal of Applied Physics **14** p1011 (1975).

[259] Shirk, M. D., P. A. Molian & A. P. Malshe. *Ultrashort pulsed laser ablation of diamond*. Journal of Laser Applications **10** p64-70 (1998).

[260] Zhang, Z., P. A. VanRompay, J. A. Nees & P. P. Pronko. *Multi-diagnostic comparison of femtosecond and nanosecond pulsed laser plasmas*. Journal of Applied Physics **92** p2867-2874 (2002).

[261] Zhang, Z., P. A. VanRompay, J. A. Nees, R. Clarke, X. Pan & P. P. Pronko. *Nitride film deposition by femtosecond and nanosecond laser ablation in low-pressure nitrogen discharge gas*. Applied Surface Science **154** p165-171 (2000).

[262] Loir, A. S., F. Garrelie, J. L. Subtil, F. Goutaland, M. Belin, R. Le Harzic, C. Donnet, Y. Ouerdane, F. Rogemond & P. Laporte. *Study of plasma expansion induced by femtosecond pulsed laser ablation and deposition of diamond-like carbon films*. Applied Surface Science **208** p553-560 (2003).

[263] Okoshi, M., K. Higashikawa & M. Hanabusa. *Pulsed laser deposition of ZnO thin films using a femtosecond laser*. Applied Surface Science **154** p424-427 (2000).

[264] Millon, E., O. Albert, J. C. Loulergue, J. Etchepare, D. Hulin, W. Seiler & J. Perriere. *Growth of heteroepitaxial ZnO thin films by femtosecond pulsed- laser deposition*. Journal of Applied Physics **88** p6937-6939 (2000).

[265] Trelenberg, T. W., L. N. Dinh, C. K. Saw, B. C. Stuart & M. Balooch. *Femtosecond pulsed laser ablation of GaAs*. Applied Surface Science **221** p364-369 (2004).

[266] Millon, E., J. Perriere, R. M. Defourneau, D. Defourneau, O. Albert & J. Etchepare. *Femtosecond pulsed-laser deposition of $BaTiO_3$.* Applied Physics a-Materials Science & Processing **77** p73-80 (2003).